The Use of Satellite-Derived Heterogeneous Surface Soil Moisture for Numerical Weather Prediction

by

Andrew S. Jones

Department of Atmospheric Science
Colorado State University
Fort Collins, Colorado

Colorado State University

Department of Atmospheric Science

Paper No. 617

THE USE OF SATELLITE-DERIVED HETEROGENEOUS SURFACE SOIL MOISTURE FOR NUMERICAL WEATHER PREDICTION

Andrew S. Jones

Department of Atmospheric Science
Colorado State University
Fort Collins, Colorado

Summer 1996

Atmospheric Science Paper No. 617

ABSTRACT

THE USE OF SATELLITE-DERIVED HETEROGENEOUS SURFACE SOIL MOISTURE FOR NUMERICAL WEATHER PREDICTION

This work's general scientific objective is to develop and apply a coupled satellite-model data assimilation approach to observe heterogeneous soil moisture effects on the mesoscale for use in understanding and quantifying the processes that have an impact on the preconvective mesoscale environment and affect initial convective cloud development related to surface-forced circulations. Several satellite-based methods are used to investigate the feasibility of retrieving surface wetness information. Passive microwave satellite data are used as a subjective indicator of surface wetness, while a quantitative satellite data assimilation method is developed to assimilate observational infrared heating rates into an atmospheric mesoscale model to retrieve model soil moisture. The data assimilation method employs a prognostic soil model with explicit bare soil and vegetation surface components.

In a case study, the data assimilation method is successful at retrieving realistic representations of the heterogeneous soil moisture. However, limitations are found regarding the ability to retrieve extreme dry or wet events using the current model surface parameterization. This has implications on the ability of the retrieved soil moisture values to affect the atmospheric model's forecast. Instrument noise is not found to be a major factor in the data assimilation method's performance.

Atmospheric-corrected microwave surface emittance results are shown to enhance the use of the microwave datasets for determining land surface characteristics, especially in regards to analysis of the data's frequency dependencies. Several problems that affect the use of the microwave brightness temperature data were examined, including natural characteristics of the spatial and temporal variability of the microwave background signature, and sub-field of view effects.

The microwave surface emittance was found to be sensitive to numerous rain events captured in the dataset. The relationship of the microwave surface emittance to a vegetation index is shown to be highly variable for all but the sparsest vegetation amounts when analyzed at high spatial resolutions. The complexity of the microwave surface emittance versus vegetation relationship limits any future quantitative use of the microwave surface emittance for direct soil moisture retrieval; however, the potential application of the microwave surface emittance for flood monitoring purposes and trafficability indices is high for non-forested regions.

ACKNOWLEDGMENTS

This work was supported by the DOD Center for Geosciences under ARO grants DAAH04-94-G-0420 and DAAL03-86-G-0190, and by NOAA through grant NA90RAH00077, to the Co-operative Institute for Research in the Atmosphere (CIRA), at CSU.

TABLE OF CONTENTS

LIST OF TABLES

LIST OF FIGURES

LIST OF SYMBOLS

b	plant dependent microwave attenuation constant
$c = 3.0 \times 10^{8}\ \mathrm{m \cdot s^{-1}}$	speed of light
c_p	atmospheric heat capacity at constant pressure
c_s	soil specific heat capacity
$d\tau / d \ln p$	infrared atmospheric weighting function
$dB_k(x, y)$	SSM/I antenna pattern (dB)
$g = 9.81\ \mathrm{m \cdot s^{-2}}$	gravitational constant
$h = 6.63 \times 10^{-34}\ \mathrm{J \cdot s}$	Planck's constant
h'	microwave roughness height parameter
h_s	top of the surface layer
$k = 1.38 \times 10^{-23}\ \mathrm{J \cdot K^{-1}}$	Boltzmann's constant
k	Von Karmann's constant
k_s	soil thermal diffusivity
m_v	cloud water content
n	relative complex index of refraction
$n_x(k)$	SSM/I antenna pattern best-fit coefficient (cross-track)
$n_y(k)$	SSM/I antenna pattern best-fit coefficient (along-track)
$p(r)$	drop-size distribution
p	atmospheric pressure
q_3''	subgrid scale specific humidity perturbation for water vapor
q_{sat}	saturated specific humidity

q_G	surface specific humidity
q_*	friction humidity
r	particle radius
u_*	friction velocity
w''	subgrid scale vertical velocity perturbation
z	height
z_0	roughness height
z_i	top of the atmospheric boundary layer
z_G	ground surface height
A	surface albedo
A	attenuation (dB)
A_a	absorption cross-section
A_e	extinction cross-section
A_s	scattering cross-section
A	SMI best fit coefficient
$B_\nu(T)$	Planck function
$B_\nu\left(T_{space}\right)$	deep space emission
$B_\nu^{-1}(L)$	inverse of the Planck function
B	SMI best fit coefficient
C_b	surface heat resistance
D_η	soil moisture flux parameter
E	latent heat flux
H	sensible heat flux
$J(\mathbf{r},\Omega_s)$	total effective source function
K_η	soil hydraulic conductivity
L	Monin length
L	SAVI soil correction term

L_{atm}	direct atmospheric radiance
L_m	"measured" out-going radiance at the top of the atmosphere
$L_{reflected}$	reflected atmospheric radiance
L_{sfc}	surface radiance
L_{space}	top of the atmosphere radiative boundary condition
L_v	latent heat of vaporization
$L_v(\mathbf{r}, \Omega_s)$	spectral radiance
P_a	power absorbed
P_s	power scattered
Q	microwave roughness polarization mixing parameter
Q_a	absorption efficiency factor
Q_e	extinction efficiency factor
Q_s	scattering efficiency factor
Q_C	convective heat flux
Q_G	conductive heat flux
Q_R	net radiative heat flux
$R_d = 287\ \mathrm{J \cdot kg^{-1} \cdot K^{-1}}$	gas constant for dry air
$\overline{R}_{\downarrow lw_G}$	downward longwave radiation flux
$\overline{R}_{\uparrow lw_G}$	upward longwave radiation flux
$\overline{R}_{\downarrow sw_G}$	direct downward shortwave radiation flux
$\overline{R}^{\,D}_{\downarrow sw_G}$	diffuse downward shortwave radiation flux
Ri	Richardson number
S_i	incident flux density
T	temperature (K)
TB_{19H}	SSM/I 19H GHz microwave brightness temperature (K)
TB_{85H}	SSM/I 85.5H GHz microwave brightness temperature (K)
TB_{v_1}	MSU 50.30 GHz microwave brightness temperature (K)

TB_{v_2}	MSU 53.74 GHz microwave brightness temperature (K)
T_a	atmospheric temperature (K)
T_e	effective temperature
T_s	surface skin temperature
T_v	virtual temperature (K)
T_B	equivalent brightness temperature (K)
T_G	surface skin-temperature
T19H	SSM/I 19H GHz microwave brightness temperature (K)
T37V	SSM/I 37V GHz microwave brightness temperature (K)
$\overline{V}$	wind speed
W	vegetation water content
$W(p)$	atmospheric weighting function
W_s	soil moisture flux
$\mathrm{WF}_k(x,y)$	SSM/I spatial weighting function
α	absorptance
$\alpha(z)$	soil attenuation coefficient
β	inverse of the Prandtl number
χ	size parameter
δ	optical thickness
δ_{veg}	vegetation optical depth
δ_D	penetration depth
ε_0	smooth soil surface emittance
ε_s	bare soil surface emittance
ε_v	spectral surface emittance
ε_D	relative complex dielectric constant (relative permittivity)
ε_{IR}	infrared surface emittance
γ	viscosity of air

γ_c	sublayer correction factor
γ_{pp}	co-polarized bistatic scattering coefficient
γ_{pq}	cross-polarized bistatic scattering coefficient
η	volumetric soil moisture content
λ	wavelength
ν	frequency (GHz)
ν	soil thermal conductivity
θ	satellite zenith angle
θ''	subgrid scale potential temperature perturbation
θ_G	surface potential temperature
θ_*	friction temperature
ρ	reflectance
$\overline{\rho}$	atmospheric density
ρ_s	soil density
ρ_w	water density
ρ_L	water density
ρ_{NIR}	AVHRR near-infrared (channel 2) reflectance
ρ_{VIS}	AVHRR visible (channel 1) reflectance
σ°	bistatic scattering coefficient
σ_a	absorption coefficient (km^{-1})
σ_e	extinction coefficient (km^{-1})
σ_s	scattering coefficient (km^{-1})
τ	transmittance
$\tilde{\omega}$	single scatter albedo
$\xi(\mathbf{r}, \Omega_i, \Omega_s)$	scattering phase function
$\psi_H(z/L)$	integrated stability parameter for heat
$\psi_M(z/L)$	integrated stability parameter for momentum

$\Delta\varepsilon$	microwave surface emittance polarization difference
Ω_s	arbitrary direction
Ψ	soil moisture potential
$\mathbf{r}$	arbitrary positional vector

LIST OF ACRONYMS

AMMR	Airborne Multichannel Microwave Radiometer
API	antecedent precipitation index
ARM	Atmospheric Radiation Measurement
AVHRR	Advanced Very High Resolution Radiometer
BATS	Biosphere-Atmosphere Transfer Scheme
BC	boundary condition
CART	Cloud and Radiation Test Bed
CDF	common data format
CIRA	Cooperative Institute for Research in the Atmosphere
CMI	USDA Crop Moisture Index
CONTROL	control model run
DEM	Digital Elevation Model
DMSP	Defense Meteorological Satellite Program
DRY	dry model run
EDC	EROS Data Center
EF	evaporative fraction

EFOV	effective field-of-view
EOS	Earth Observing System
EOSDIS	EOS Data and Information System
ESMR	Electronically Scanning Microwave Radiometer
ESTAR	Electronically Scanned Thinned Array Radiometer
FIFE	First International Satellite Land Surface Climatology Project (ISLSCP) Field Experiment
FOV	field-of-view
GCIP	GEWEX Continental-scale International Project
GCM	general circulation model
GDF	Generalized Data Format
GEWEX	Global Energy and Water Cycle Experiment
GIS	Geographical Information Systems
GOES	Geostationary Operational Environmental Satellite
HAPEX-MOBILHY	Hydrologic Atmospheric Pilot Experiment — Modelisation du Bilan Hydrique
HDF	hierarchical data format
HRV	SPOT high-resolution visible data
HSL	hue-saturation-lightness
IAMAP	International Association of Meteorology and Atmospheric Physics
IOP	intensive observing period
ISLSCP	International Satellite Land Surface Climatology Project

LAI	leaf-area index
LDAS	Land-Surface Data Assimilation System
LST	land surface temperature
MMS	Landsat Multispectral Scanner
MPDT	microwave polarization difference temperature
MPM	Millimeter-wave Propagation Model
MSU	Microwave Sounding Unit
NCEP	National Center for Environmental Prediction
NDVI	Normalized Difference Vegetation Index
NGDC	National Geophysical Data Center
NMC	National Meteorological Center
NOAA	National Oceanic and Atmospheric Administration
NWS	National Weather Service
PBMR	Pushbroom Microwave Radiometer
PILPS	Project for the Intercomparison of Land Surface Parameterization Schemes
PORTAL	Polar Orbiter Remapping and Transformation Application Library
RAMS	Regional Atmospheric Modeling System
SAR	synthetic aperture radar
SAT	satellite data assimilation model run
SAVI	soil-adjusted vegetation index

SiB	Simplified Biosphere Model
SIR-B	Shuttle Imaging Radar
SMI	McFarland and Neale Surface Moisture Index
SMMR	Scanning Multichannel Microwave Radiometer
SSM/I	Special Sensor Microwave/Imager
SSM/T	Special Sensor Microwave/Temperature Sounder
SVAT	Soil vegetation atmospheric transfer
SWI	NOAA Soil Wetness Index
TIMS	Thermal Infrared Multispectral Scanner
UF	universal format
USAFETAC	United States Air Force Environmental Technical Applications Center
UTM	Universal Transverse Mercator
VAS	VISSR Atmospheric Sounder
VISSR	Visible Infrared Spin Scan Radiometer

Chapter 1

INTRODUCTION

Several challenging scientific questions remain to be answered about important atmospheric-land surface processes. This work's objective is to develop and apply a coupled satellite-model data assimilation approach to observe heterogeneous soil moisture and vegetation effects on the mesoscale for use in understanding and quantifying the processes that have an impact on the pre-convective mesoscale environment and affect initial convective cloud development.

1.1 SIGNIFICANCE OF SOIL MOISTURE ON ATMOSPHERIC CIRCULATIONS

Several studies have suggested that sea-breeze-like circulations can be generated over areas of heterogeneous vegetation and soil moisture conditions due to surface forcing (Ookouchi et al. 1984; Segal et al. 1988). In addition, the importance of soil moisture initialization has been demonstrated at several modeling scales, from the mesoscale to general circulation model (GCM) resolutions (Diak et al. 1986; Fast and McCorcle 1991; Sellers et al. 1988). In the operational forecasting and mesoscale research modeling communities, there are ever greater requirements to produce high resolution soil moisture estimates for data assimilation into the models to improve operational forecasts, and research analysis, development, and validation. Recent work (e.g. Betts et al. 1996) has shown improvements to model precipitation forecasts when soil moisture initialization is more carefully treated, and also suggests that some predictability exists in the extended range as a result of the memory of the soil moisture reservoir. At the larger scale, GCM modelers are also seeking to improve land-surface parameterizations, and they must continue to do so if they are to accurately answer the questions regarding the climate change issue (Dickinson 1994).

Beyond the needs of the weather modeling community, a reliable source of regional soil moisture information also needs to be available for the assessment of potential economic effects related to the climate change question and its impact on national policy decisions (Schmalensee 1993). All are pressing issues of our day.

The Global Energy and Water Cycle Experiment (GEWEX) is designed to address several scientific issues related to climate change. In particular, the GEWEX Continental-scale International Project (GCIP) is intended to address the GCM land surface parameterization problem. GCIP's primary study area is the Mississippi Basin watershed in central North America. Preparation for a 5 year intensive observing period (IOP) (1995-2000) began in 1993. During the preparation phase of GCIP, satellite remote sensing methods to estimate soil moisture are expected to be developed and validated for use during the IOP to extend the analysis and results from the Mississippi Basin to other geographical areas around the world. Satellite data in particular is important to the GEWEX/GCIP goals since the results are expected to be transported to other regions in which conventional hydrological and surface observations may be lacking or nonexistent. Even in the highly instrumented Mississippi Basin, satellite data will be an important information source to spatially interpolate the in situ data sets. The satellite data sets are also important for GCM model validation with observations, and acts as a reference data set for model-to-model intercomparisons of improved GCM land surface parameterizations.

One of the primary goals of GEWEX is to estimate global water and energy budgets of the earth. Remote sensing alone can not produce all the information required to create such budgets. The fluxes for such a calculation will from necessity come from the models that have 3D wind fields for the flux calculations in the atmosphere. However, for accurate estimates, the models will require information for several model parameters, such as soil moisture, which are not well known without remote sensing techniques. Thus the continental scale water and energy budget

calculations of GEWEX/GCIP need highly developed data assimilation procedures for incorporating remote sensing information into the mesoscale models.

Satellite data sets are well suited to observe spatial and temporal variations of clouds and of the land surface characteristics. Several studies have observed significant relationships between surface geographical features such as lakes and rivers, topography, albedo and soil moisture to cloud formation (Chang and Wetzel 1991; Gibson and Vonder Haar 1990; Rabin et al. 1990). Quantification of the satellite observed surface features and applicability of these results to model parameterizations is a remaining challenge. However, recent attempts have been made to include satellite observations of vegetation into model land surface parameterizations (Chang and Wetzel 1991). This work extends this to include satellite observations of surface soil moisture into a coupled satellite-model land surface parameterization scheme. This is an important next-step in the development of satellite-model coupling techniques from Lipton and Vonder Haar's (1990a, 1990b) earlier work.

Assimilating satellite data into mesoscale models is traditionally a two-step process where the satellite retrieval is separate from the model objective analysis and initialization. However, recent work (Eyre and Lorenc 1989; Lipton and Vonder Haar 1990a; 1990b; McNider et al. 1994) has shown that significant improvements are to be gained in both steps by coupling the satellite data assimilation with the model such that the model and the satellite retrieval process are interdependent. (This will be referred to as a satellite-model coupled system.) Due to the surface turbulence mixing effects on the partitioning of the sensible and latent heat fluxes at the surface, such an interdependent relationship should improve surface soil moisture retrieval results by obtaining more accurate important meteorological parameters for the remote sensing retrieval process, while also improving the model analysis with better soil moisture information. Chapter 5 details the satellite-model coupled system developed for this particular work.

A major problem in developing GCM land surface parameterizations is how to accurately represent the subgrid scale interactions that determine the hydrological and energy balance at the surface (Avissar and Pielke 1989; Henderson-Sellers and Pitman 1992). Even future GCMs with grid intervals of 100 km will have subgrid scale parameterization problems. For example, in two regions with identical mean values of soil moisture but different spatial distributions, a heterogeneous distribution on the scale of 10 km could induce mesoscale sea-breeze-like circulations which would be completely different from circulations associated with a homogeneous distribution of soil moisture with the same mean soil moisture. Thus characterization of the spatial and temporal distribution of parameters related to surface forcing are very important for correct parameterization of the land surface processes at the GCM scale. Mesoscale models with appropriate data assimilation are an excellent tool by which to gain understanding of these subgrid scale effects. Such understanding is crucial for better parameterizations at the scale of the GCM. Thus mesoscale model output would serve as a test bed for GCM model parameterization efforts.

Small scale effects are also important at the mesoscale. Remote sensing retrieval results are averaged values over an entire sensor field-of-view. Consideration of subgrid resolution effects could be important to remote sensing applications regarding model data assimilation (Wetzel and Chang 1987). High resolution remote sensing data, rather than data that has been degraded by averaging, is therefore crucial for accurate remote sensing results (Guo and Schuepp 1994). However, even at reduced resolutions used in current studies, variations of soil moisture and vegetation have a noticeable impact on the evolution of the preconvective environment (Chang and Wetzel 1991).

Mesoscale model land surface parameterizations also need high resolution soil moisture data sets for model development and validation. Initialization of mesoscale models with accurate high resolution soil moisture and vegetation information can significantly improve model forecast ac-

curacy (Coates et al. 1984). Recent land surface parameterization efforts have been based on rain gauge indices such as the antecedent precipitation index (API) (Wetzel and Chang 1987). Satellite soil moisture data sets for mesoscale data assimilation will have higher spatial and temporal resolution than is available with conventional in situ derived data sets. Comparing and/or combining API-like methods with satellite soil moisture estimates will allow extrapolation of available in situ measurements in space and time, yielding a more optimum data set for high resolution model development and validation. Results from an extensive intercomparison of satellite-derived surface soil moisture products and an API method are shown later in Chapter 4.

Other fundamental remote sensing problems remain over land surfaces. It is well known that microwave brightness temperatures measured by satellite are physically related to land surface properties such as soil wetness, vegetation, and surface roughness (Jackson and Schmugge 1989; Heymsfield and Fulton 1992), but understanding and quantifying the relationship of these interrelated parameters is a challenging and complex problem. The microwave spectral emittance is a fundamental surface radiometric parameter that can be measured from space and is also often related to the physical hydrological parameters in theoretical work (Isaacs et al. 1989; Kerr and Njoku 1990). The ability to combine microwave and infrared satellite data makes the calculation of this fundamental radiometric surface parameter possible (Jones and Vonder Haar 1990). In turn, the measurement of microwave surface emittance makes possible the minimization of the background problem over land for microwave remote sensing of precipitation and cloud liquid water (Spencer 1984; Jones and Vonder Haar 1990). A major result of this work is the production of a high resolution microwave spectral emittance for use in such studies. Other meteorological parameters, such as boundary-layer turbulence and mixing, further complicate the retrieval of accurate soil moisture estimates (Wetzel and Woodward 1987). A soil moisture retrieval method should ideally include these atmospheric effects. This work accomplishes this by using a satellite-

model coupled system to incorporate the surface meteorological parameters that affect the soil moisture retrieval results and thereby improve overall retrieval accuracy.

1.2 RESEARCH OBJECTIVES

This work's general scientific objective is to develop and apply a coupled satellite-model data assimilation approach to observe heterogeneous soil moisture effects on the mesoscale for use in understanding and quantifying the processes that have an impact on the preconvective mesoscale environment and affect initial convective cloud development related to surface-forced circulations. The primary objectives are:

1. to develop, validate, and intercompare multi-sensor satellite soil moisture retrieval algorithms in the context of a satellite-model coupled system, and

2. application of the developed satellite-model coupled system to a 3D case study to assess the impact of observed soil moisture on the preconvective mesoscale environment.

Closely related ideas which information will be provided for are:

1. determination of the space and time variability of high resolution microwave satellite surface emittance for use in understanding the nature of processes which control the hydrological balance and radiometric surface properties of the land surface at a 10-15 km grid scale,

2. determination of the relative roles and important interactions that observed soil moisture and vegetation have on initial convective cloud development at the mesoscale, and

3. demonstration of multi-sensor satellite data fusion technology in conjunction with data assimilation for mesoscale models.

1.3 SCOPE AND SEQUENCE

The two major parts of this study, remote sensing and the coupled satellite-model work, have unique characteristics that require that the work be performed on two temporal scales and slightly different spatial scales. This requirement is primarily driven by the large computational demands of the mesoscale atmospheric model, and the desire to have a spatial domain and time period large enough to minimize the potential loss of understanding of the remote sensing phenomenon if the data were processed on a smaller domain.

In brief, the remote sensing work consists of calculating the microwave surface emittance and comparing the results with other surface wetness information sources (including satellite data, and other available in situ and geographical information sources). The coupled satellite-model work is broken down into two parts: the development and testing stage, and the application of the satellite-model coupled system to a case study. So in summary, the work will be performed in a total of two stages:

1. satellite related work observing microwave surface emittance and the processing of satellite and geographical data sets necessary for the satellite-model parameterization development, and
2. satellite-model work consisting of:
    a) development and testing of the satellite-model coupled system, and
    b) application of the satellite-model coupled system to a 3D case study.

The remote sensing aspect of the study will cover a continental-scale domain area, with the data set being selected over the Mississippi Basin watershed area (25-55° N, 85-110° W). The remote sensing work will benefit from the geographical diversity that the larger continental scale area offers. Thus greater understanding will be possible due to the wider range of environmental

conditions and situations. The satellite data set is approximately 70 days in duration occurring in late summer (Aug.-Oct., 1991). The 70 day time period will allow for observation of cyclical surface hydrological processes such as surface moistening and drying due to precipitation events (Serafini 1990). The late summer time period should also focus our work on air mass convection rather than convection that is driven by the larger synoptic scale conditions.

The coupled satellite-model work will be performed on a smaller scale of approximately 500×500 km with a 5 km grid interval, with larger parent grids of approximately the same domain size as the satellite analysis work mentioned previously. The smaller spatial domain is due to the large computational requirements of the mesoscale model. A special case study on 9 September 1991 has been selected from the larger remote sensing data set for data assimilation into the coupled satellite-model system. The central Great Plains (Kansas-Oklahoma area) was selected for the coupled satellite-model system data assimilation work due to its small topographic relief, relatively low vegetation amounts and high diurnal surface temperature fluctuations. Features of particular interest is the dryline which should be strongly influenced by land surface properties in a non-synoptically forced environment (Sun and Ogura 1979; Benjamin and Carlson 1986; Lanicci et al. 1987; Sun and Wu 1992; Ziegler et al. 1995). The modeling work continues a heritage of recent dryline studies performed using the CSU-RAMS (e.g., Shaw 1995; Ziegler et al. 1995; Grasso 1996).

1.4 READER'S GUIDE

The following chapters draw upon diverse literature sources due to the interdisciplinary nature of this study. The original intent was to present sufficient material for all potential readers to be able to review material unfamiliar to them and to be able to skip others that might be related to their specialties. Thus it is encouraged that the reader skips to the "meat" when he feels the material is perhaps too basic for his needs, while understanding that not all readers will be from the

same background as his own. An attempt has been made to move as much material as possible into the appendices to remove as many of the burdensome details from the reader as possible while still including material that is relevant to the study. Of particular note is placement of a microwave remote sensing review in Appendix A, and the absence of the PORTAL software package in the main text which has been placed into Appendix C. While interesting in its own right, especially with regard to satellite data processing methods, such details have been omitted from the main text, with more emphasis placed on the scientific algorithms instead.

Chapter 2 contains background material that discusses previous studies that involved remote sensing of surface soil moisture and related numerical studies. The microwave remote sensing background chapter contained in Appendix A may be skipped by the remote sensing specialist, while Chapter 2 would be beneficial for those desiring a stronger background in current research regarding atmospheric land surface effects. Data sources are described in Chapter 3, while the satellite portion of this work is discussed in Chapter 4. Chapter 5 discusses the data assimilation work using the coupled satellite-model system, with conclusions and summary following in Chapter 6.

Chapter 2

BACKGROUND

Early in the development of boundary layer and mesoscale models it was recognized that the correct specification and partitioning of surface fluxes of moisture and sensible heat was critical to the accurate prediction of boundary layer behavior and subsequent mesoscale circulations (Deardorff 1978; Wetzel 1978; Blackadar 1979; McCumber and Pielke 1981; Zhang and Anthes 1982). Numerous simulations and studies have been performed since using various parameterization methods to link the model's atmospheric dynamics to the land surface boundary layer processes. A review of the fundamental physical concepts is required to set the framework for these methods and also to place the remote sensing work in its proper context. This section introduces the fundamental physical concepts in section 2.1 and then reviews previous studies, in sections 2.2-2.4, which are relevant to this work. It should be pointed out that the body of literature available on this topic is rather large and loosely associated. A diverse group of scientific communities have contributed to this research area and thus presented a challenge to the author to condense and correlate the relevant material into a cohesive whole, thus the overview which follows should not be construed as being all encompassing. However, an effort is made to cite additional material when possible to allow further exploration on the part of the reader.

2.1 FUNDAMENTALS

Critical to the proper functioning of an atmospheric model is the linkage of the land surface forcing effects and the atmospheric dynamics of the model at higher model levels. This is accomplished through parameterization methods since the model is unable to explicitly resolve the

subgrid-scale turbulent effects which are important in the transport of heat and water at this scale. The parameterizations are usually based on experimental data and contain simplified fundamental concepts. However there is no requirement that a "good" parameterization contain any physics, just that it performs well for a given set of conditions (and in general, the presence of some physical mechanisms usually helps to achieve this goal). This section is meant to enhance the discussion of specific physical mechanisms and provide a common framework for further developments.

The interaction of the land surface with the atmosphere occurs on scales from leaf, field, landscape, and biome spatial scales. In trying to understand the complex processes which interact on such a small scale, the fundamental principles are introduced first with regards to the land surface and then from an atmospheric perspective, but first, let's begin with the concept of how energy is transported between the air and land surface systems.

2.1.1 Surface Energy Budget over Land

The air-surface interface is the location at which the atmosphere and the surface exchange energy with respect to several state parameters. If we assume the actual interface is infinitesimally thin, then the energy "balance" or "budget" can be defined. If the surface interface is parameterized by a finite soil slab (i.e. with mass), the energy fluxes at the air-surface interface may not balance due to storage within the system and perhaps also by the physical limitations of the system to produce fluxes of the magnitude required to balance the energy exchange. The following discussion is therefore in the context of an infinitesimally-thin interface.

The surface energy balance at the air-surface interface is,

$$-Q_G + Q_C + Q_R = 0, \tag{2.1}$$

where Q_G, Q_C, Q_R, are the conductive, convective, and net radiative heat fluxes (positive fluxes being directed toward the ground), respectively (Pielke 1984). The conductive heat flux, Q_G, is the heat which is being transported (or conducted) through the soil. An example of this would be a cooling (heating) of the atmosphere through the sink (source) of heat produced by contact with the cooler (hotter) low-level soil temperatures. The convective heat flux has two components, one from the transport of sensible heat and the other from the transport of latent heat. Both components are very important, and in practice it is the partitioning of the energy between a more readily measured quantity, sensible heat flux, H, and the more elusive latent heat flux, E, which makes the remote sensing of surface soil moisture difficult. Methods to remotely measure these components will be reviewed in section 2.2. The total convective heat flux is thus the sum of the sensible and latent heat fluxes and is given by,

$$Q_C = H + E = -\bar{\rho} c_p \overline{w'' \theta''} - \bar{\rho} L_v \overline{w'' q_3''}, \tag{2.2}$$

where the sensible and latent heat flux terms also depend on the atmospheric density, $\bar{\rho}$, the atmospheric heat capacity at constant pressure, c_p, the latent heat of vaporization, L_v, and the subgrid scale correlation terms, $\overline{w'' \theta''}$ and $\overline{w'' q_3''}$. The subgrid scale correlation terms consist of the correlation of the subgrid scale vertical velocity perturbation, w'', with respect to the subgrid scale potential temperature perturbation, θ'', and the subgrid scale specific humidity perturbation for water vapor, q_3'', where the overbar, $\overline{(\ )}$, denotes the average taken over the grid interval in space and time. The correlation terms denote the vertical subgrid scale mixing and transport of heat in both of its possible forms. The third term of the surface energy balance, the net radiation heat flux, is represented by,

$$Q_R = (1-A)\left(\overline{R}_{\downarrow sw_G} + \overline{R}_{\downarrow sw_G}^{\,D}\right) + \overline{R}_{\downarrow lw_G} - \overline{R}_{\uparrow lw_G}, \tag{2.3}$$

where A is the surface albedo, $\overline{R}_{\downarrow sw_G}$ is the direct downward shortwave radiation flux, $\overline{R}_{\downarrow sw_G}^{\,D}$ is the diffuse downward shortwave radiation flux, and $\overline{R}_{\downarrow lw_G}$ and $\overline{R}_{\uparrow lw_G}$ are the downward and upward longwave radiation fluxes, respectively.

To evaluate the conductive heat flux, Q_G, it is helpful to examine the vertical distribution of heat and moisture throughout the soil profile, however it should be noted that the primary concern is with the conductive heat flux at the *surface*. The representation of the heat and moisture flux in the soil levels below the air-surface interface are used to enhance the physical understanding of the integration processes and thus the coupling of the energy fluxes in time and space. This introduces the next two topics, the soil heat flux and soil moisture flux.

2.1.2 Soil Heat Flux

The soil heat flux is the functional equivalent of the atmospheric sensible heat flux in that it transports heat in a sensible form, but it consists of different underlying dominant physical transfer mechanisms (e.g., the soil is nonconvective) and therefore requires a substantially different method of solution. The soil heat flux is evaluated using a one-dimensional diffusion equation,

$$\frac{\partial T}{\partial t} = \frac{\partial}{\partial z}\frac{\nu}{\rho_s c_s}\frac{\partial T}{\partial z} = \frac{\partial}{\partial z} k_s \frac{\partial T}{\partial z}, \tag{2.4}$$

where ν, c_s, and ρ_s are the thermal conductivity, specific heat capacity and soil density, respectively. The coefficients of Equation 2.4 can be gathered into one term called the thermal diffusivity which is given by $k_s = \nu/\rho_s c_s = f(\eta)$; a function of the volumetric soil moisture content, η. Since the soil heat flux depends on the volumetric soil moisture content, the soil moisture flux must be solved simultaneously with the soil heat flux.

2.1.3 Soil Moisture Flux

Various methods are possible to represent the soil moisture flux, however for the purposes of this section the method of McCumber (1980) as summarized in Pielke (1984) will be used. This parameterization is also used in the data assimilation method described in Chapter 5.

The local time rate of change of the volumetric moisture content, η, is related to the soil moisture flux, W_s, and is given by

$$\frac{\partial \eta}{\partial t} = \frac{1}{\rho_w} \frac{\partial W_s}{\partial z}, \tag{2.5}$$

where ρ_w is the water density, and conservation of water has been assumed without advective processes such as runoff and/or additional sources and sinks of water such as from rainfall or plant root uptake. This relationship may then be parameterized with the following expression,

$$\frac{\partial \eta}{\partial t} = \frac{\partial}{\partial z}\left[D_\eta \frac{\partial \eta}{\partial z} + K_\eta \right], \tag{2.6}$$

where

$$W_s = D_\eta \rho_w \frac{\partial \eta}{\partial z} + K_\eta \rho_w, \tag{2.7}$$

has been used to replace W_s from Equation 2.5, and D_η and K_η are parameters which vary depending on the particular soil textural class (e.g., sand, clay, peat, etc.). K_η is called the hydraulic conductivity and $D_\eta = K_\eta \partial \Psi / \partial \eta$ is related to the derivative of the moisture potential, Ψ, with respect to the volumetric moisture content, η. The hydraulic conductivity accounts for the gravity drainage in the viscous soil, while the moisture potential represents the potential energy (negative in sign) needed to extract water from the soil due to the capillary action of the particular soil type structure.

In addition to the representations of the soil heat flux and the soil moisture flux are the boundary condition (BC) requirements to completely specify the solution. If one assumes that all moisture comes in and out of the top BC, and that at a sufficiently deep soil-level the soil temperature and moisture are fixed, the BC's which remain to be specified are limited to the surface (i.e. at $z = z_G$). The moisture flux continuity must be preserved at the air-surface interface, thus

$$W_s\big|_G \cong E, \tag{2.8}$$

and, as mentioned previously, thermal equilibrium must also be maintained at the air-surface interface such that Equation 2.1 is satisfied. Given that the soil's heat and moisture fluxes can be properly represented, the conductive heat flux at the air-surface interface is given by

$$Q_G = \rho_s c_s k_s \frac{\partial T}{\partial z}\bigg|_G = \nu \frac{\partial T}{\partial z}\bigg|_G, \tag{2.9}$$

where the temperature gradient at the air-surface interface (i.e. ground level) is $\partial T/\partial z\big|_G$.

2.1.4 Similarity Theory

The atmospheric boundary layer can be thought of as three layers, the viscous sublayer, the surface layer, and the transition layer. The height of the top of the atmospheric boundary layer, z_i, can extend from 100 m to several kilometers or more, and is defined to be "the lowest level in the atmosphere at which the ground surface no longer influences the dependent variables through the turbulent transfer of mass" (Pielke 1984). Different parameterization methods are used in each layer to estimate the subgrid fluxes of temperature, moisture and momentum. The following discussion begins with the lowest layer, the viscous sublayer, and progresses to the higher levels of the atmosphere.

The viscous sublayer $\left(z < z_0\right)$ is at the bottom of the atmosphere, below the roughness height, z_0, and it is in this region where molecular motions become important. An empirical relationship has been developed which relates the temperature and specific humidity of the ground $\left(z = z_G\right)$ to variables measured at the top of the viscous sublayer (at $z = z_0$) (Ziltinkevich 1970; Deardorff 1974),

$$\overline{\theta_{z_0}} = \theta_G + \frac{\theta_*}{k}\gamma_c, \tag{2.10}$$

$$\overline{q_{z_0}} = q_G + \frac{q_*}{k}\gamma_c, \tag{2.11}$$

where k is Von Karmann's constant ($k \sim 0.35$), and where a correction factor, γ_c, is used to relate surface values to values at the height of the roughness length, z_0. The proportionality factor is given by,

$$\gamma_c = 0.0962\frac{u_* z_0}{\gamma}, \tag{2.12}$$

where γ is the viscosity of air (1.5×10^{-5} $m^2 s^{-1}$), and u_*, q_*, and θ_* are the friction velocity, friction humidity, and the friction temperature, respectively.

The surface layer $\left(z_0 < z < h_s\right)$ is the region of the atmosphere where the subgrid scale fluxes are assumed to be independent of height and where veering of the wind with height owing to the Coriolis effect is neglected, with the top of the surface layer, h_s, usually ranging from 10 m to 100 m in height (Pielke 1984). It is in this layer that the parameterization formulated by Businger (1973) is commonly used which is based on Monin-Obukov similarity theory. The Businger parameterization consists of the following equation set:

$$u_* = k\frac{\overline{V}}{\left[\ln\left(z/z_0\right) - \psi_M\left(z/L\right)\right]}, \tag{2.13}$$

$$\theta_* = \beta k\frac{\left(\overline{\theta}(z) - \overline{\theta}_{z_0}\right)}{\left[\ln\left(z/z_0\right) - \psi_H\left(z/L\right)\right]}, \tag{2.14}$$

$$q_* = \beta k\frac{\left(\overline{q}_3(z) - \overline{q}_{z_0}\right)}{\left[\ln\left(z/z_0\right) - \psi_H\left(z/L\right)\right]}, \tag{2.15}$$

where β is the inverse of the Prandtl number for a neutrally stable atmosphere ($\beta \sim 1.35$), $\overline{V}$ is wind speed and $\psi_M\left(z/L\right)$ and $\psi_H\left(z/L\right)$ are the integrated stability parameters for momentum and heat given by Businger et al. (1971), and are a function of height, z, and the Monin length, $L = -\theta_0 u_*^3 / g\overline{w''\theta''} = \overline{\theta} u_*^2 / kg\theta_*$, where the assumption has been made that $\overline{w''\theta''}$ can be approximated by $u_*\theta_*$.

The transition layer $\left(h_s < z < z_i\right)$ is the portion of the atmosphere which is below the top of the atmospheric boundary layer, z_i, and above the height of the surface layer, h_s. Several methods are available to parameterize the subgrid scale fluxes within the transition layer. Pielke (1984) contains a useful review of the various methods which will not be repeated here. In general, the methods are classified according to their "closure" order, which is the statistical level (e.g., variance, skewness, kurtosis, etc. of the grid volume subgrid scale products of the dependent variables) in which quantities of higher level statistics are represented in terms of lower order statistics and empirical proportionality values. Depending on conditions (e.g., stability criteria), certain parameterizations perform better or worse than others. However, in regard to the closure order of the parameterization, it must be held in mind that the parameterization should not be overly complex, the real goal is to obtain an accurate parameterization scheme. Higher-order

closure is not necessarily better since they introduce additional degrees of freedom in their representation, for which adequate empirical data to provide an accurate closure are usually not available.

2.2 REMOTE SENSING STUDIES

Remote sensing of soil moisture is comprised of a large group of scientists each with their own unique background and reason for attempting to remotely sense soil moisture. Areas of expertise include ecologists interested in vegetation-soil moisture feedback, soil scientists interested in relatively deep soil moisture, atmospheric boundary layer scientists working on the interaction of the surface with the atmosphere, etc. The list is a long one. The principle problem in grouping this body of literature together is that the emphasis of the work tends to differ depending on the perspective that the original task was addressed from. In this subsection an attempt is made to give a broad overview of current research in this area pointing out the context of the work. It is beyond the scope of this background section to provide a complete summary, but an effort is made to specifically mention the most directly relevant work. However, for further reading, several good texts exist in the literature which describe current techniques in remote sensing of soil moisture (Mulders 1987; Pampaloni 1989; Schmugge and André 1991), including several relevant review articles (Schmugge et al. 1980; Schmugge 1983; Freeland 1989; Jackson and Schmugge 1989; Engman 1990; Gutman 1990; Sellers 1990; Choudhury 1991a; Choudhury 1991b; Engman 1991; Gutman 1991; Kairu 1991; Townshend 1991; Schmugge et al. 1992). This subsection is divided into three subdivisions, the remote sensing of vegetation, infrared remote sensing of soil moisture, and microwave remote sensing of soil moisture.

2.2.1 Remote Sensing of Vegetation

The remote sensing of vegetation is a large category which includes microscale remote sensing efforts using land-based active and passive microwave sensors, an active research group

which emphasize multispectral infrared and visible data sets from the Landsat and SPOT satellite series (Thelin and Heimes 1987), active microwave remote sensing using synthetic aperture radar (SAR) technology (Engman 1991), and global analyses using the Advanced Very High Resolution Radiometer (AVHRR) sensor on the NOAA polar orbiting satellite series (Sellers 1990; Loveland et al. 1991; Gutman et al. 1995). The Landsat series data set provides high resolution (30 m footprint) and is thus preferred for many of the regional studies, however it has a return time of 16 days, and in cloudy regions this can restrict its practical usage. The SAR data is also a high resolution data set and suffers from similar sampling problems as the Landsat data set. Thus for regional and global vegetation studies, the AVHRR with its 1 km resolution and approximately twice daily coverage is most ideally suited to monitor the global vegetation of the earth.

The primary method to estimate vegetation cover on regional and global scales using the AVHRR is the Normalized Difference Vegetation Index (NDVI) (Nemani and Running 1989; Gutman 1991; Kalb 1991; Loveland et al. 1991; Gutman et al. 1995; Nemani et al. 1996). The index is based on the difference between the spectral reflectivity in the near-infrared and visible radiances which is dependent on the vegetation cover. The NDVI is defined as

$$NDVI = \frac{\rho_{NIR} - \rho_{VIS}}{\rho_{NIR} + \rho_{VIS}}, \tag{2.16}$$

where ρ_{NIR} and ρ_{VIS} are the AVHRR near-infrared (channel 2), and visible (channel 1) reflectance values that cover the spectral regions of 0.58-0.68 μm and 0.73-1.0 μm, respectively. This equation produces NDVI values in the range of -1.0 to 1.0, where negative values generally represent clouds, snow, water and non-vegetated surfaces while positive values represent vegetated surfaces (Loveland et al. 1991). It has also been shown that the NDVI is correlated with such vegetation parameters as green leaf biomass and green leaf area (Tucker 1979; Justice et al. 1985). In heavily vegetated regions, the NDVI has been shown to saturate in comparison with

other vegetation measures, such as leaf area index (LAI) (Carlson et al. 1990). Conversely in sparse vegetation the NDVI may also not be informative, in that most bare surfaces have positive vegetation index values, so that it is difficult to discriminate a sparsely vegetated surface from one with no vegetation (Sellers 1990). Work by van de Griend and Owe (1993) has shown that the NDVI is also correlated to the thermal infrared emittance, but since the in situ infrared emittance measurements can only be performed on a small scale (on the order of 1-10 m), the estimation of an "effective" infrared emittance by using the NDVI poses a serious problem regarding the scale of the processes involved.

Monitoring interannual variability with NDVI can be problematic, in that it requires the removal of residual trends/noise in the NDVI data set, which are on the order of the magnitude of interannual variability (Gutman et al. 1995). The variability is caused by satellite/sensor change, by sensor instability (Kaufman and Holden 1993), and by satellite orbit drift (Price 1991). Stratospheric aerosols such as was observed from Mt. Pinatubo can also affect the AVHRR measurements, particularly the visible channels (Stowe et al. 1992). Monitoring of interannual effects therefore requires additional care in the processing of the data set; however, for the cases involved in this work, the time period is about 2 months, and such long term AVHRR calibration difficulties are avoided.

Additional vegetation indexes have been developed which extend upon the concepts in the NDVI. Among these is the soil-adjusted vegetation index (SAVI) developed by Huete (1988) to minimize the influence of the soil background

$$SAVI = \left(\frac{\rho_{NIR} - \rho_{VIS}}{\rho_{NIR} + \rho_{VIS} + L} \right)(1 + L), \tag{2.17}$$

where L is the soil correction term. An experiment in Arizona showed that the linear correlation between SAVI and observed vegetation cover was small $\left(r^2 \approx 0.36\right)$ and suggests that the relationship probably changes significantly as a function of vegetation type as well as amount (e.g., grasses versus shrubs) (Ormsby et al. 1987; Kustas 1993).

The combination of NDVI and land surface temperature (LST) has also been an active research area for development of a method to retrieve surface moisture and fractional vegetation coverage (Carlson et al. 1990; Price 1990; Nemani et al. 1993). The basic physical assumption is that the more heavily vegetated surfaces are associated with greater transpiration and hence should be cooler than the less vegetated ones (Gutman et al. 1995). The NDVI has also been compared with surface temperature observations over southeastern Australia (Smith and Choudhury 1991) and with day-time range of surface skin temperature (Diak et al. 1995). The results show similar results for both the absolute skin temperature measurements and the heating rate skin temperatures. The correlation between the surface skin temperature and NDVI is poor, but does exhibit a unique triangular structure which may suggest a sensitivity of the NDVI to soil moisture. This is discussed further in section 2.2.2.

Microwave data have also been used to remotely sense vegetation. The depolarization of the microwave radiation emitted by the soil surface is the identifying signature of heavier vegetation amounts (Mo 1982). Experimental microwave vegetation indices have been developed to exploit this signature. A comparison of the NDVI versus one of these indices, the Microwave Polarization Difference Temperature (MPDT), is shown later in section 4.3.6. The microwave data set is more complex in its interpretation, since significant physical features such as surface roughness and water content of the foliage have a significant effect on the observed microwave brightness temperatures (see the discussion about microwave surface effects in Appendix A.3).

The main emphasis from this summary is not that the NDVI is the only vegetation index available, but that it has been thoroughly tested within the remote sensing vegetation community (Gutman 1991; Gutman et al. 1995) and represents a defacto remote sensing vegetation reference from which to infer vegetation dependencies in remote sensing studies. The AVHRR NDVI is used later in this work in the remote sensing comparisons of section 4.3.6, and in Chapter 5 for initialization of the atmospheric model's surface parameterization.

2.2.2 Infrared Remote Sensing of Soil Moisture

Infrared remote sensing of soil moisture is best suited to semi-arid conditions in which relatively sparse vegetation amounts exist. This results in the soil surface having a major influence on the partitioning of the energy fluxes between the soil and vegetation. Several modeling approaches are available that evaluate the energy balance of individual soil and vegetation components (Kustas 1990; Shuttleworth and Gurney 1990; Schmugge et al. 1991; Massman 1992; Nichols 1992). However in many of the methods, significant limitations exist due to the necessity to accurately separate the composite surface temperature into soil and vegetation temperature components (Smith and Choudhury 1991) and difficulties involved with correctly specifying important vegetation parameters such as fractional vegetation cover and leaf-area index (LAI) from remotely sensed data (Myneni et al. 1992). Infrared methods have been considered by some to be largely limited to bare soil conditions (van de Griend et al. 1985). The relationship between diurnal temperature and soil moisture is also variable and depends upon soil type (Idso et al. 1975). However, when soil water content is transformed into pressure potential, a single relationship was found to be valid for all the different soil types investigated. This is the basis for expressing moisture values as a percentage of field capacity, where field capacity is the moisture content of the -33 kPa pressure potential (Schmugge et al. 1980). Along with the previous problems, application of an independent regression analysis between radiometer temperatures and sensible heat

flux calculations have indicated poor skill, and reinforces the notion that for satellite applications the radiometric approach is also only feasible on a site-specific basis (Cooper et al. 1995). Other work has shown that at times the additional satellite information of surface skin temperature was neither helpful nor harmful to the mesoscale analysis fields (Lipton et al. 1995). However, even for all of its short comings, infrared techniques have several distinct advantages. Among those advantages are the availability of infrared measurements at relatively high spatial and temporal resolutions, the unique role of surface skin temperature in the surface energy budget and its importance for other surface physical properties, and the presence of a relatively large diurnal signal for most situations and conditions. The soil moisture information is there, but obscured to various degrees.

In earlier work, the mid-morning differential of surface temperature with respect to absorbed solar radiation was found to be most sensitive to soil moisture, and sensitivity studies based on model simulations have shown that only under deep cold thermal advection is the surface temperature heating rate seriously affected (Wetzel et al. 1984). To avoid the need for direct wind speed measurements, methods have been developed which use geostrophic wind speed derived from routine measurements of the surface pressure field (Crago 1995). A common technique is to calculate latent heat fluxes as the residual term of the surface energy balance, thus mixing satellite observations and model simulation results. An example of a simple straight-forward implementation is given by Kustas et al. (1996).

API methods that correlate the surface skin temperature information with an API have also produced useful insights into the physical relationship of the surface skin temperature on the surface energy balance. From these results, the relatively narrow range of API values over which soil moisture is sensitive to changes in rainfall suggest that the infrared method is most suitable for deriving surface moisture availability over plains or semiarid vegetation and where there are

large horizontal precipitation gradients (Carlson et al. 1984). This work also showed that agreement between soil moisture and API was poorest on the smallest scales. This might suggest a mismatch in scale between precipitation and the satellite measurements, or an inability of the satellite to distinguish between wet and dry surfaces when differences in dryness are masked by complex vegetation cover or confused by lakes or underground aquifers or local irrigation practices (Carlson et al. 1984). In related work, Wetzel and Chang (1987) examined a simple statistical method using infrared surface temperature. Their approach relied on numerical model results to identify important variables other than soil moisture that have a significant effect on the surface temperature, and to define linear relationships between these variables and surface temperature. Results showed good agreement between estimated and observed soil moisture features $\left(r^2 = 0.71\right)$; however, when advection was neglected the average r^2 value drops to 0.57. The method developed for this work (discussed in Chapter 5) implicitly includes the advection effects through the atmospheric model state variables.

A significant improvement over previous methods was the use of surface temperature heating rates rather than a single temperature. Methods which involve time differencing offer advantages over the direct method, because they almost completely eliminate the effects of systematic bias in the surface temperature due to sensor problems or view angle, and they operate on a time integral of heat flux which effectively reduces the impact of random errors (Hall and Sellers 1995). As an example, twelve-hour daytime totals of surface sensible heat flux were estimated using satellite measured surface skin temperatures and a model of the land surface and planetary boundary layer during the First International Satellite Land Surface Climatology Project (ISLSCP) Field Experiment (FIFE) 1989 (Diak and Whipple 1995). On an even longer time-scale, monthly evapotranspiration has been measured from infrared satellite data by (1994). Time integration is a strength that should be exploited in future methods.

Another critical area of research regards the use of aerodynamic values versus radiometric quantities. Radiometric values of the exchange coefficient and roughness length have been shown to not agree with their aerodynamic equivalents (Sun and Mahrt 1995). The radiometric roughness height was found to be flow dependent and not systematically related to the roughness height for momentum. This has serious implications on the methods that rely upon infrared surface skin temperatures as a surrogate for aerodynamic surface temperature, and suggests that a more complete surface parameterization is needed, especially for partially vegetated surfaces. As an example, observations of countergradient heat fluxes, as defined from the satellite radiative skin temperature and in situ temperature just above the surface, are observed over irrigated crops, apparently due to domination of the heat flux by the unshaded bare soil between the rows, while the radiation footprint is dominated by the cooler transpiring vegetation (Sun and Mahrt 1995). Additional model simulations have shown systematic differences between soil and vegetation temperatures that help to explain the complex relationship between surface radiometric and aerodynamic temperatures, and clearly demonstrated the need to distinguish between canopy and soil background temperatures in the surface energy balance models that use thermal infrared data to estimate land surface fluxes (Friedl 1995).

Observational attempts to address the fractional vegetation effects have shown that the NDVI versus the surface skin temperature produces a unique relationship between the data sets and is the basis of a nomogram, called the "universal triangle". This universal triangle simplifies the interpretation of the satellite data sets and is a possible step toward future methods that integrate multisensor datasets (Gillies and Carlson 1995). Soil vegetation atmospheric transfer (SVAT) models have also been used in conjunction with infrared satellite measurements to estimate the evaporation and transpiration at the surface (Olioso et al. 1995). The method developed in Chapter 5 can be thought of as a simple SVAT-based method since it employs the CSU-RAMS land

surface and vegetation parameterization scheme. Other methods using the coupled satellite-model approach have, for example, included explicit cloud information for the solar fluxes (Lipton 1993).

2.2.3 Microwave Remote Sensing of Soil Moisture

Microwave radiometers have the potential to measure soil moisture because of the large difference between wet and dry soil dielectric constants as reflected in the emissivity values. The best frequencies are lower (such as 1.4 GHz) because the upwelling radiance comes from greater soil depths (3-5 cm) compared with higher frequencies (Njoku and Kong 1977), the dielectric constant is higher, and the measurements are relatively unaffected by clouds and vegetation (Schmugge 1989). Higher frequencies sense only a very shallow layer, and vegetation produces attenuation and scattering that partially obscures the soil radiance contribution upwelling from below the vegetation canopy (Jackson et al. 1982; Mo 1982).

In some of the earliest microwave soil moisture work, McFarland (1976) showed a strong relationship between the Skylab 21-cm brightness temperatures and the antecedent precipitation index (API) for data collected during a pass starting over the Texas and Oklahoma panhandles and continuing southeast toward the Gulf of Mexico. A modern aircraft-based version of this sensor with much higher spatial resolution, the Pushbroom Microwave Radiometer (PBMR), has been used to conduct experiments using low frequency (21-cm wavelength) microwave radiometers to determine soil moisture (Kustas 1993). These microwave frequencies have been shown to be highly correlated with 0-5 cm soil moisture (Schmugge et al. 1992; Schmugge et al. 1994). Results from the Hydrologic Atmospheric Pilot Experiment— Modelisation du Bilan Hydrique program (HAPEX-MOBILHY) showed smaller correlations $\left(r^2 \approx 0.4\right)$, while data from FIFE had better results with a 4.5% RMS difference and a 1.8% bias between estimated and measured values of soil moisture (Schmugge et al. 1992). In MONSOON 90 (Kustas et al. 1991)

which had lower vegetation amounts than the previously mentioned experiments, comparisons of the brightness temperature difference between two days 48 hours apart with corresponding rainfall amounts had even higher correlations $\left(r^2 = 0.87\right)$ (Schmugge et al. 1992). It was also found that adequate estimates of vegetation biomass are needed to obtain reliable retrieval of surface soil moisture from the L-band radiometric measurements (Wang 1995). An example of high resolution microwave soil moisture estimates from the PBMR combined with in situ soil moisture measurements is given by Peck and Hope (1995) for the FIFE study area. Results from the PBMR over the FIFE study region during 1985-1989 are summarized by Wang (1995). The PBMR has also been compared with active (SAR) microwave sensors, but the results were non-conclusive as to which instrument performed better. The final opinion was that the choice of instrument be based on the intended applications and information that is available (Wood et al. 1993).

Wang (1985) examined Skylab (1.4 GHz) and Scanning Multichannel Microwave Radiometer (SMMR) (6.6 GHz and 10.7 GHz) microwave data in a bare soil and a densely vegetated region in Texas. He found that the vegetation reduced the sensitivity of the 6.6 GHz and 10.7 GHz microwave channels to the soil moisture signal. At a slightly higher frequency, Barton (1978) showed that soil moisture estimates based on 11 GHz airborne microwave measurements were quite good over bare soil but very poor in vegetated regions due to the effects of scattering and absorption and reemission by the vegetation canopy.

Nimbus-5 Electronically Scanning Microwave Radiometer (ESMR) satellite measurements have also been shown to be responsive to soil-moisture conditions over large land areas (Schmugge et al. 1977). At the ESMR frequency (19.35 GHz), correlations with soil moisture were found to be limited to predominantly bare soil and low vegetation density areas (Njoku 1982). Further studies by McFarland and Blanchard (1977) extended these results to the use of

API algorithms for ESMR data obtained over the Great Plains where little or no vegetation exists (Jackson and Schmugge 1989). Allison et al. (1979) also used ESMR data to observe flooding conditions in East Australia.

Using 37 GHz SMMR data, Spencer (1984) found polarization differences exceeding 16 K over wet soil regions. Additional studies by Choudhury and Blanchard (1983), and Choudhury and Monteith (1988) have used API as a surrogate soil moisture observation to correlate with microwave brightness temperatures from SMMR. Results from Choudhury and Monteith (1988) demonstrated that the relationship of microwave brightness temperature with API is also sensitive to the NDVI. However, two sites with different vegetation amounts also had similar correlations of microwave brightness temperature with API $\left(r^2 = 0.72\right)$. Flooding conditions were also observed in South America with the 37 GHz channels of SMMR (Giddings and 1989). Figure 2.1 shows the observed temporal variation of the Negro river stage at Manaus and the difference between the vertical and horizontal polarization at 37 GHz, ΔT. The maxima and minima of the river height match the ΔT values extremely well. As the river height increases, the low-lying areas of the river banks progressively become flooded. As the area of exposed water increases, the ΔT value increases. Other work has attempted to extend the single sensor data analysis to the use of multiple sensors to remotely sense soil moisture with various combinations of microwave, infrared and optical sensor data (e.g., Perry and Carlson 1988; Soarès et al. 1988; van de Griend and Gurney 1988; Choudhury 1990; Choudhury 1992).

Heymsfield and Fulton (1992) used higher frequency (19 GHz, 37 GHz and 85.5 GHz) SSM/I data in a case study over Oklahoma and found that rainfall has an important effect of the background microwave brightness temperatures at the SSM/I frequencies and found that a region of abnormally cold brightness temperatures coincided with a region dominated by recently planted wheat fields. Dew formation did not appear to cause a significant impact on the SSM/I

brightness temperatures. However, the effect of vegetation was shown to strongly dampen the soil moisture response at the SSM/I frequencies, even at the lowest 19 GHz frequency. In addition, a time series of observations was used to relate evaporation and transpiration to SSM/I brightness temperatures and API. Microwave emissivities were also used to normalize the brightness temperatures for the changing thermometric temperature of the background. These emissivities were based on in situ measurements of soil temperature at 10.2 cm depth and surface air temperatures. However, as mentioned in section 2.2.2 the surface air temperature is not generally the same as the radiometric surface temperature (Friedl 1995). The SSM/I radiances however are more affected by atmospheric features such as clouds and rain than lower frequency measurements (Hollinger et al. 1987), thus interpretation of the higher frequency microwave data is made more complex and difficult compared to lower frequency measurements. Appendix A.2 and A.3 contain further details regarding the behavior of microwave brightness temperatures due to atmospheric and surface conditions. Work by Heymsfield and Fulton (1992) showed that it would be very difficult to monitor soil moisture variations with any SSM/I frequency in vegetated regions. It was also not clear from that work whether soil moisture was being sensed, or whether the vegetation moisture content itself was measured. Thus the SSM/I does not have the most appropriate sensor frequencies to use for remote sensing of soil moisture. However, the SSM/I is currently the only available satellite-based passive microwave imaging sensor in orbit. Other passive microwave sensors such as the Microwave Sounding Unit (MSU) and the Special Sensor Microwave/Temperature Sounder (SSM/T and SSM/T-2) are sounders with reduced resolution capabilities.

Given multifrequency microwave observations, it is theoretically possible to determine a crude soil moisture profile since the depth of penetration of microwaves is a function of the frequency (Njoku and Kong 1977). However, Burke et al. (1979) have found that in practice this is

difficult to achieve. They found that even at 1.4 GHz the surface soil layer (1-2 cm deep) dominated the microwave signature. Heymsfield and Fulton (1992) also found that the SSM/I frequencies exhibited no clear difference in the period of recovery because of the very shallow surface soil layer being sensed at all frequencies. This suggests that soil moisture profiling does not seem feasible with the SSM/I channels. Long time periods of recovery were observed for the SSM/I which is likely due to the shallow surface layer being replenished by the hydraulic conductivity from deeper, wetter soil layers during the recovery period. Thus the SSM/I frequencies offer the possibility of gross monitoring of soil moisture in bare soil regions and perhaps even quantitative soil moisture retrievals with the use of radiative transfer models and additional data including in situ soil moisture measurements (Heymsfield and Fulton 1992). An explicit solution to the inverse problem of soil moisture using coherent wave radiative transfer theory has been derived by Entekhabi et al. (1994). However, this method has not been tested using actual observations.

Soil vegetation atmospheric transfer (SVAT) models have been developed to estimate bare-soil evaporation using microwave remote sensing data to initialize or update near-surface soil moisture conditions (e.g., Bernard et al. 1981; Prevot et al. 1984; Bernard et al. 1986; Bruckler and Witono 1989; Olioso et al. 1994). These models require atmospheric forcing inputs (e.g., wind speed, air temperature, and humidity at screen height) and information on soil properties that are usually difficult to obtain for regional energy balance estimates (Kustas 1993). However, results from this work show that at the higher microwave frequencies of the SSM/I the complexity of the vegetation influences on the microwave signature makes such a direct relationship quite tenuous.

Another idea that has been introduced recently is microwave brightness temperature correlations against the evaporative fraction (EF) $\left(EF = -E/\left(Q_R + Q_G\right)\right)$. The microwave brightness temperatures were correlated against EF and it was found that an inverse relationship existed with

a significant correlation $\left(r^2 = 0.69\right)$. The variation in EF in dry near-surface soil moisture conditions was correlated to the amount of vegetation cover estimated with a remotely sensed vegetation index. Thus the microwave data can indicate when soil evaporation is significantly contributing to EF, while the optical data is helpful for quantifying the spatial variation in EF due to the distribution of vegetation cover. In addition, using only microwave frequencies is a major limitation in estimating EF because the influence of vegetation and moisture below 5 cm in regulating EF cannot be addressed (Kustas 1993).

A method known as Radiobrightness Thermal Inertia (RTI) has also been proposed which uses day-night (12 h) differences in satellite-sensed brightness temperatures to monitor soil moisture (England et al. 1992). Again vegetation tends to mask both the thermal infrared and microwave signatures, so the attenuation of the diurnal brightness temperature range is expected to be less severe in prairie regions where the vegetation is short or sparse. The optimum day/night sampling times are during peak heating of the soil, since the method relies on a strong surface temperature range. The RTI method is a microwave analog of the infrared methods discussed in section 2.2.2.

An additional approach for detecting soil moisture using microwave data is through change detection. This approach can be used for both passive and active microwave data. The change detection method minimizes the impact of target variables such as soil texture, roughness and vegetation because these tend to change slowly, if at all with time. With change detection it is assumed that the only target change occurring is the soil moisture. Thus any measured changes in brightness temperature or roughness can be related directly to changes in soil moisture. Fortunately for many applications, the changes in soil moisture may be more important than the actual absolute value of soil moisture (Engman 1991).

2.3 ATMOSPHERIC MODELING STUDIES

The Project for the Intercomparison of Land Surface Parameterization Schemes (PILPS) has shown that a significant amount of the variability among models can be tracked to the soil moisture parameterization (Henderson-Sellers et al. 1995). In addition, when a hypothetical initial soil moisture field derived from forecast errors instead of a climatological estimate is used to initialize the Canadian global forecast model, it showed that the standard deviation of the temperature error is reduced by 20% (Delage and Verseghy 1995). That work is typical of other's experience with improving the soil moisture representation of their land surface parameterization schemes (see Chapter 1). Recently as part of a continuing sequence of model improvements, the National Meteorological Center (NMC) has implemented a Land-Surface Data Assimilation System (LDAS) that executes continuously in real time over the conterminous United States to provide initial soil moisture to the National Center for Environmental Prediction (NCEP) mesoscale Eta model (Black 1994).

In general, atmospheric land surface parameterization methods can be classified into two categories, one quasi-statistical and one deterministic. An example of the first group is an extended bucket model developed by Schaake (1990) which is being used successfully with limited data in the Nile River basin. The deterministic methods include explicit multilayer soils and vegetation canopies. Examples of these include the simplified SiBmodel of Xue et al. (1991) and the soil and vegetation model of Pan and Mahrt (1987), among numerous others. Of the deterministic methods, the variational data assimilation methods consist of a subgroup that have also been used to estimate soil moisture from the evolution of atmospheric parameters near the surface (temperature and relative humidity) (Mahfouf 1991). Classification of the methods can be subdivided further by data source requirements (e.g., various surface observations, satellite data sets, spatial and temporal sampling requirements), assumptions made for simplification or to ensure

closure of the land surface parameterization equation set, and the relative complexity and detail of the land surface system that the method attempts to simulate.

Application of the land surface parameterizations is typically much harder to do in the "real world" than with idealized simulations. Several factors can combine to make the anticipated thermally induced flows obscure. For example, in work by Segal et al. (1989) the circulations were reflected in the measurements, but only by modest changes in the wind speed and wind direction across the region of strong surface contrast. It was suggested that the synoptic flow, and the daytime elevated terrain-forced flow in the area, combined to mask to varying degrees the circulation due to the irrigated versus dry land effect. Numerical model simulations were performed over the studied region and were found to support this hypothesis. For simpler methods that employ bulk transfer coefficients, a systematic error of $\pm$ 1 K in the surface temperature has been found to lead to erroneous bulk transfer coefficient estimates (Matsushima and Kondo 1995). Thus implementation and validation of land surface parameterization schemes with observations can be a difficult task.

However, simulations of hypothetical situations can lead to a more in-depth understanding of the physical processes involved. For example, additional moistening in numerical simulations of the drought of 1988, showed a large relative increase in precipitation, often by as much as a factor of 2. Conversely, in the flood year of 1993, drying of the land surface resulted in a relative decrease in simulated rainfall by as much as 30%-40% (Pan et al. 1995). Temporal issues can also be addressed, such as in Clark and Arritt's (1995) work where larger values of initial soil moisture were found to delay the onset of precipitation and to increase the precipitation amount. It was also found that the greatest rainfall amounts were generally predicted to occur for moist fully vegetated surfaces, and that vegetation cover had a pronounced moderating influence, decreasing the sensitivity of the results to the soil moisture content. Also the inclusion of shading by

shallow cumulus clouds has been shown to have a tendency to reduce the convection for moist, bare (or partly bare) soil (Clark and Arritt 1995). The analysis of Chen and Avissar (1994b) showed that land-surface moisture discontinuities seem to play a more important role in a relatively dry atmosphere, and that the strongest precipitation is produced by a wavelength of land-surface forcing equivalent to the local Rossby radius of deformation. In another paper, Chen and Avissar (1994a) examined the mesoscale heat fluxes and found that the fluxes weaken in the presence of large-scale background winds but can remain significant even under moderate winds. Such work as this is helpful in the planning of field projects, and in focusing efforts toward areas that hopefully will produce a better understanding of the complex physical mechanisms involved with land surface-atmospheric interactions.

2.4 MCNIDER DATA ASSIMILATION METHOD

Several studies have been performed using surface skin-temperatures as retrieved from satellite for use in mesoscale models. Among these studies is work by Price (1982), Carlson et al. (1981), Wetzel et al. (1984), Carlson (1986), Wetzel and Woodward (1987), and Wetzel and Chang (1988). A major shortcoming of dynamic assimilation techniques has been that nudging the near-surface temperature has not been successful (Stauffer et al. 1991). This is primarily because nudging of the surface temperature alters the delicate balance in near-surface stability, drastically changes the momentum balance, and leads to sharp changes in velocity and boundary-layer behavior. Also, the surface energy budget may become unbalanced and prevent convergence (McNider et al. 1994). A recent development has been to force the atmospheric model surface parameterization with surface skin-temperature heating rates, rather than with the absolute magnitudes of the remotely sensed skin-temperatures. This has the benefit of eliminating the systematic bias due to sensor errors and view angle (Hall and Sellers 1995), and conversely, biases that may exist in the model parameterization scheme are also minimized. For example, an

imperfect model forced with absolutely accurate satellite data would produce invalid results and may not converge to a solution at all, while an imperfect model forced by relative satellite data (i.e. heating rates) may perform quite well, since a model based on heating rates requires only relative temperature accuracy rather than absolute temperature accuracy.

A study by McNider et al. (1994) used Geostationary Operational Environmental Satellite (GOES) Visible Infrared Spin Scan Radiometer (VISSR) infrared brightness temperatures coupled to an atmospheric mesoscale model to diagnose the surface friction humidity, q_*. The technique is based on analytically recovering surface moisture from similarity expressions derived from an evaporation residual obtained as a difference between the unadjusted model evapotranspiration and the satellite inferred evaporation and transpiration. It assumes that the largest error in the surface energy budget is in the evaporation and transpiration term. The method was tested on data from FIFE and a three-dimensional test over Oklahoma.

The technique of McNider et al. (1994) requires the use of surface skin-temperatures over the time period of interest, and is most applicable to the period from early to mid-morning when cloud-free views of the surface are more frequent and the assumptions of the technique are best satisfied (see section 2.2.2). The method is based on an alternative form of the surface energy budget (see Equation 2.1)

$$C_b \frac{\partial T_G}{\partial t} = Q_R + Q_C - Q_G, \tag{2.18}$$

(Blackadar 1979) which contains a prognostic term $C_b \partial T_G / \partial t$ that accounts for the resistance to changes in the surface temperature. This is different in approach than the original surface energy budget (Equation 2.1). Previously we had assumed that all changes in the surface energy budget occurred instantaneously within an infinitesimally-thin air-surface interface. The representation of Equation 2.18 is now capable of including temporal "lags" induced by heat storage

and other factors, similar in concept to thermal inertial, but more general in scope. Thus, to avoid confusion, the parameter, C_b, is called the surface heat resistance, rather than thermal inertia, i.e., the thermal inertia term is reserved for referring to the narrowly defined physics phenomena relating directly to the heat capacity of a material, while surface heat resistance is a more generalized composite term which can include multiple heat capacities in addition of other physical mechanisms.

Given the satellite-observed temperature change and Equation 2.2, Equation 2.18 can be inverted to give

$$E_s = Q_G - Q_R - H + C_b\left(\frac{\partial T_G}{\partial t}\right)_s, \tag{2.19}$$

where H is the sensible heat flux, and E_s is the satellite inferred latent heat flux as a function of the satellite derived time rate of change of the surface skin-temperature (the subscript s denotes satellite observed values). By writing the model's surface energy budget in a similar manner,

$$E_m = Q_G - Q_R - H + C_b\left(\frac{\partial T_G}{\partial t}\right)_m, \tag{2.20}$$

where the subscript m denotes the model values, there are two equations that can be combined given certain assumptions. The biggest assumption is that all the terms in the model's surface energy budget are the same as for the actual energy budget except for the latent heat flux term, E. So by taking the difference of Equations 2.19 and 2.20 we obtain

$$E_s - E_m = C_b\left[\left(\frac{\partial T_G}{\partial t}\right)_s - \left(\frac{\partial T_G}{\partial t}\right)_m\right]. \tag{2.21}$$

The term on the left-hand-side of Equation 2.21 can be expanded substituting with Equation 2.2, which results in

$$\overline{\rho} L_v \left(u_{*_s} q_{*_s} - u_{*_m} q_{*_m} \right) = C_b \left[\left(\frac{\partial T_G}{\partial t} \right)_s - \left(\frac{\partial T_G}{\partial t} \right)_m \right]. \tag{2.22}$$

By assuming that $u_{*_s} = u_{*_m}$ in Equation 2.22, we can solve for q_{*_s}

$$q_{*_s} = \frac{1}{u_{*_m}} \left\{ \frac{C_b}{\overline{\rho} L_v} \left[\left(\frac{\partial T_G}{\partial t} \right)_s - \left(\frac{\partial T_G}{\partial t} \right)_m \right] + \left(u_{*_m} q_{*_m} \right) \right\}, \tag{2.23}$$

were u_{*_m} has a specified minimum value for calm wind conditions. Once q_{*_s} is in terms of the model variables and satellite observations, it may be used in combination with Equations 2.15 and 2.11 to obtain the surface wetness using similarity theory,

$$q_G = q(z) - \frac{q_{*_s}}{\beta k} \left\{ \left[\ln\left(z/z_0 \right) - \phi_H \left(z/L \right) \right] + \gamma_c \right\}. \tag{2.24}$$

Equation 2.24 is the revised surface humidity deduced from the rate of change of the satellite skin-temperature. In practice, limits are imposed on q_G such that $q_G < q_{sat}\left(T_G\right)$, where q_{sat} is the saturated specific humidity at the surface temperature, T_G, and $q_G > 0$. As shown in Figure 2.2, the method iterates to converge upon a sensible heat flux value before attempting to calculate the surface humidity. Another piece of information required by the method is the surface heat resistance which must be calculated by inverting Equation 2.20 and solving for C_b,

$$C_b = \frac{Q_R + H + E_m - Q_G}{\left(\frac{\partial T_G}{\partial t} \right)_m}. \tag{2.25}$$

This parameter can be highly variable and McNider et al. (1994) suggest that more work needs to be done in diagnosing this parameter. The main limitations of the method are the unknown errors involved in the assumptions of the method, and in the rather limited time period for which is it

valid (morning to early afternoon). An extension of this method that includes vegetation effects and eliminates the problematic C_h term is developed for the CSU-RAMS surface parameterization scheme in Chapter 5.

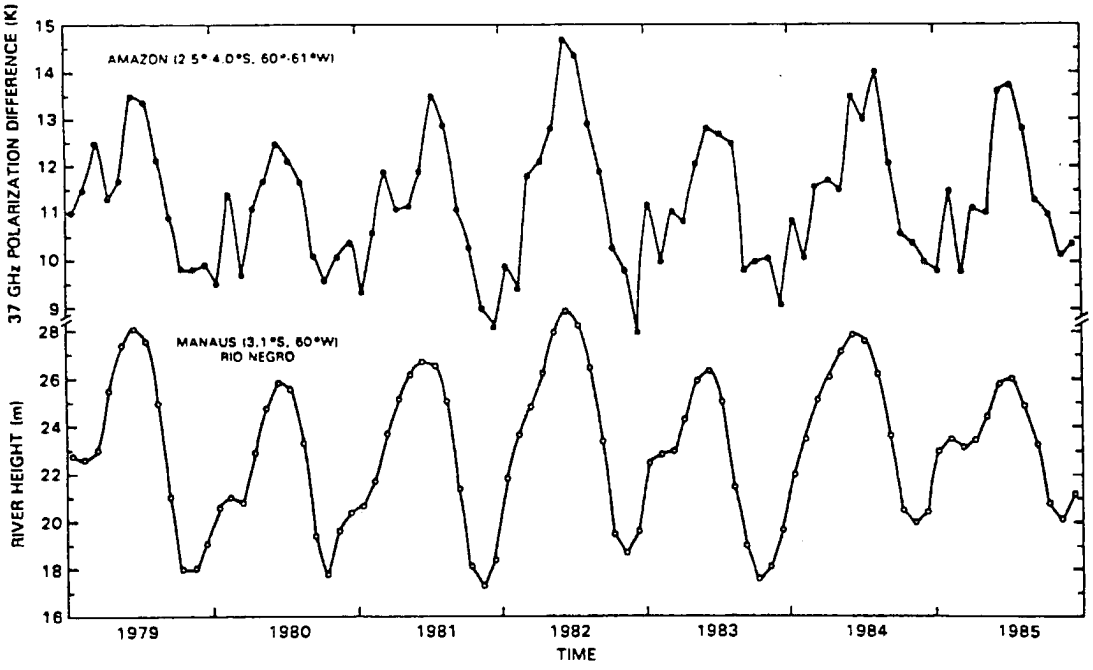

Figure 2.1: Temporal variation of 37 GHz emission over a region of Amazon and Negro rivers and the Negro river height measured at Manaus (from Choudhury 1991a).

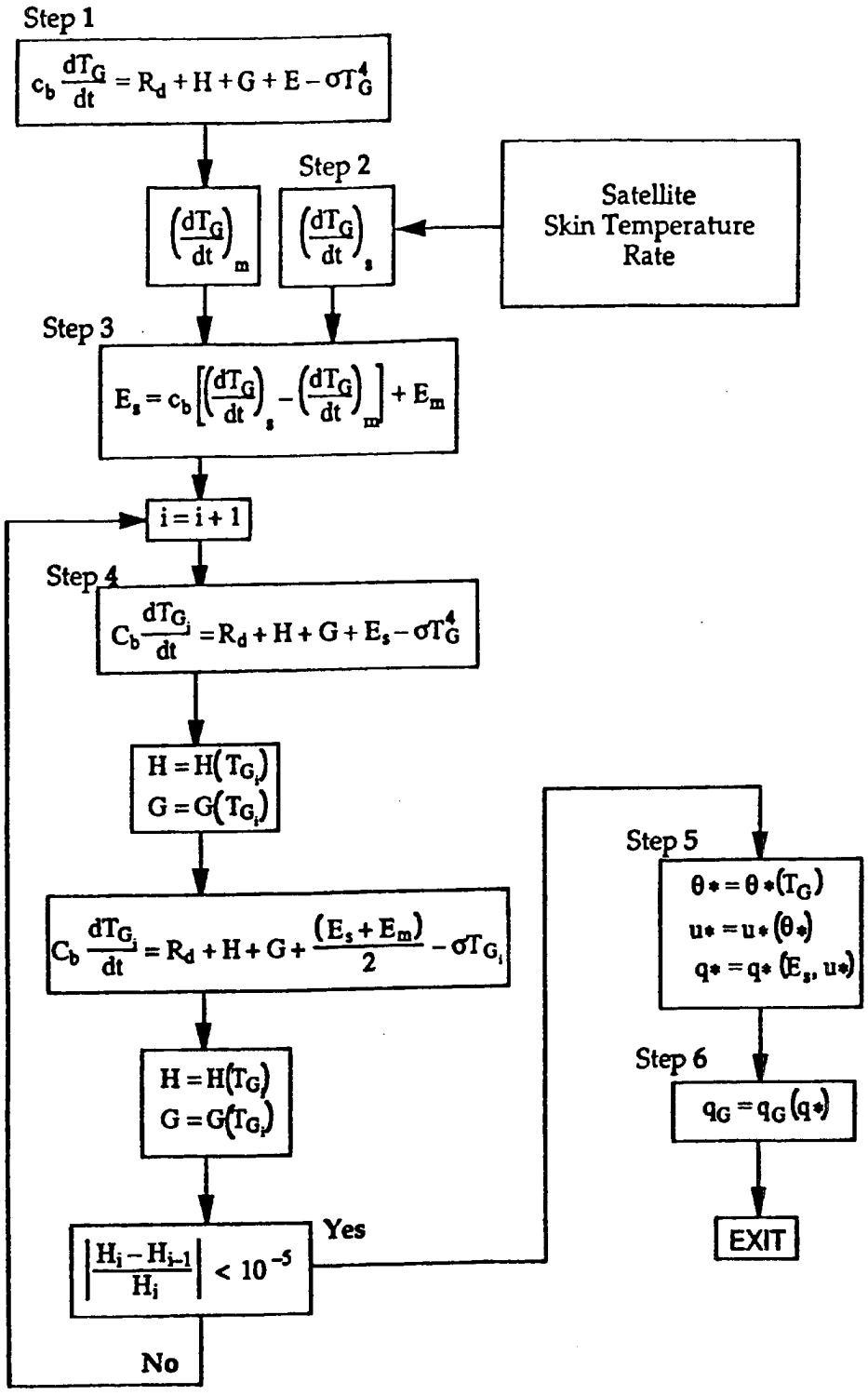

Figure 2.2: Flow chart of the skin-temperature data assimilation process (from McNider et al. 1994).

Chapter 3

DATA

By the very nature of this work, the data sets involved are varied and diverse. This chapter provides summary information for reference throughout the text. In particular, the satellite sensors and data sets are discussed in sections 3.1 and 3.2, and various ancillary data sets are discussed in section 3.3, while the meteorological backgrounds for the two major case studies of this work are discussed in section 3.6. Additional information regarding the specific NDVI data set used in this work is presented in section 3.3.5. A brief reference is made to the satellite data fusion methodology in section 3.5. However, a complete description is contained in Appendix C.

3.1 VISSR INSTRUMENT DESCRIPTION

The GOES series are operated by the National Oceanic and Atmospheric Administration (NOAA). Presently, three such satellites are in operation over the Western Hemisphere, GOES-7, GOES-8, and GOES-9, maintaining a geosynchronous orbit at the equator at an altitude of 35,800 km. The satellite used in this study, GOES-7, is commonly called GOES WEST due to its stationary longitudinal position at approximately 135° W. This position can vary depending on NOAA needs. During the time period of this study, the actual longitudinal position was at 97.5° W and was relatively stable. The GOES-8 and GOES-9 satellites are the first of a new generation of satellites known as the GOES-NEXT series (Menzel and Purdom 1994). Thus, GOES-7 is the last satellite of an older GOES satellite series.

The instrument on board the GOES-7 satellite used in this study is the Visible and Infrared Spin Scan Radiometer (VISSR) and when operated in dwell sounding mode (a mode in which all

12 infrared channels are repeatedly scanned to improve instrument noise characteristics for sounding retrieval purposes) it is known as the VISSR Atmospheric Sounder (VAS). The instrument is capable of measuring the upwelling radiance from the earth in the visible and in 12 infrared spectral channels from 3.9 μm to 15 μm. Table 3.1 adapted from Chesters and Robinson (1983) lists the spectral characteristics of the VAS channels. The pre-launch noise specifications were originally given in terms of Noise Equivalent Radiance Differences but are listed in Table 3.1 as noise equivalent temperature differences (NEΔTs). The absolute accuracy of the VISSR infrared data is ± 1.5 K. In normal VISSR mode, the visible and surface infrared channel, channel 8, are transmitted each half hour for the whole hemisphere. Channel 8 is a surface channel with a high sensitivity to the surface as the atmospheric weighting function, $d\tau/d\ln p$, for channel 8 in Figure 3.1 indicates. The other VAS channels are used for sounding retrievals since their weighting functions peak at a higher level in the atmosphere.

The instrument is actually several detectors combined. The visible detector is a separate unit with 8 sensors that scan the earth West-to-East (W-E) in parallel. Three infrared sensors of multiple types with different field-of-views (FOVs) are used in conjunction with a selectable narrowband filter creating a quite complex arrangement that is capable of several modes of operation (Clark 1983). The instrument scans the earth by moving a mirror in the north-to-south (N-S) direction in angular increments of 0.192 mrad as the satellite spins at 100 rpm about its axis that is perpendicular to the earth's equatorial plane. The sampling rate for the infrared data is 8 μs, which produces 3822 elements for each line of data, and for the maximum mirror steps there are 1821 lines, which result in hemispheric coverage of approximately ± 70° in longitude with respect to the satellite subpoint. The visible data with its 8 sensors has a possible 14568 lines and elements. The visible resolution at nadir is 0.9 km and channel 8 has a nadir resolution of 6.9 km. During the scanning process the E-W direction is over sampled, which results in 4×8 km

rectangular infrared sensor FOVs. The VISSR data is navigated based on the automatic navigation parameters that the satellite transmits to the groundstation which are updated daily. The apparent navigation error during the case study was ± 2 pixels for the infrared imagery which roughly corresponds to ± 14 km. Examples of the VISSR infrared, water vapor, and visible imagery over the case study region for 1532-1535 UTC 8 September 1991 are shown in Figures 3.2 - 3.4. The infrared and water vapor imagery are displayed in terms of brightness temperature (K), while the visible imagery is in terms of raw 6-bit visible count values (with a range of 0 to 63). As Figure 3.4 shows, the visible spatial resolution is significantly better than the infrared imagery resolution.

3.2 SSM/I INSTRUMENT DESCRIPTION

The Special Sensor Microwave/Imager (SSM/I) has flown on at least three Defense Meteorological Satellite Program (DMSP) satellites, F-8 (launched 19 June 1987), F-10 (launched 1 December 1990), and F-11 (launched 28 November 1991). The DMSP satellites are in a sun-synchronous near-polar orbit at an altitude of 833 km with a period of 102 minutes. The orbit equator crossing times are approximately 0612 local time and has an orbit inclination of 98.8° which allows for twice daily coverage poleward of 50° latitude (Hollinger et al. 1987).

The instrument consists of an offset parabolic reflector which is 61 cm × 66 cm in size and is mounted on a rotating drum which also contains the feedhorn and various supporting electronics. The simultaneous rotation of the feedhorn assembly with the reflector is an improvement over earlier microwave imaging systems such as SMMR that had a fixed feedhorn assembly. The simultaneous rotation allows for more accurate polarization measurements since the direction of polarized radiation with respect to the feedhorn is the same as the feedhorn rotates with the reflector. The SMMR data must have polarization corrections applied to overcome this problem (Njoku 1980). The SSM/I has four frequencies (19.35, 22.235, 37.0, and 85.5 GHz) and dual

polarization capabilities on all except the 22.235 GHz frequency which records only the vertical polarization (see Table 3.2). The data is collected during the rearward 102° portion of the instrument rotation which results in a conical scanning pattern 1394 km wide (see Figure 3.5). The conical scanning pattern has a constant zenith angle of 53.1°, eliminating changing limb effects due to varying zenith angle. Since the instrument uses the same antenna for the various channels, the effective-field-of-view (EFOV) of the sensor varies with frequency, with the highest frequency, 85.5 GHz, having the highest resolution. The resolutions given in Table 3.2 and shown schematically in Figure 3.5 are for the 3 dB (half-power) antenna beam widths. The data are sampled at 64 positions (every 1.6°) per scan line (128 samples at 85.5 GHz) with an integration time of 7.95 ms (3.89 ms at 85.5 GHz). Since the 85.5 GHz is of higher resolution, the lower resolution channels are sampled every other scan line with the 85.5 GHz channels being sampled for each line continuously. This pattern results in a sample resolution of 12.5 km × 12.5 km for the 85.5 GHz channels and 25 km × 25 km for the lower resolution channels. Figure 3.6 presents the beam sizes and sampling grid for a region near the ground track of the sub-satellite point and near the edge of the swath. The effect of the radiometer integration times is to increase the effective along scan beam diameter and make the beams at 37 and 85 GHz nearly circular. Note the greater overlapping of beams near the edge of the swath in Figure 3.6. Examples of DMSP F-10 SSM/I microwave brightness temperature data from the 37H GHz and 85.5H GHz channels (channels 5 and 7) for 1525-1534 UTC 8 September 1991 are shown in Figures 3.7 and 3.8.

The F-8 SSM/I sensor developed technical problems with its 85.5 GHz channels (Hollinger et al. 1990) (see Table 3.3). Thus the 85.5 GHz data for the time period of this study (late summer of 1991) originates exclusively from the F-10 SSM/I sensor (the F-11 was not yet launched). However, the lower frequency SSM/I channel data (channels 1-5) were unaffected by the F-8 85.5 GHz problems and are available for both SSM/I sensors (F-8 and F-10).

The raw data is processed by several algorithms that provide antenna corrections for the calibrated sensor brightness temperatures and navigation parameters which will not be explained in detail here (for more information see Hollinger et al. 1987). The navigation for each data location was assigned from the satellite ephemeris data. Data archived after July 1989 have absolute navigation errors reduced to approximately 7 km (half of the 85.5 GHz sample resolution) due to improved satellite ephemeris data and an additional constant navigation correction (Poe and Conway 1990; Poe 1990).

3.3 ANCILLARY DATA SETS

3.3.1 SAO/UPA Data

The United States Air Force Environmental Technical Applications Center (USAFETAC) DATSAV Upper-Air Data Set (USAF 1977) was the source of the atmospheric soundings of temperature and water vapor that were used in this study. In particular, it was the source for the radiative transfer calculations that require measurements of the atmospheric state variables. The data was quality controlled to remove potential errors in the data set. Soundings were required to extend to the 400 mb level and have at least 5 sounding levels with valid temperature and water vapor mixing ratios spread over a 650 mb range. Many soundings exceeded these criteria and data quality was not found to be a significant problem.

3.3.2 USAFETAC Climatic Database — Surface Observations

The USAFETAC Climatic Database (DATSAV2 Surface) was used in the precipitation comparison data analysis (USAF 1986). In the database, precipitation totals were reported for each 6 hour period for the central United States, with some additional irregular reporting periods. The data were quality controlled by removing redundant reports, temporally interpolating irregular reporting periods, and eliminating stations that reported less than 80% of the time. The remaining

296 post-quality-controlled stations are shown in Figure 3.9. Over 11,000 precipitation events are included in the data set.

3.3.3 USDA Crop Moisture Index

The USDA produces crop moisture estimates for the United States from local USDA agricultural offices distributed throughout the country. Each division reports a numerical crop moisture index (CMI) which is then spatially interpolated to generate the final product. The divisions have a spacing of roughly 100 km in the East with much larger distances in parts of the western United States (up to 500 km). The estimate is based on crop need versus the available water in a 1.5 m soil profile. The USDA crop moisture estimates are considered short term (up to about 4 weeks) and can change considerably on a weekly basis. Table 3.4 contains the numerical crop moisture ratings and their verbal equivalents.

3.3.4 NGDC Digital Elevation Model Database

The National Geophysical Data Center (NGDC) Digital Elevation Model (DEM) data were used to correct the radiative transfer calculations for topographic effects. Primarily the radiative transfer topographic effect is due to surface pressure changes associated with elevation differences. This effect is largest in the mountainous regions. The DEM data were derived from the 30-arc second data set distributed by NGDC. The EROS Data Center (EDC) has edited this version of the NGDC DEM data for obvious errors in the Great Lakes. The only important difference between the NGDC product and the EDC version is that the EDC has reprojected the file using bilinear resampling to the Lambert projection with 1-km cells. These data were originally created by the U.S. Army Mapping Service with a 64 m Universal Transverse Mercator (UTM) cell and were resampled (at 3 arc seconds) by Defense Mapping Agency Topographic Command. For the NGDC product, sampling was done by selecting every 10th line and element (1 percent sample), and elevations were rounded to the nearest 6 m (20 ft.). The DEM for the case study

region is shown in Figure 3.10. The data are limited to the United States and were not available for Canada or Mexico. Therefore, results that rely on the DEM data set are also limited to the United States.

3.3.5 CSU-RAMS Initialization Datasets

Atmospheric variables of the CSU-RAMS model were initialized using a combination of the NMC gridded 2.5 degree pressure data, upper air soundings and surface observations for 1200 UTC and 0000 UTC. The data were obtained through the internet from the NCAR mass storage system. Topography, vegetation type, land percentage, and climatological sea surface temperature were read from the standard CSU-RAMS 10 minute initialization data files. Vegetation categories for the land surface vegetation parameterization scheme were obtained from USGS NDVI-derived datasets (see Lee 1992).

3.4 NORMALIZED DIFFERENCE VEGETATION INDEX (NDVI)

As discussed in section 2.2.1, the NDVI is based on channels 1 and 2 of the AVHRR sensor (Gutman 1991; Kidwell 1994; Gutman et al. 1995). The NDVI dataset used in this work is the USGS EDC's Land-cover Characteristics Database for the Conterminous United States that includes a biweekly 1 km NDVI dataset (Loveland et al. 1991). The NDVI data have been remapped to a Lambert projection in a similar fashion as the DEM data described in section 3.3.4. Figure 3.11 shows average NDVI values for the central United States for Julian Days 200-284 of 1991. The main vegetation feature is the strong east-west gradient in the NDVI field, with maximum NDVI values over the upper Midwest, and minimum NDVI values scattered thoughout desert regions of the West. The NDVI values were observed to change slowly with seasonal vegtational effects.

3.5 CO-LOCATION OF SATELLITE AND GEOPHYSICAL DATA SETS

Multisensor-multispectral scientific data applications require a tremendous investment regarding data preparation and analysis. A data fusion method was developed for this work that is general enough for use with any scan-line-based datasets (satellite and ground based) and enables multisensor-multispectral datasets to be merged on a routine basis (Jones et al. 1995). A self-describing generalized data format is used to modularize the data processing flow and obtain significant improvements in terms of flexibility, extensibility, and generality of application. While comparable processing times are needed to physically merge datasets, results show significant performance gains on any subsequent analysis of the merged datasets since scientific algorithms operate within the original satellite projection space. The advanced software processing techniques used in the Polar Orbiter Remapping and Transformation Application Library (PORTAL) are discussed further in Appendix C.

3.6 GENERAL DESCRIPTION OF SELECTED CASE STUDIES

As discussed in section 1.3, there are two major parts of this study. This section reviews relevant background information and conditions for each part for future reference throughout the remainder of this work.

3.6.1 Case A: Mississippi Basin

The Mississippi Basin watershed area (25-55° N, 85-110° W) was selected for the continental-scale portion of this work. The period selected was late summer (Aug.-Oct., 1991) and was approximately 70 days in length. The year of 1991 was noted for the mid-summer drought over the Midwest with several locations receiving less than 50% of their normal rainfall (see Figure 3.12). However, during the late summer time period of this case study, the Midwest drought started to break by September, so this case study includes a significant transitional period. Monthly total precipitation and percentage of normal precipitation for July 1991 through

September 1991 is shown in Figures 3.13-3.15. Features to notice are the generally moist conditions throughout the period for the upper Midwest, the early dry conditions in the lower Midwest that later receive significant rainfall, and the highly variable situation in the central Great Plains region. July's rainfall (see Figure 3.13) was not unusual except for south-central Nebraska receiving more than 4 inches (10.24 cm) of rain. August brought heavy rains to most of Kansas while sparing Oklahoma (Figure 3.14). Conversely, during September west Kansas had little if any rain, while most of Oklahoma, and the southern Plains in general, received very heavy rain, with a large region receiving more than 8 inches (20.48 cm) of rain (Figure 3.15). Thus the late summer of 1991 is a very good time period to observe surface soil moisture changes. The correspondence of these rain events to the satellite observations is discussed in detail in Chapter 4.

3.6.2 Case B: Oklahoma/Kansas Region

The coupled satellite-model work was performed on a much smaller time scale. A single day was selected (1991 September 8) in which morning conditions were mostly clear, and afternoon observations showed a weak dryline formation in the central Great Plains (Kansas-Oklahoma region). Additionally, soil moisture contrasts were particularly strong for this case. Thus this represented an excellent opportunity to test the coupled satellite-model soil moisture retrieval system that is developed in Chapter 5.

The day before September 8 heavily influenced the surface soil moisture field, with morning rain in south-central Kansas and northwest Oklahoma moving northeastward with time. Eastern South Dakota also experienced rain on September 7. The basic synoptic flow was dominated by an upper level trough over the Rockies with a surface low in eastern Wyoming moving into South Dakota by late evening. Radar indicated a persistent pattern of rain showers in the eastern part of Kansas. Details of the radar field will be shown in Chapter 5 along with the satellite-model-derived surface soil moisture fields. Flood watches were issued for parts of north-central Texas.

During September 7 forecasts were calling for a dryline to appear in central Oklahoma extending southwestward into west-central Texas. By late evening a line of precipitation that was slowly propagating eastward extended from west Minnesota south to east Texas.

On September 8 a flood watch was issued for southeast and south-central North Dakota. Windy conditions were pervasive throughout most of the Great Plains in association with the surface low which at this time was in western South Dakota. Morning temperatures were generally in the low-20's (°C) for most Great Plains stations. By the afternoon of September 8, the dryline location had been reforecasted to appear slightly west (100-200 km west) of the original forecast location, which corresponded to its eventual location as observed by satellite later in the afternoon. A tornado watch box was issued extending until 10 PM (local time) for southeast North Dakota and northeast South Dakota. A severe thunderstorm watch box was issued for central Kansas. High's extended into the low to mid 30's (°C) in the central Great Plains. The strength of the dryline was weak. By evening, the severe thunderstorm watch box had been canceled while only the southeast quadrant of the tornado watch box remained for the Dakotas. In the late evening of September 8, a rather strong thunderstorm did eventually form in extreme north-central Kansas.

Table 3.1: VAS instrument characteristics (GOES-7) (adapted from Chesters and Robinson 1983).

VAS channel number	Central wavelength (μm)	Weighting function peak (hPa)	Absorbing constituent	single sample noise values* (K)
1	14.68	40	CO_2	3.1
2	14.46	70	CO_2	2.0
3	14.19	150	CO_2	1.4
4	13.97	450	CO_2	1.0
5	13.33	950	CO_2	0.5
6	4.52	850	CO_2	0.4
7	12.67	surface	H_2O	0.6
8	11.18	surface	window	0.2
9	7.26	600	H_2O	1.6
10	6.72	400	H_2O	1.0
11	4.48	500	CO_2	1.8
12	3.95	surface	window	0.3

* VAS large field of view sensor

Table 3.2: SSM/I instrument characteristics (adapted from Hollinger et al. 1987).

Channel number	Frequency (GHz)	Polar-ization (H or V)	Effective-field-of-view (EFOV)* (km)	Sensitivity (NEΔT)** (K)	Accuracy (K)
1	19.35	V	70 × 45	0.45	1.5
2	19.35	H	70 × 45	0.42	1.5
3	22.235	V	60 × 40	0.74	1.5
4	37.0	V	38 × 30	0.37	1.5
5	37.0	H	38 × 30	0.38	1.5
6	85.5	V	16 × 14	0.69	1.5
7	85.5	H	16 × 14	0.73	1.5

* 3 dB limits.

** Average of laboratory measurements.

Table 3.3: F-8 SSM/I 85.5 GHz channel performance summary.

Polarization V	Polarization H	time period
off	off	02-Dec-1987 to 12-Jan-1988
poor	good	12-Jan-1988 to end of Jan-1988
failed	good	end of Jan-1988
	good	til Dec-1988/Jan-1988
	poor	Dec-1988/Jan-1988 to Mar-1990
	failed	Mar-1990

Table 3.4: USDA Crop Moisture Index (CMI) and verbal equivalents.

USDA Crop Moisture Index Range	wetter or stable conditions	drying conditions
CMI > 3	excessively wet, some fields flooded	some drying but still excessively wet
2 > CMI >3	too wet, some standing water	some dry weather needed, work delayed
1 > CMI > 2	prospects above normal, some fields too wet	favorable, except still too wet in spots
0 > CMI > 1	moisture adequate for present needs	favorable for normal growth and fieldwork
-1 > CMI > 0	prospects improved but rain still needed	topsoil moisture short, germination slow
-2 > CMI > -1	some improvement but still too dry	abnormally dry, prospects deteriorating
-3 > CMI > -2	drought eased but still serious	too dry, yield prospects reduced
-4 > CMI > -3	drought continues, rain urgently needed	potential yields severely cut by drought
CMI < -4	not enough rain, still extremely dry	extremely dry, most crops ruined

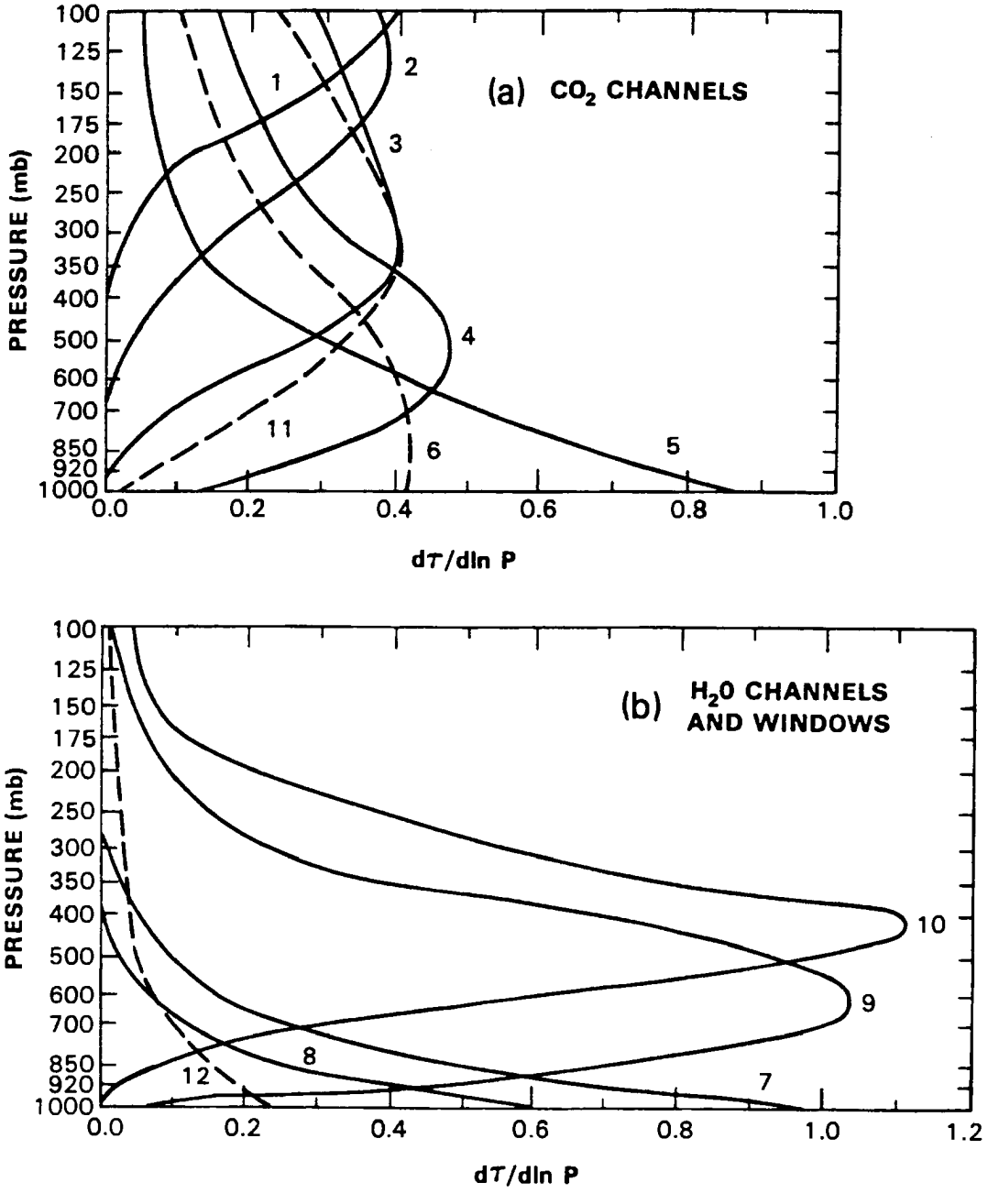

Figure 3.1: Comparison of VAS CO_2 sounding channel atmospheric weighting functions with VAS channel 8 (from Montgomery and Uccellini 1985).

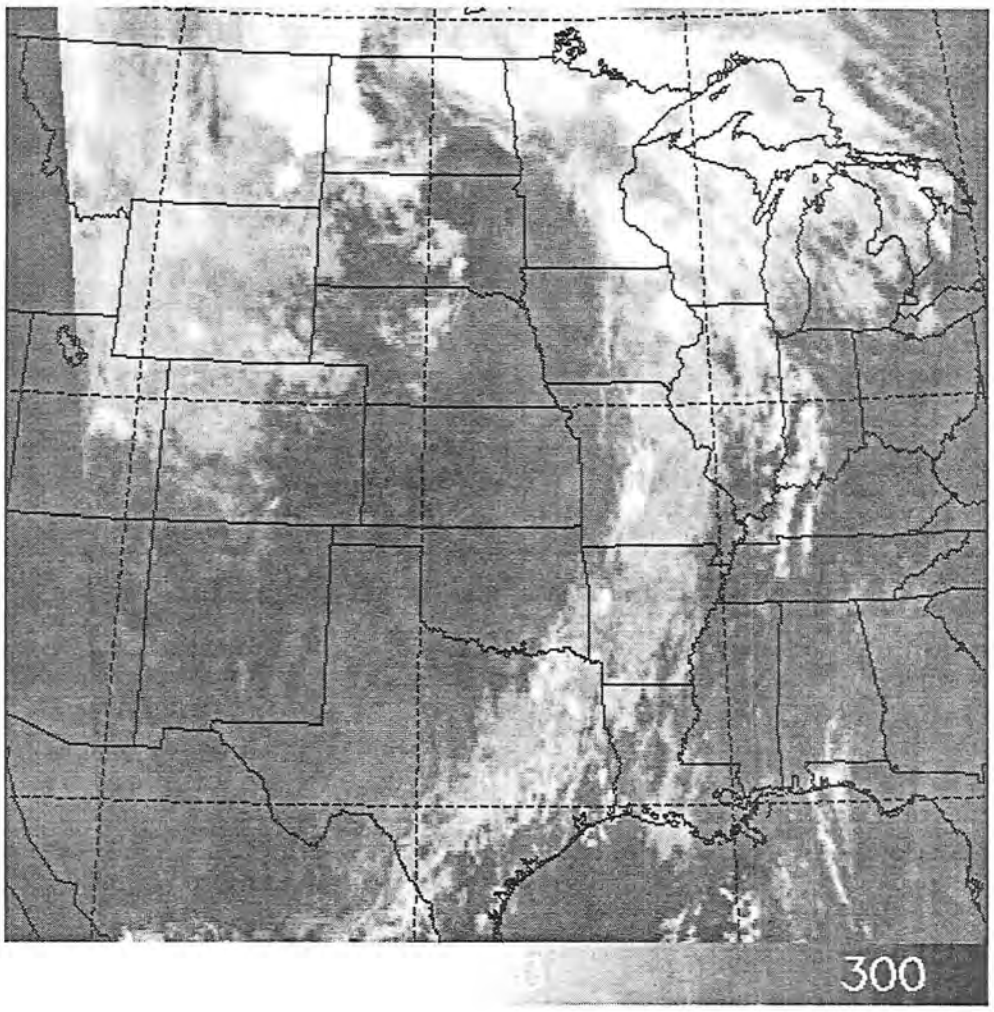

Figure 3.2: An example of VISSR infrared imagery for 1532-1535 UTC 8 September 1991 over the case study region. Values are displayed in terms of brightness temperature (K).

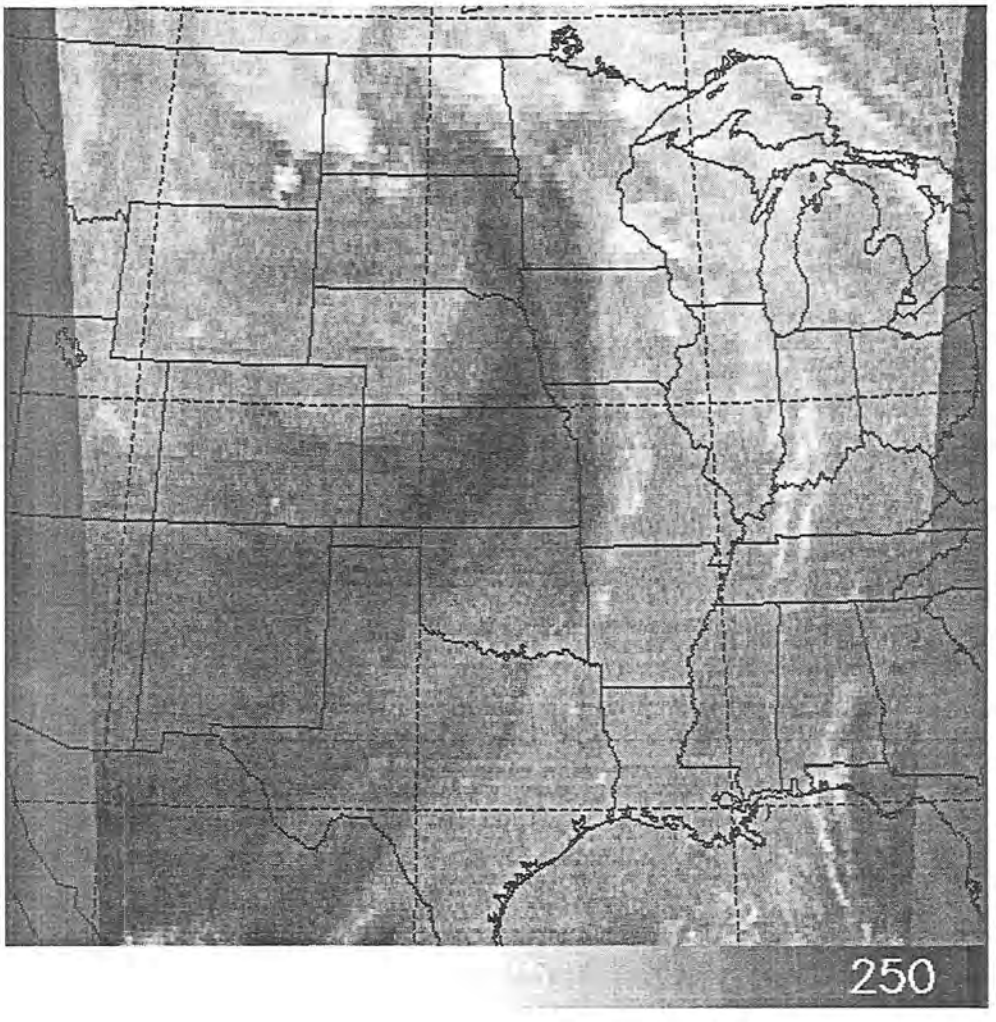

Figure 3.3: Same as Figure 3.2, except for VISSR water vapor imagery.

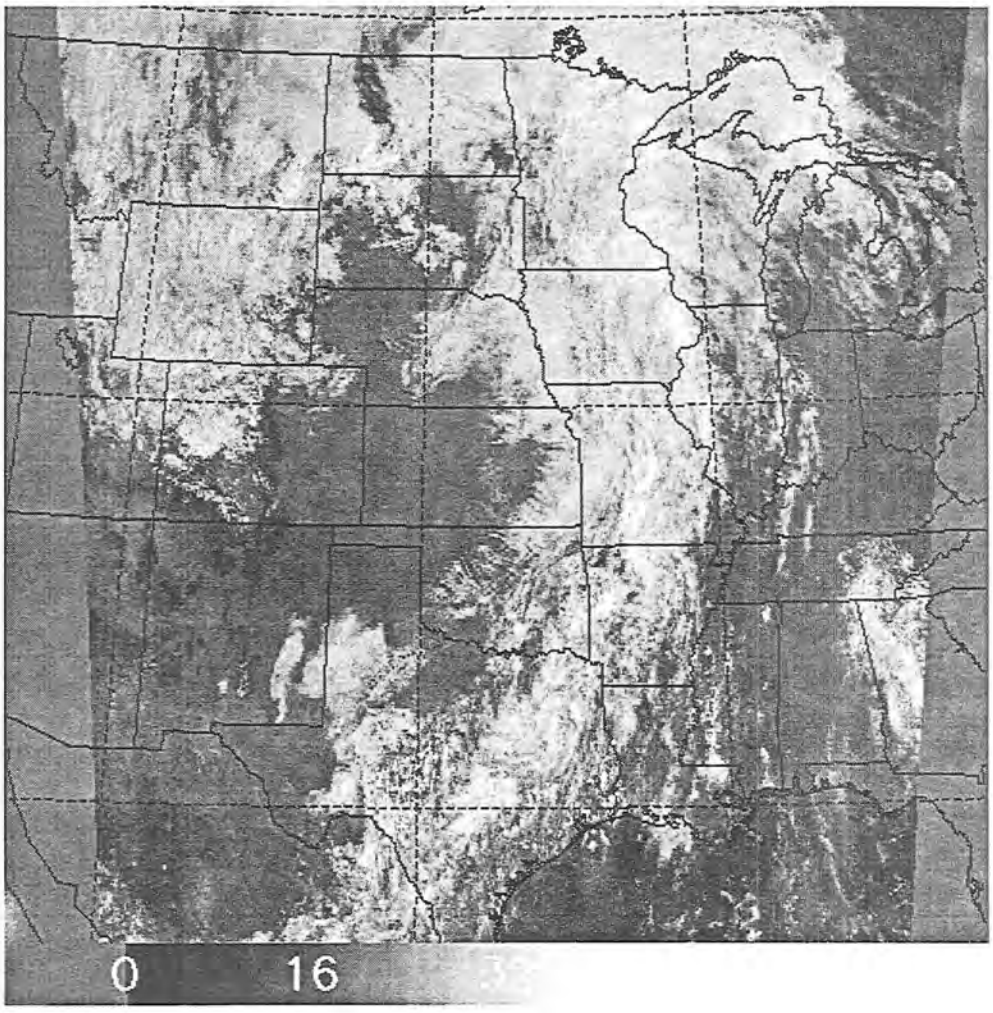

Figure 3.4: Same as Figure 3.2, except for VISSR visible imagery. Values displayed are in terms of raw 6-bit count values.

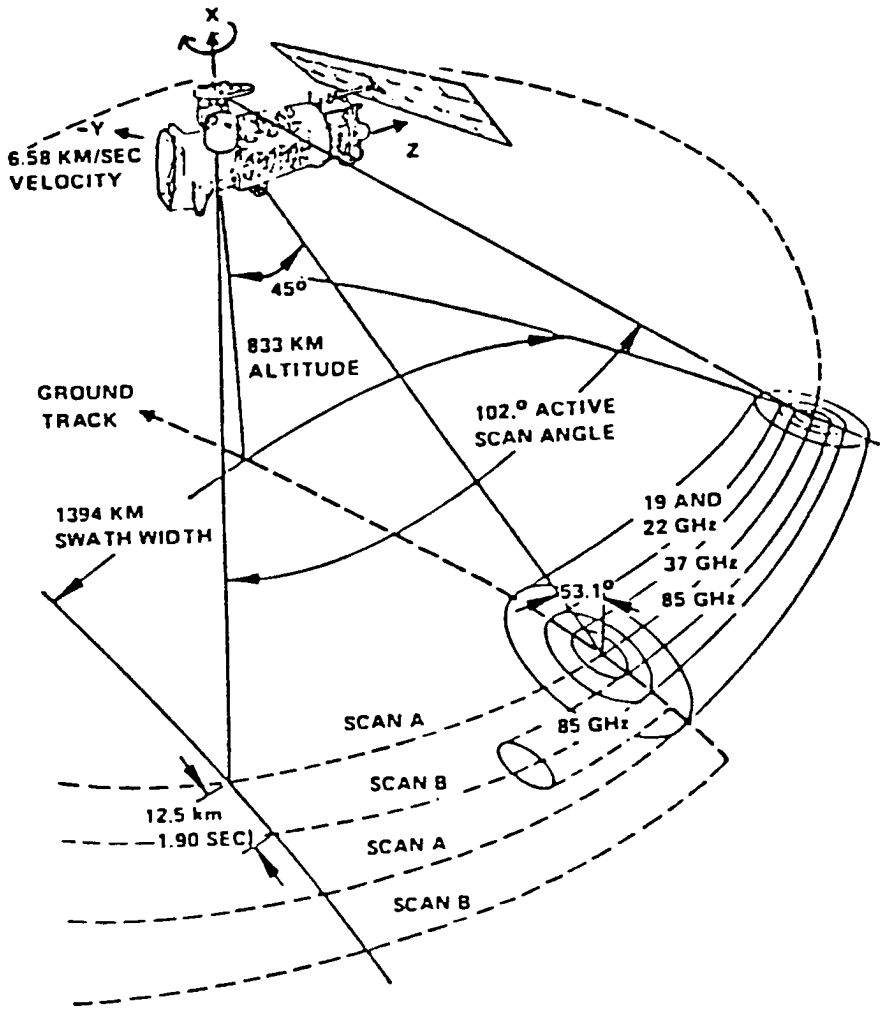

Figure 3.5: SSM/I conical scanning geometry (Hollinger et al. 1987).

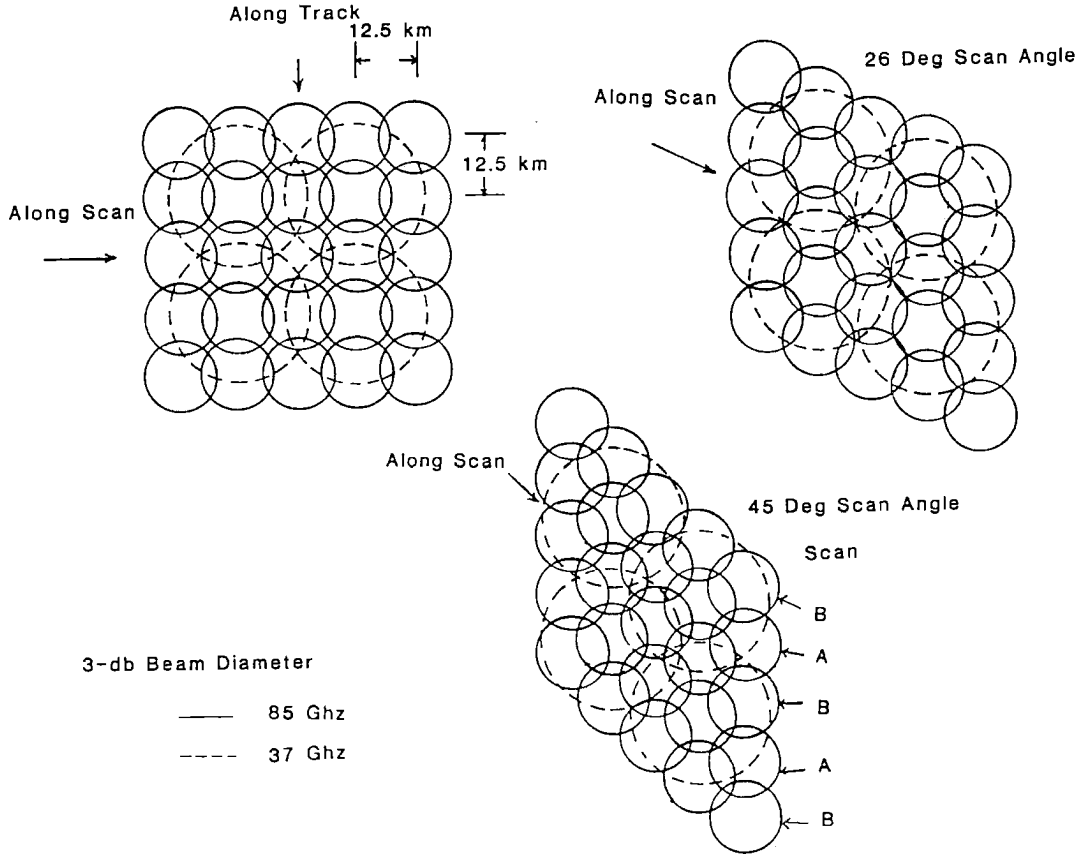

Figure 3.6: SSM/I spatial sampling (Hollinger et al. 1987).

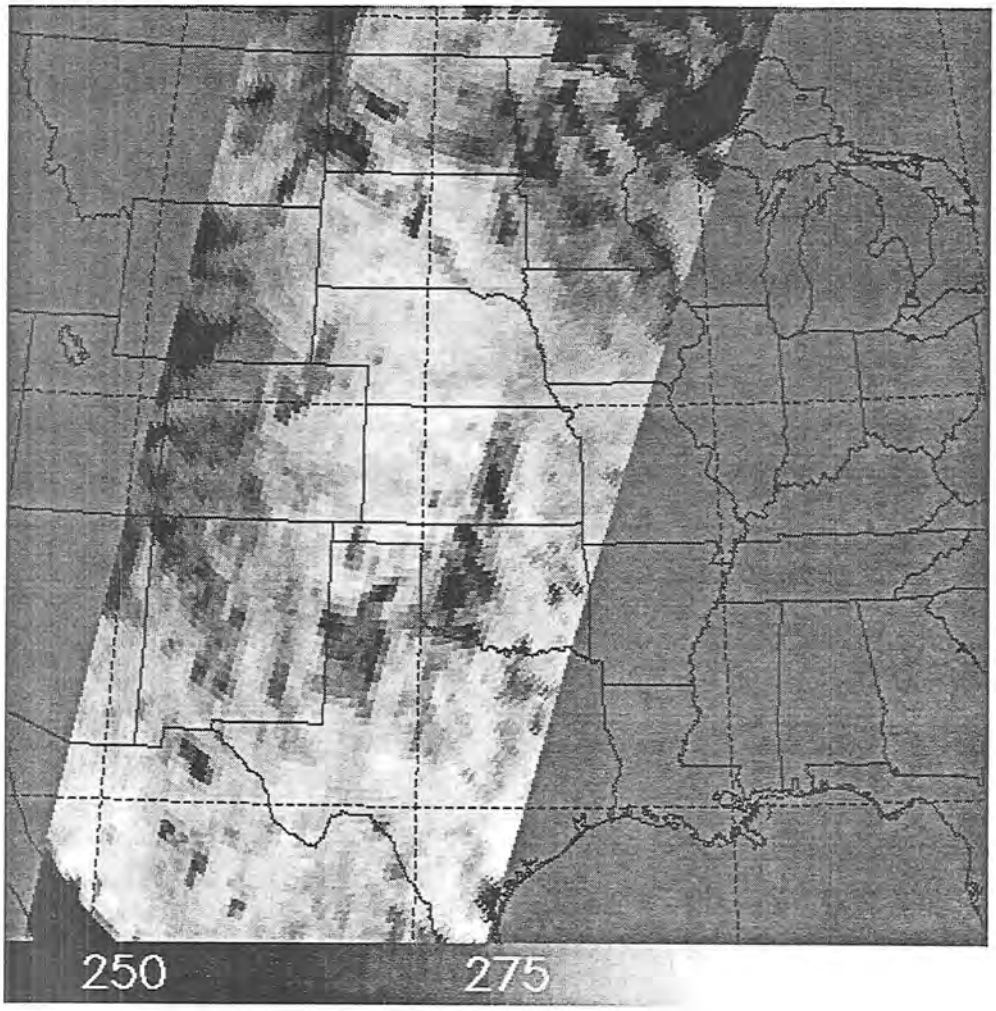

Figure 3.7: DMSP F-10 SSM/I 37H GHz (channel 5) microwave brightness temperature (K) for 1525-1534 UTC 8 September 1991.

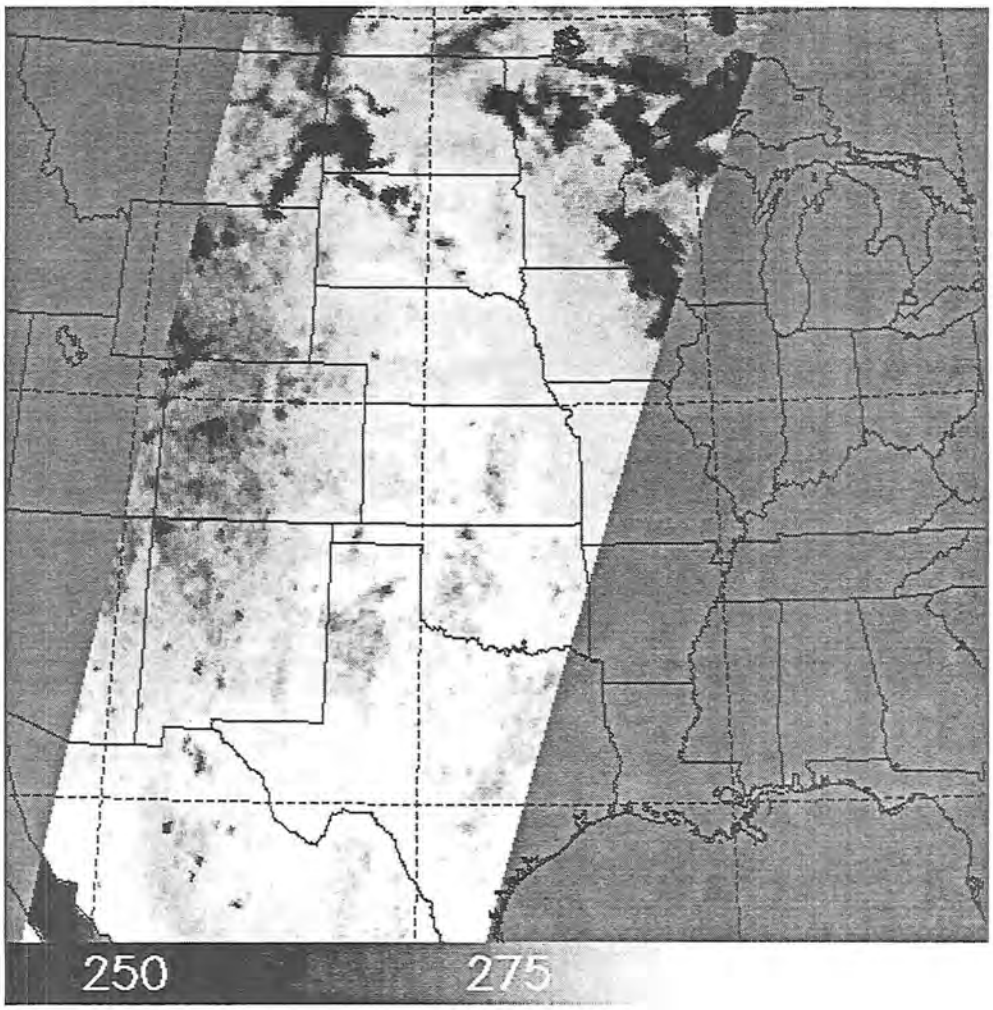

Figure 3.8: Same as Figure 3.7, except for the SSM/I 85.5H GHz (channel 7) microwave brightness temperature (K).

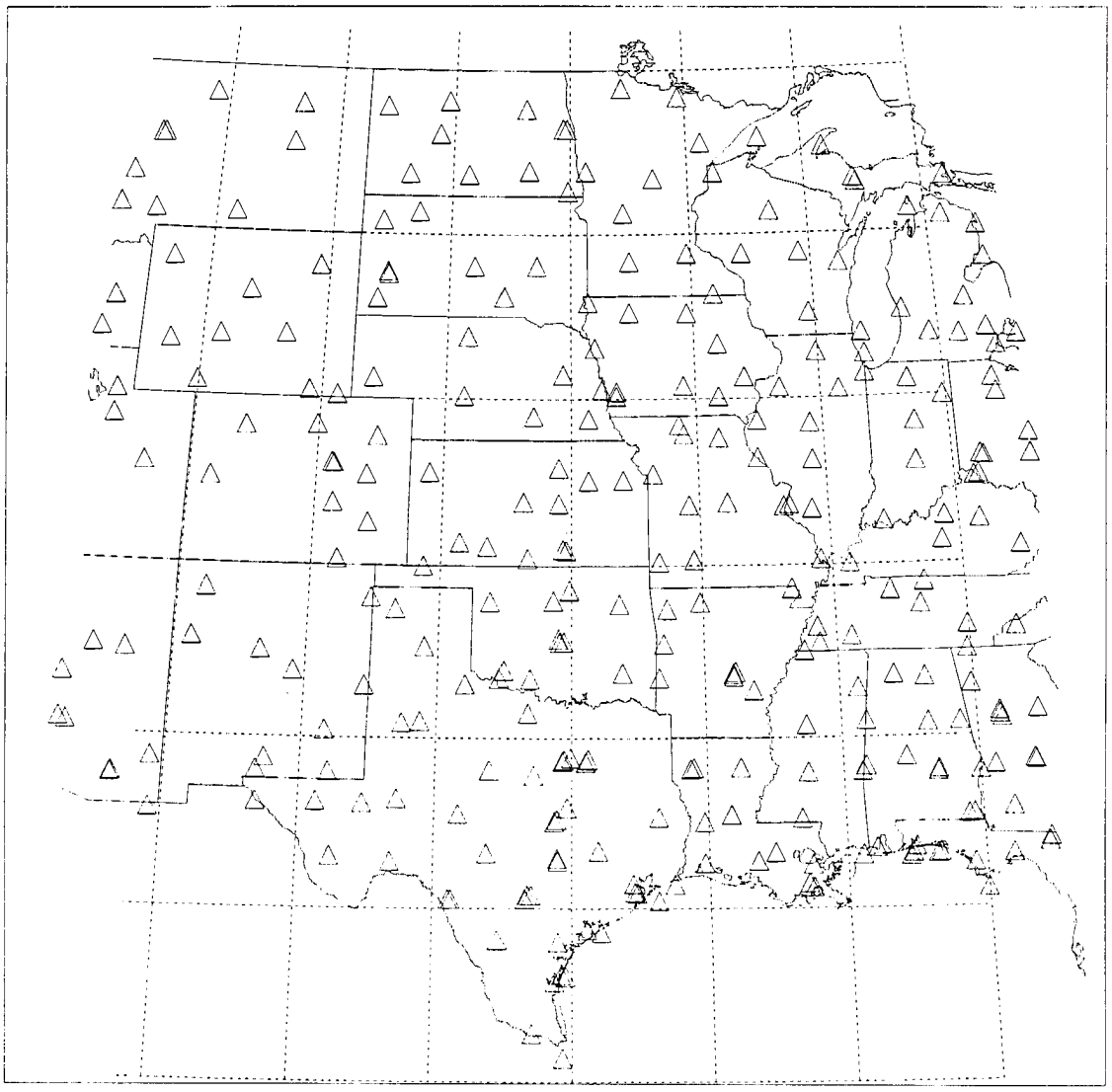

Figure 3.9: Locations of quality-controlled precipitation stations. Triangles denote the station locations.

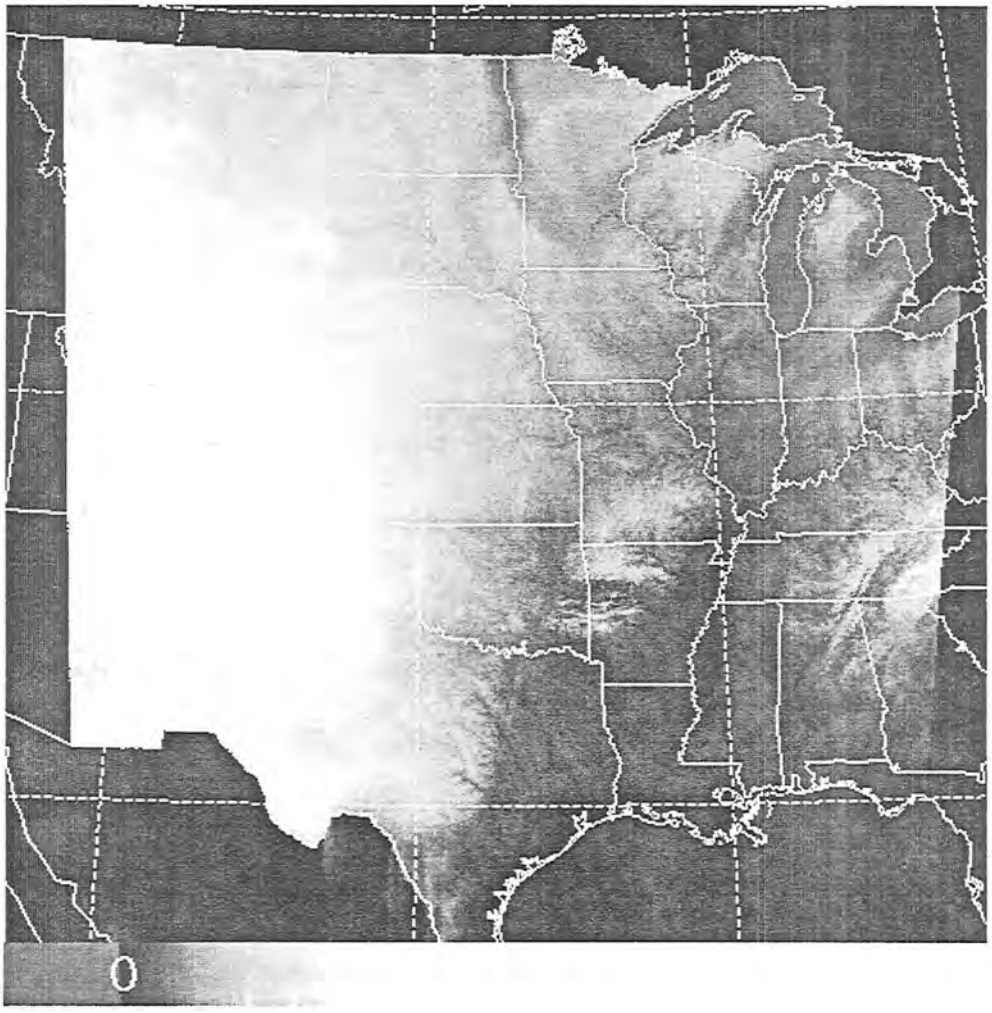

Figure 3.10: The NGDC Digital Elevation Model Database. Heights are measured in meters.

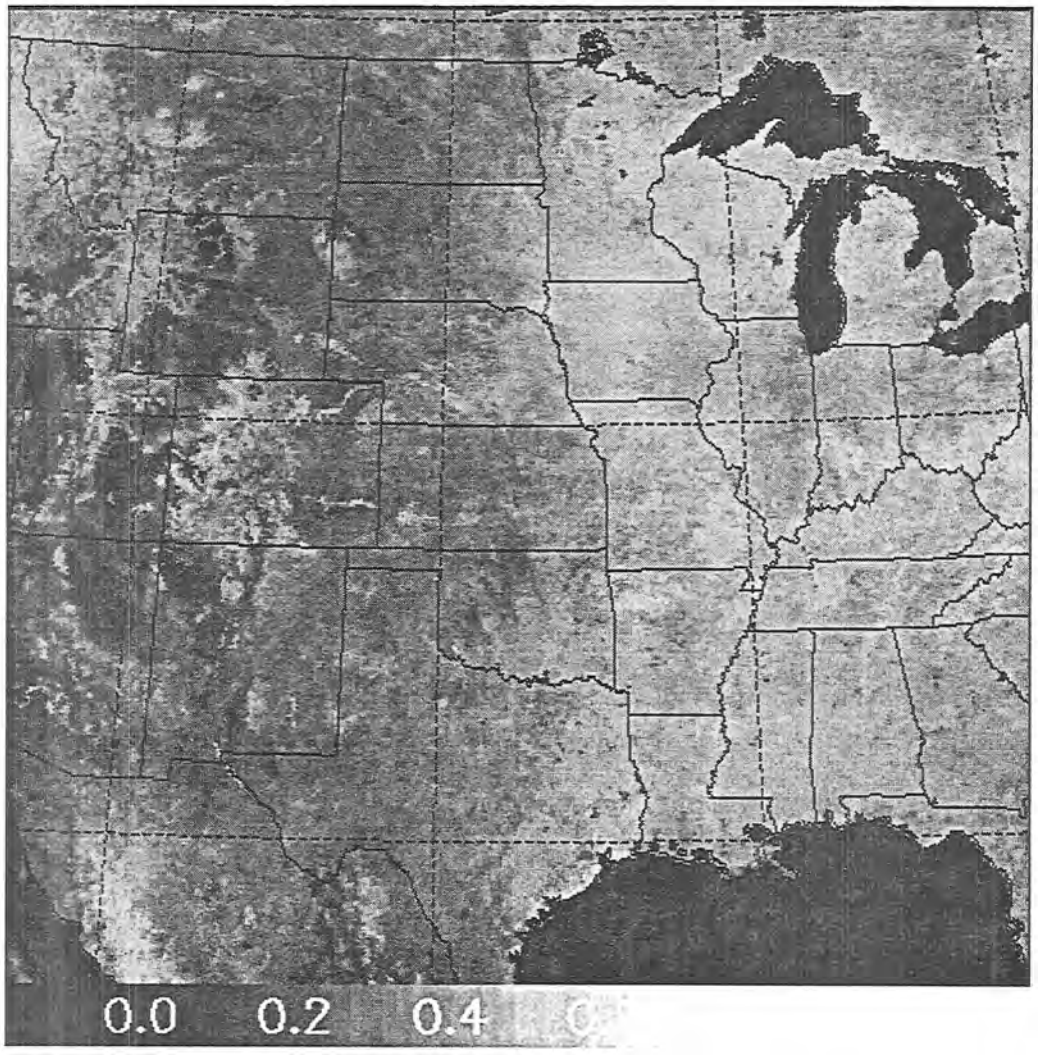

Figure 3.11: Average NDVI values for Julian Days 200-284 of 1991. Lightly shaded areas have high NDVI values and dark regions have low NDVI values.

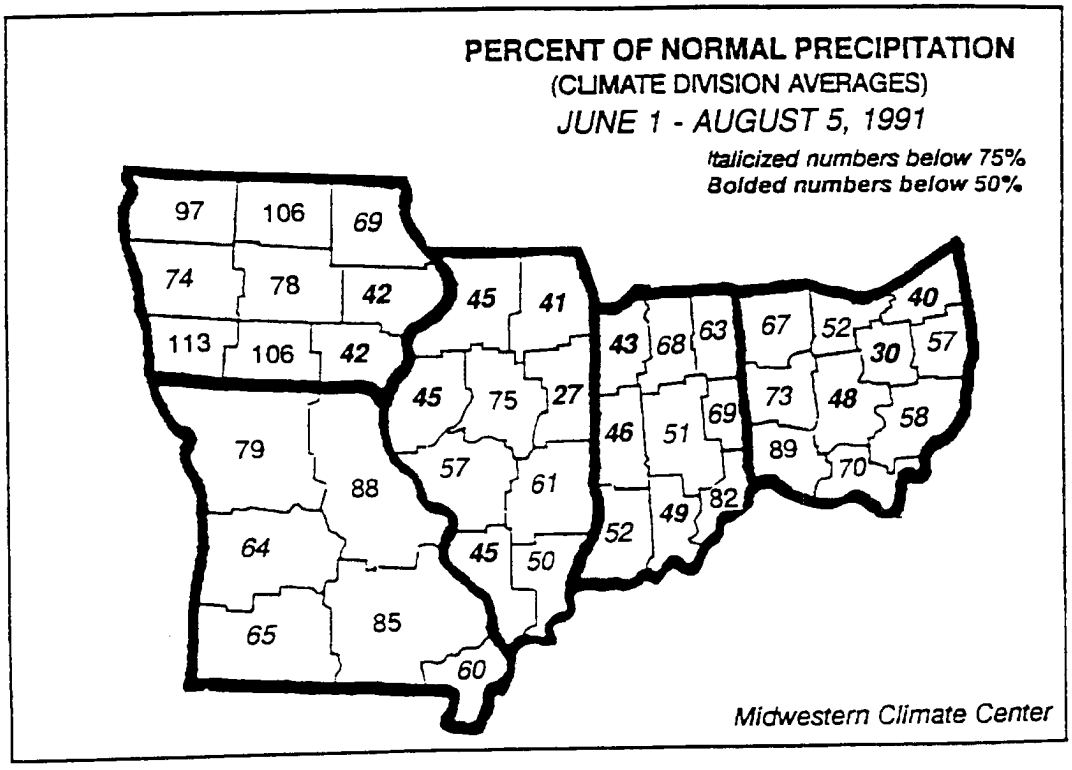

Figure 3.12: Percent of normal precipitation for the Midwest region, June 1 - August 5, 1991.

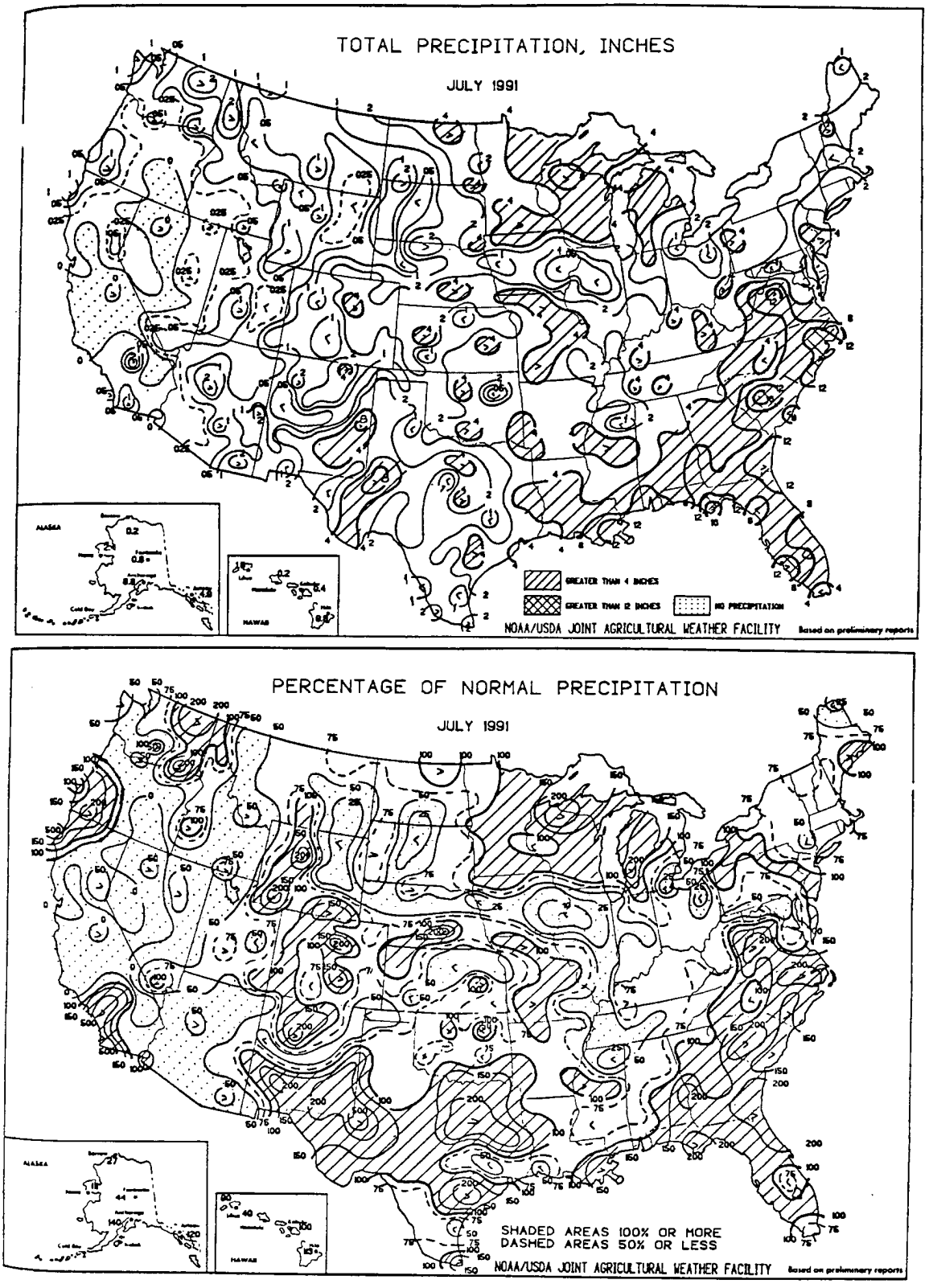

Figure 3.13: Total precipitation and percentage of normal precipitation for July 1991.

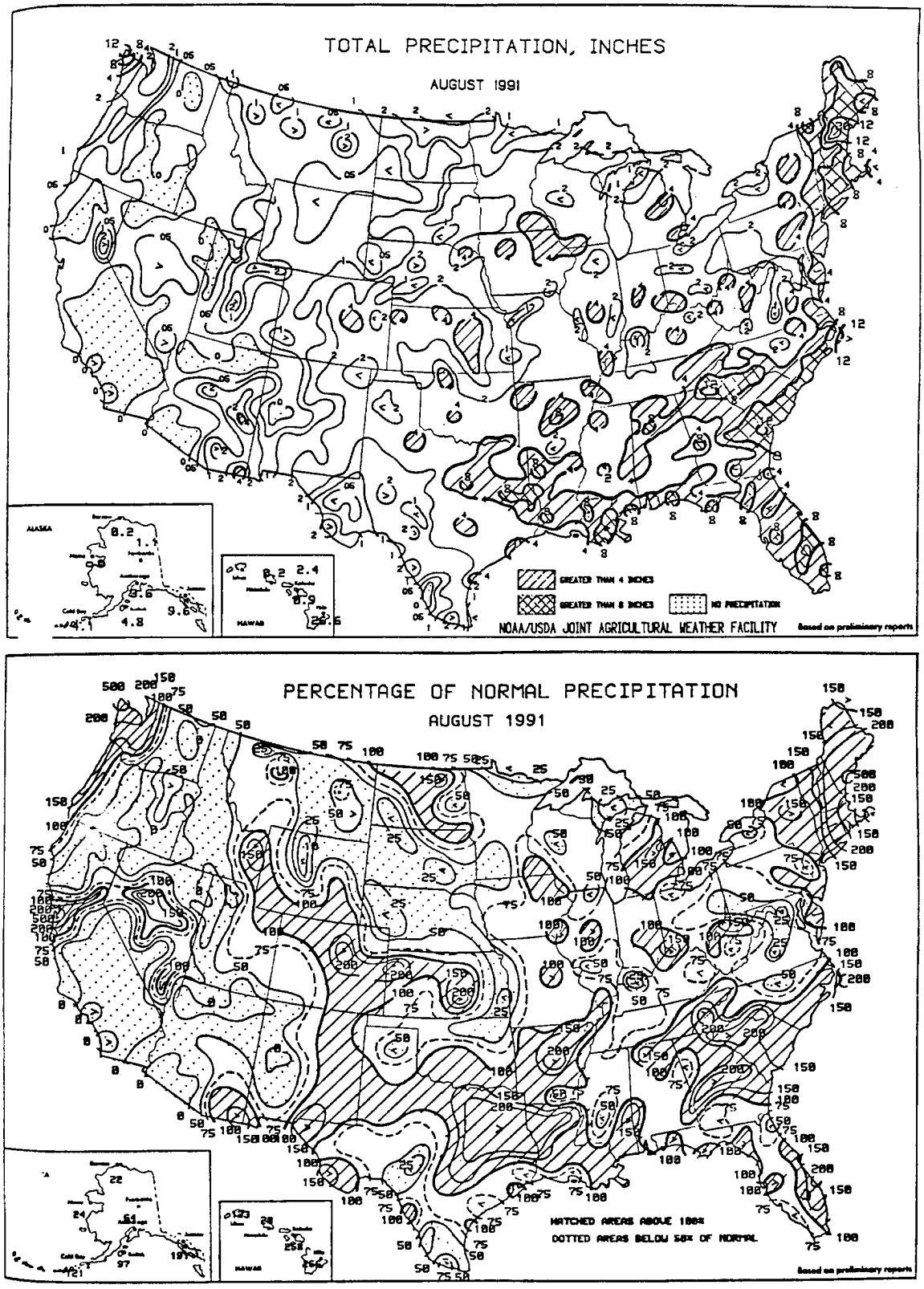

Figure 3.14: Same as Figure 3.13, except for August 1991.

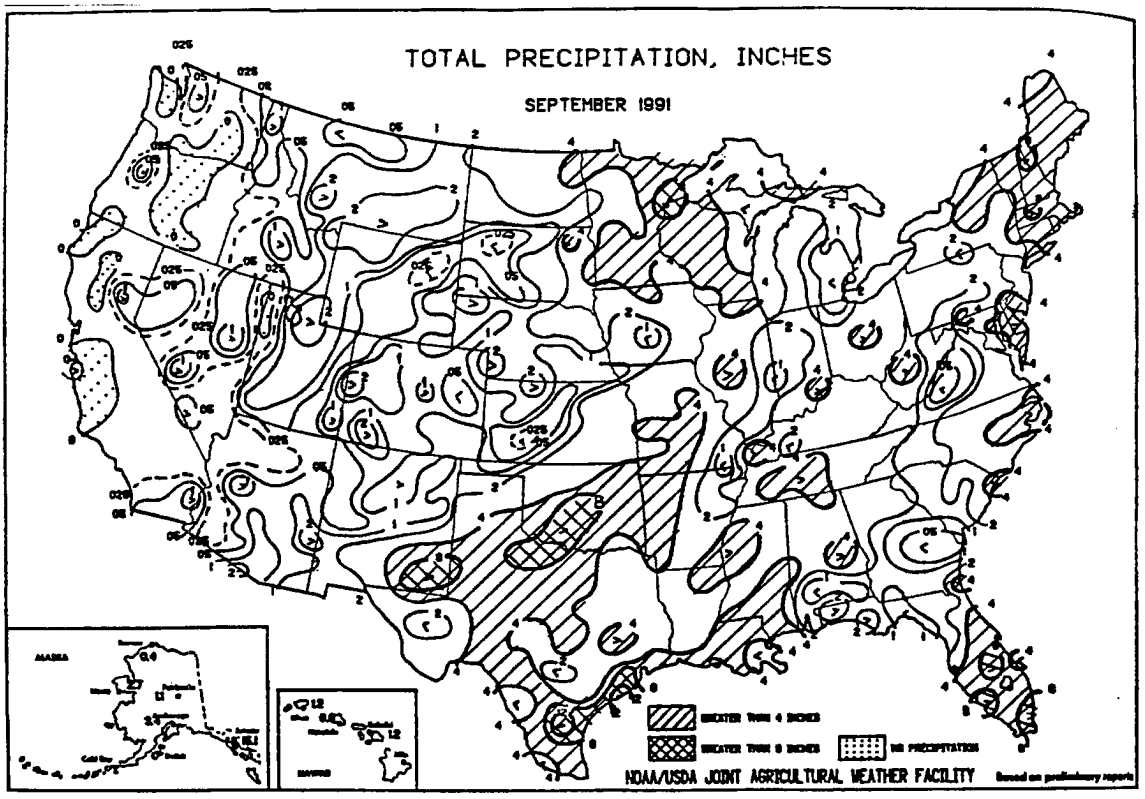

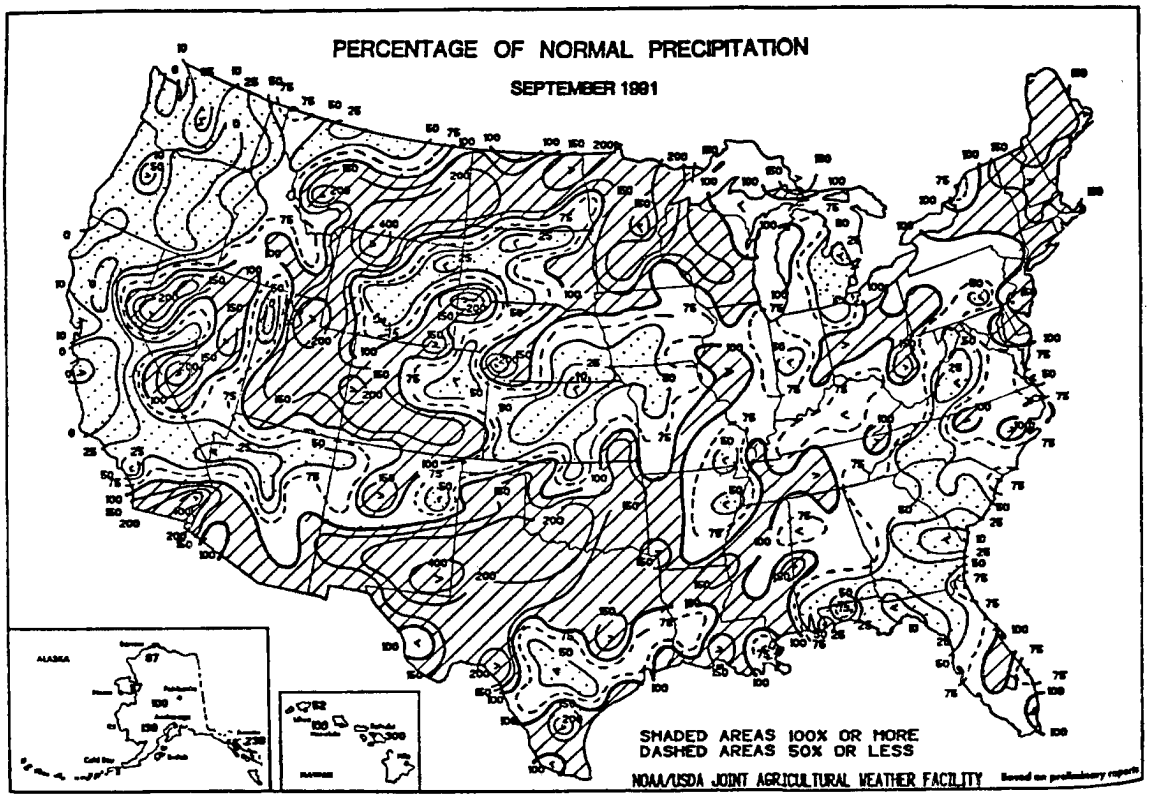

Figure 3.15: Same as Figure 3.13, except for September 1991.

Chapter 4

REMOTE SENSING OF SURFACE WETNESS

This chapter is divided into three major sections. In the first section, current microwave surface wetness retrieval techniques are introduced and applied to data from the central United States during July 30 - Oct. 7 1991. The following section, section 4.2, introduces the microwave surface emittance retrieval procedure that is based on both microwave and infrared satellite data. The microwave surface emittance results are then discussed and compared with various other data sets in the last section, section 4.3.

4.1 SSM/I SOIL WETNESS INDICES

This section reviews results from some selected SSM/I surface wetness and land classification algorithms. The first method, developed by McFarland and Neale (1991), is based on extensive empirical comparisons of SSM/I microwave brightness temperatures with an Antecedent Precipitation Index (API), in the context of a land classification method. The second method, the NOAA Soil Wetness Index (SWI) (Achutuni et al. 1994), is simpler and was designed for use as a surface flooding index.

4.1.1 McFarland Surface Moisture Index

The McFarland and Neale Surface Moisture Index (SMI) is described in detail in the DMSP Cal/Val Final Report (McFarland and Neale 1991). The basic premise is to narrow the domain of the algorithm to those areas that have moderate to low vegetation, since high vegetation amounts obscure the soil wetness signature. Filtering of the data is accomplished with the Neale et al.

(1990) land classification method, then various combinations of the SSM/I microwave brightness temperatures were correlated with a variety of API indices to find an optimal correlation. The results of their study showed that the 19H GHz channel normalized by the 37V GHz channel had the highest correlations with the API of the SSM/I derived variables studied. A linear regression analysis was performed for 3 different vegetation classes where the vegetation classes were inferred by the average polarization in the 19 and 37 GHz channels. The method is limited to the moist soils and wet soils classifications of the Neale land classification scheme.

The updated Neale et al. (1990) land classification scheme as reported in McFarland and Neale (1991) is used in the following data analysis. Several versions of the method are available to account for one, or even two, failed 85 GHz channels on the SSM/I. However, in this study, the full 7 channel algorithm was selected for use with the DMSP F-10 data to not bias the results by incorporating the 5 channel algorithm results that are of reduced quality. Table 4.1 describes the 7 channel Neale land classification scheme. An additional classification class of "Unclassified" was added for data that did not meet any of the classification criteria. The data were sampled at the sample resolution of the SSM/I channels 1-5 (25 km) with the corresponding 85 GHz channels being averaged to match the low resolution data. Figures 4.1 - 4.3 are the Neale land classifications for "Moist soil", "Composite soil and water/wet soils", and "Flooded conditions" respectively, for the entire 70 day case study area. The DMSP F-10 SSM/I has relatively uniform coverage over the study area, but with a gradual increase in the number of data points for the northern portions of the domain. Appendix D contains results from all 15 classification categories, along with a density plot of the DMSP F-10 SSM/I sampling.

In summary, the McFarland and Neale SMI method is as follows.

1. Determine the Neale land classification category (see Table 4.1). If the classification is moist soil or wet soil a surface moisture index retrieval is possible, otherwise vegetation or other

conditions prevent the retrieval of surface moisture. As an addition to the method, land classifications of "Flood conditions" are assigned an SMI value of 70, the maximum SMI value allowed in the algorithm. This allows for flood conditions to contribute to the overall composite SMI values.

2. Determine the vegetation density class and select the appropriate SMI algorithm coefficients for that vegetation density class (see Table 4.2).

3. Calculate the surface moisture index,

$$SMI = A + B(T19H/T37V), \quad (4.1)$$

where A and B are the SMI best fit coefficients determined from Table 4.2, and T19H and T37V are the SSM/I microwave brightness temperatures for the 19H GHz and 37V GHz channels, respectively. The SMI values are restricted to the range of ($0 < SMI < 70$), since values greater than 70 were removed from the original analysis used to derive Table 4.2. The values greater than 70 were removed since signal saturation occurs at such high SMI values.

An example of the SMI method is shown in Figures 4.4 and 4.5 for a single DMSP F-10 SSM/I orbit pass at 1525-1534 UTC 8 September 1991. The Neale land classification results in Figure 4.4 are dominated by three rather large classification categories: the "Composite soil and water/wet soil" category (category 11) over the eastern New Mexico/northern Texas/western Oklahoma/central Kansas region and a smaller region in North Dakota; the "Dry arable soil" category (category 4) over most of the northwest Great Plains region and south-central Texas area; and finally, the "Composite vegetation and water" category (category 10) that occurs in parts of Missouri, most of Iowa, and portions of Minnesota and Wisconsin. The SMI algorithm is thus primarily limited to the "Composite soil and water/wet soil" category (category 11) areas. Figure 4.5 contains the SMI results for the same orbit pass. The SMI values show a maximum in the Oklahoma/Kansas region, which matches the USDA crop moisture availability reports for the

same time period (see section 4.3.2.5 for more details). In addition, a small region of "Flooded conditions" is retrieved by the Neale land classification algorithm near the center of the SMI maximum. Relatively low SMI values are found in North Dakota, while the large waterbodies such as Lake Superior and the Gulf of California have been correctly identified.

SMI composites for the entire 70 day case study are shown in Figures 4.6 - 4.10. The mean SMI values for the period (see Figure 4.6) show a strong large waterbody signal since they are easily identified by the Neale land classification method. The remaining regions show a strong positive bias over the desert regions of Wyoming, Utah, Arizona, and New Mexico. The south-east plains of Colorado also have a strong positive bias. These areas also correlate well with the "Unclassified" category (see Appendix D) and indicate a problem with the Neale land classification algorithm in these regions. The northern Minnesota and southwest Ontario areas also have consistently high SMI values, which is probably due to the small lake effects in the region. The moist region near central Oklahoma/Kansas is correctly identified throughout the period and suggests that the wheat regions in that area enable the SMI method to perform much better in that region than in other regions. This would confirm the findings of Heymsfield and Fulton (1992). Minimum SMI values retrieved during the entire period (Figure 4.7) suggest a problem with an oversensitivity or an inability to cope with arid soil conditions, especially in the desert regions mentioned previously. The maximum SMI values (Figure 4.8) exhibit similar behavior over the desert regions, however this could be a realistic event since it only takes one rain event to create a wet surface signature, but when considered with the high mean and minimum SMI values, it indicates that the SMI method is consistently over reporting surface wetness conditions in the desert regions. The standard deviation of the SMI values during the 70 day period (Figure 4.9) shows high variability near coastal features, southwest Ontario, northwest Texas, and the Oklahoma/Kansas regions. The high variability in the coastal regions and possibly the southwest

Ontario region is due to sub-FOV effects of waterbodies. Depending on the particular FOV orientation significantly different percentages of land and water are within the SSM/I FOV thus increasing the SMI standard deviation for those conditions. The north Texas region corresponds to an irrigated grain sorghum region, while the Oklahoma/Kansas region experienced a wide range of soil wetness conditions, from severe drought to standing water. The spatial coverage of the SMI retrievals is not uniform (see Figure 4.10) since the SMI uses the Neale land classification method as a filter. The regions with the most consistent coverage are the large waterbodies (including major lakes along the Missouri River, and portions of the lower Mississippi River) and the northern Great Lakes region. The Oklahoma/Kansas and north Texas regions also have relatively good coverage during the period.

4.1.2 NOAA Soil Wetness Index

Developed during the Great Flood of 1993 in the United States Midwest, the NOAA experimental Soil Wetness Index (SWI) (Achutuni et al. 1994) was designed to be primarily a surface flooding index. It is conceptually much simpler than the SMI method discussed in section 4.1.1. The SWI uses the brightness temperature difference between the 85.5 GHz and 19 GHz horizontally polarized SSM/I microwave data, since for flooded SSM/I FOVs this brightness temperature difference was found to be the largest brightness temperature combination. The SWI is defined as follows

$$\mathrm{SWI} = TB_{85H} - TB_{19H}, \tag{4.2}$$

where ($10 \leq \mathrm{SWI} \leq 30$) and TB_{85H} and TB_{19H} are the 85.5H GHz and 19H GHz SSM/I microwave brightness temperature data, respectively. The range limitation on the SWI value functions as a simple filter to remove rain and vegetation effects.

An example of the SWI method is shown in Figure 4.11 for a single DMSP F-10 SSM/I orbit pass at 1525-1534 UTC 8 September 1991. The SWI results are nearly identical in spatial distribution to the SMI results shown in Figure 4.5. The high SWI values are centered on the Oklahoma/Kansas region that experienced flood conditions at this time. A smaller region in North Dakota and western Minnesota also has high SWI values indicated. The very low SMI values tend to be missing from the SWI results suggesting that the SWI is a slightly more conservative index. This is most likely due to the particular SWI threshold values that are used to filter the SWI values. If the SWI threshold value constraints were relaxed, the low SWI value results would also tend to match the low valued SMI results.

SWI composites for the entire 70 day case study are shown in Figures 4.12 - 4.14. The mean SWI results (Figure 4.12) indicate a ringing effect around coastal features, where the SWI experiences high SWI values adjacent to resolvable waterbodies. This feature was also present in the SMI mean value composite results (see Figure 4.6) except that with the addition of the "Flooded conditions" land classification the ringing effect tapered into maximum SMI values. Thus if a similar "Flooded condition" land classification algorithm was added to the SWI method, the ringing effect would be made less obvious and perhaps therefore more useful for operational use. The more conservative filtering of the SWI as opposed to the SMI is apparent in the composite SWI results as it was in the individual orbit pass results of Figure 4.11. Major features are the same except with a noticeable improvement on the noisy appearance of some of the lower SMI values shown in Figure 4.6. Again, this would be due to the more conservative filtering of the data in the SWI method. The maximum SWI value composite (see Figure 4.13) more clearly shows those regions that had a significant SWI signal. This pattern closely resembles the SMI results (see Figure 4.8). The spatial coverage of the SWI algorithm as it is applied (Figure 4.14) is much more uniform than the SMI method's spatial coverage (Figure 4.10), however the SWI

implements a filter which substantially alters the final spatial coverage and is even more sparse than the SMI composite results as the maximum SWI composite results indicate (Figure 4.13).

4.1.3 Summary of SSM/I Soil Wetness Indices

The SMI and SWI methods produce very similar results, especially with regard to the spatial distribution of the values. Both methods appear to perform best in the central Great Plains region. Coastal regions and areas with small lakes tend to obscure the surface wetness signature due to sub-FOV effects and the exact viewing geometries which can change subtly with each orbit overpass. Desert regions also posed significant problems for both methods, with false surface wetness signatures being rather common. The additional help of a land surface classification scheme did not seem to obviously improve the SMI results as opposed to the SWI. The main benefit of the land classification scheme was the addition made to the SMI method for this study which assigned maximum SMI values to those regions categorized as "Flood conditions". The benefit was mainly a superficial cosmetic one, in that the retrieved SMI and SWI results for areas with non-flood conditions were unaffected. The primary difference between the methods' results was the suppression of noise in the low index values of the SWI as compared to the SMI. This is primarily due to the stronger filtering imposed by the SWI method.

4.2 MEASUREMENT OF MICROWAVE SURFACE EMITTANCE

The surface emittance retrieval method of Wilke and McFarland (1986) divided the microwave brightness temperature by the minimum air temperature for a nighttime overpass and the maximum air temperature for a daytime overpass, so that,

$$\varepsilon_v = \frac{T_B}{T_a}, \tag{4.3}$$

where T_a is the atmospheric temperature. This assumes that the atmospheric transmittance is 1.0 and that the influence of clouds is negligible. For the SSM/I 85.5 GHz channels the atmospheric transmittance for the 1962 standard atmosphere is approximately 0.71. Transmittances for the SMMR channels used by Wilke and McFarland are approximately 0.88 and above under clear sky conditions.

A method used by Grody (1983) with the MSU, that has a set of sounding channels in the oxygen band (50.30 GHz, 53.74 GHz, 54.96 GHz, and 57.95 GHz), is to compare the surface channel to a lower sounding channel that is relatively unaffected by the surface. Theoretical calculations were performed using various surface emittance assumptions and atmospheric soundings and were compared with the observed microwave brightness temperatures in the surface channel (50.30 GHz) and the lowest sounding channel (53.74 GHz). A parametric equation was developed relating the measured brightness temperatures at 50.30 GHz and 53.74 GHz to the surface emittance,

$$\varepsilon_{\nu} = a_0(\theta) + a_1(\theta)TB_{\nu_1} - a_2(\theta)TB_{\nu_2}, \tag{4.4}$$

where $a_i(\theta)$ ($I = 1, 2, 3$) are coefficients as a function of zenith angle and TB_{ν_1} and TB_{ν_2} are the brightness temperatures for the surface and lower sounding channels of the MSU instrument. At larger zenith angles however, the increased attenuation decreases the sensitivity of the surface channel to the surface emittance. Another problem noted by Grody was the poor resolution of the MSU data (a 110 km footprint at nadir) which smoothed the results. Values of surface emittance ranged from above 0.95 to values below 0.8. Some of the low values using Grody's method were due to cloud contamination.

The microwave surface emittance retrieval method used in this study uses VISSR infrared data to determine surface skin temperature which in turn is used in the microwave radiative

transfer calculations to determine the microwave surface emittance. As a simple example, consider a planet with no atmosphere, and a surface skin temperature of 300 K and a microwave brightness temperature of 270 K. From the definition of emittance given in Appendix A,

$$\varepsilon_v = \frac{T_B}{T_{B_{\varepsilon_v=1}}}, \tag{4.5}$$

the surface emittance would be 0.9. The same principle is used in the full surface emittance retrieval method except that atmospheric contributions due to water vapor and oxygen absorption must be accounted for, and care taken to avoid cloudy regions that can significantly affect the infrared data. The following sections (sections 4.2.1 - 4.2.6) describe in detail the microwave surface emittance retrieval method and its various necessary components.

4.2.1 SSM/I Antenna Effective Field-of-view Adjustment

The effective field-of-view (EFOV) of the SSM/I data in Table 3.2 is for the antenna beam's half-power limit (3 dB). The area checked for cloud contamination for each SSM/I data point was expanded beyond the 3 dB EFOV limits to eliminate as much cloud influence as possible due to the microwave antenna's sensitivity to the area outside the 3 dB limits. As an example, the antenna pattern for the 85.5 GHz vertical polarization channel in Figure 4.15 has a strong center lobe with several smaller side lobes. The 3 dB EFOV limits include a large portion of the center lobe but exclude a significant portion of the sides of the center lobe. Thus it is necessary to create a spatial weighting function from the antenna pattern for use in accounting for possible cloud contamination outside the 3 dB limits. The center portion of the SSM/I antenna pattern was fitted to a spatial weighting function for each channel. The functions selected to represent the dB values are:

$$dB_k(x) = 3\left(\frac{x}{\mathrm{EFOV}_x(k)}\right)^{n_x(k)},$$
$$dB_k(y) = 3\left(\frac{y}{\mathrm{EFOV}_y(k)}\right)^{n_y(k)}, \tag{4.6}$$

where k denotes the channel number, x and y are the horizontal earth coordinates, and $n_x(k)$ and $n_y(k)$ are the cross-track and along-track antenna pattern best-fit coefficients. The implied assumption of Equation 4.6 is that the 0 dB and 3 dB limits are assumed to be exact fits to the function. The spatial values are normalized in terms of the 3 dB EFOV limits. Equation 4.6 was selected as a crude fit to the actual antenna patterns (e.g., see Figure 4.15) and the coefficients were optimized to be a best-fit at the measured values of 5, 10, 15 and 20 dB. Table 4.3 contains the best-fit coefficients $n_x(k)$ and $n_y(k)$, and the standard deviation, σ, which is represented in terms of the gain. The spatial weighting function of the antenna is related to the dB values by

$$\mathrm{WF}_k(x,y) = 10^{\left(\frac{-dB_k(x,y)}{10}\right)}, \tag{4.7}$$

where $\mathrm{WF}_k(x,y)$ is the spatial weighting function, and $dB_k(x,y)$ is the azimuthally dependent dB_k value as determined from the best-fit orthogonal dB_k values:

$$dB_k(x,y) = \left[\left(dB_k(x)\right)^2 + \left(dB_k(y)\right)^2\right]^{1/2}. \tag{4.8}$$

The spatial weighting function has a maximum value of 1 for the center point of the beam, decreases to 0.5 at the 3 dB EFOV limits given in Table 3.2. In practice, the fit is rather good for most channels, as the σ values in Table 4.3 indicate, but some minor problems arose due to the flattening of the center lobe sides and stronger side-lobes of the antenna pattern at the higher frequencies. Thus only the 5 and 10 dB values were used in the estimation of the best-fit coefficients

of Equation 4.6 for channels 4-7. The standard deviations of the best-fit line compared to the measured values for all channels are at or below 0.01.

4.2.2 Cloud Discrimination

The microwave surface emittance is calculated only for clear sky conditions since clouds can have a measurable impact on the observed microwave brightness temperatures (Jones and Vonder Haar 1990). The cloud discrimination is accomplished during the surface skin temperature calculations as a residual of the surface skin temperature atmospheric correction. The method is a dynamic radiative transfer threshold technique which is determined from the failure of the radiative transfer equations to balance in the presence of clouds, thus allowing identification of cloudy regions. The dynamic thresholds were selected conservatively so that no significant cloud contamination is likely in the microwave surface emittance results (with the exception of some fog situations discussed in section 4.2.4). The dynamic threshold technique is explained in detail in section 4.2.3. Static threshold methods that apply a fixed threshold determined subjectively from interactive image analysis were initially attempted but the methods performed unsatisfactorily due to the widely varying conditions of the case study.

4.2.3 Surface Skin Temperature Calculation

The surface skin temperature is calculated in clear sky regions using the infrared data (VAS channel 8) from the GOES VISSR instrument. Additional data from the USAFETAC Upper-Air Data Set and the NGDC DEM data base (see sections 3.3.1 and 3.3.4) were used in the radiative transfer calculations that correct for the infrared atmospheric effects. Equation A.40 from Appendix section A.1.5, describes the radiative transfer for a non-scattering, plane-parallel atmosphere with a non-blackbody surface boundary condition and can be written more compactly as,

$$L_m = \varepsilon_v L_{sfc} + L_{atm} + (1-\varepsilon_v) L_{reflected} + (1-\varepsilon_v) L_{space}, \tag{4.9}$$

where L_{sfc}, L_{atm}, $L_{reflected}$, and L_{space} are given by,

$$L_{sfc} = B_\nu(T_s)\tau_\nu(p_s,0), \tag{4.10}$$

$$L_{atm} = \int_{p_s}^{0} B_\nu[T(p)]\frac{\partial\tau_\nu(p,0)}{\partial p}dp, \tag{4.11}$$

$$L_{reflected} = [\tau_\nu(p_s,0)]^2 \int_{p_s}^{0} \frac{B_\nu[T(p)]}{[\tau_\nu(p,0)]^2}\frac{\partial\tau_\nu(p,0)}{\partial p}dp, \tag{4.12}$$

$$L_{space} = [\tau_\nu(p_s,0)]^2 B_\nu(T_{space}), \tag{4.13}$$

where L_m is the "measured" out-going radiance at the top of the atmosphere (i.e. the satellite observed radiance), L_{sfc} is the surface radiance component, L_{atm} and $L_{reflected}$ are the direct and reflected atmospheric radiances, respectively, and L_{space} is the top of the atmosphere radiative boundary condition. Notice that the surface emittance has been factored out of Equations 4.10 - 4.13, thus the terms are the pre-reflected (or pre-emitted) radiances of the radiative transfer equation. This simplifies subsequent equation notation. Equations 4.9 and 4.10 are then solved for the surface skin temperature,

$$T_s = B_\nu^{-1}\left[\frac{L_m - L_{atm} - (1-\varepsilon_{IR})L_{reflected}}{\varepsilon_{IR}\tau(p_s,0)}\right], \tag{4.14}$$

where $B_\nu^{-1}(L)$ is the inverse of the Planck function, and ε_{IR} is the infrared surface emittance. Since the infrared surface emittance is near 1.0, and the infrared space emission term is small, the space emission term, L_{space}, is neglected in Equation 4.14.

Typically the infrared surface emittance is assumed to be 1.0, but more recent results show that some variability of the infrared surface emittance exists under certain conditions, particularly

in regions of bare soil (Becker 1987; Schmugge et al. 1991; Schmugge et al. 1995) and can contribute approximately 3 K in error to the surface skin temperature retrievals (Perry and Moran 1994). Work using the Thermal Infrared Multispectral Scanner (TIMS) has also shown that under vegetated conditions infrared surface emittances approach a value of 0.99 with a variability less than 0.02 while the largest infrared emittance differences are spectral in nature and confined to the 8.0-9.25 μm wavelengths (see Figure 4.16). Infrared surface emittance variability over mostly bare soil in the HAPEX-Sahel savanna environment was found to be about 0.09 (Schmugge et al. 1995). Another study found that grass and shrub-dominated portions of a semiarid watershed had mean composite infrared emittances of 0.98 (Humes et al. 1994). The accurate measurement of infrared surface emittance is difficult and is a matter of current research. A benefit to the current work in this study is that the VISSR infrared sensor 10.2-12.0 μm band width (Montgomery and Uccellini 1985) is outside the spectral region of strongest infrared surface emittance variability. Therefore, as a compromise concerning the preceding studies, the infrared surface emittance was assumed to be 0.98.

Measurements of the atmospheric temperature and water vapor mixing ratio profiles from the USAFETAC Upper-Air Data Set are used to compute the infrared transmittance profile, $\tau(p,0)$, using a 40-level VAS transmittance software package (McMillin and Fleming 1976; Fleming and McMillin 1977). The VAS transmittance software is based on a set of polynomials for each model pressure level and are functions of the atmospheric temperature, water vapor, and satellite viewing zenith angle. Before insertion into the VAS transmittance software package, the atmospheric sounding profiles were spatially interpolated using a 2-pass Barnes objective analysis scheme (Barnes 1964; Koch et al. 1983). The 2-pass Barnes analysis scheme was modified to determine hydrostatically adjusted surface pressures based on elevations from the NGDC DEM data base. From the hypsometric equation (Holton 1979),

$$\Delta Z \equiv \frac{R_d}{g} \int_{p_2}^{p_1} T_v d(\ln p), \tag{4.15}$$

it can be shown that the interpolated pressure is,

$$p_2 = p_1 \exp\left(\frac{-\Delta Z\, g}{\overline{T_v} R_d}\right), \tag{4.16}$$

where ΔZ is the elevation difference between the DEM data base and the sounding elevation, $R_d = 287\ \mathrm{J \cdot kg^{-1} \cdot K^{-1}}$ is the gas constant for dry air, $g = 9.81\ \mathrm{m \cdot s^{-2}}$ is the global average gravitational constant at mean sea level and $\overline{T_v}$ is the mean virtual temperature and is used to account for moisture effects. The interpolated surface pressure is used to adjust the surface transmittance values to account for changes in elevation using a logarithmically weighted mean,

$$\tau_{sfc} = \tau_{ng-1} + \left(\frac{\tau_{ng} - \tau_{ng-1}}{\ln p_{ng} - \ln p_{ng-1}}\right)\left(\ln p_{sfc} - \ln p_{ng-1}\right), \tag{4.17}$$

where the ng and $ng-1$ subscripts denote the two consecutive VAS transmittance software pressure levels which bracket the interpolated surface pressure within their respective pressure range. The total path transmittance, $\tau(p_s, 0)$, and the direct and reflected atmospheric terms, L_{atm} and $L_{reflected}$, are calculated using the spatially interpolated transmittances from the VAS transmittance software.

The surface skin temperature is initially calculated for both clear and cloudy regions. The discrimination between clear and cloudy conditions is based upon the infrared atmospheric correction that the surface skin temperature retrieval applies. For cloudy conditions, the infrared brightness temperature is actually the cloud top temperature since clouds act as near blackbodies in the infrared (except for thin cirrus which are greybodies). The surface skin temperature

retrieval method compensates for the lower than expected infrared brightness temperature and produces a lower than expected atmospheric correction. The magnitude of the infrared atmospheric correction can therefore be used as a dynamic radiative transfer threshold. The cloud discrimination method is dynamic in that the threshold is based on individual properties of the interpolated atmospheric conditions. Different atmospheric conditions produce distinct radiative transfer balances that in turn produce unique equivalent infrared brightness temperature thresholds. Thus the dynamic radiative transfer threshold method can be applied over large regions without the assumption that each location has the same infrared brightness temperature cloud threshold. For this study the thresholds used to determine the presence of clouds were,

$$\Delta T > 30\,\mathrm{K}, \tag{4.18}$$

$$\Delta T < 3\,\mathrm{K} \text{ and } T_s < 295\,\mathrm{K}, \tag{4.19}$$

where ΔT is the magnitude of the infrared atmospheric correction (the retrieved surface skin temperature minus the original infrared brightness temperature). The first condition in Equation 4.18 is for data quality control (i.e. it was used to check for bad soundings that would corrupt the results) and in practice rarely occurred. The second condition, Equation 4.19, is the dynamic cloud threshold used to determine the presence of clouds. It is based on the principle, that given no cloud, the atmospheric correction should be greater than approximately 3 K, and that atmospheric corrections below this amount are thus likely cloud contaminated. Cloud contaminated FOVs tend to have very small or negative atmospheric correction values due to improperly specified surface skin temperatures due to the cloud top features. Using the infrared atmospheric correction as a threshold, allows the method to determine a spatially variable infrared brightness temperature threshold field that is quasi-independent of the surface skin temperature and provides a mechanism by which atmospheric sounding information is feed into the cloud/no cloud discrimination through elements of the radiative transfer model. As Equation 4.19 indicates, no

clouds were permitted to occur with a retrieved surface skin temperature of greater than 295 K. This constrained the method to eliminate only those clouds that have significant impact on the microwave surface emittance retrieval (i.e. clouds that are colder than the background signature). Some fog situations (as will be shown in the following examples) did escape the cloud detection method. The method relies only upon the infrared data set since visible data are of marginal use with the SSM/I sensor due to its dawn-dusk orbit crossing times (see section 3.2). However, the DMSP F-10 has a precessing orbit due to initial launch problems that allow the morning GOES VISSR visible imagery to be used for comparison and evaluation of the dynamic cloud threshold method.

An example of the surface skin temperature retrieval method is shown in Figures 4.17 - 4.22. The original VISSR infrared and visible imagery for 1532-1535 UTC 8 September 1991 (Figures 4.17 and 4.18) shows a large synoptic system moving through the central United States (this system is described in more detail in section 3.6.2). A large clear region exists behind the large system. Cloud free conditions are prevalent for most of Nebraska, Kansas, Oklahoma, northwest Texas, and New Mexico. Additionally, regions east of the system are also clear. In anticipation of its inclusion into the surface skin temperature retrieval method, the DEM data base is merged into the VISSR infrared projection space using the PORTAL software package (Figure 4.19). The surface skin temperature is retrieved using the merged DEM data, the USAFETAC Upper-Air Data Set, and the VISSR infrared imagery using Equation 4.14 (Figure 4.20). The results show the highest surface skin temperatures in the north-central Kansas region with temperatures approaching 310 K. The infrared atmospheric correction (Figure 4.21) is largest for regions near the Gulf of Mexico, in the deep South, and in the central Great Plains east of 100° W. Surface skin temperature atmospheric correction magnitudes are less than 10 K, which is reasonable considering the effects that the 0.98 infrared surface emittance assumption has on the results (one would

expect a 2% adjustment of approximately 6 K based on the infrared surface emittance effect alone). The temperature difference between the retrieved surface skin temperature for clear-sky regions and the surface level of the interpolated atmospheric sounding air temperature at 12 UTC (Figure 4.22) shows the amount of diurnal heating which has occurred since 12 UTC until the time of the VISSR data (1532-1535 UTC) (the Central Time Zone is -0600 from UTC time). Thus nearly 20 K of warming relative to the surface air temperature has occurred during the past 3.5 hours for portions of north-central Kansas. Regions of partial or broken cloudiness have reduced temperature differences. Some areas that have been marked as clear using the dynamic threshold method in reality have fog. The fog is most apparent in the VISSR visible imagery (Figure 4.18). A region of fog exists in south-central Kansas and in portions of south-east Kansas. The effect of the fog is to reduce the retrieved surface skin temperatures, but since the fog is so near to the ground (some fog had surface temperatures of 295 K) its effect is only marginal. It could be assumed that the fog is shading the ground and preventing its surface from heating as rapidly as other areas perhaps resulting in a very similar pattern of surface skin temperatures as that which is actually retrieved (in fact, the data shown in Figure 4.20 displays this pattern). As a computational artifact, the field in Figure 4.22 is not as smooth as the surface skin temperature results because of how interpolation between the surface levels was accomplished (i.e. only soundings which are below a given pressure level are used in the comparison which results in a small discontinuity that is apparent in eastern Colorado and eastern New Mexico). Overall however, the surface skin temperature retrieval method appeared to perform well for a variety of conditions found during the 70 day case study over the central United States. Further enhancements to the surface skin temperature retrieval method would have to be made to reliably extend it during other seasonal conditions, especially with regard to the cloud detection algorithm.

4.2.4 Microwave Surface Emittance Calculation

The microwave surface emittance is calculated by solving the integrated microwave radiative transfer equation (Equation 4.9) for ε_v, which results in (Jones and Vonder Haar 1990):

$$\varepsilon_v = \left[\frac{L_m - L_{atm} - L_{reflected} - L_{space}}{L_{sfc} - L_{reflected} - L_{space}} \right], \tag{4.20}$$

where L_m is the measured microwave radiance from the SSM/I instrument. The remaining terms on the right hand side of Equation 4.20 are defined by Equations 4.10 - 4.13 and are determined using a Millimeter-wave Propagation Model (MPM) (described in Appendix B) and integrating the terms numerically. The surface skin temperature used in the microwave surface emittance calculations are from the surface skin temperature retrieval results of section 4.2.3. The mean surface skin temperature, $\overline{T_s}$, and mean infrared cloud fraction, $\overline{\mathrm{CF}}$, is calculated for each SSM/I FOV using spatially weighted averages,

$$\overline{T_s}(k) = \frac{\sum \mathrm{WF}_k(x,y) T_s(x,y)}{\sum \mathrm{WF}_k(x,y)}, \tag{4.21}$$

$$\overline{\mathrm{CF}}(k) = \frac{\sum \mathrm{WF}_k(x,y) \mathrm{CF}(x,y)}{\sum \mathrm{WF}_k(x,y)}, \tag{4.22}$$

where the SSM/I spatial weighting function, $\mathrm{WF}_k(x,y)$, is given by Equation 4.7, x and y are the horizontal earth coordinates, and k is the SSM/I sensor channel number. The spatial average is performed over both horizontal coordinates within the SSM/I sensor's projection space using the PORTAL software to merge the various data sets. The infrared cloud fraction, $\mathrm{CF}(\mathrm{x},\mathrm{y})$, for a given VISSR infrared sensor position is determined to be either clear or cloudy (see section 4.2.2), with a value assigned for the associated cloud condition,

$$\begin{aligned} CF &= 0, \text{ clear,} \\ CF &= 1, \text{ cloudy.} \end{aligned} \tag{4.23}$$

Since the SSM/I FOV overlaps several GOES VISSR FOVs a minimum cloud threshold was used to determine if the cloudiness was significant enough to prevent successful retrieval of the microwave surface emittance. Since clouds can have an undesirable effect on the microwave surface emittance retrieval (Jones and Vonder Haar 1990), FOVs with a $\overline{CF} > 0.05$ were considered cloud contaminated. The surface emittance retrieval was not performed on those areas identified as having possible cloud contamination. Merged DEM data is used to apply an elevation correction to the microwave atmospheric transmittances in a manner similar to that of the surface skin temperature retrieval method of section 4.2.3, with the exception that interpolation of the surface transmittances is unnecessary since the MPM is not a fixed-level transmittance model. The USAFETAC Upper-Air Data Set is spatially interpolated using the same 2-pass Barnes objective analysis scheme that was described previously in section 4.2.3. Data quality control is performed to ensure that bad SSM/I data did not produce invalid microwave surface emittance results. A minimum microwave surface emittance threshold of 0.5 was used over land surfaces (based on the Wentz surface identification database (Wentz 1988) included with the SSM/I data set), with no minimum threshold used over water surfaces. A maximum microwave surface emittance of 1.05 was allowed. Instances of these thresholds being used to filter data out were limited to data errors within the SSM/I data set.

An example of the microwave surface emittance retrieval method is shown in Figures 4.23 - 4.26. The microwave surface emittance is retrieved from the DMSP F-10 SSM/I 85.5H GHz (channel 7) microwave brightness temperature for 1525-1534 UTC 8 September 1991 (Figure 4.23). The DEM Database and the clear-sky surface skin temperature retrieval results from section 4.2.3 are merged to the SSM/I projection space using the PORTAL software

(Figures 4.24 and 4.25). The VISSR and SSM/I data sets have time periods that overlap (thus possibly providing instantaneous infrared and microwave measurements) to a worst-case time difference of 10 minutes. The microwave surface emittance is then retrieved using Equation 4.20 and the interpolated sounding information provided from the USAFETAC Upper-Air Data Set (Figure 4.26). Low microwave surface emittance values were retrieved in portions of central Kansas that were associated with very wet ground conditions during this time. The maximum microwave surface emittance value is 0.994, which suggests that the surface skin temperature retrieval is performing accurately. More discussion of the microwave surface emittance results will be deferred until section 4.3, where in-depth comparisons are made with other ancillary data sets.

4.2.5 Microwave Surface Emittance Retrieval Errors

In clear-sky conditions the surface contributes a majority of the total upwelling radiance $\left(\tau(p_s,0) \cong 0.71\right)$ which heavily links the retrieved microwave surface emittance and the surface skin temperature. Since the same surface skin temperature is used in the retrieval process for all channels at a given location, any bias in the surface skin temperature would affect all channels similarly. Inter-channel biases must be due to the microwave brightness temperature biases and errors in the microwave transmittance algorithm. The microwave brightness temperatures are the most likely cause of inter-channel biases since the atmospheric component of the upwelling radiation is small (less than 1/4). Estimates of absolute brightness temperature errors are difficult even with co-located infrared data since the surface emittance has a wide range of reasonable values (Hollinger et al. 1990).

Numerical simulations using random perturbations were used to estimate errors in the retrieved surface emittances. A control case that had a surface emittance of 0.95 and the 1962 Standard Atmosphere (Valley 1965) was used to determine the magnitudes expected for microwave

surface emittance retrieval errors. Simulated data was generated with various amounts of random noise added to several parameters that influence the retrieved surface emittances. The surface emittance was found to be most sensitive to two parameters, the microwave brightness temperature and the surface skin temperature. The relative and absolute instrument errors of the VISSR and SSM/I instruments (see Tables 3.1 and 3.2) were used to calculate the propagation of error through the surface emittance retrieval algorithm (Beers 1957). Results from the analysis in Table 4.4 show absolute accuracies ranging from 0.008 to 0.012. Frequencies with higher atmospheric attenuation have the largest errors (e.g., 22.235 GHz and 85.5 GHz). In a physical sense the high attenuation is obscuring the surface from view which makes it more difficult to measure the surface emittance accurately. The lower relative error at 37 GHz is due to the lower relative instrument noise at that frequency.

The highest microwave surface emittance retrieved during the entire 70 day case study (30 July - 7 October 1991) was a value of 1.049 for the 85.5V GHz channel (see Table 4.5). Other values also greater than 1.0 occurred for the remaining vertical polarization channels, and the 85.5H GHz channel. The magnitudes of the extreme values indicate that the error analysis can reasonably account for the errors contained in the microwave surface emittance results except for the 85.5 GHz channels and possibly also the 22.235V GHz channel. Closer examination of the spatial location of the maxima occurrences indicates that the 85.5 GHz errors are most likely due to sub-FOV cloud contamination since the maxima tend to occur near the edges of the observed cloud fields. Since both the 22.235V GHz and 85.5 GHz channels are sensitive to the distribution of atmospheric water vapor is also likely that the Barnes objective analysis interpolation can not account for the heterogeneous nature of the water vapor distribution in between sounding locations and thus interpolation of the atmospheric water vapor profiles is an additional source of error that is contributing to the extreme results. The mean surface emittance values in Table 4.5

indicate that the vertical polarization is always higher than the horizontal polarization value as expected. There appears to be a very small downward trend with respect to frequency in the vertical polarization results. However, no significant frequency dependency is observed in the horizontal polarization results.

4.2.6 Summary of the Microwave Surface Emittance Retrieval Method

A flowchart is presented in Figure 4.27 that represents the microwave surface emittance retrieval procedure. Two major steps are performed:

1. determine the surface skin temperature, and

2. determine the microwave surface emittance for each SSM/I channel using the retrieved surface skin temperature.

These steps are accomplished using the programs GDFTSFC and GDFEMIT, both of which read the data from the Generalized Data Format (GDF), hence the GDF prefix in their names. GDFTSFC is the surface skin temperature retrieval program and GDFEMIT is the microwave surface emittance retrieval program. Additional PORTAL programs merge the data into the proper satellite projection spaces to allow easy manipulation of the data by the two main programs (see Appendix C for more details). The PORTAL program that does the merging is called GDF2GDF since it merges one GDF data file into another GDF data file's target projection space. The output of the GDF2GDF program is another GDF file, so the entire processing chain is very modular. The DEM data is merged into both the VISSR and SSM/I projection spaces since both GDFTSFC and GDFEMIT require elevation data. The surface skin temperature retrieval results are also merged into the SSM/I projection space to allow the GDFEMIT program to incorporate the high resolution surface skin temperature retrievals into the final microwave surface emittance results. The only data set which bypasses the PORTAL software is the

USAFETAC Upper-Air Data Set. Since the upper-air data is a sparse data set, it is more efficient to spatially interpolate the data "on-the-fly", otherwise massive data storage (>200MB per orbit pass) would be required for its 40-level representation within the transmittance models. The algorithm was able to retrieve microwave surface emittance for one orbit pass over the case study region in approximately 20 minutes on a DEC 3000-400 AXP workstation (a 135 specFP92 machine).

4.3 MICROWAVE SURFACE EMITTANCE RESULTS

4.3.1 Effective Microwave Surface Emittance Calculation

An alternative microwave surface emittance retrieval method that does not include an atmospheric correction was also developed for comparison purposes. It uses a simple effective microwave surface emittance concept. In Equation 4.5 it is assumed that the infrared brightness temperature is a close approximation to the actual blackbody temperature, i.e.,

$$\varepsilon_k = \frac{TB_{MW}(k)}{\overline{TB_{IR}}(k)}, \tag{4.24}$$

(Ulaby et al. 1986) where $TB_{MW}(k)$ and $\overline{TB_{IR}}(k)$ are the microwave and mean infrared brightness temperatures for the SSM/I channel k. The mean infrared brightness temperature is

$$\overline{TB_{IR}}(k) = B_{IR}^{-1}\left\{\frac{\sum \mathrm{WF_k}(x,y)B_{IR}\left[TB_{IR}(x,y)\right]}{\sum \mathrm{WF_k}(x,y)}\right\}, \tag{4.25}$$

(Jones et al. 1995) where the spatial weighting function $\mathrm{WF}_k(x,y)$ is given by Equation 4.7. The cloud discrimination method of section 4.2.2 is used to make the results consistent with the previous method. Thus, the effective microwave surface emittance retrieval method is identical with the complete microwave surface emittance retrieval method discussed in section 4.2.4,

except that no atmospheric corrections are applied. Results corresponding to the examples presented in section 4.2.4 are shown in Figure 4.28. In general, higher microwave surface emittance results are retrieved, with the atmospheric attenuation effects becoming more obvious at the higher frequencies.

Theoretical results using a standard midlatitude summer sounding are shown in Figure 4.29. In Figure 4.29, the difference between the effective microwave surface emittance and the atmospheric corrected microwave surface emittance is plotted as a function of the effective microwave surface emittance for each of the SSM/I frequencies. For the theoretical calculations, the infrared surface skin temperature is assumed to be 300 K. The noticeable feature in Figure 4.29 is that the 85.5 GHz channel is more sensitive to water vapor than the lower frequencies, and can have atmospheric corrections approaching -40% when the effective microwave surface emittance is particularly low. The atmospheric correction magnitude is a strong function of the effective microwave surface emittance value, with the atmospheric correction becoming larger with lower effective microwave surface emittance values. This result is expected since the low effective microwave surface emittance regions are areas with higher microwave reflectivity and this amplifies the water vapor effect of the atmosphere. The water vapor effect is amplified for this situation since the land surface's radiance boundary condition can not balance Equation 4.20 as easily as if the surface term had contributed more to the overall radiative transfer balance, and the atmospheric correction to the microwave surface emittance is thus larger. Significant corrections (-10%) can also be found for the lower frequency channels. The 22 GHz data occurs on a water vapor absorption line and is more sensitive to the water vapor effects than the 19 GHz and 37 GHz channels. When the effective microwave surface emittance is at a value of 0.98, the atmospheric correction magnitudes merge to a constant negative value of -3% and are independent of frequency, and then reverse the order of their frequency dependence at higher effective

microwave surface emittances. This is because the infrared surface emittance is assumed to be 0.98 in the microwave surface emittance retrieval method. The infrared surface emittance acts as a pivot point in the microwave surface emittance retrieval method since it controls how much the land surface can contribute to the overall radiative transfer balance and thus directly influences the radiative transfer balance.

4.3.2 Composite Microwave Surface Emittance Values

The retrieved microwave surface emittance values were composited for the entire case study period of 30 July - 7 October 1991 (≈70 days). The PORTAL software was used to merge the microwave surface emittance values onto a common grid that was in a Lambert Equal-area projection. The PORTAL programs GDFGRID and GDFCOMP were used in the compositing (see Appendix C for more details). The composite grid spacing is about 4 km, which is sufficient given the SSM/I navigation accuracy of ±7 km (see section 3.2). Results for the 85.5 GHz channels are from the DMSP F-10 since the F-8's 85.5 GHz channels had failed by this time. All other SSM/I channel results are from both the DMSP F-8 and F-10. The following subsections (sections 4.3.2.1 - 4.3.2.5) contain various composite microwave surface emittance results.

4.3.2.1 Total Composites

Although all channels of the SSM/I surface emittance results were individually composited, only composite 85.5H GHz surface emittance results are presented in this section as an example for general discussion. The remaining SSM/I channel results are similar but with frequency dependencies that are related to the SSM/I sensor FOV size. The complete multispectral results are presented in Appendix E. Polarization differences will be discussed in section 4.3.2.4.

The composite mean 85.5H GHz surface emittance results (Figure 4.30) show an intricate web of detailed surface features. The horizontal polarization shows surface water effects more readily than the vertical polarization since there is a larger dynamic range of microwave surface

emittances (see Appendix section A.3). The microwave surface emittance ranges from about 0.5 for large waterbodies to near 1.0 for the most arid or heavily vegetated regions (see Table 4.5). Appendix E contains detailed statistical information regarding the retrieved microwave surface emittance results. The minimum and maximum 85.5H GHz surface emittance results retrieved during the entire time period are shown in Figures 4.31 and 4.32. The microwave surface emittance is not a constant field (see Figure 4.33) and contains many temporal features of interest. Since the microwave surface emittance is retrieved only over clear-sky areas, it is not uniformly measured across the entire case study domain (Figure 4.34). Some regions have greater coverage than others due to the absence of clouds, or even the ability of the cloud algorithm to detect clouds in given regions. Areas that were particularly problematic were the higher elevations of the Rocky Mountains and the Great Lakes region. Both locations suffered from the same physical problem. They were relatively cold and nearly the same temperature as the low clouds that could have formed over the area. Thus these regions offered no signal from which to detect clear-sky conditions and were nearly always identified as cloud covered by the cloud detection algorithm. This does not pose a significant problem since the opposite alternative is the inclusion of cloud contaminated microwave surface emittances which would be an even greater problem affecting the analysis of the results. From the data sample density shown in Figure 4.34, the cloudiest areas are in the upper Midwest and in the Southeast United States as one would expect. The orographic effects upon the cloud algorithm makes it difficult to draw cloud coverage conclusions in the Rocky Mountain regions.

Lakes and large river systems are the most prominent feature of the microwave surface emittance results (Figure 4.30). The Missouri River and its associated man-made lakes in the Dakotas and Montana are easily recognized. The Great Lakes and the Great Salt Lake have very low microwave surface emittances since unobstructed water-only FOVs are their primary component.

Other relatively large lake features include three integrated lake features in Minnesota (the Upper and Lower Red Lakes; Winnibigoshish and Leech Lake; and Mille Lacs). Other particularly prominent waterbodies are: Lake Winnebago, Wisconsin; Lake Powell, Utah; and Kentucky Lake, Kentucky. The polka-dot pattern (especially in the east Texas, east Oklahoma, and Ozark regions) is due to smaller lakes that have partial footprint coverage (lakes about 5-10 km in size). Flood plains in west Mississippi on the Yazoo River, and the much larger lower Mississippi River flood plain also exhibit lower microwave emittances. Since the flood plains are not permanent waterbody features, they should be thought of as transient lakes, thus it would be expected that more variability would be associated with these features (Figure 4.33 confirms this hypothesis).

Non-lake features are also prevalent in Figure 4.30. These include deserts, irrigation areas, heavy crop regions, and coniferous forests, and temporal surface wetness signatures. The temporal surface wetness features are best seen in the individual orbit passes or the 7 day composites (section 4.3.2.5). However, the strength of the effect of prolonged sequences between flooded and dry conditions can even be seen in the mean composite values by a lower microwave surface emittance in the central Oklahoma, and central Kansas region (also note the high surface emittance variability in this region, see Figure 4.33). Other rainfall events recorded in this data set tend to be washed out in the mean total composite results. By comparing the minimum and maximum microwave surface emittance results (Figures 4.31 and 4.32), the rainfall event influence is more clearly seen, however the spatial sampling of the SSM/I sensor of sub-FOV features (such as lakes) introduces some ambiguities into the interpretation of the maximum and minimum microwave surface emittance results. Further detailed discussion of the rain events is reserved for sections 4.3.2.5 - 4.3.4.

The desert regions in eastern Utah, parts of Arizona and New Mexico, and the intermountain basins of Wyoming, show rather low microwave surface emittances over a broad region. These are the same regions that are poorly classified in the Neale land classification algorithm (see Appendix D, Figure D.15). The desert regions have low microwave surface emittance due to the high dielectric constant of quartz. Since the material has a high dielectric constant it also acts in a manner similar to water (another material with a high dielectric constant). A comparison of two desert regions was performed to determine if different sand types make a significant impact on the microwave surface emittance. A small region was selected for analysis surrounding White Sands, New Mexico (32.65 - 33.15° N, 105.96 - 106.62° W) and a randomly selected similar sized area in the intermountain Red Desert of southwest Wyoming (41.64 - 42.16° N, 108.16 - 108.91° W). Figure 4.35 is a graphical depiction of the comparison results that are in Tables 4.6 and 4.7. The conclusion of the comparison is that the different desert regions have similar microwave surface emittance features that are within the natural variability of the data set and measurement noise levels and thus are nearly indistinguishable from each other as a unique desert type. The only noticeable feature is the slightly lower absolute minima of the White Sands region versus that of the Red Desert region (see Tables 4.6 and 4.7). This is probably due to sub-FOV effects in which the small but non-vegetated White Sands region is centered within the SSM/I FOV providing optimum FOV coverage. On the other hand, the Red Desert has some scattered desert shrubs that may prevent its microwave emittance from approaching the non-vegetated minima values of the White Sands region.

Irrigation and moist croplands have lower microwave surface emittances as well. These regions change only slowly with time and thus appear in the total composite results better than some of the other features that have smaller spatial features or have a significant temporal factor to their existence. Regions of particular significance are the Platte River, eastern Nebraska; the

North Platte River, western Nebraska; the South Platte River, northeastern Colorado, the Arkansas River, southeastern Colorado; southwest Kansas, and a relatively large region in west Texas near Lubbock, Texas. Direct comparisons with irrigation maps will be made in section 4.3.4.

Intensive crop regions also influence the microwave surface emittance. Areas in northern Iowa and southern Minnesota have low stable microwave surface emittances. Since the region was not under flooding conditions at the time, it is possible that the water content within the vegetation is causing the lowering of the microwave surface emittance. Given conditions where the LAI is approximately constant, this would indicate that the health of a crop could be estimated from microwave surface emittance observations, with the assumption that stressed crops would have a lower plant water content and thus higher microwave surface emittances.

Coniferous forests have high microwave surface emittances and are one of the few high surface emittance signatures found (excluding dry arid soil). Particularly noticeable regions are the foothills of western Montana; the Wind River Range and Big Horn Mountains of Wyoming; the Black Hills, western South Dakota; the Pine Ridge forest of southwestern South Dakota and extreme northwestern Nebraska; portions of the Colorado Rockies; the Apache and Gila National Forests of Arizona and New Mexico; the Sacramento Mountains, New Mexico; Northern Minnesota; and the Florida Panhandle. Upon first inspection it appears that an elevation bias must be present due to the large number of mountainous locations identified. However, this hypothesis fails once the low elevations of the identified Florida, Minnesota, and Nebraska-South Dakota regions are considered. The composite minimum microwave surface emittance (see Figure 4.31) highlights these high surface emittance areas, since these regions also have small microwave surface emittance ranges. The conifer vegetation most likely has 1) a higher infrared surface emittance than the surrounding vegetation that biases the surface skin temperature and thus the microwave surface emittances, 2) the coniferous vegetation is extremely dry compared with other

dry ground vegetation, 3) the coniferous vegetation is particularly rough in appearance to the SSM/I microwave frequencies, or 4) a possible combination of these effects.

4.3.2.2 Atmospheric Correction Effects

The effect of the atmospheric correction on the microwave surface emittance results was examined by comparing the microwave surface emittance retrieval method results with the simpler effective microwave surface emittance retrieval method of section 4.3.1. The composite effective microwave surface emittance results for 30 July - 7 October 1991 are shown in Figure 4.36. Contrasting these results with the atmospheric corrected microwave surface emittance values (Figure 4.30) shows that the atmospheric corrected microwave surface emittances are lower in value and that the image contrast is enhanced between surface water features and land.

A statistical analysis was performed to examine the frequency dependencies of the atmospheric correction. The microwave surface emittances were filtered to minimize the large waterbody bias on the statistical results. Thus, microwave surface emittances below a value of 0.5 were removed from the analysis. The composite mean values (Figure 4.37) indicate that the atmospheric corrected microwave surface emittance is approximately 1.5% lower at 19V GHz compared with the effective microwave surface emittance results. The magnitude of the correction increases with frequency, with an atmospheric correction of 3.5% at 85.5H GHz. A larger atmospheric correction is present for the horizontal polarizations than for the vertical polarizations, as would be expected from their lower effective microwave values (see Figure 4.29). The microwave surface emittance standard deviation is reduced by 20-25% with the application of the atmospheric correction for the 19 and 37 GHz channels. The 22V and 85.5 GHz channels are much less responsive and instead have increased standard deviation values after the application of the atmospheric correction. At first glance, this implies that the atmospheric correction is introducing noise into the retrieved microwave surface emittance values. This might be caused by incorrect

specification of the atmospheric conditions, or by problems within the radiative transfer modeling code at these frequencies. However, these channels are at frequencies where the atmosphere is the most opaque, thus the effective microwave surface emittance values are partially obscured by the atmosphere effectively damping the true surface emittance signal. The microwave surface emittance standard deviations are relatively uniform for a given polarization indicating that the retrieved atmospheric-corrected microwave surface emittances are consistent with the other frequencies. This supports the idea of a near frequency-independent surface emittance model of the surface conditions. While some noise must be introduced by the retrieval method due to the previously mentioned factors, the frequency dependence of the effective microwave surface emittance values is not at all obvious (Figure 4.37). Thus, efforts to support a surface emittance model with a high frequency dependent component would be difficult if not impossible. The relatively constant microwave surface emittance standard deviations support the conclusion that the effective surface emittance variability is damped by the atmosphere at the 22V and 85.5 GHz channels, and that the surface emittance retrieval method has compensated for this effect.

4.3.2.3 Diurnal Effects

Diurnal effects were examined by compositing the microwave surface emittance results for morning and afternoon overpasses of the DMSP satellites. The morning period (0600 - 1800 UTC) mean composite surface emittance results (Figure 4.39) were nearly identical to the afternoon period (1800 - 0600 UTC) results (Figure 4.40). Only small differences were observed in very localized regions, namely south Texas and west Mississippi. Other areas experienced almost no diurnal effects. The south Texas area had a positive morning bias of approximately 0.01 suggesting that perhaps heavy early morning dews had a measurable impact in this particular region. The west Mississippi area is in the Yazoo River flood plain and experienced a small positive afternoon bias (<0.01). This could be the result of a bias in the time of flooding events that affect

this region. The rather poor temporal sampling that the DMSP platforms provide could be another possible cause. A closer inspection of Figures 4.39 and 4.40 reveals that the afternoon results are more sparse than the morning overpass results. This is due to the additional afternoon cloudiness compared to the morning overpasses.

The small data overlap with the U.S. - Mexico border and the U. S. - Canada borders is not a navigation error but rather an artifact of the image compositing. The SSM/I FOVs were composited as quadrilaterals. For FOVs near the beginning and end of the SSM/I scan line the polygons are rather oblique in the forward direction due to the SSM/I conical scanning pattern. Thus for the morning ascending orbit pass, the most acute polygon points are at the top border, and vise versa for the afternoon descending orbit passes.

4.3.2.4 Polarization Effects

The microwave surface emittance polarization difference, $\Delta\varepsilon$, at 85.5 GHz was calculated for each SSM/I orbit pass from 30 July - 7 October 1991. The mean, minimum, maximum and standard deviation of the microwave surface emittance polarization difference is shown in Figures 4.41 - 4.44, respectively. The mean polarization difference (Figure 4.41) is large over waterbodies and desert regions as expected. In the desert regions, values of $\Delta\varepsilon$ range from 0.03 - 0.05, while the large lakes can have $\Delta\varepsilon$ values greater than 0.2. Additional areas in the central Great Plains also exhibit large polarization differences. A wide region in west Kansas, Oklahoma, and north Texas has $\Delta\varepsilon$ values greater than 0.02, with some mean values above 0.05 in certain locations. The Arkansas River valley in Colorado also has relatively high mean $\Delta\varepsilon$ values of approximately 0.03. Another anomalous region exists in west Mississippi in the Yazoo River flood plain where mean values exceed 0.04.

The more permanent features are more obvious in the minimum microwave surface emittance polarization difference results (Figure 4.42). The lakes and desert regions stand out. The lakes are smaller in spatial extent due to the repetitive SSM/I sampling of a region with slightly different sub-FOV effects. Only the large lake features remain after compositing. An interesting feature of the data is the relatively high minimum polarization differences in west-central Texas and the South Platte and Arkansas River valleys of Colorado. Some of the polarization is due to irrigation. However, the widespread region of high minimums on the eastern Plains of Colorado suggests the region is also rather arid and from the SSM/I's perspective appears more desert-like than the other Great Plains regions. A similar interesting band is found in southeast New Mexico extending into west Texas. North Iowa also has relatively high minimum polarization differences. From the NDVI information (see section 4.3.6) this region is heavily vegetated. Thus, this anomalous region must be due to sub-FOV lakes dotting the region or perhaps poor cloud-free SSM/I sampling coverage. More data from a longer period, perhaps from multiyear seasonal composites, would be necessary to answer this question satisfactorily.

The maximum microwave surface emittance polarization difference (Figure 4.43) indicates the more temporal surface features. The region of most interest is the central Great Plains. Some areas in north-central Oklahoma have $\Delta\varepsilon$ values greater than 0.2. Such a high extreme value indicates that nearly the entire SSM/I FOV was flooded. Transitory lakes appear due to rainfall events throughout the central Great Plains. Many locations experience polarization differences larger than 0.05. Figure 4.43 also indicates regions that have small polarization differences. These regions are the heavily vegetated regions. The most noticeable low maximum polarization difference areas are the forest regions in the Rocky Mountains, the Black Hills of South Dakota, a small band-like feature in northwest Nebraska and southwest South Dakota, the Ozarks, the Great Lakes region, and areas throughout a large portion east of the Mississippi River.

The variability of the polarization difference signal is shown in Figure 4.44. These results are similar to the standard deviation of the mean microwave surface emittance results (Figure 4.33). The main feature is again the ringing effect around the waterbodies and the highly variable region in the central Great Plains. There is also a noticeable northwest-southeast gradient in the results, with generally higher values in the southeast regions particularly around the Gulf of Mexico. This could be due to several effects. More rain events would occur in the high precipitation areas of the southeast regions. Patchiness of the vegetation might increase in the direction of the gradient. If large tree groves are interspersed with crop regions, this would make the results more variable due the sensor sub-FOV sampling problem mentioned earlier. Without higher spatial resolution data, this question might not be answerable with the current sensor capabilities.

These results have implications for the remote sensing of atmospheric properties over land surfaces. The areas with significant surface polarization can be used as a multichannel background signature from which to retrieve non-polarizing atmospheric constituents. For example, the retrieval of cloud liquid water might be possible by differencing the radiative transfer equation (Equation 4.9) to come up with a polarization difference form of the radiative transfer equation. This results in an equation of the form

$$\Delta L_m = \Delta\varepsilon\left(L_{sfc} - L_{reflected} - L_{space}\right), \tag{4.26}$$

where ΔL_m, is the satellite observed polarization difference radiance, and L_{sfc}, $L_{reflected}$, and L_{space} are defined in section 4.2.3 and specified by Equations 4.10 - 4.13. While such an equation would be sensitive to measurement noise since it uses a difference equation form, possible quantification of cloud liquid water into 3-5 categories might be feasible. The advantage of this method over single channel methods is that the absolute bias of the instrument is removed. This

improves the instrument noise characteristics since inter-channel relative accuracies are much better than the instrument absolute accuracies (see Table 3.2).

On average, the application of this method would be limited to areas that have mean microwave surface emittance polarization difference signatures (Figure 4.41) greater than the natural background variability (Figure 4.44). The region where this condition occurs is shown in Figure 4.45. In Figure 4.45, mean surface emittance polarization difference values that are less than the measured standard deviation are shaded black. Values that remain are signals that are one standard deviation above the natural background variability. A large region remains in Figure 4.45. This shows potential for such a polarization difference method to work. Perhaps a better overall cloud liquid water retrieval method would be a composite of the polarization difference method and a single channel method such as that of Jones and Vonder Haar (1990).

4.3.2.5 7 Day Composites

Weekly composites of the microwave surface emittance were made to determine the spatial structure and coherence of the weekly temporal variability. Figures 4.46 - 4.48 present results from the weekly composite mean 85.5H GHz surface emittance values. Composites with a period of less than one week would have poor spatial coverage due to cloud contamination. Thus, higher temporal resolution composites would have limited value. Analysis of individual orbit pass results would provide nearly the same limited benefit.

The statistics from the 30 July - 7 October composites are further illuminated by studying the higher time resolution results. The consistent nature of the waterbody features is obvious in the sequence of figures. The less than desirable spatial coverage is due to the limited DMSP overpasses coinciding with clear sky conditions. This problem would be much less severe if for instance the GOES had a microwave imager scanning hourly.

The primary region of interest is the central Great Plains. Rain events frequently modify the microwave surface emittance over a large region. Comparing Figures 4.46 (a) and (b) for the Kansas region indicates that the microwave surface emittance values are noticeably lower within a one week period. In Figure 4.46 (c), the spatial features of the low surface emittance area are further defined by more intense individual rain events. By the next week, (Figure 4.46 (d)) the region begins to "dry out". Figure 4.47 (a) is particularly ordinary, lacking any significant temporal features, but within two weeks (Figure 4.47 (b)) more rain events have dotted the Great Plains again. The data coverage then becomes poorer during a rather long period (two to three weeks) due to clouds interfering with the successful retrieval of the microwave surface emittance. By Julian day 272, the rain event signatures are once again gone from the Kansas/Oklahoma region. Less than two days of data were available for the final composite period (Figure 4.48 (c)) and its spatial coverage was particularly sparse.

Some cloud contamination is also evident for regions with particularly high microwave surface emittance (notice the Texas Panhandle region in Figure 4.46 (c)). However, the weekly composite results show that the cloud contamination was not persistent or wide spread. Thus the mean statistics are still valid but with a small bias due to cloud contamination. However, the maximum microwave surface emittances should be viewed with caution since these results indicate that the cloudiest pixel was most likely used in the maximum microwave surface emittance composite results. Since the maximum microwave surface emittance results are not worse, it is perhaps an indicator of the robustness of the cloud discrimination method.

4.3.3 Comparison with Weekly USDA Crop Moisture and Precipitation Data

Results are compared with the weekly USDA Crop Moisture Index (CMI) and total precipitation. Appendix F contains figures of the CMI and of the observed total precipitation. The discussion in this section is based on those figures and the 7 day 85.5H GHz surface emittance

composites shown in Figures 4.46 - 4.48. Composites using the other SSM/I frequencies were also performed and compared. Results were found to be similar, except that the cloud problem which degrades the sampling characteristics is aggravated due to the larger sensor FOV at the lower frequencies.

4.3.3.1 Week 1: Julian Days 209-215

The starting time period experienced general drought conditions that existed in the central Great Plains and the Midwest (see Figures F.1 and 3.12). However, precipitation of more than 2.5 cm occurred in the Yazoo River floodplain in Mississippi. This region exhibits a corresponding low microwave surface emittance anomaly. Otherwise, the microwave surface emittance results show no significant rain event signatures for this period.

4.3.3.2 Week 2: Julian Days 216-222

Kansas experienced some relief from the drought but it is still too dry. A widespread region of greater than 5 cm rainfall occurred in Iowa and parts of Illinois. Potentially interesting parts of this region are obscured by clouds. The Illinois microwave surface emittances are low during the period of widespread heavy rain. North-central Iowa and southern Minnesota experienced flood conditions due to the heavy rain, but most of the wettest region is obscured.

4.3.3.3 Week 3: Julian Days 223-229

The drought began to break in the central Great Plains. However, the CMI indicates that parts of central Kansas still urgently needed rain (CMI = -3.3), even though relatively heavy precipitation (> 1 cm widespread, > 10 cm in localized regions) had occurred. The comparable microwave surface emittance results show much lower emittances during this period. The lowest microwave surface emittance retrieved over land occurred in north-central Oklahoma, coincident with a > 5 cm precipitation event. A major rain event with a large region of > 10 cm precipitation totals

occurred in east Texas and had rainfall > 5 cm throughout much of north Texas, but again the wettest regions were mostly obscured by clouds.

4.3.3.4 Week 4: Julian Days 230-236

Scattered storms occurred during this period. Some remains of last week's intense precipitation in west Texas is still apparent, with low microwave surface emittances again in the region. A region of low microwave surface emittance again occurs in northeast Mississippi. This corresponds to one rain event that was greater than 2.5 cm in magnitude. A spatially-small isolated rain event greater than 5 cm occurred on the Colorado High Plains, but the microwave surface emittance response is small and is represented by only a small dot on the microwave surface emittance results.

4.3.3.5 Week 5: Julian Days 237-243

During this period, significant rain occurred for parts of Kansas and Oklahoma. Oklahoma is now experiencing moist conditions (CMI = 0.3) in its southwestern reaches that 3 weeks ago were severely dry (CMI = -3.5). The first clear weekly composite of Iowa shows a widespread region of low microwave surface emittance. Rainfall occurred in Iowa during this period, however total rainfall had not been sufficient for crop needs and the CMI is reported as "abnormally dry" for Iowa.

4.3.3.6 Week 6: Julian Days 244-250

This period had particularly poor microwave surface emittance coverage due to cloud contamination. Heavy rains fell throughout the south-central Great Plains. Rain in southwest Illinois also exhibits lower microwave surface emittances during this period. The CMI reports flooded conditions for a large area in Oklahoma, but this region is obscured by clouds in the microwave surface emittance results.

4.3.3.7 Week 7: Julian Days 251-257

Flood conditions were still prevalent in Oklahoma and were larger in extent than the previous week. Individual storms can be identified on the microwave surface emittance results and are seen as low microwave surface emittance anomalies. The lower rainfall amounts result in generally lower microwave surface emittances throughout Kansas and Oklahoma.

4.3.3.8 Week 8: Julian Days 258-264

This was an extremely active and wet week in the southern Great Plains. Unfortunately, the cloud cover prevented retrieval of the microwave surface emittance over a large region.

4.3.3.9 Week 9: Julian Days 265-271

Conditions in the southern Great Plains remained wet. However, conditions were slightly drier than the previous week. Most precipitation occurred in the eastern half of the region from east Texas to Ohio. Over 5 cm of rain fell throughout most of Mississippi and Alabama. The microwave surface emittance results are lower in the Ohio Valley region, where over 2.5 cm of rain has fallen in some locations. For this one week composite, the Mississippi and Alabama regions do not appear to have lower microwave surface emittance values. This indicates insensitivity to rain for these regions, or perhaps that the rain occurred near the end of the period and was not sampled in the composite results. Again, relatively poor microwave surface emittance coverage due to cloudiness is a significant problem.

4.3.3.10 Week 10: Julian Days 272-278

The only regions that experienced significant rainfall are northeast Missouri and Northern Illinois with more than 10 cm over a relatively large region. This event was not observed by the microwave surface emittance results. The other non-rain areas however appear to have rebounded to their higher dry state they had in early August.

4.3.3.11 Week 11: Julian Days 279-285

Only 2 days of data were available for this week's composite period. For short time periods (e.g., 2 days) the cloud problem is much more acute. Microwave surface emittance results were available only for the desert regions in the extreme southwest part of the case study region.

4.3.4 Comparison with Irrigation Regions and Spatial Crop-type Information

Irrigation has a significant impact on the microwave surface emittances. The density of irrigated land in farms for 1982 is shown in Figure 4.49. The most striking features are the California Imperial Valley, the Idaho Snake River Valley, a large region in the High Plains and Nebraska, and the Mississippi Alluvial Plain in Arkansas. For the case study region in the central United States, the regions of most importance are the last three. Results from Landsat can be used to determine irrigation densities over regional areas (see Figure 4.50). Two Landsat channels (bands 5 and 6) were used to determine the irrigation areas in a rather labor and computer intensive method (Thelin and Heimes 1987). The irrigation regions correspond well with the mean microwave surface emittance results (Figure 4.30). The regions along the Platte River in Nebraska, and in western Nebraska on the North Platte have lower microwave surface emittances than other surrounding regions. The correspondence of the region in southwest Kansas is less obvious due to low contrast with the surrounding areas. The irrigation region in west Texas is particularly well defined by a low microwave surface emittances. The irrigation signature in this region maintains consistently low microwave surface emittances. The composite maximum microwave surface emittance results (Figure 4.31) indicate that this region has consistently low microwave emittances. Irrigation in Colorado is primarily confined to the South Platte and Arkansas River Valleys (Figure 4.51). However, some intermittent irrigation occurs in east-central Colorado as well (indicated by the light hash pattern in Figure 4.51). The two Colorado irrigation areas are well indicated on the composite mean microwave surface emittance results (Figure 4.30).

Further irrigation information can be inferred from ground water withdrawal information. Since the Great Plains States depend more heavily on ground water than do Western States that rely on off-farm supplies such as runoff from snowmelt, the ground water withdrawal information can be used to infer irrigation water usage. This can provide information where detailed remote sensing studies have not been performed. The magnitude of the irrigation in the Arkansas is found to be also relatively large. Over 2 million acres are irrigated in Arkansas (Bajwa et al. 1987). That is more than 20 percent of the entire cropland in the state. The Mississippi irrigation area is smaller in scope (20% of the total irrigation in Arkansas). Appendix G contains more detailed information regarding ground water withdrawal by state.

Excluding California and Idaho, the primary crops that depend on irrigation include corn (22%), hay (17%), and wheat (9%) (Bajwa et al. 1987). Nebraska alone contributes 51 percent of all irrigated corn acres. However, rice is the primary irrigation crop in Arkansas and Mississippi and Texas' primary irrigated crops are cotton, sorghum, and wheat. Figures 4.52 - 4.53 show the crop production regions for corn, grain sorghum and rice. From this information, it is more obvious which crop and irrigation region is causing the microwave surface emittance depressions. As mentioned before, the Nebraska region and the low microwave emittance region in southern Minnesota and Iowa are dominated by corn. The regions in Illinois and Indiana were experiencing a severe drought at this time (Figure 3.12) which may explain why those regions did not also have lower microwave surface emittances. The west Texas irrigation region is a grain sorghum production area (Figure 4.53). Some cotton production is also present. The Arkansas and Mississippi irrigation regions are primarily involved in rice production. These regions may have a stronger influence than other regions due to flooding that rice requires at certain stages of its development. The crops that were observed to depress the microwave surface emittance values are

all high water-content crops. Wheat crops that should be maturing or already harvested during this case study appear to have little influence on the microwave surface emittances.

The results over heavier vegetation are contrary to what some have observed using ground based microwave instruments (Barton 1978; Newton and Rouse 1988). This suggests that the low microwave surface emittances could be due to flooding in irrigation canals, rather than scattering from the plant canopy. Another possibility is that the water content of the plant is being measured as has been assumed at lower frequencies (Jackson and Schmugge 1991). The final interpretation is still a matter of debate and deserves further study.

4.3.5 Comparison with an Antecedent Precipitation Index

An Antecedent Precipitation Index (API) was calculated from precipitation measurements from the 6 h USAFETAC DATSAV2 precipitation database (see section 3.3.2). The API for day i is given by

$$\mathrm{API}_i = k' \, \mathrm{API}_{i-1} + P_i, \tag{4.27}$$

where P_i is the 6 h total precipitation and k' is the 6 h depletion coefficient. To make results comparable with other studies which employed 24 h precipitation data, an equivalent 24 h depletion coefficient was defined such that

$$k = (k')^4, \tag{4.28}$$

where k is the 24 h depletion coefficient. This 24 h depletion coefficient value will be referenced throughout this work rather than the 6 h value to limit the terminology confusion. All stations were initialized with an API of 10 mm on July 15. Within 15 days, less than 21% of this value remains (assuming $k = 0.9$). Stations with fewer than 5 sample times matching the microwave surface emittance observations were discarded. Since the depletion coefficient can be a function

of location, the selection of the depletion coefficient was obtained by varying the value from 0.85 to 0.93 and selecting the value that provided the best correlations for each site. The depletion coefficient was then held constant for each site through the remainder of the correlation calculations.

The mean microwave surface emittance results were compared with the API measurements for each precipitation station location. Precipitation stations that had less then 10 mm of precipitation were excluded from the analysis, as were locations that had microwave surface emittance ranges less than 0.03. This prevents stations that contain especially noisy signals from corrupting the analysis. The microwave surface emittance results were spatially filtered to correspond to the precipitation locations using PORTAL. The point location data sets were then correlated against each other for each precipitation site. No other attempts were made to further filter the data. However, it should be recalled that the microwave surface emittance results are inherently cloud free.

Histograms of the API correlation results show some correlation of the microwave surface emittance with the API but the results are not outstanding (see Figures 4.55 and 4.56). Some individual locations have correlations as low as -0.95. Conversely, some sites had high correlation values (0.95). In Figures 4.55 and 4.56, the histograms have a rather broad distribution with a significant skewness toward the lower correlation values. The skewness in the correlation distribution increases with lower frequencies, indicating that the lower frequency channels are on average better correlated to the API results. The 85.5 GHz results show a pronounced peak at zero correlation suggesting that the results at 85.5 GHz are random for a majority of the locations, although a small group of locations exhibits negative correlation with the API that is above the random Gaussian-like background distribution. The horizontal polarization correlation results (Figure 4.56) show similar features as that of the vertical polarization results. However, the

skewness in the correlation distribution is stronger for the horizontal polarization results than for the vertical. This is expected since the horizontal should have a correspondingly larger range than that of the vertical polarization data and hence more of a signal to measure.

In an effort to understand the correlation distributions, the mean microwave surface emittance, and its standard deviation, along with the API standard deviation were plotted against the API correlation results (Figures 4.57 - 4.59). The skewness of the API correlation toward negative correlation values is apparent in all the figures. No obvious relationship was found between the mean microwave surface emittance and the API correlation values. The microwave surface emittance standard deviation and API standard deviation versus the API correlation results (Figures 4.58 and 4.59) indicate a small trend of higher variability in the API and microwave surface emittance with more negative API correlation values. This is most likely due to the quality of the data sample at each site. For sites that undergo a wider range of conditions the correlation results are more negative, since similar conditions (low standard deviations of either quantity) would not allow accurate determination of the correlation relationship. These results show how important long time series data sets are to the accurate determination of surface relationships involving intermittent features such as rain. The overall high amount of scatter in Figures 4.57 - 4.59 also indicates the difficulty involved with the point-measurement comparison method.

The spatial location of high correlation sites is also of considerable interest. The API correlation results for the 85.5H GHz surface emittance are shown as an example. In Figure 4.60, the locations of sites where the microwave surface emittance versus the API correlation values are less than -0.5 are indicated. A wide range of locations are shown (35 stations) which have significant negative correlation values. Many of these same locations were observed and discussed in detail in section 4.3.3. Many stations are in areas that traditionally have been viewed as being poor candidates for remote sensing of soil moisture due to their vegetation coverage (Heymsfield

and Fulton 1992). Conversely, locations of stations with API correlation results greater than 0.5 are shown in Figure 4.61. It is counterintuitive to expect that high microwave surface emittance would be correlated with high API values. However, this can occur due to SSM/I FOV placement near large waterbodies or other surface features that experience large microwave surface emittance variability due to their sub-FOV features. Another possibility could be due to cloud contamination effects which would most likely have a positive correlation with rain events since clouds are always present with rain. Thus, this figure can be thought of as a measure of noise within the system due to sub-FOV effects and cloud contamination. An equal probability would exist that similar errors occur in the negative API correlation results of Figure 4.60 as well. Thus, it is likely that approximately seven stations are also misrepresented by similar effects in the results shown in Figure 4.60. When all 7 channels of the SSM/I are considered, 95 station locations have API correlation values below -0.5 (Figure 4.62). This represents a wide range of possible locations and conditions from which to develop satellite based soil wetness retrieval methods.

4.3.6 Comparison with a Normalized Difference Vegetation Index (NDVI)

The microwave surface emittance was also compared with 1 km biweekly NDVI observations. The NDVI data set used in the study is described in detail in section 3.3.5. The NDVI data were composited for NDVI data within the July 30 - Oct. 7 data period of the case study. Mean NDVI values were then compared with their respective mean microwave surface emittance values for a given location. In Figure 4.63 and 4.64 results are shown for the vertical and horizontal polarizations of the SSM/I channels. The results are rather surprising. The microwave surface emittance is largely independent of the NDVI. Low microwave surface emittance values are as frequently associated with high NDVI values as with low NDVI values. High microwave surface emittance values tend to have slightly lower maximum microwave surface emittance values for both high and low NDVI extremes. For mid-range NDVI values (0.2 - 0.3) the microwave

surface emittance tends to be slightly higher. The large scatter of points with low microwave surface emittance is due to small waterbody features and surface wetness effects due to rainfall events. The horizontal polarization results (Figure 4.64) show more variability and a more noticeable dog-leg in the data distribution that occurs at an NDVI value of 0.2.

The data were separated into 4 smaller areas (A - D) for more detailed analysis. Sector definitions are described in Table 4.8. Area A includes the Black Hills of South Dakota, area B covers a large part of Kansas and Oklahoma, area C includes a more heavily vegetated region in the Ozark Mountains of Arkansas, and area D is in west Texas and includes a region of intensive irrigation. In Figure 4.65, scatterplots of NDVI versus the 85.5 GHz surface emittance is shown for each area. Area A (Figure 4.65a) shows the least surface emittance variability of the 4 regions, possibly due to the dryness of the region and to the type of vegetation (prairie grass and conifer forest). The remaining areas (Figure 4.65b-d) show little difference in their data distributions other than the extent of their NDVI ranges. All the regions have a considerable range of microwave surface emittance values, which indicates that the scatter in the composite plots for the entire area (Figures 4.63 and 4.64) is not due to significantly different signatures from the selected regions. Another interesting result is that few NDVI values in Figure 4.65 are below 0.2. Closer examination of the results (not shown in the figure) indicates that the desert regions of the West are primarily responsible for the dog-leg effect noticed in Figures 4.63 and 4.64.

The microwave surface emittance polarization difference, $\Delta\varepsilon$, was also calculated for comparison with the composite NDVI results. The microwave surface emittance polarization differences at 85.5 GHz are plotted against the corresponding NDVI values in Figure 4.66. The distribution is similar to the previous NDVI versus microwave surface emittance plots, with the exception that the dog-leg feature is now oriented in the opposite direction since the vertical polarization is subtracted from the horizontal polarization. The standard deviation of the microwave

surface emittance difference (Figure 4.67) shows quite a bit of variability in the results. NDVI results that correspond to open water, values of zero, exhibit the largest variability. To examine the regional behavior, the mean and maximum $\Delta\varepsilon$ values from the 4 small regions described in Table 4.8 are plotted against the mean NDVI values for each area (see Figures 4.68 and 4.69). Figure 4.68 shows that the mean $\Delta\varepsilon$ values tend to have more structure to their distributions than the previous large area composite would indicate. There is a steep negative slope along the minimum values of the mean $\Delta\varepsilon$ values in areas A, B, and C. Area D does not have this feature. This relationship is due to the surface roughness effect that increased vegetation amounts have on the microwave polarization (see Appendix section A.3.6). Area D's behavior could be due to the constantly wet conditions at the high NDVI values and thus does not exhibit the steep negative slope feature, since the high NDVI values are nearly always polarized to some extent (see Figure 4.68d). The maximum $\Delta\varepsilon$ values versus the NDVI for the 4 small regions (Figure 4.69) emphasize the temporal surface wetness features. Again, a steep negative slope is present for the lowest maximum $\Delta\varepsilon$ values for areas A - C, but area D is independent of the NDVI. The maximum $\Delta\varepsilon$ values show more variability since the strongest polarizing rain events are represented in this plot, along with static waterbody features which are also present in the mean $\Delta\varepsilon$ results of Figure 4.68. The polarization is larger in the irrigated region of Area D that has high NDVI, while the low NDVI regions that are not irrigated are slightly polarized due to the sparse vegetation effect (the same effect that is present in areas A - C). The combination of the irrigated land with the non-irrigated land overcomes the steep negative slope relationship that the NDVI has with $\Delta\varepsilon$ and results in the poor correlation shown in Figure 4.69d.

4.3.7 Comparison with the SSM/I Soil Moisture and Surface Wetness Indices

The microwave surface emittance results share some significant features with the SWI and SMI results. While the microwave surface emittance results show significant amounts of detail

(see for example Figure 4.30), the SWI and SMI results for the same period appear more crude due to resolution differences as a result of their multichannel processing requirements. The standard deviation of the microwave surface emittance (Figure 4.33) shows that regions with large microwave surface emittance standard deviations (> 0.05) resemble the maximum SWI and SMI composite results (Figures 4.13 and 4.8). For example, the wet area in the central Great Plains in Oklahoma and Kansas is present in both indices. Since the SWI and SMI are relatively sporadic in the their temporal coverage due to their threshold nature as opposed to the microwave surface emittance, the maximum SWI and SMI corresponds best with the microwave surface emittance standard deviation results. Further differences between the microwave surface emittance are more difficult to explain and are more a function of the particular index method than on the microwave surface emittance results. The SWI and SMI are compared in more detail in section 4.1.3. Since the microwave surface emittance includes all surface conditions into the final product its results appear to have wider scope and more detail due to physical mechanisms that may be unrelated to the surface wetting events that are captured in the SWI and SMI. Also some station locations that had high correlations of microwave surface emittance with the API are not present in the index results, suggesting that the SWI and SMI are incomplete indices for measuring surface wetness.

The microwave surface emittance results also provide information about the physical mechanism behind the SWI method. The SWI method relies on a microwave brightness temperature difference between frequencies with a horizontal polarization. From the atmospheric correction results it is known that this frequency dependence is primarily an atmospheric effect from water vapor absorption. So how can the SWI work? Very simply, the surface emittance is being indirectly measured through water vapor attenuation. The water vapor signal is strongest for areas with low microwave surface emittance. Thus, regions with low microwave surface emittance

have the largest SWI value. Regions that have high microwave surface emittances can not measure the water vapor effects as well and the frequency difference is small resulting in a small SWI value.

4.3.8 Summary of Microwave Surface Emittance Results

The microwave surface emittance contains important information about the surface. Besides the expected waterbody signature due to permanent hydrological features, the data show an ability to measure surface wetness features temporally for some conditions. Irrigation regions are also able to be detected by the microwave surface emittance. The reason for the low microwave surface emittance for irrigation regions may be due to standing water from the result of the irrigation or from very high plant water content. The results from this work were inconclusive on this point. Coniferous vegetation was found to have a particularly high microwave surface emittance signature which allowed for its identification in some regions. Deserts also had very low microwave surface emittance features as expected, but no noticeable difference was found between desert sand types in a comparison of the Red Desert of Wyoming and of White Sands, New Mexico. This suggests that the low desert microwave surface emittance is primarily due to the high dielectric constant of sand instead of scattering influences that are due to sand particle shape and size differences. Further work over larger desert regions is needed to confirm this hypothesis.

The atmospheric correction applied in the retrieval of the microwave surface emittance tend to normalize the microwave surface emittance statistics so that only small differences with frequency are observed. A small negative gradient with frequency is found with retrieved microwave surface emittance, which is opposite of the expected frequency dependence due to water. A non-uniform sampling size due to a frequency dependent FOV-size is suggested as the cause of this frequency dependent feature. A frequency dependence was also found in the microwave

surface emittance comparisons with API, which could be due to penetration depth dependence with frequency, or also of the decreased signal with frequency due to atmospheric attenuation. The microwave surface emittance variability at 85.5 GHz increased with the application of the atmospheric correction, suggesting that previous studies using non-atmospheric corrected microwave brightness temperatures could experience decreased sensitivity at higher frequencies due to atmospheric effects along with the effect of the frequency dependent penetration depth of the microwave radiation. Only limited diurnal effects were found in the microwave surface emittance data set; this suggests that the frequency penetration depth has little effect, since the penetration depth should experience a diurnal cycle due to an out-of-phase vertical heating profile for the surface and near-surface layers.

The microwave surface emittance polarization difference was found to be a good visual indicator of surface wetness. The results also indicate the possibility of using this parameter for the determination of cloud liquid water over land. Although some highly vegetated regions do not experience sufficient polarization differences to produce measurable cloud liquid water amounts, the method should be highly complementary to single channel microwave cloud liquid water retrieval methods. Error propagation of such a method should also be improved over single channel methods since the relative interchannel calibration error is less than the single channel absolute brightness temperature accuracy.

The weekly composites graphically show the temporal nature of the microwave surface emittance fields, and thus their potential for retrieval of temporal surface features such as surface wetness. Large rain events were observed in the data set for a wide range of regions. From this data set, the region of most sensitivity appears to be the central Great Plains. However, significant features related to rainfall were also found in highly vegetated regions such as Illinois and west Mississippi. Not all rain events appear in the microwave surface emittance data set,

especially in the forested regions of the East. The microwave surface emittance is thus spatially inconsistent as an indicator of all precipitation events. Comparisons with an API showed that some of the best correlations were to be found in Illinois in addition to the Oklahoma and Kansas regions. Since Illinois was experiencing a drought during the first part of the data period, it might be reasonable to assume that the vegetation was sufficiently dried to become less of an obscurant to the land's surface wetness conditions. The rapidly changing wet and dry surface conditions in Oklahoma and Kansas were particularly visible in the microwave surface emittance results.

The NDVI comparisons with the microwave surface emittance retrieval results were rather surprising, since the NDVI showed little correspondence to the microwave surface emittance, except at very low NDVI values (< 0.2). Upon closer examination of the results, it was found that some regions did experience a steep negative slope relationship with their lowest microwave surface emittance polarization difference. This suggests that the NDVI relationship to the microwave brightness temperature data is regional in nature at the higher NDVI levels. Irrigation regions did not exhibit any noticeable correlation. This is explained by the low microwave surface emittances being associated with the irrigation areas with their higher NDVI values, thus effectively canceling the steep negative slope relationship. However, when the mean NDVI and mean microwave surface emittance values are compared, areas with NDVI values above 0.2 show little relationship to the microwave surface emittance. Regions with NDVI values below 0.2 show the expected NDVI and microwave polarization difference temperature (MPDT) correspondence. This work highlights the inappropriateness of using the annualized MPDT versus NDVI relationship for generalizations about the sensitivity of the microwave surface emittance to vegetation greenness as measured by the NDVI. This has serious implications regarding recent attempts to use generalized SVAT models (Olioso et al. 1995) which require a deterministic NDVI versus MPDT relationship that is simply not observed at the SSM/I frequencies. The microwave data is not

responsive to vegetation in the same manner as NDVI except on a regional basis and at extremely low NDVI values. Irrigation effects are thus a substantial source of noise in the MPDT versus NDVI relationship.

As opposed to the SWI and SMI retrievals, all cloud-free microwave FOVs are used to retrieve the microwave surface emittance. This eliminates the strong filtering of the SWI and SMI methods, and allows the microwave surface emittance results to provide information on regions that would have had no coverage by either of the above methods. However, since the microwave surface emittance also requires infrared data, the cloud-free condition is a major hindrance to practical use of the microwave surface emittance using the limited temporal coverage available from current polar orbiting satellites. The higher temporal resolution available from a geostationary microwave imager could significantly improve the microwave surface emittance coverage.

Table 4.1: Summary of surface type classification rules using the seven channels of the SSM/I (from McFarland and Neale 1991).

LAND SURF. TYPE	Brightness Temperature Threshold Values [a] (K)	[b] (K)	[c] (K)	[d] (K)	[e] (K)	[g] (K)	[h] (K)	[j] (K)
1 Flooded Conditions	> 4							
2 Dense Vegetation	≤ 4	≤ 1.9		≥ -1	< 4.5	> 262		
3 Dense Agric./ Range Veg.	≤ 4	> 1.9 ≤ 4		≥ -1	< 4.5	> 262		
4 Dry Arable Soil	≤ 4	> 4 ≤ 9.8	≥ -6.5	< 0.5 ≥ -5	< 4.2			
5 Moist Soil	≤ 4	> 4 < 19.7	≥ -6.5	≥ 0.5 < 4	< 4.2			
6 Semi-Arid Surface	≤ 4	> 9.8 < 19.7		< 0.5	< 6			< -1.8
7 Desert	≤ 2	≥ 19.7			> -1	> 268		
8 Precip. Over Veg.	≤ 4	≤ 4		< -1		> 268		
9 Precip. Over Soil	≤ 4	> 4	< -3	< -5	< -4.1	> 268		
10 Comp. Veg. and Water	≤ 4	< 6.4		≥ -1	≥ 4.5		> 257	
11 Comp. Soil & Water/ Wet Soil	≤ 4	≥ 6.4	≥ -6.5	≥ 0.5	≥ 4.2			
12 Dry Snow [1]	≤ 4	> 4	< -6.5				> 225 ≤ 257	
13 Wet Snow	≤ 4	> 9.8	≤ -0.8 ≥ -6.5	< 0.5			≤ 268 > 253	≥ -1.8 ≤ 6.5
14 Refrozen Snow [2]	≤ 4	> 4	< -6.5				≤ 225	
15 Unclassified	otherwise							

[a] 22V - 19V [b] (19V + 37V)/2 - (19H + 37H)/2 [c] 37V - 19V

[d] 85V - 37V [e] 85H - 37H [f] 37V - 37H

[g] 19V [h] 37V [j] 37H - 19H

Additional conditions: [1] 19V - 19H ≥ 5, [2] 19V > 37V > 85V, 19H > 37H > 85H

Table 4.2: McFarland and Neale surface moisture retrieval algorithms for three vegetation classes (adapted from McFarland and Neale 1991).

Vegetation Density Class	A	B	TEST
Low	659.35	-675.22	[b] > 8 K
Medium	1126.58	-1145.48	6 < [b] ≤ 8 K
Medium-High	1707.24	-1724.14	4 < [b] ≤ 6 K

SMI = A + B (T19H / T37V) [b] (19V + 37V)/2 - (19H + 37H)/2

Table 4.3: SSM/I best-fit spatial weighting function coefficients and standard deviations.

channel	n_x*	n_y*	σ_{G_x}**	σ_{G_y}**
1	2.06	2.17	0.01	0.01
2	2.10	2.16	0.00	0.00
3	2.24	2.20	0.00	0.01
4	1.96	2.52	0.01	0.01
5	2.49	1.95	0.01	0.01
6	2.30	2.19	0.00	0.00
7	2.24	1.54	0.00	0.01

* Values are valid for 0-20 dB, except for channels 4-7 which are valid for 0-10 dB.

** Standard deviation values are in terms of gain.

Table 4.4: Error sensitivity analysis for retrieved microwave surface emittance (adapted from Jones and Vonder Haar 1990).

frequency (GHz)	microwave surface emittance errors	
	relative	absolute
19.35	0.0021	0.0078
22.235	0.0041	0.0094
37.0	0.0020	0.0084
85.5	0.0053	0.0123

Table 4.5: Mean and maximum microwave surface emittance values for 30 July - 7 October 1991.

frequency and polarization (GHz)	microwave surface emittance values	
	mean	maximum
19.35V	0.962	1.017
19.35H	0.933	0.991
22.235V	0.954	1.027
37.0V	0.951	1.010
37.0H	0.928	0.994
85.5V	0.945	1.049
85.5H	0.927	1.023

Table 4.6: Mean, minimum, maximum, and standard deviation microwave surface emittance statistics for White Sands, New Mexico for 30 July - 7 October 1991.

	frequency (GHz)	mean value	standard deviation	minimum value	maximum value
mean	19V	0.960	0.003	0.955	0.966
	19H	0.886	0.012	0.866	0.920
	22V	0.951	0.004	0.943	0.960
	37V	0.952	0.004	0.945	0.960
	37H	0.887	0.015	0.857	0.922
	85V	0.947	0.007	0.931	0.960
	85H	0.902	0.019	0.852	0.933
minima	19V	0.947	0.005	0.940	0.960
	19H	0.856	0.018	0.831	0.907
	22V	0.934	0.007	0.925	0.951
	37V	0.937	0.007	0.930	0.954
	37H	0.853	0.022	0.819	0.911
	85V	0.925	0.011	0.906	0.945
	85H	0.865	0.029	0.807	0.909
maxima	19V	0.973	0.004	0.968	0.978
	19H	0.906	0.014	0.887	0.939
	22V	0.967	0.005	0.960	0.978
	37V	0.966	0.005	0.956	0.976
	37H	0.914	0.012	0.878	0.941
	85V	0.969	0.010	0.949	0.987
	85H	0.932	0.016	0.875	0.962
standard deviation	19V	0.008	0.001	0.005	0.011
	19H	0.016	0.004	0.008	0.029
	22V	0.010	0.003	0.004	0.015
	37V	0.009	0.002	0.004	0.012
	37H	0.018	0.004	0.007	0.031
	85V	0.012	0.002	0.008	0.016
	85H	0.019	0.006	0.009	0.038

Table 4.7: Mean, minimum, maximum, and standard deviation microwave surface emittance statistics for the Red Desert of southwest Wyoming for 30 July - 7 October 1991.

	frequency (GHz)	mean value	standard deviation	minimum value	maximum value
mean	19V	0.956	0.002	0.950	0.959
	19H	0.888	0.006	0.878	0.901
	22V	0.947	0.002	0.942	0.952
	37V	0.947	0.002	0.943	0.951
	37H	0.890	0.006	0.880	0.907
	85V	0.943	0.003	0.936	0.950
	85H	0.898	0.008	0.881	0.923
minima	19V	0.940	0.002	0.937	0.943
	19H	0.871	0.007	0.859	0.885
	22V	0.931	0.002	0.927	0.935
	37V	0.930	0.002	0.927	0.936
	37H	0.869	0.008	0.859	0.891
	85V	0.922	0.004	0.914	0.932
	85H	0.873	0.011	0.857	0.903
maxima	19V	0.969	0.002	0.958	0.973
	19H	0.902	0.006	0.893	0.918
	22V	0.961	0.004	0.953	0.965
	37V	0.961	0.002	0.957	0.966
	37H	0.907	0.007	0.895	0.922
	85V	0.964	0.008	0.947	0.981
	85H	0.921	0.009	0.902	0.948
standard deviation	19V	0.010	0.001	0.006	0.012
	19H	0.011	0.001	0.008	0.014
	22V	0.011	0.001	0.007	0.012
	37V	0.010	0.001	0.007	0.012
	37H	0.013	0.002	0.008	0.016
	85V	0.013	0.002	0.008	0.018
	85H	0.015	0.002	0.010	0.020

Table 4.8: Small sector definitions for the NDVI versus microwave surface emittance comparisons.

area	states	features	latitude range		longitude range	
			min.	max.	min.	max.
A	MT, WY, SD	Prairie/Black Hills	-106°	-101°	42°	46°
B	OK, KS	Central Great Plains	-100°	-95°	34°	40°
C	AK, MO, OK	Ozark Mountains	-95°	-92°	34°	38°
D	NM, TX	Irrigated High Plains	-104°	-100°	32°	36°

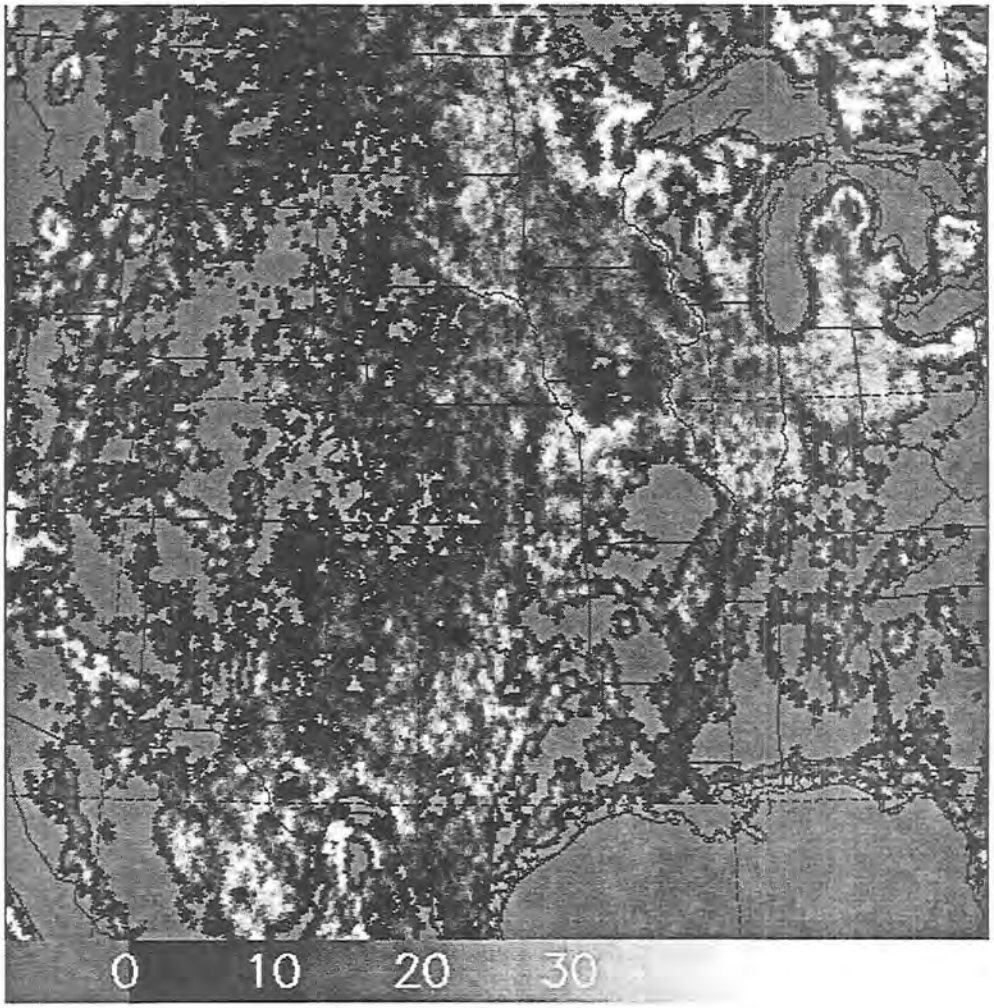

Figure 4.1: Percent occurrence of "Moist soil" land classification category for 30 July - 7 October 1991 from DMSP F-10 SSM/I data.

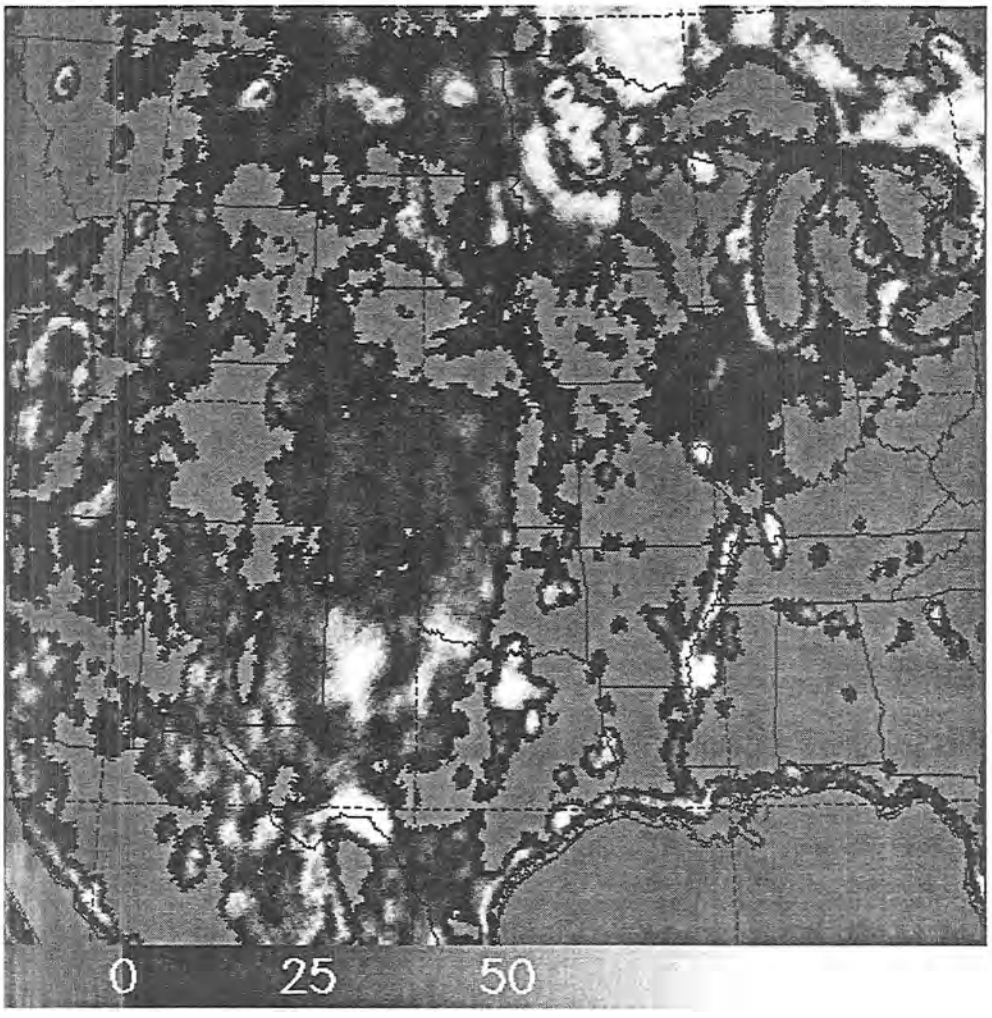

Figure 4.2: Same as Figure 4.1, except for percent occurrence of "Composite soil and water/wet soil" land classification category.

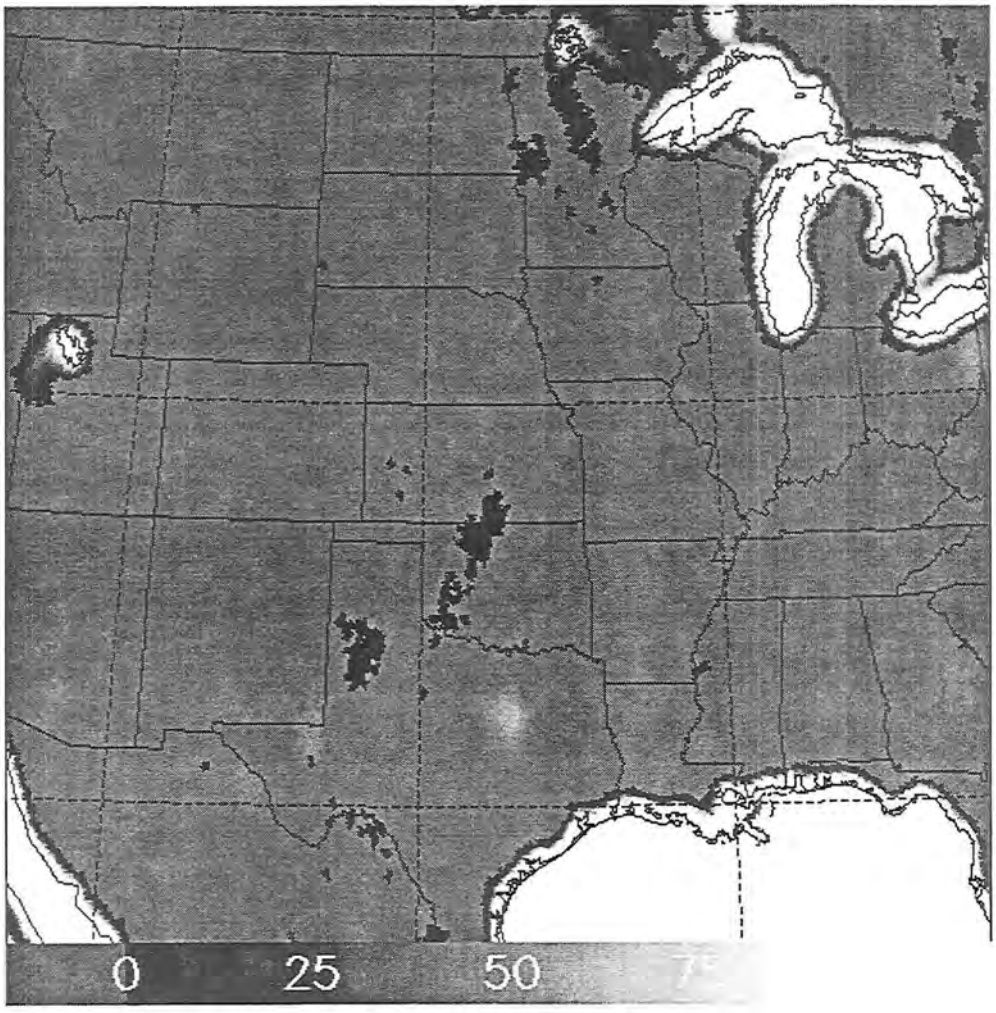

Figure 4.3: Same as Figure 4.1, except for percent occurrence of "Flooded conditions" land classification category.

Figure 4.4: Neale land classification for 1525-1534 UTC 8 September 1991. Land classification categories are described in Table 4.1.

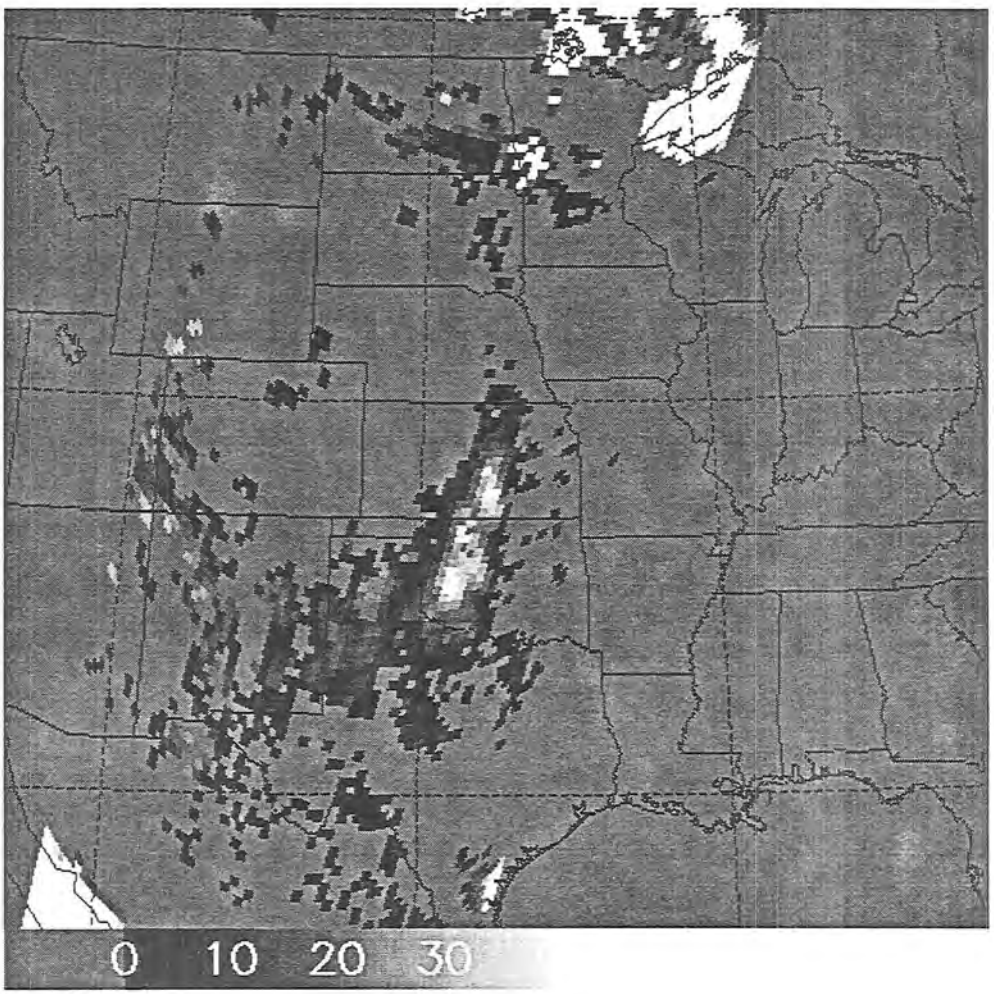

Figure 4.5: Same as Figure 4.4, except for SMI algorithm results.

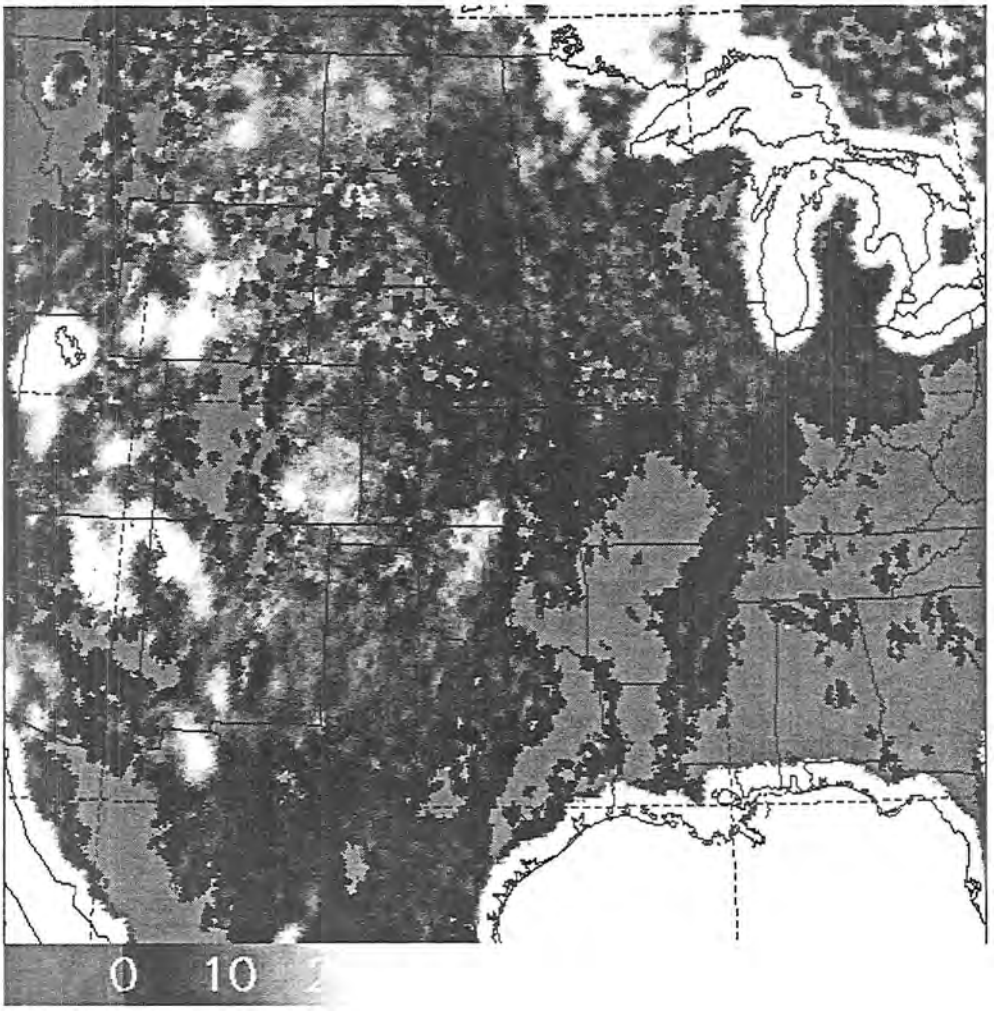

Figure 4.6: Composite mean SMI values derived using DMSP F-10 SSM/I data for 30 July - 7 October 1991.

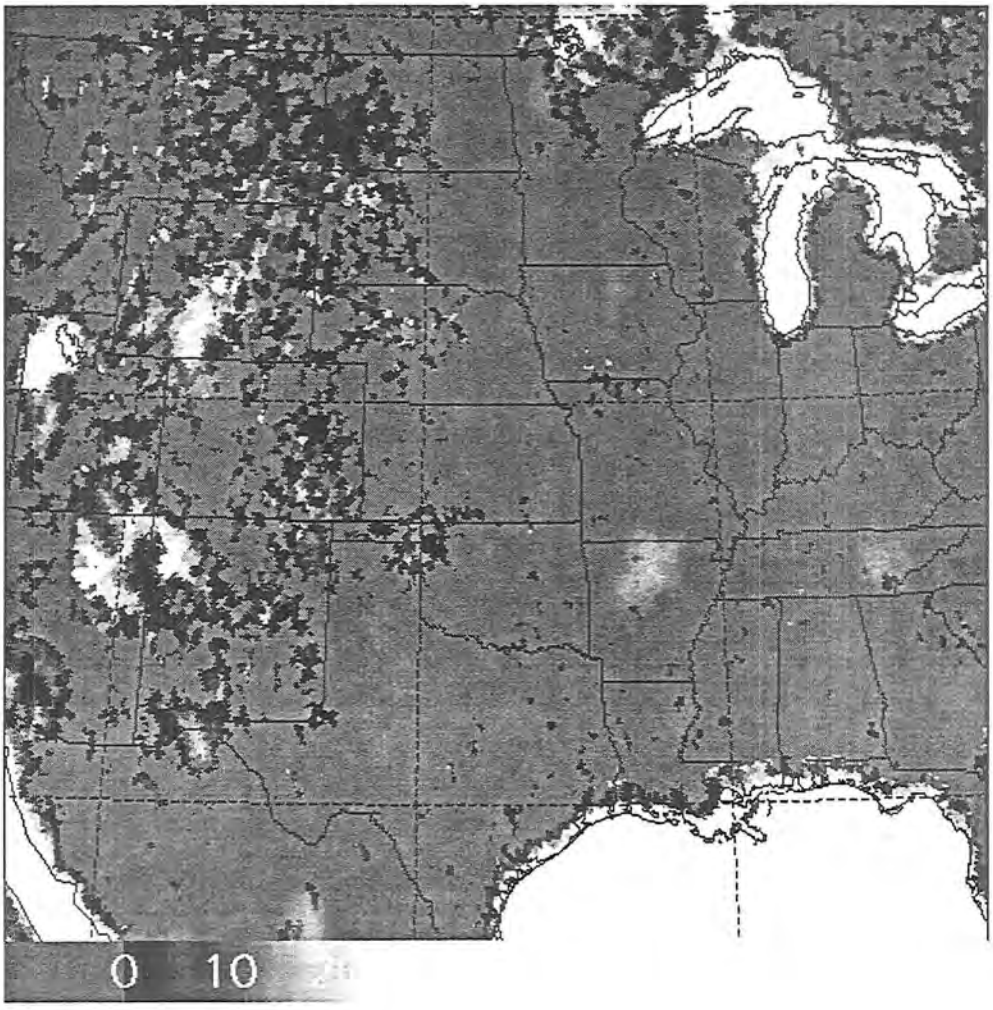

Figure 4.7: Same as Figure 4.6, except for the minimum SMI values.

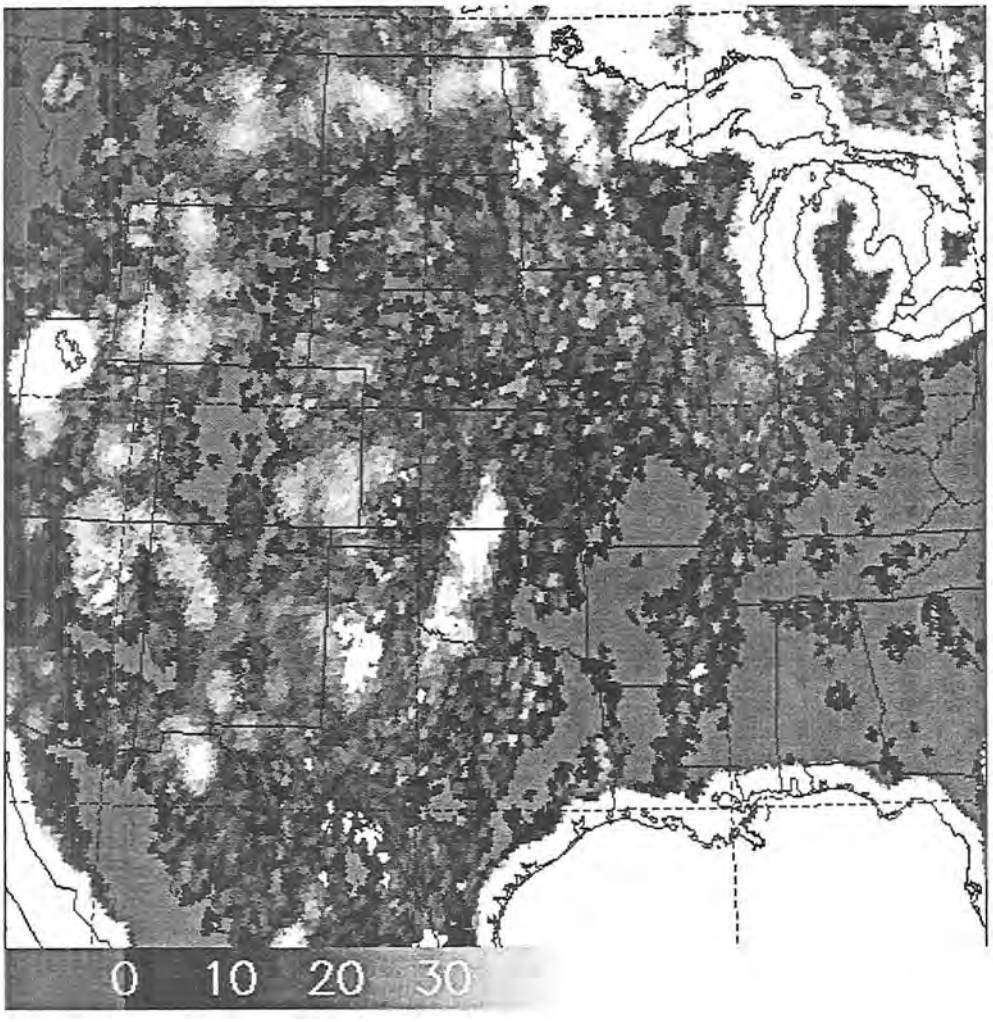

Figure 4.8: Same as Figure 4.6, except for the maximum SMI values.

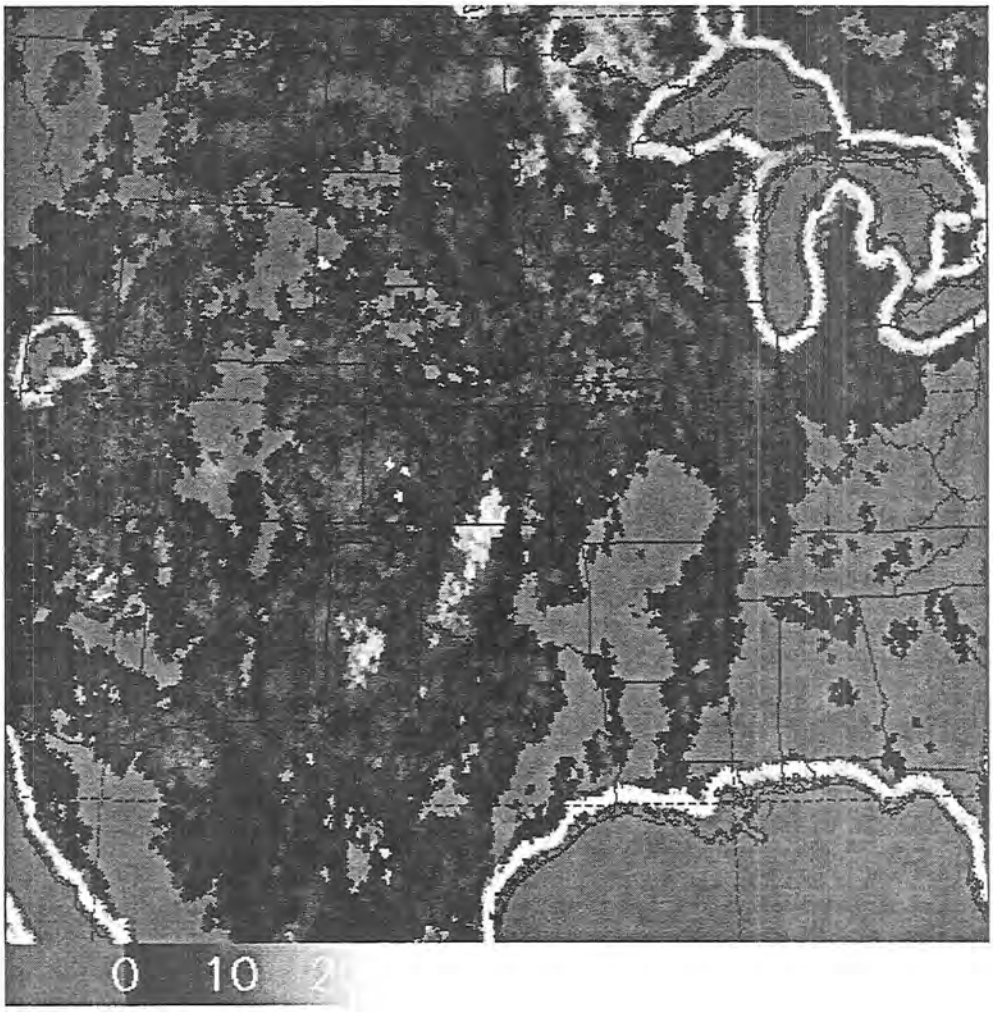

Figure 4.9: Same as Figure 4.6, except for the standard deviation of the SMI values.

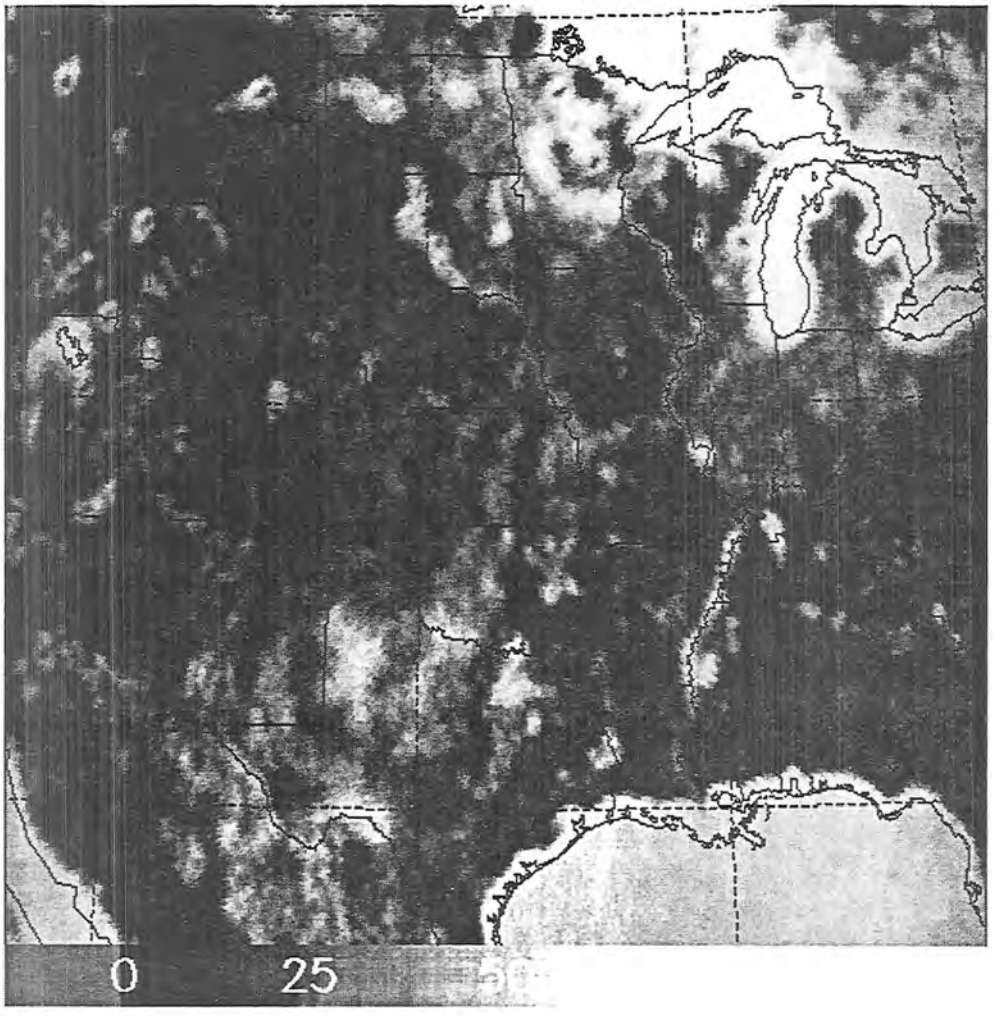

Figure 4.10: Same as Figure 4.6. except for the number of SSM/I data samples used in the SMI algorithm composites.

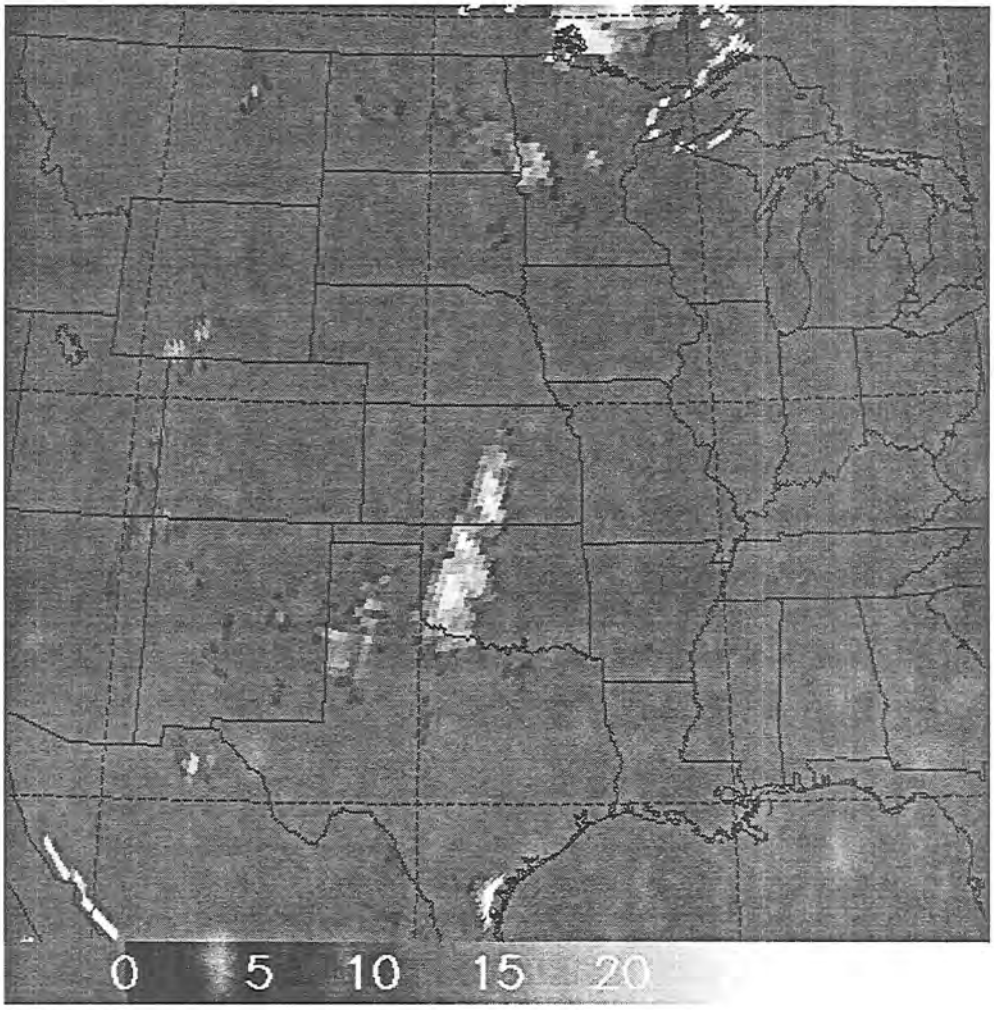

Figure 4.11: SWI results for 1525-1534 UTC 8 September 1991.

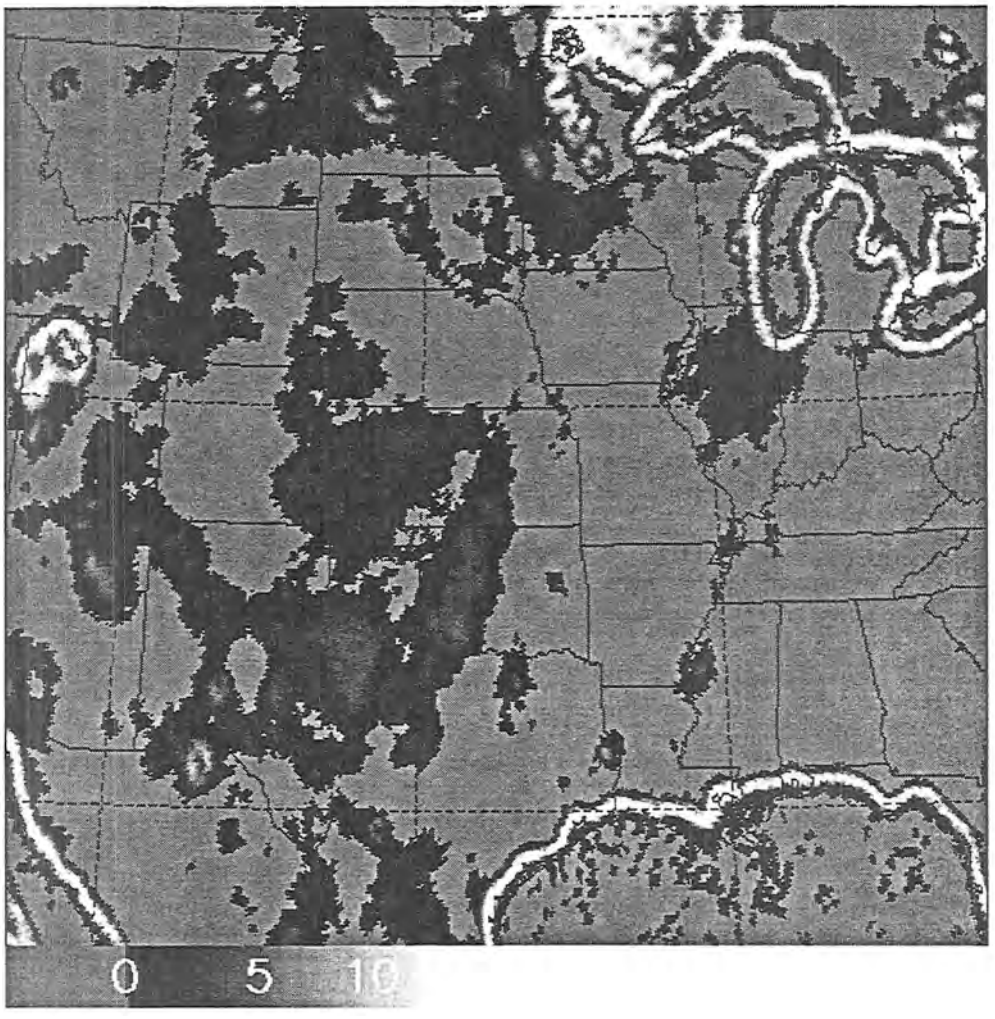

Figure 4.12: Composite mean SWI values derived using DMSP F-10 SSM/I data for 30 July - 7 October 1991.

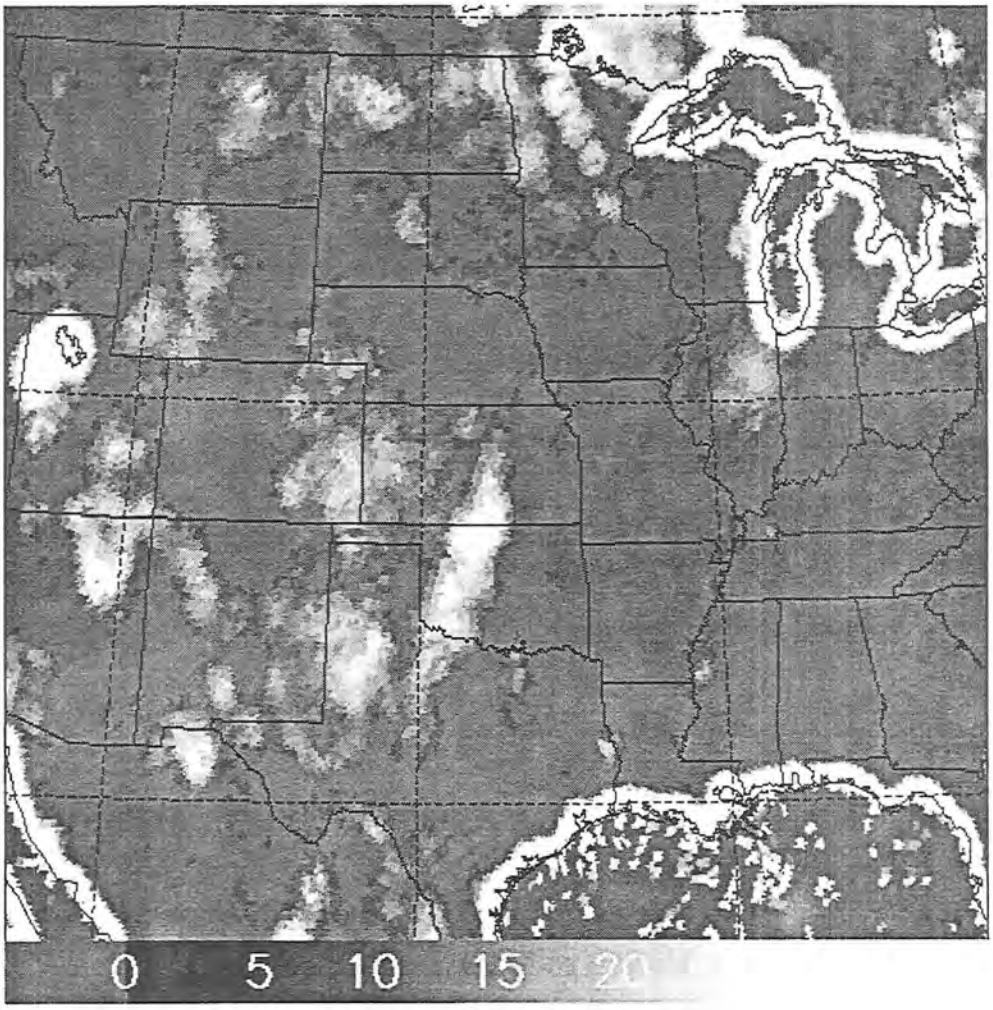

Figure 4.13: Same as Figure 4.12, except for the maximum SWI values.

Figure 4.14: Same as Figure 4.12, except for the sample density of the SWI values.

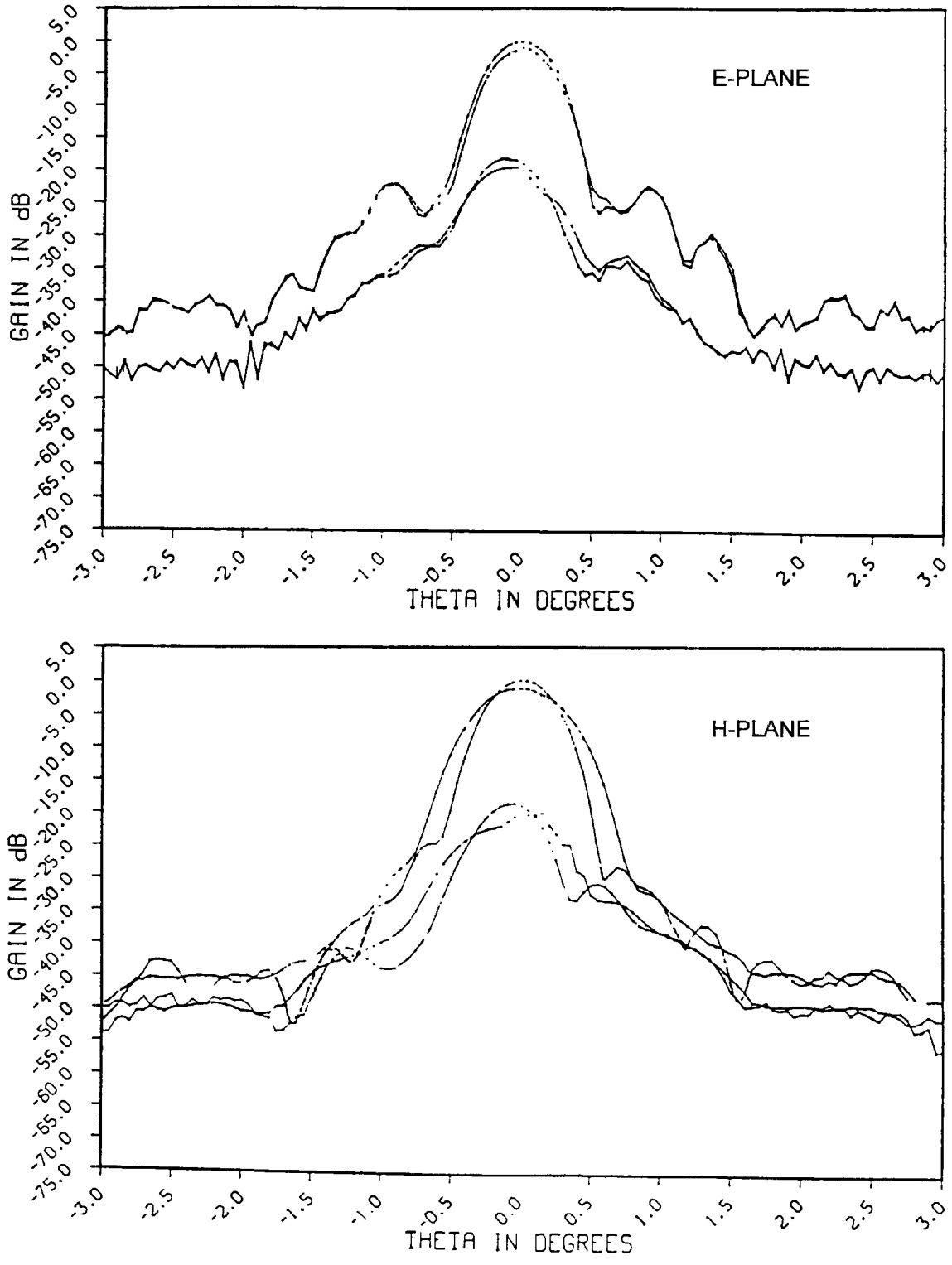

Figure 4.15: Antenna pattern for SSM/I channel 6 (85.5 GHz vertical polarization). The lines denote laboratory measurements, for more detail see Hollinger et al. (1987).

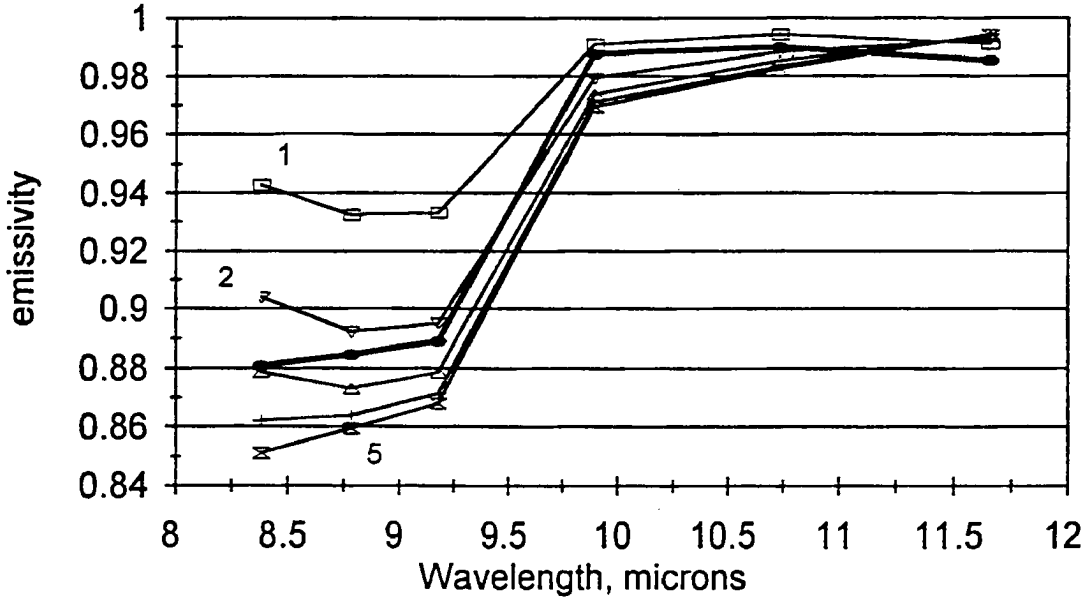

Figure 4.16: Derived infrared surface emissivity values from TIMS using two infrared surface emissivity retrieval methods (from Schmugge et al. 1995).

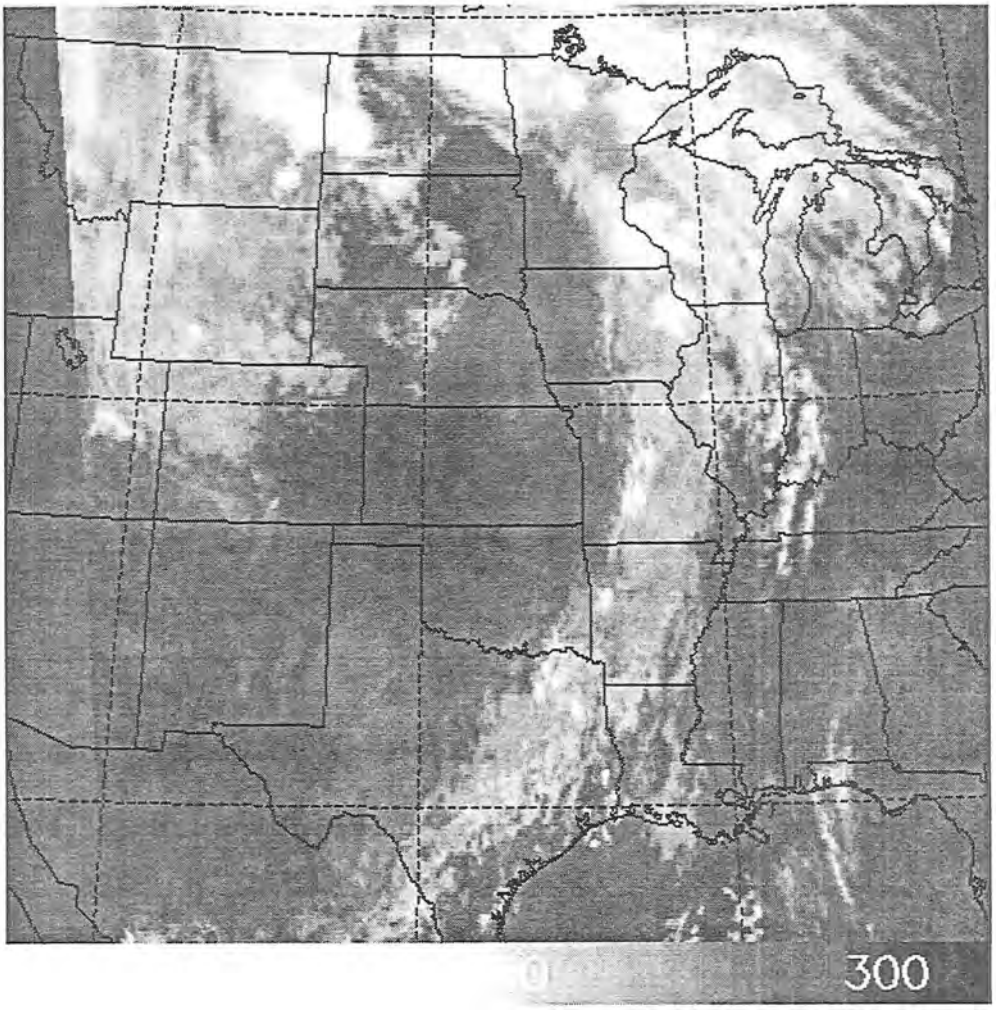

Figure 4.17: GOES VISSR infrared (channel 8) imagery for 1532-1535 UTC 8 September 1991. Values are displayed in terms of brightness temperature (K).

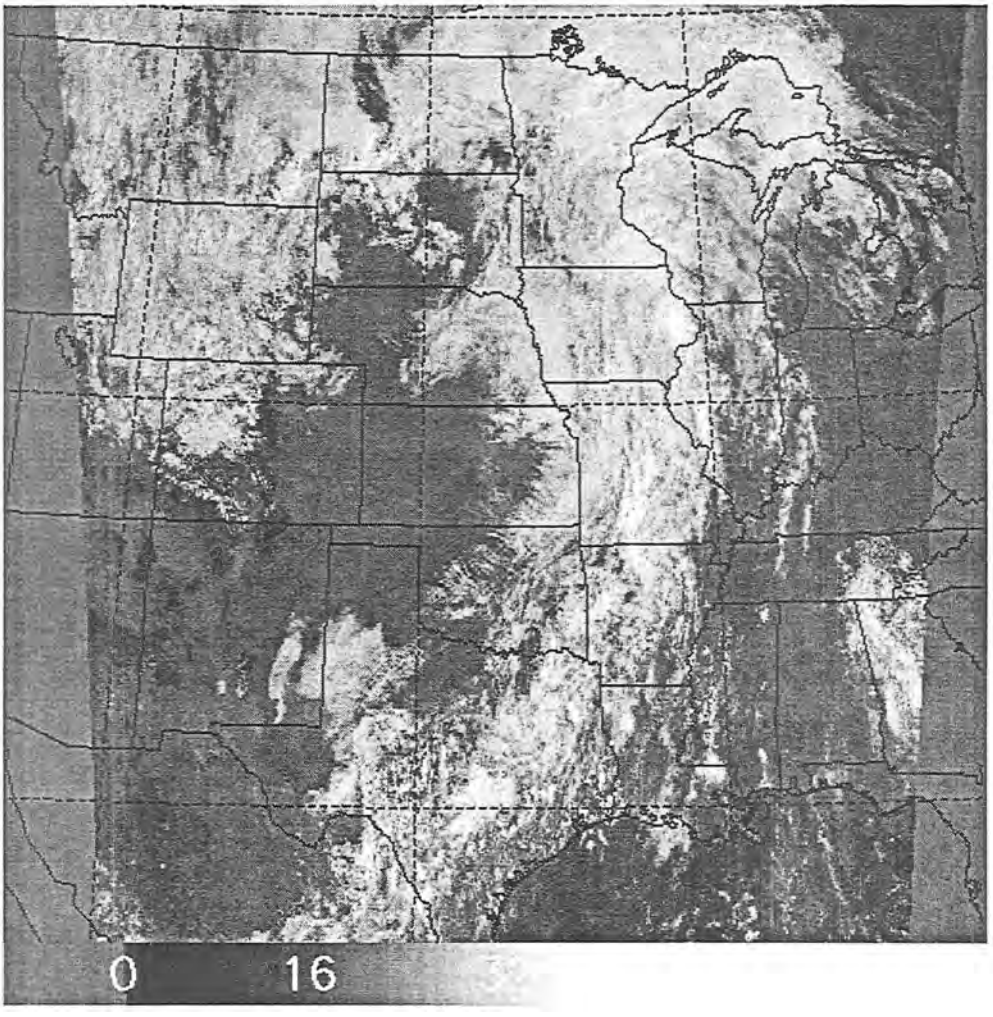

Figure 4.18: Same as Figure 4.17, except for the GOES VISSR visible imagery. Values displayed are in terms of raw 6-bit count values.

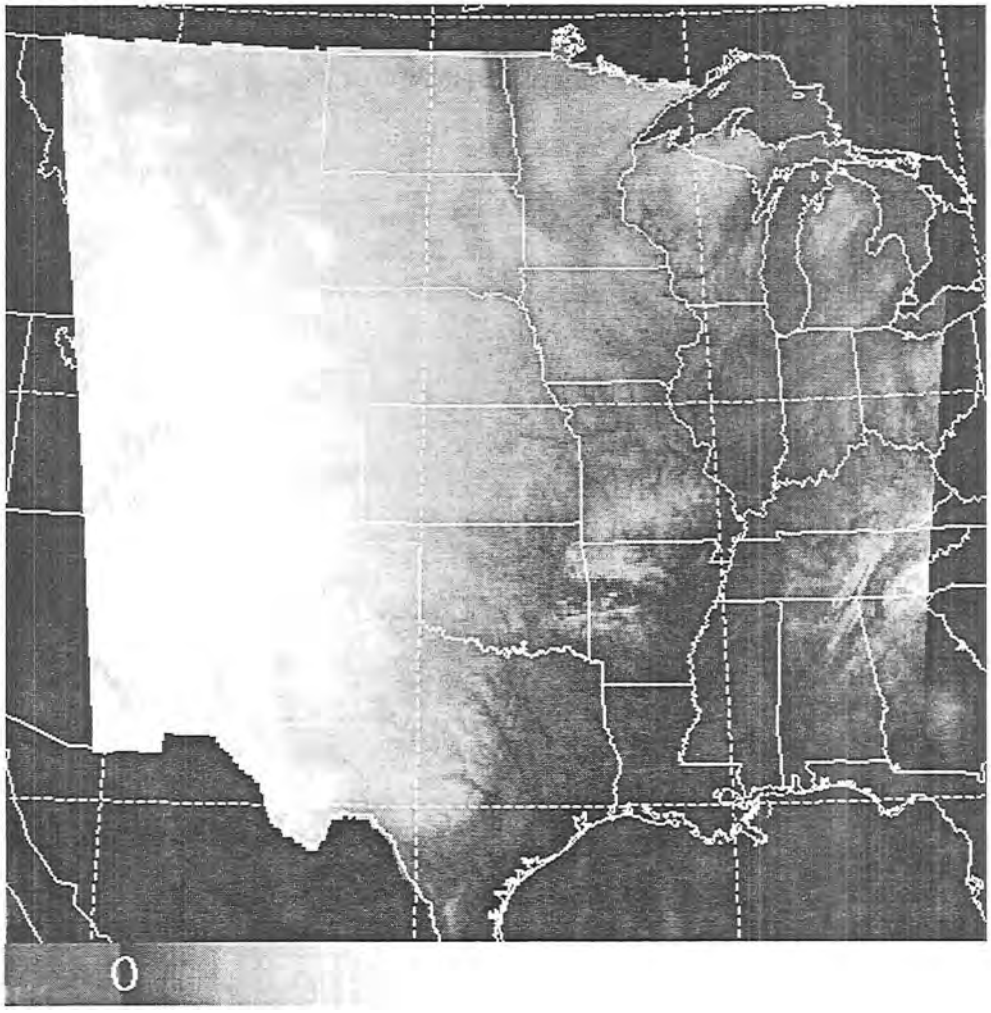

Figure 4.19: NGDC DEM Database merged to the GOES VISSR infrared projection space shown in Figure 4.17. Heights are in meters.

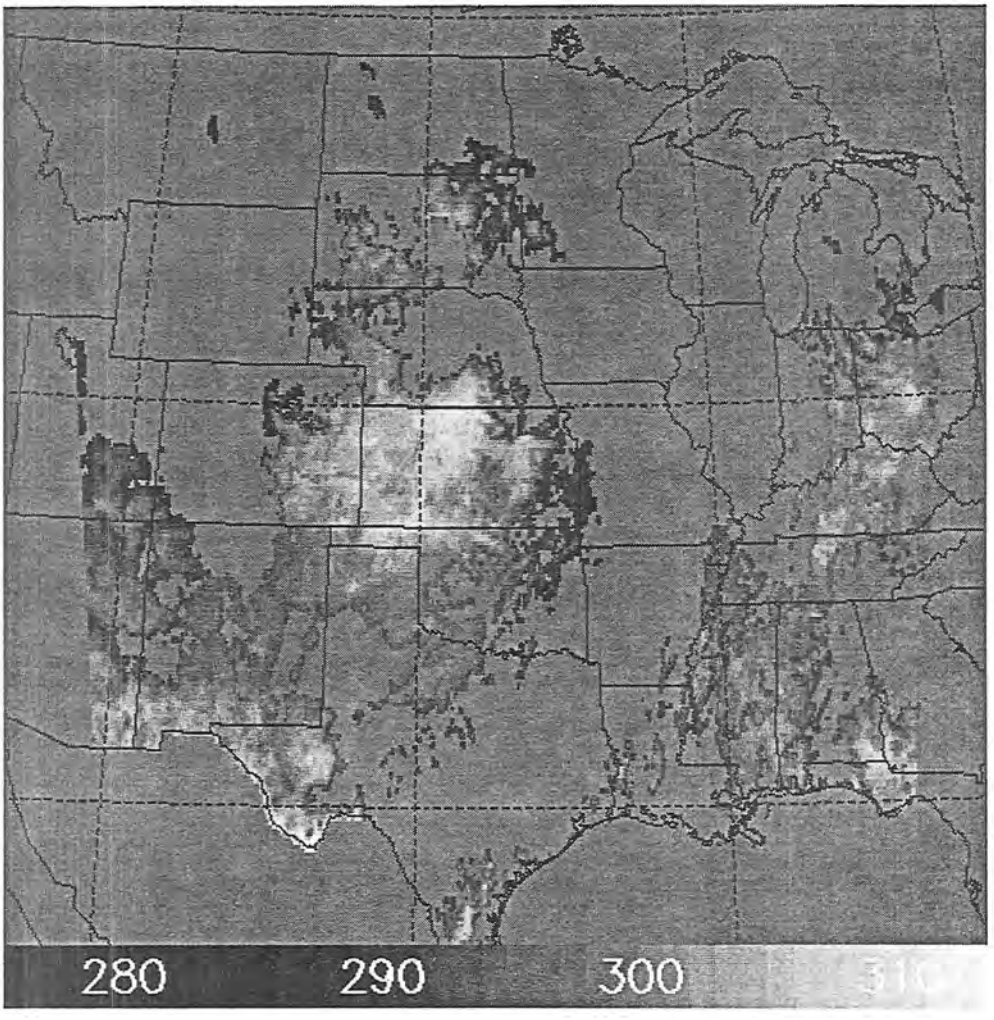

Figure 4.20: Same as Figure 4.17, except for surface skin temperature retrieval (K) for clear-sky regions.

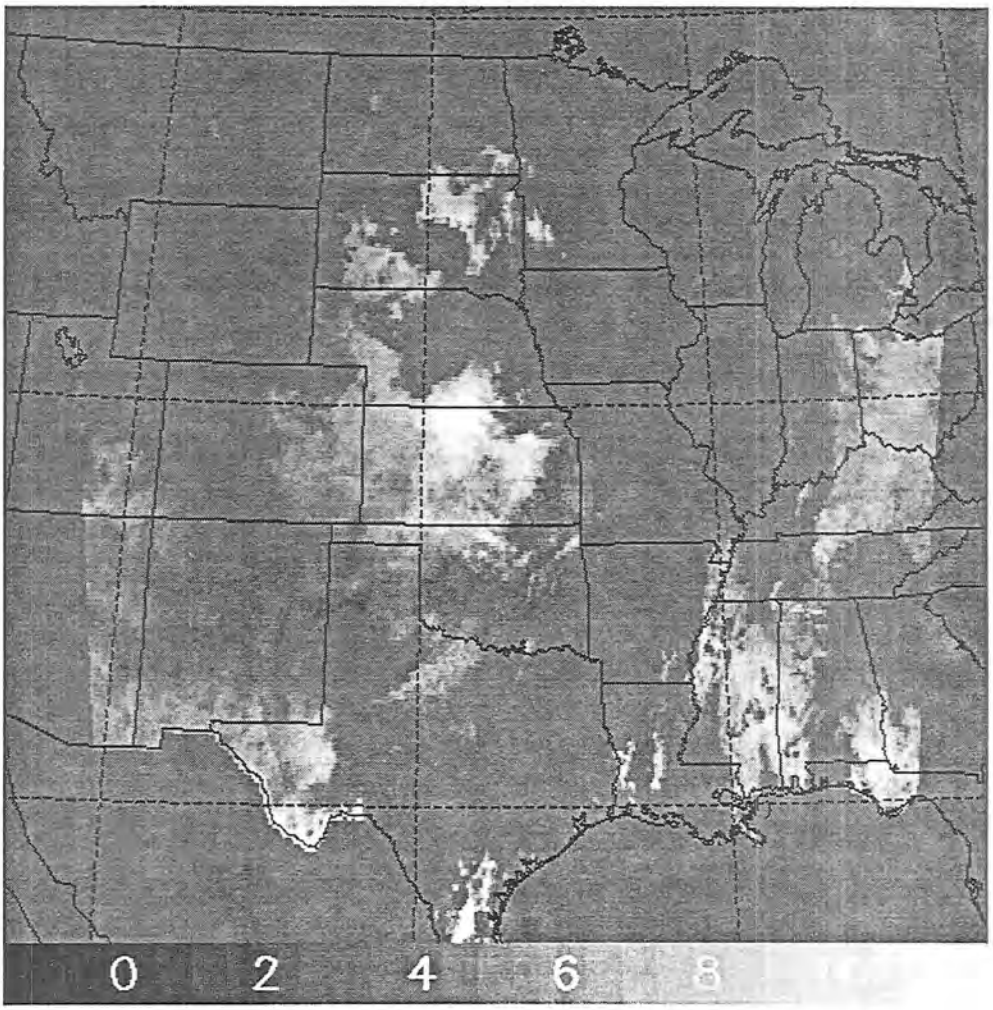

Figure 4.21: Same as Figure 4.17, except for the magnitude of the atmospheric correction (K) applied during the surface skin temperature retrieval for clear-sky regions.

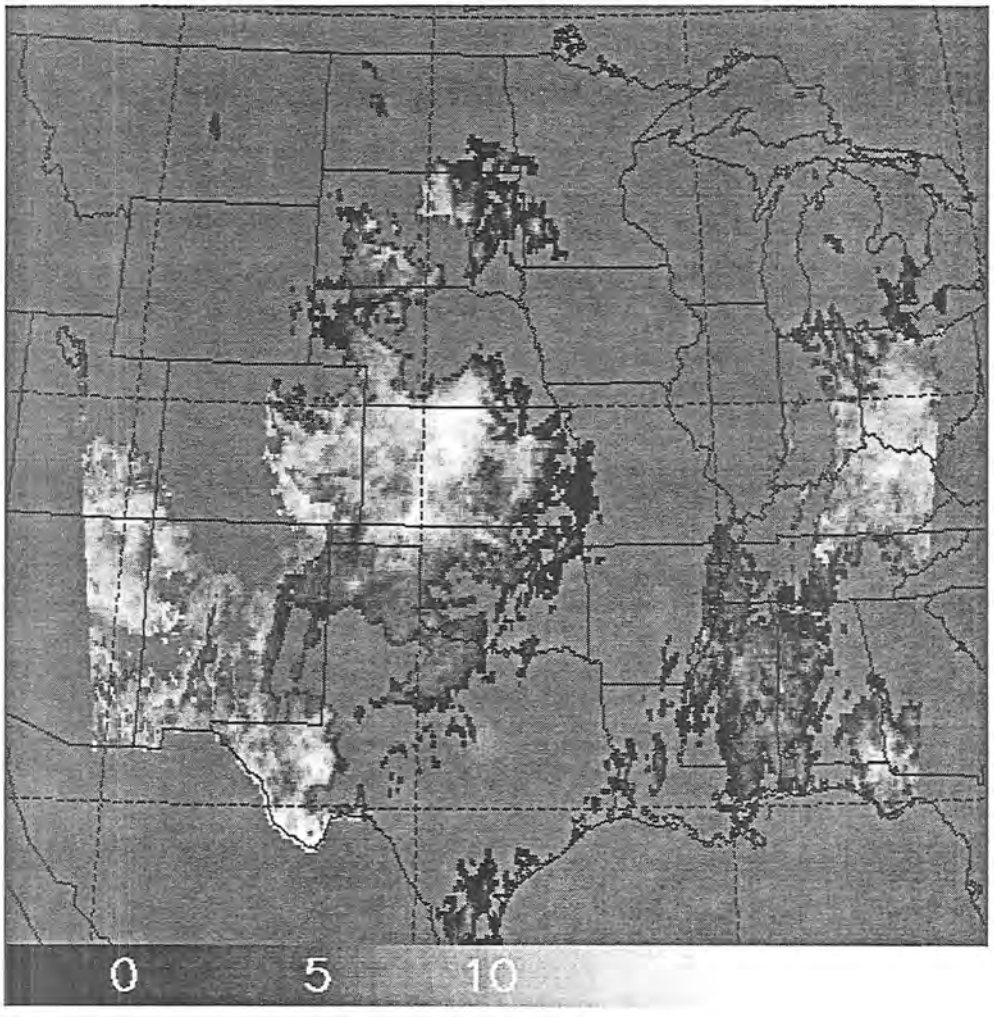

Figure 4.22: Same as Figure 4.17, except for the temperature difference (K) between the retrieved surface skin temperature for clear-sky regions and the surface level of the interpolated atmospheric sounding air temperatures (12 UTC).

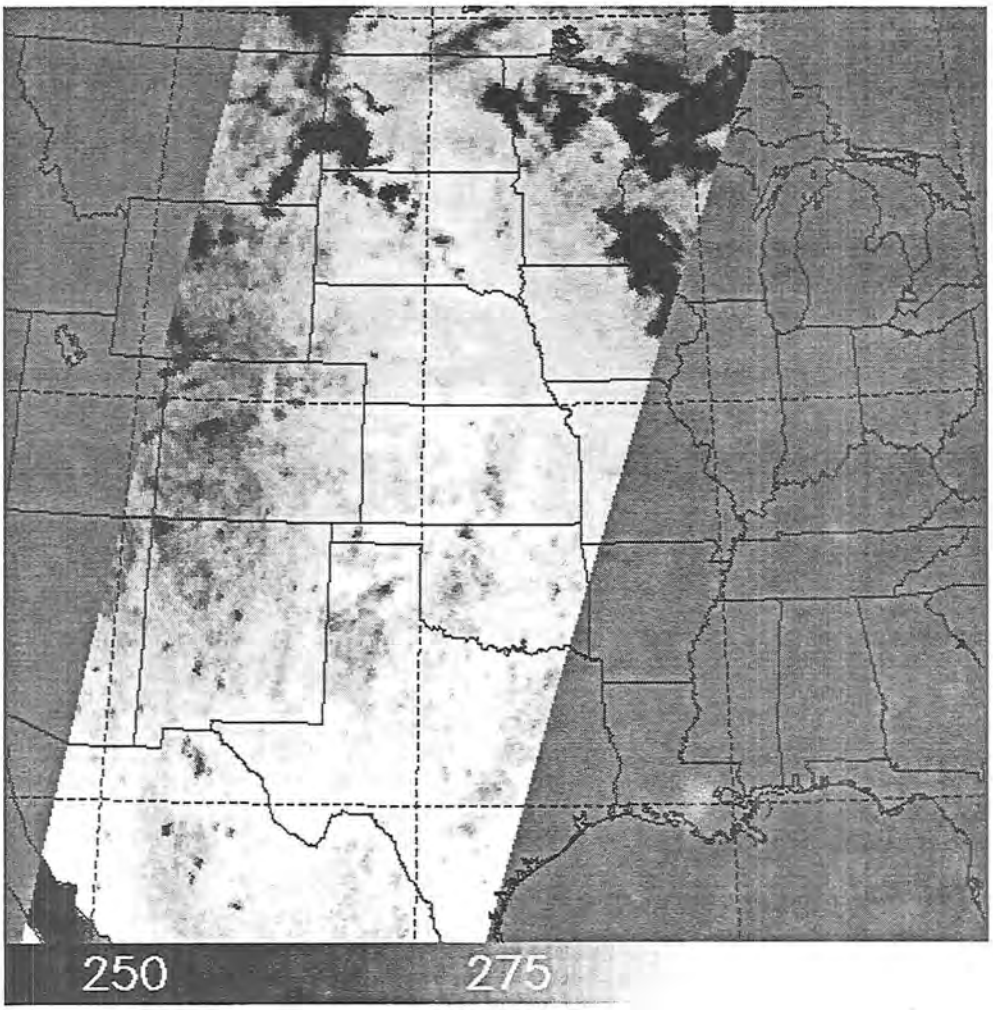

Figure 4.23: DMSP F-10 SSM/I 85.5H GHz microwave brightness temperature (K) for 1525-1534 UTC 8 September 1991.

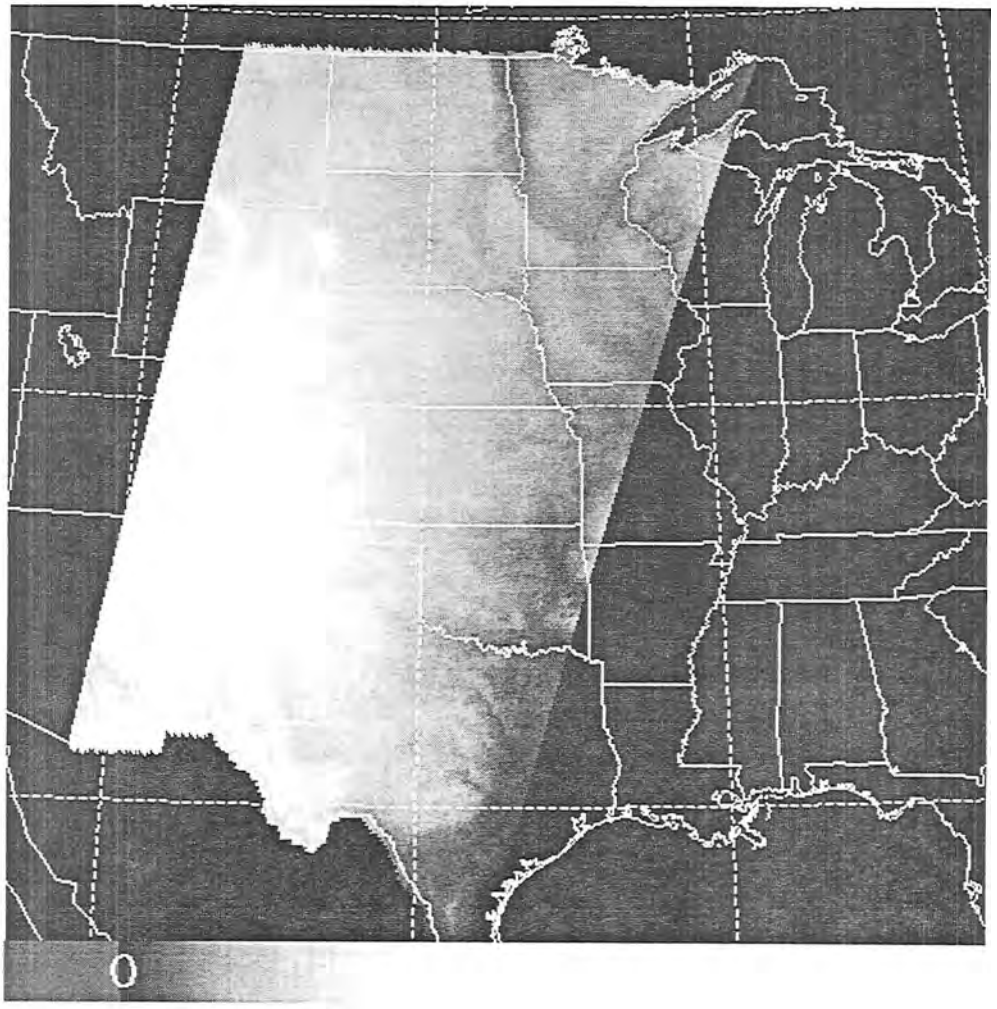

Figure 4.24: NGDC DEM Database merged to the DMSP F-10 SSM/I projection space shown in Figure 4.23. Heights are in meters.

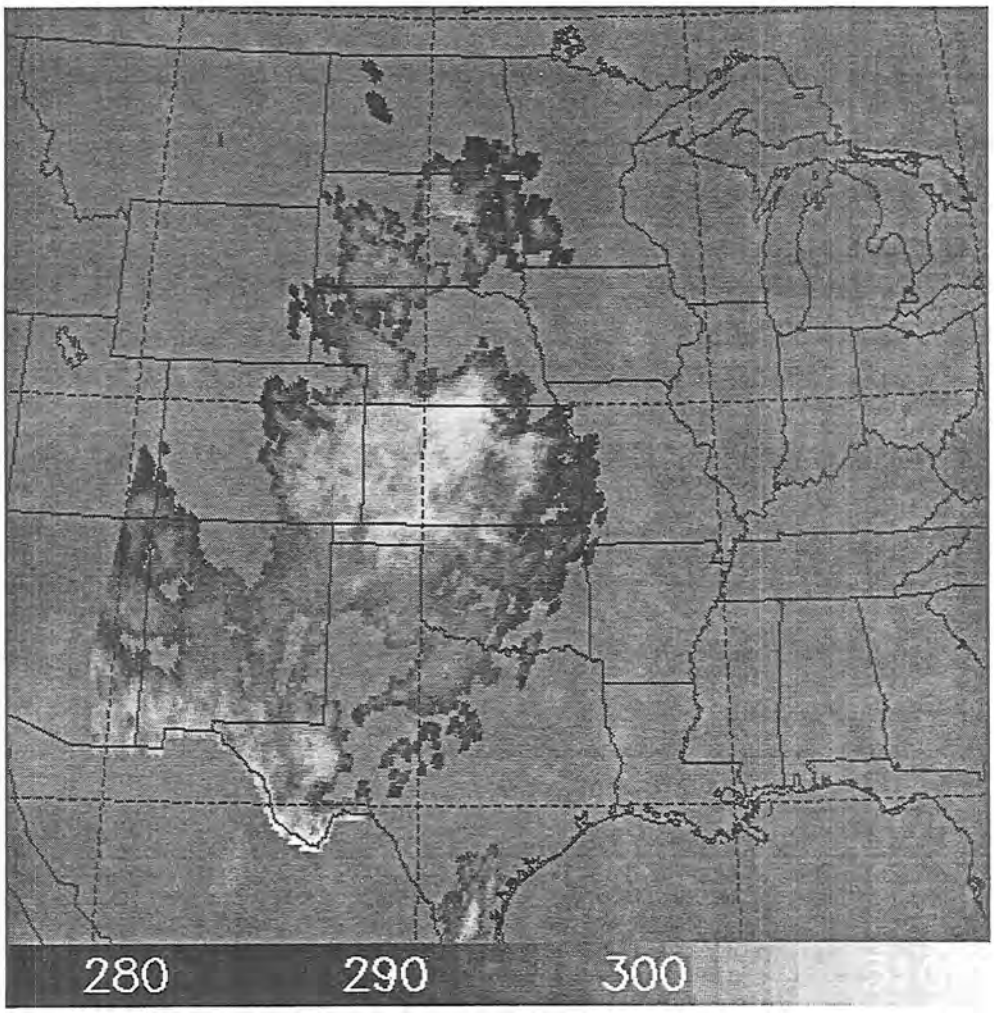

Figure 4.25: Surface skin temperature retrieval (K) for clear-sky regions merged to the DMSP F-10 projection space shown in Figure 4.23.

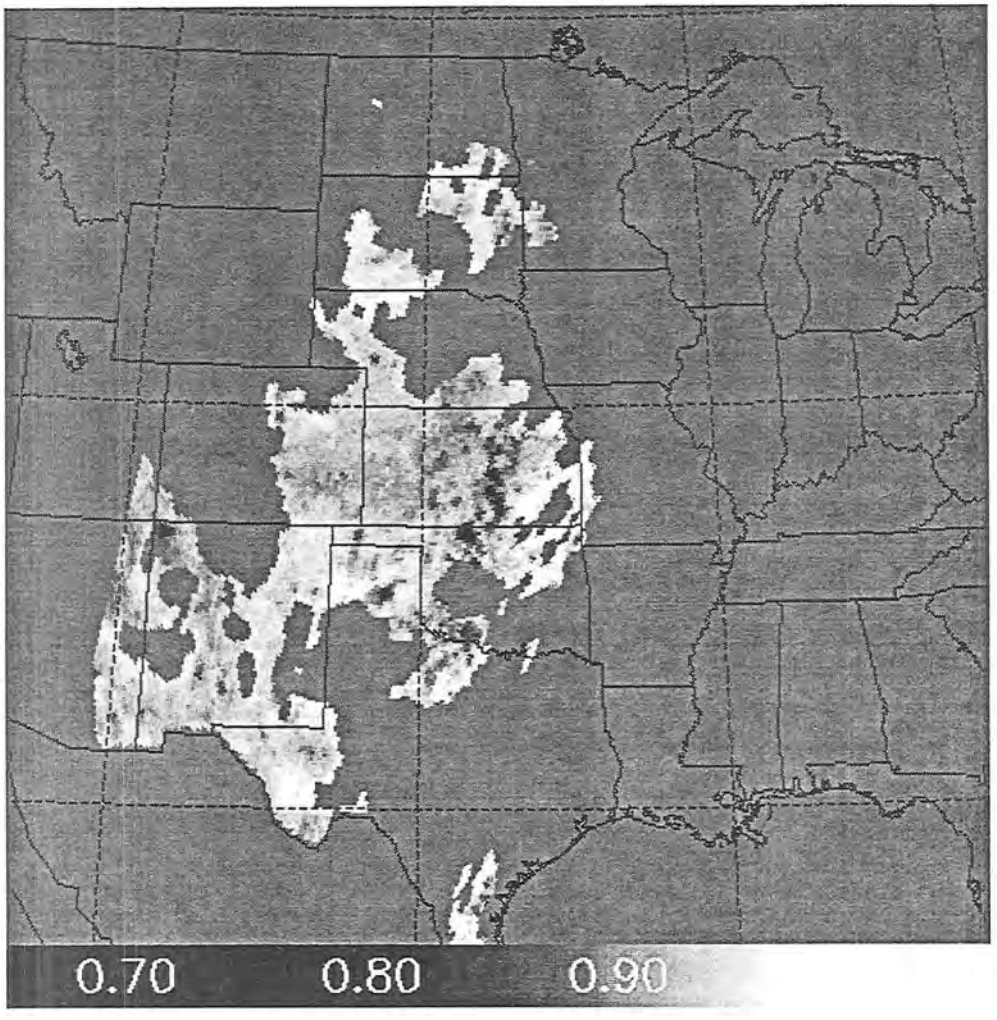

Figure 4.26: Same as Figure 4.23, except for retrieved 85.5H GHz surface emittance.

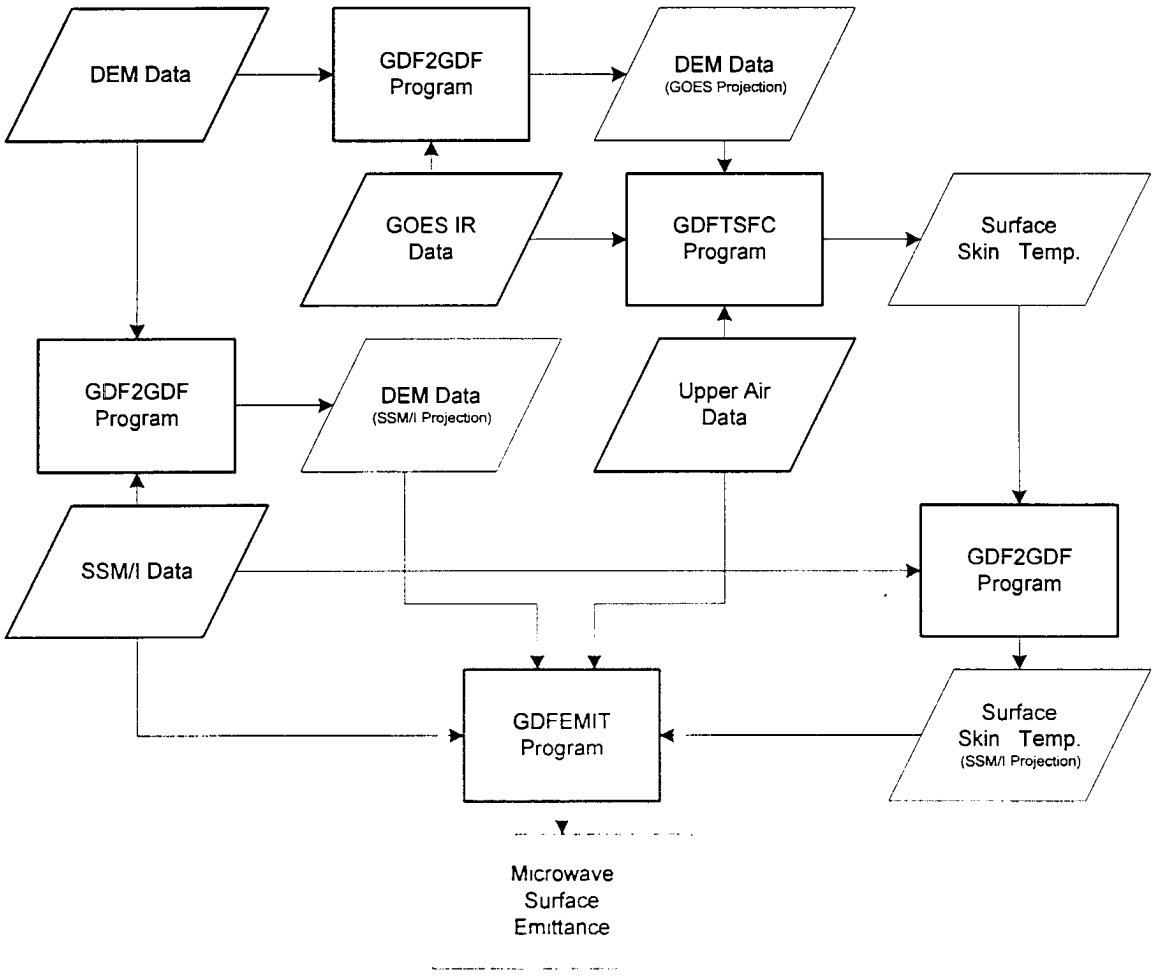

Figure 4.27: Flowchart of the microwave surface emittance retrieval method.

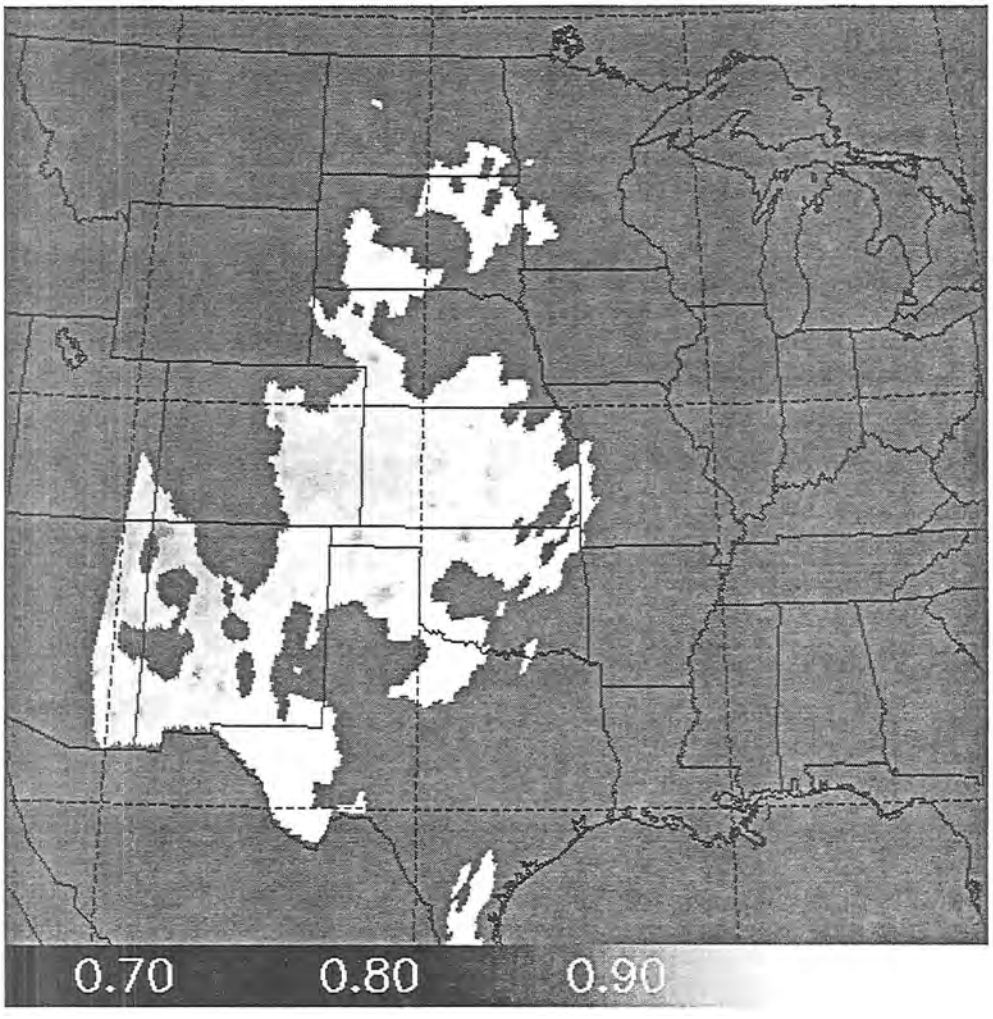

Figure 4.28: Same as Figure 4.23, except for 85.5H GHz surface emittance calculated without applying infrared and microwave atmospheric corrections.

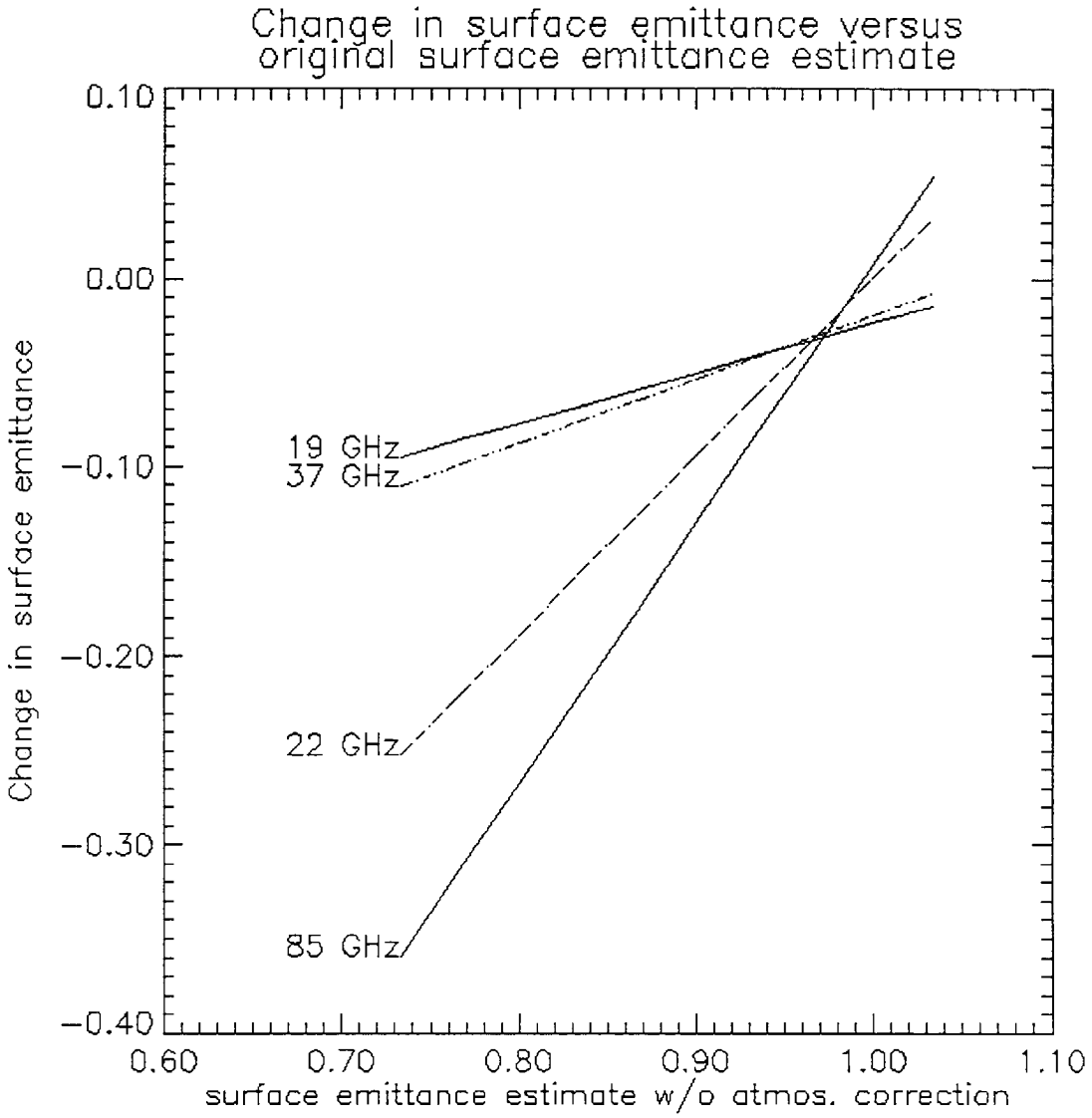

Figure 4.29: Change in the surface emittance versus the effective surface emittance estimate using a standard midlatitude summer sounding.

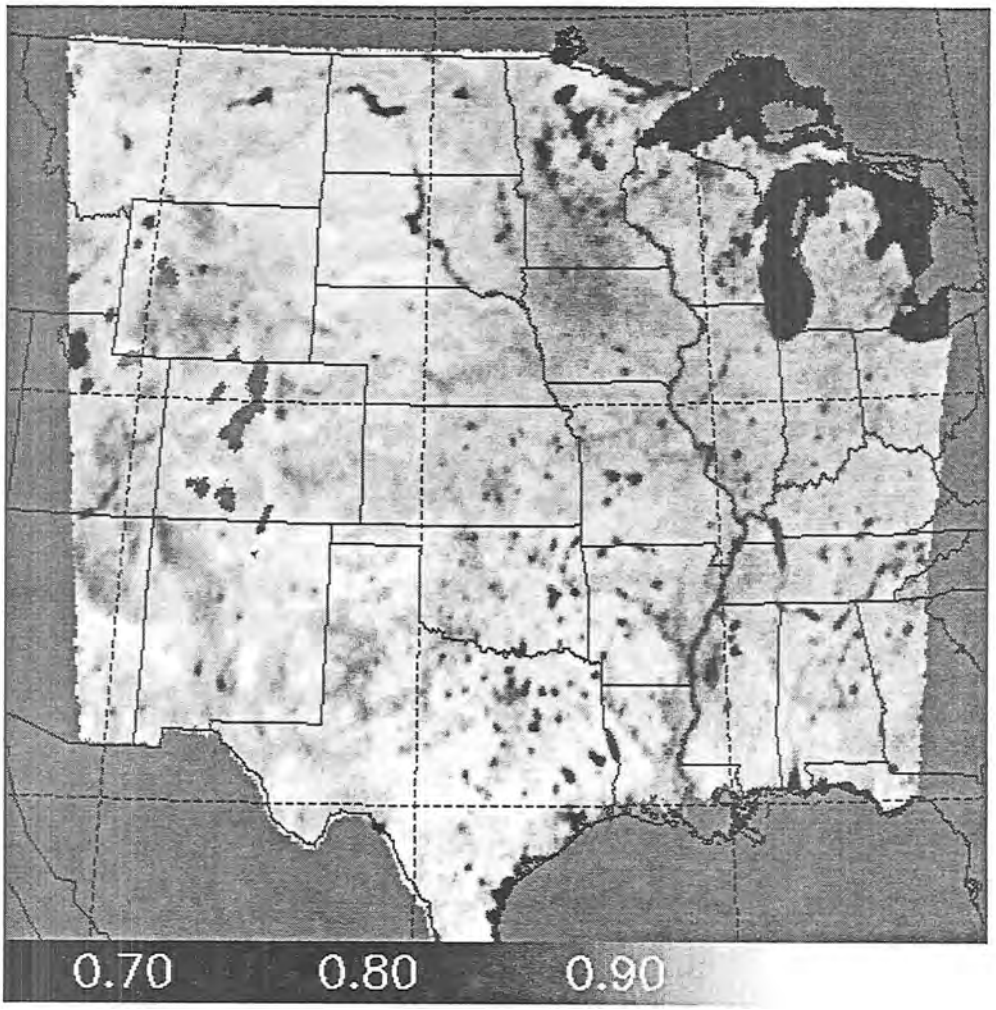

Figure 4.30: Composite mean 85.5H GHz surface emittance derived using DMSP F-10 SSM/I data for 30 July - 7 October 1991.

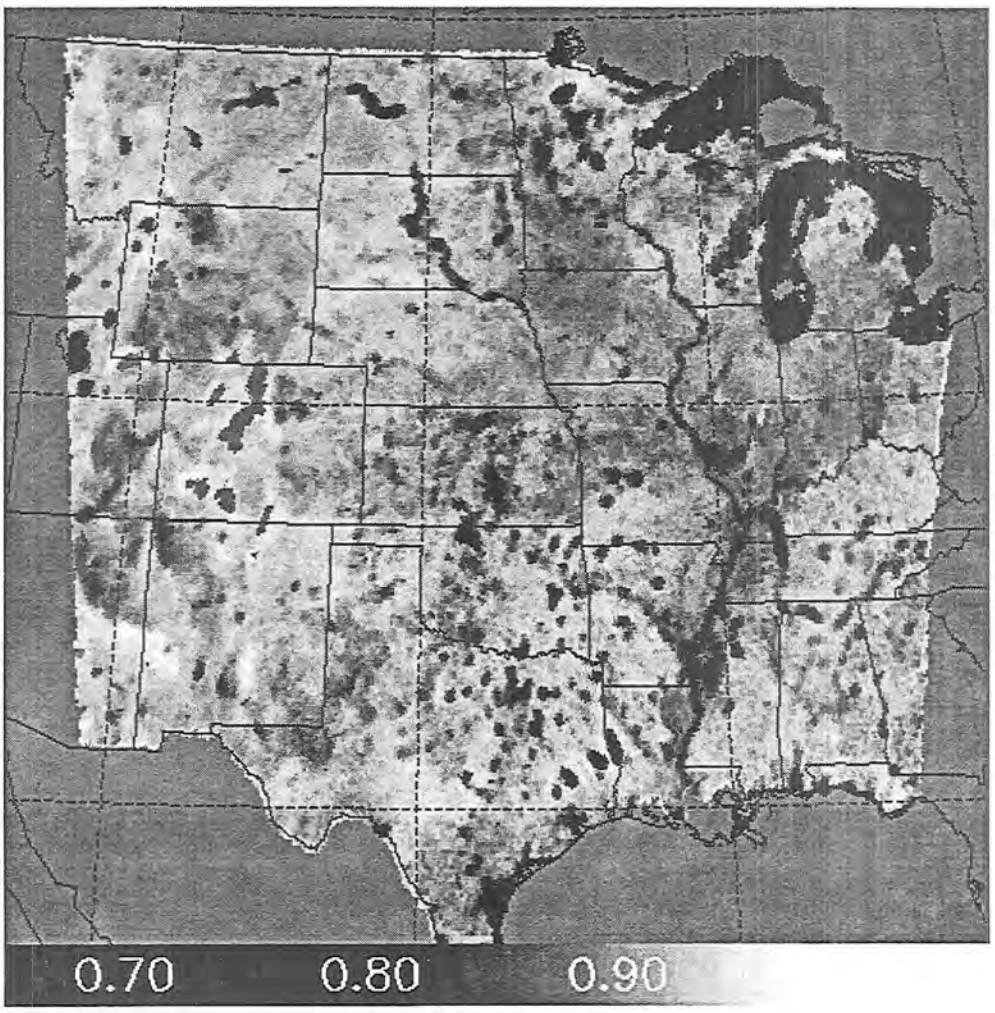

Figure 4.31: Same as Figure 4.30, except for the minimum composite 85.5H GHz surface emittance values.

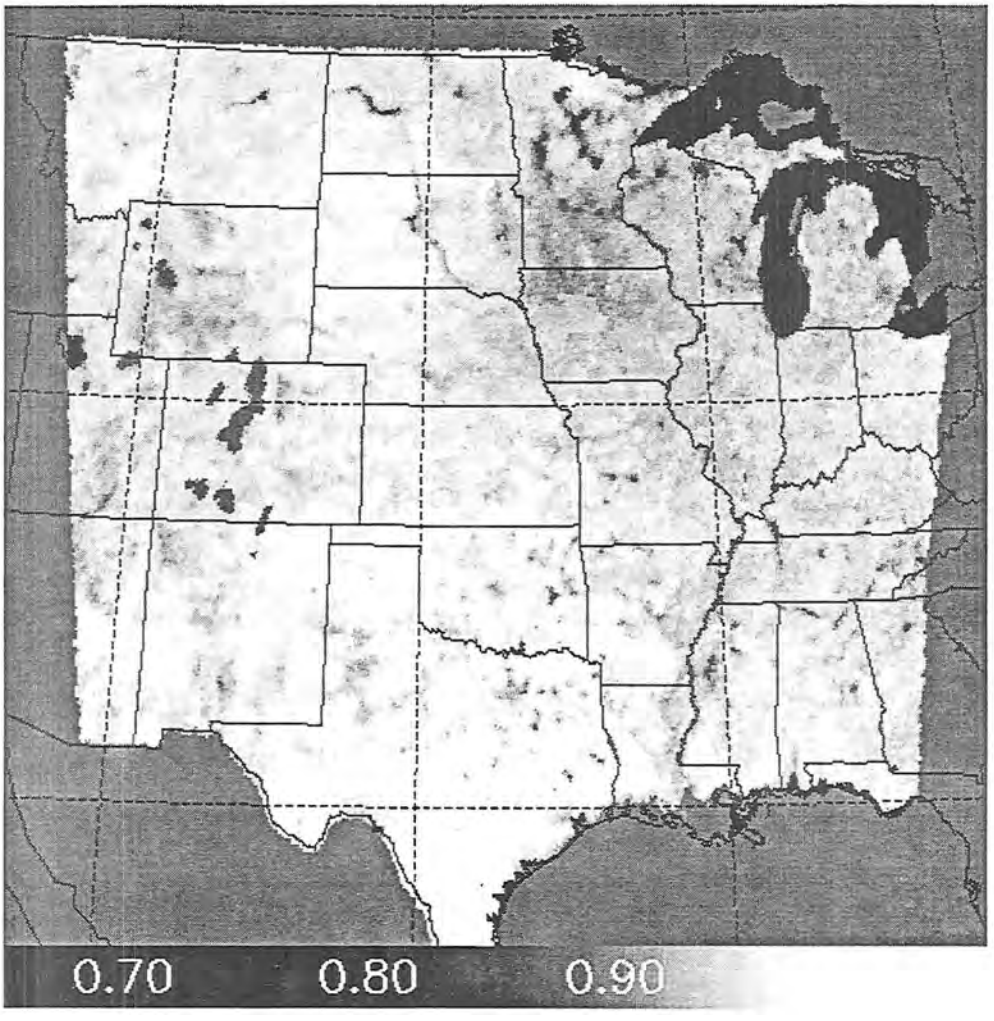

Figure 4.32: Same as Figure 4.30, except for the maximum composite 85.5H GHz surface emittance values.

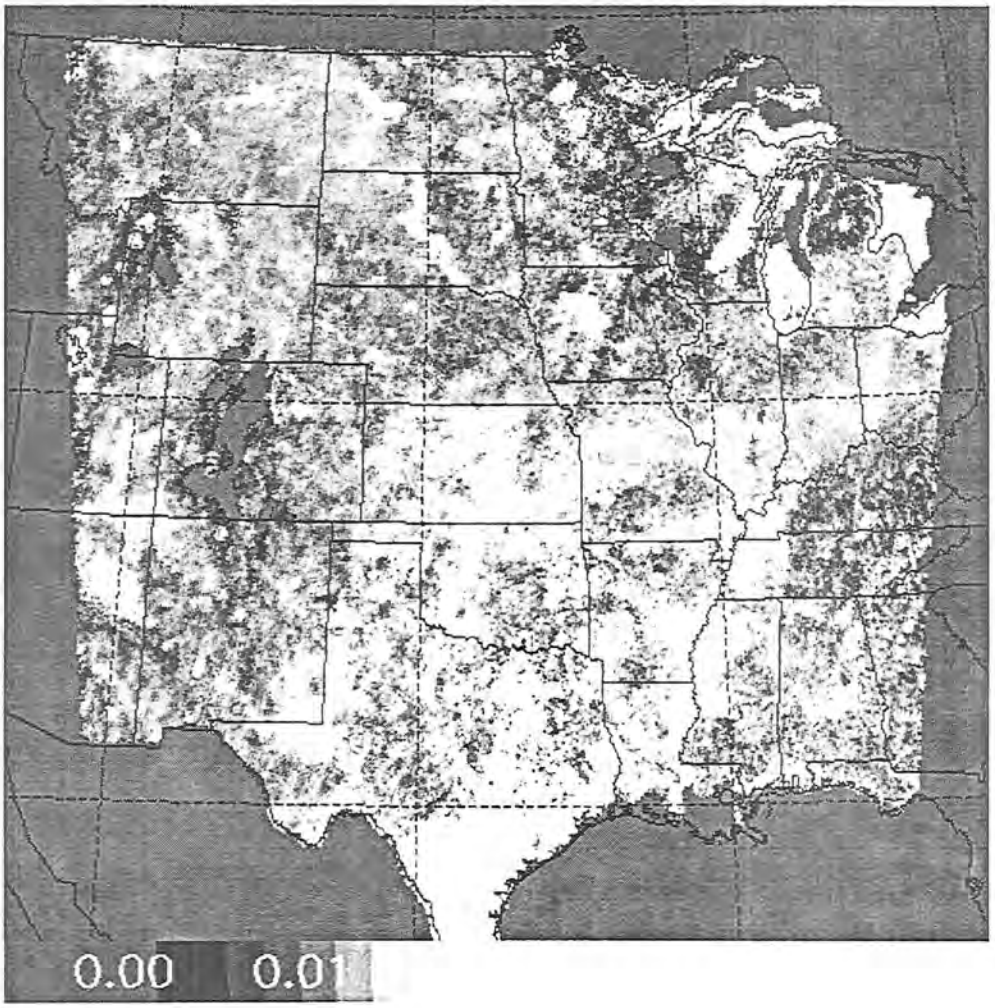

Figure 4.33: Same as Figure 4.30, except for the standard deviation of the composite 85.5H GHz surface emittance values.

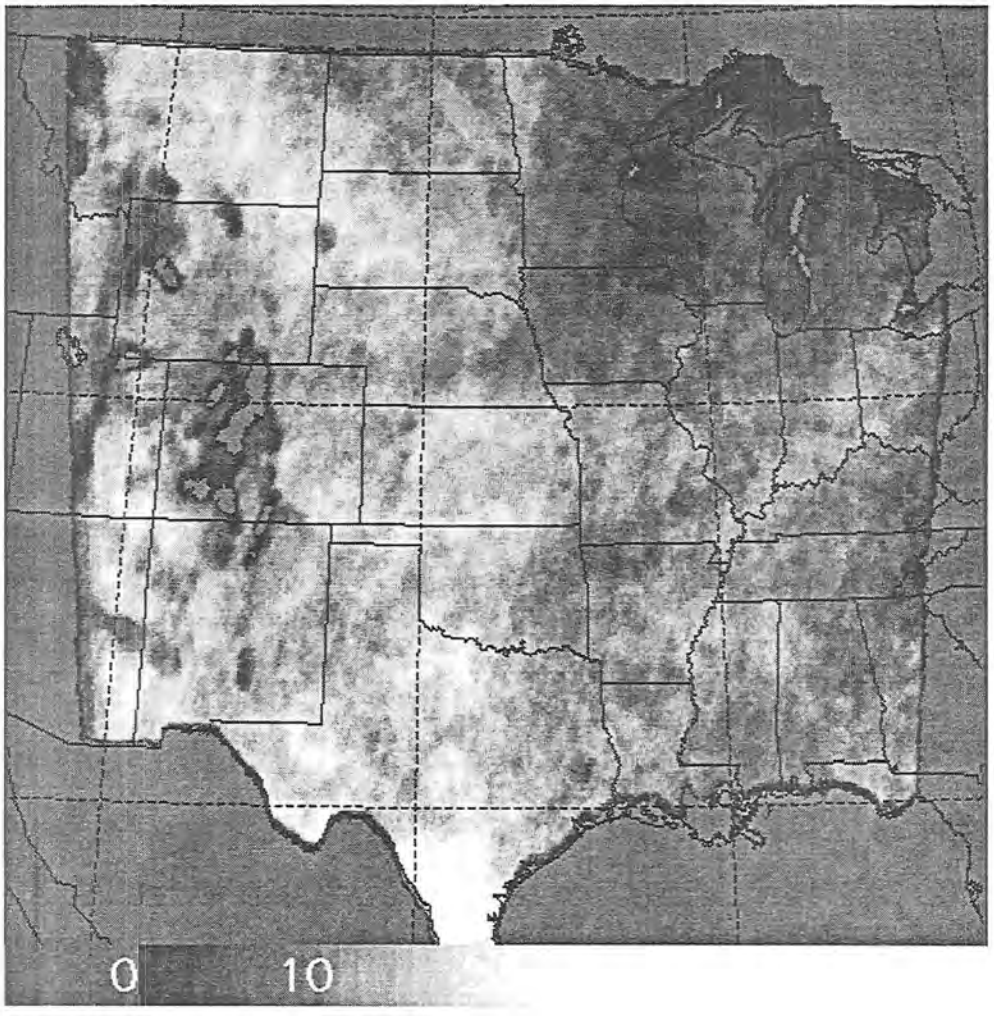

Figure 4.34: Same as Figure 4.30, except for the number of SSM/I data samples used in the 85.5H GHz surface emittance composites.

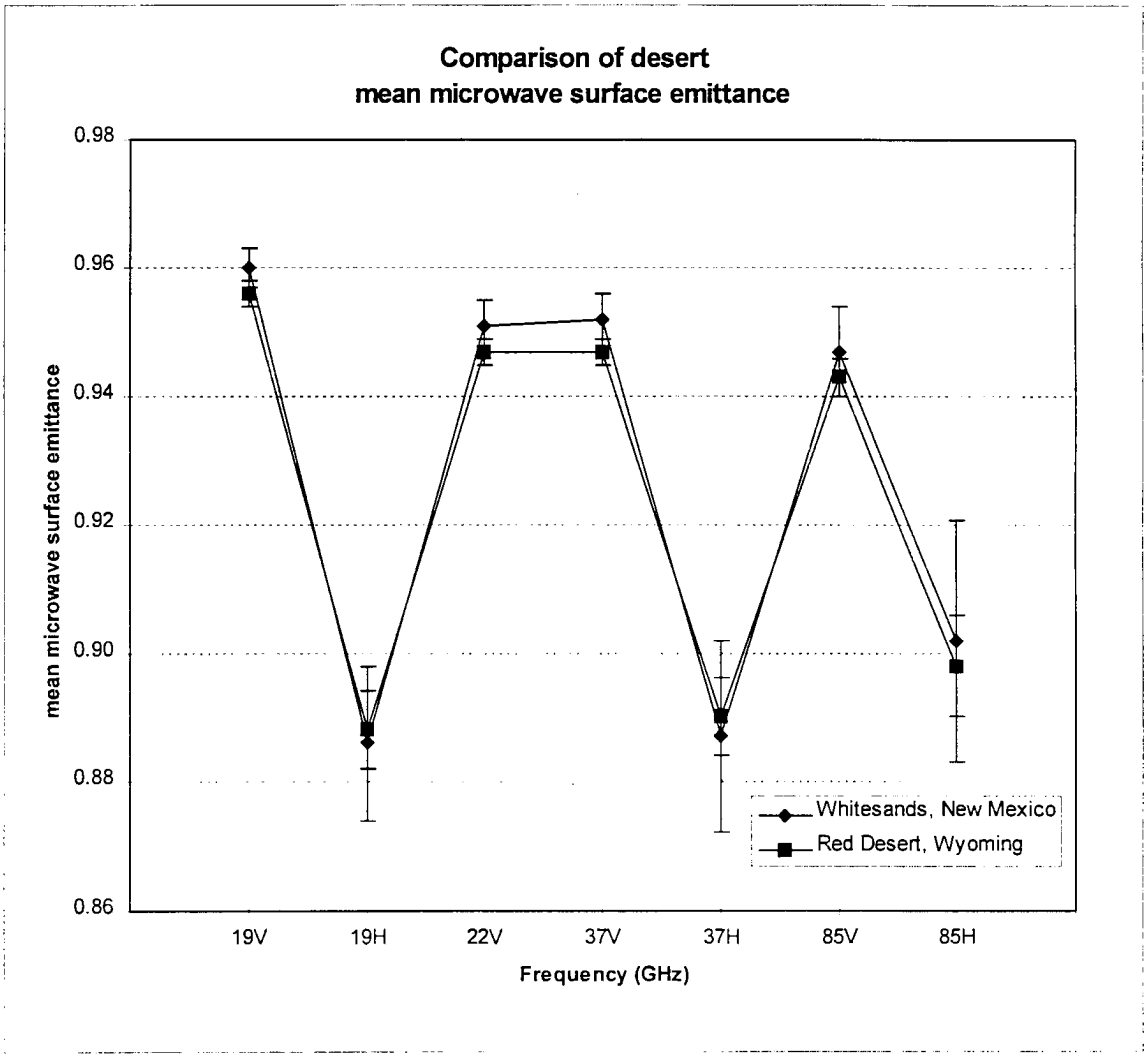

Figure 4.35: Comparison of desert mean microwave surface emittance for 30 July - 7 October 1991. The error bars indicate standard deviation values.

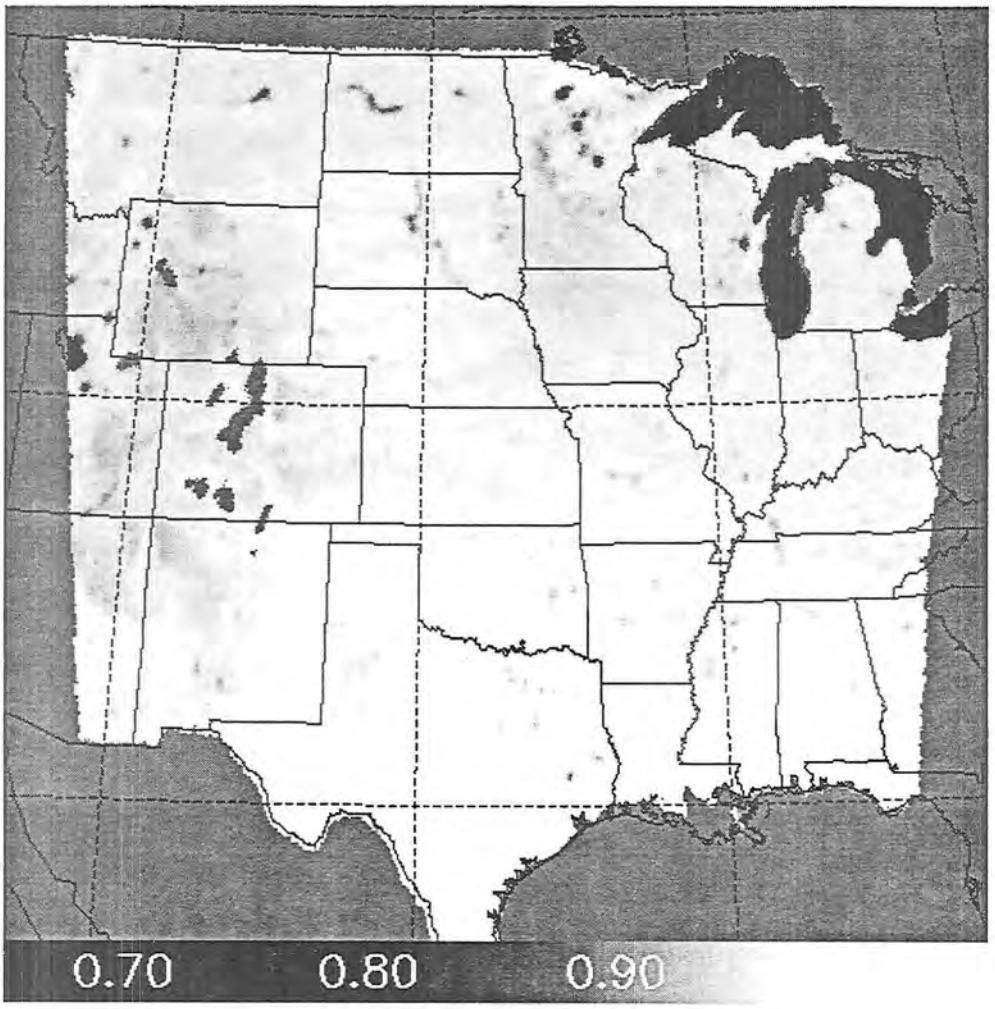

Figure 4.36: Same as Figure 4.30, except for composite mean 85.5 GHz effective surface emittance.

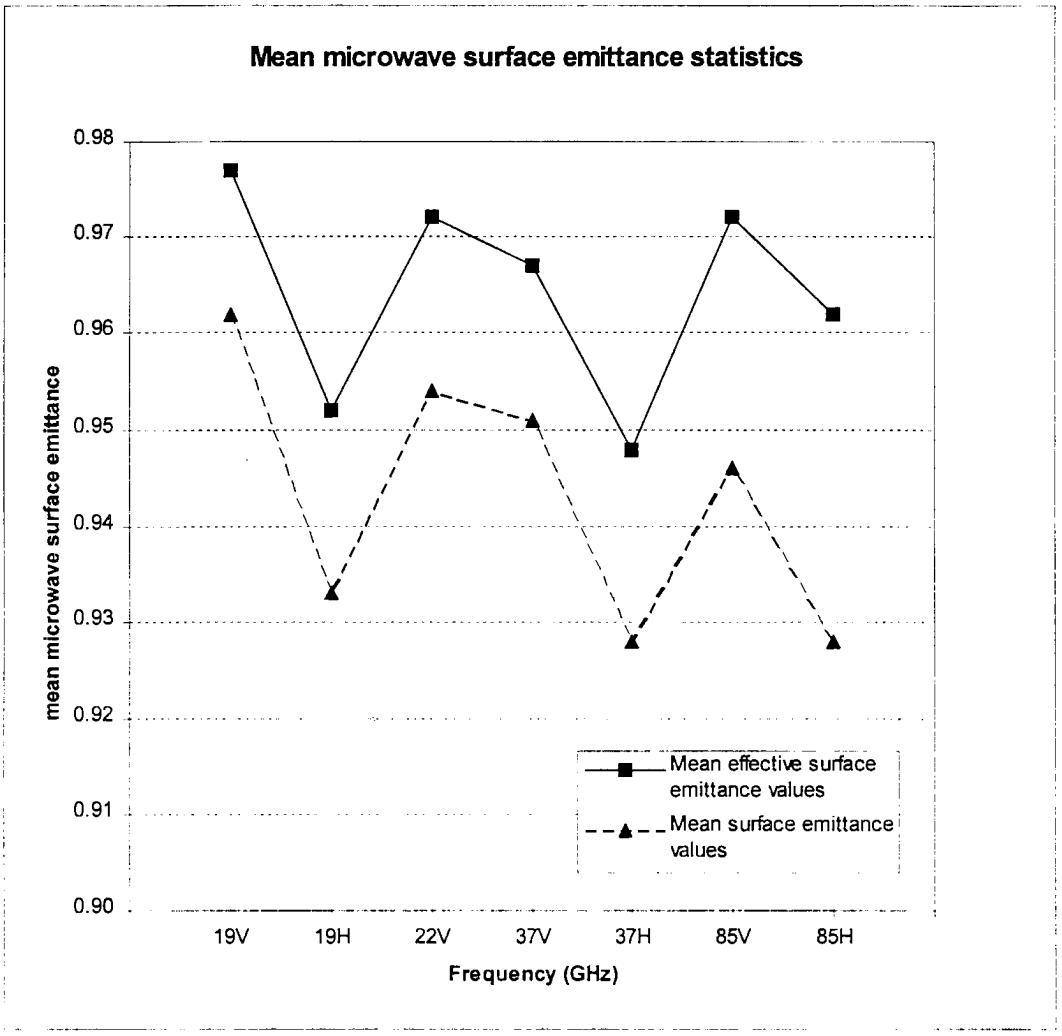

Figure 4.37: Mean microwave surface emittances for 30 July - 7 October 1991. The effective microwave surface emittance does not include an atmospheric correction.

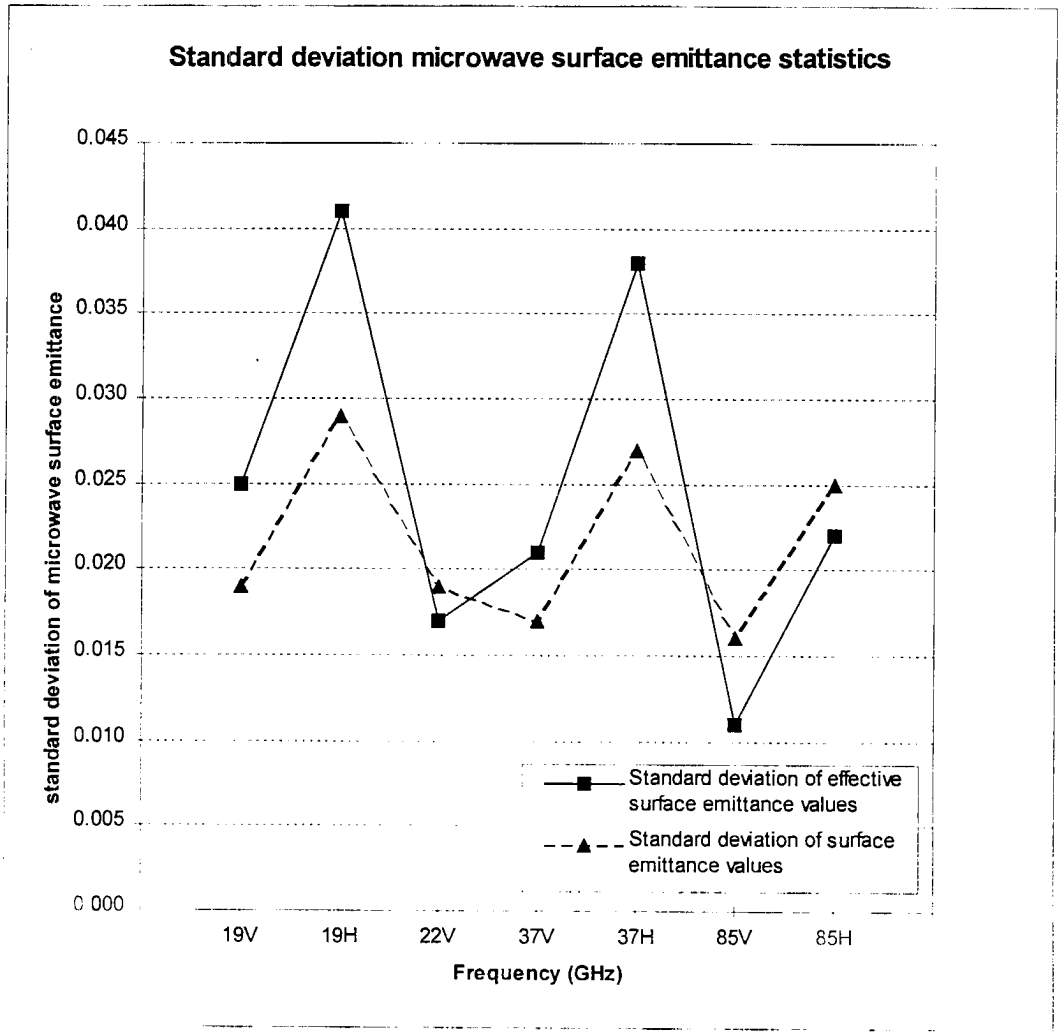

Figure 4.38: Same as Figure 4.37, except for the standard deviation of the microwave surface emittance.

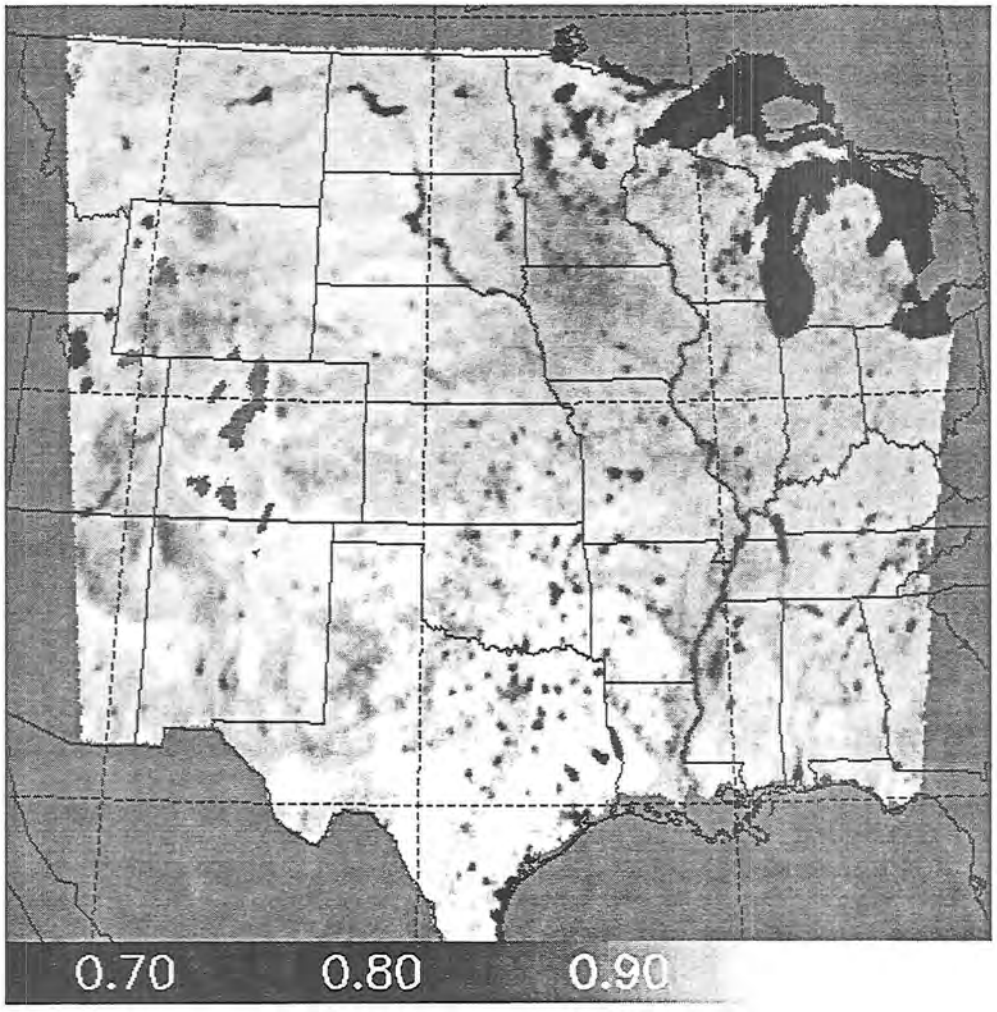

Figure 4.39: Composite mean 85.5H GHz surface emittance derived using morning overpasses (0600 - 1800 UTC) from DMSP F-10 SSM/I data for 30 July - 7 October 1991.

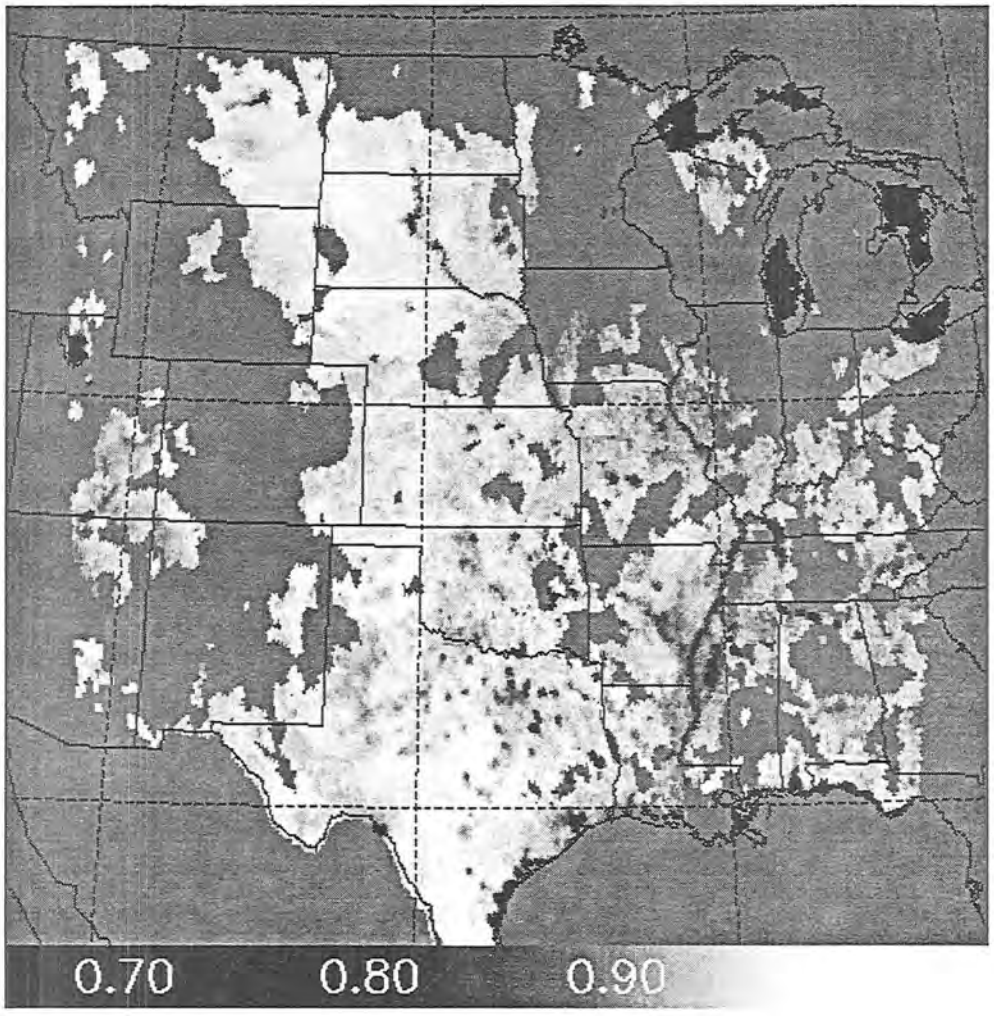

Figure 4.40: Same as Figure 4.39, except for afternoon overpasses (1800 - 0600 UTC).

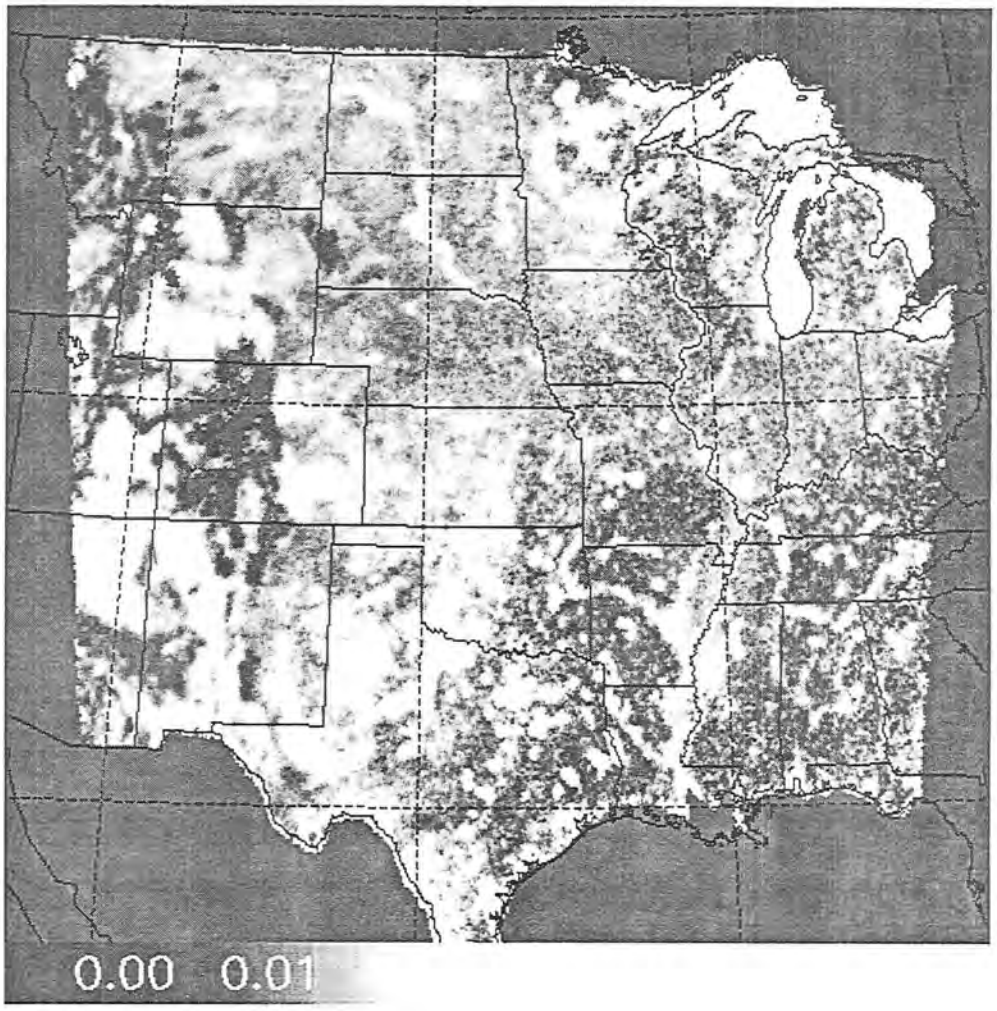

Figure 4.41: Composite mean 85.5 GHz surface emittance polarization difference (85V - 85H) derived using DMSP F-10 SSM/I data for 30 July - 7 October 1991.

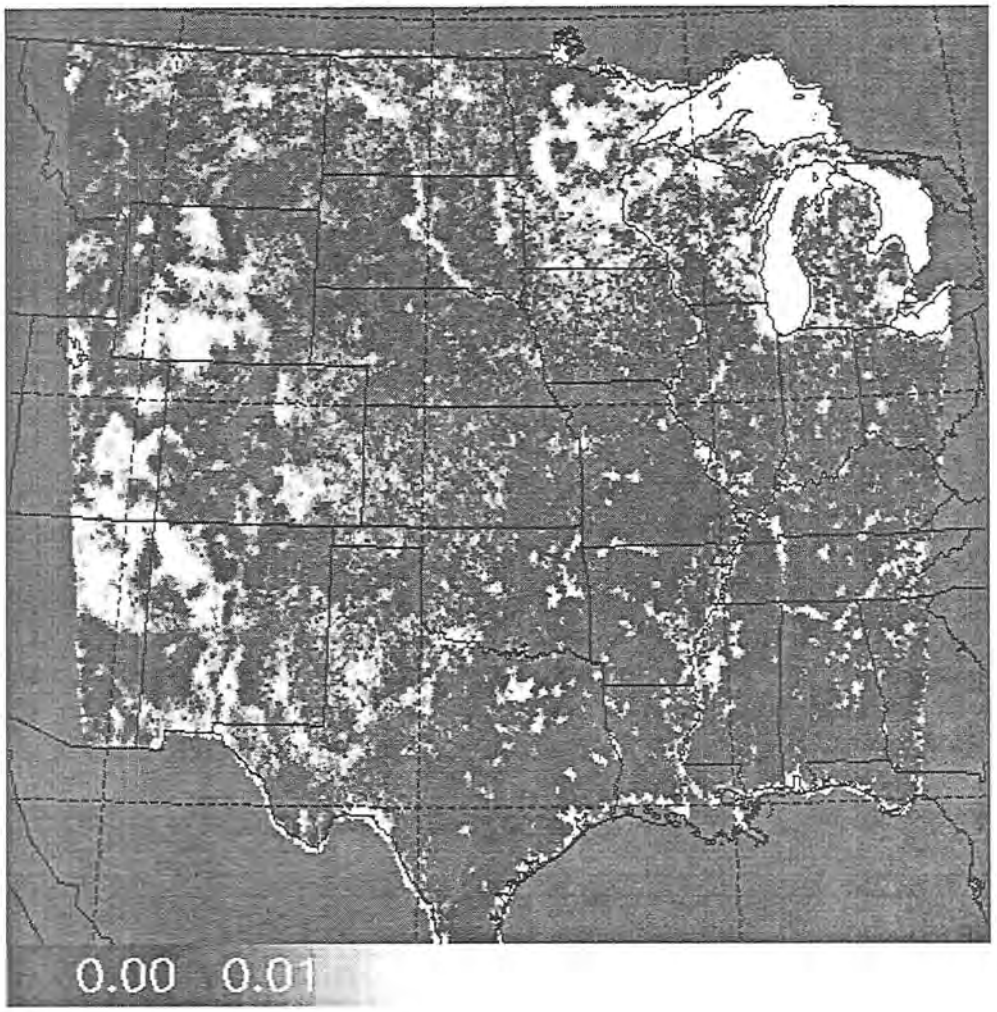

Figure 4.42: Same as Figure 4.41, except for the minimum 85.5 GHz surface emittance polarization difference values.

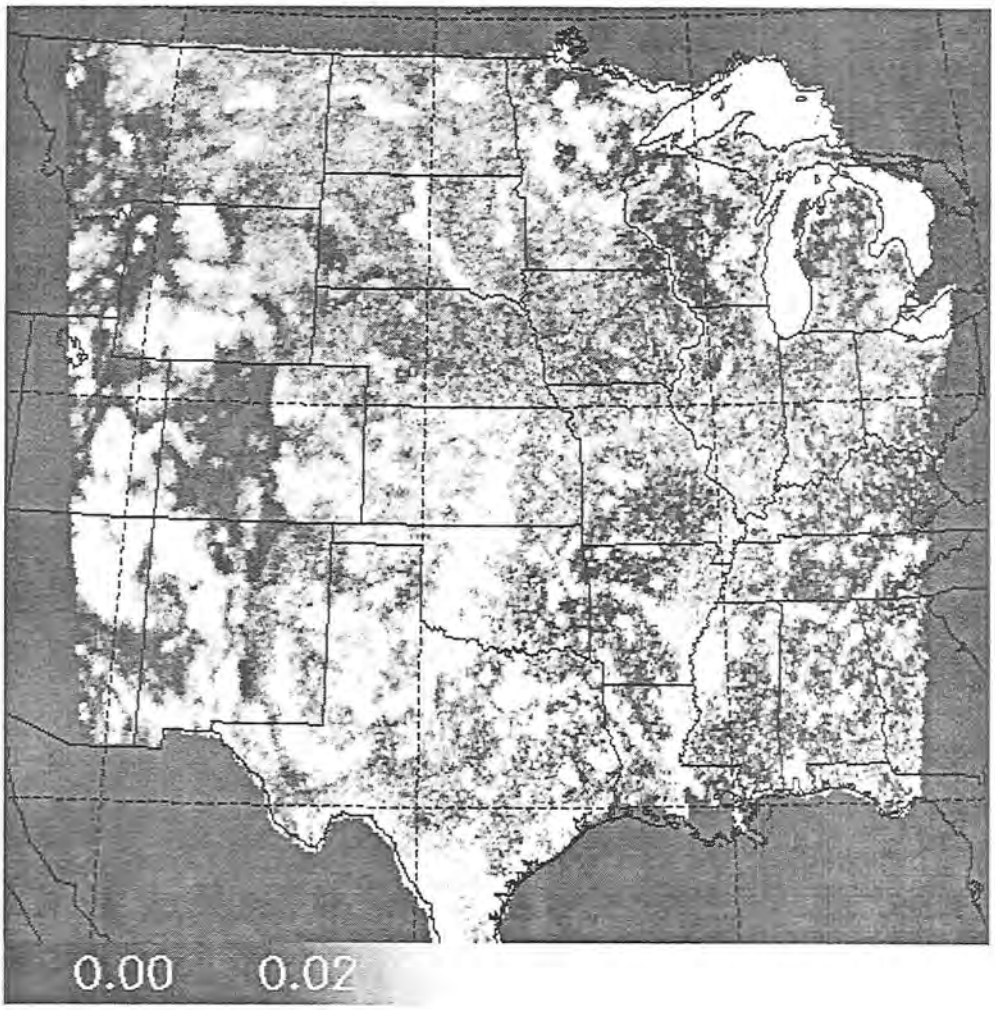

Figure 4.43 Same as Figure 4.41, except for the maximum 85.5 GHz surface emittance polarization difference values.

Figure 4.44 Same as Figure 4.41, except for the standard deviation of the 85.5 GHz surface emittance polarization difference values.

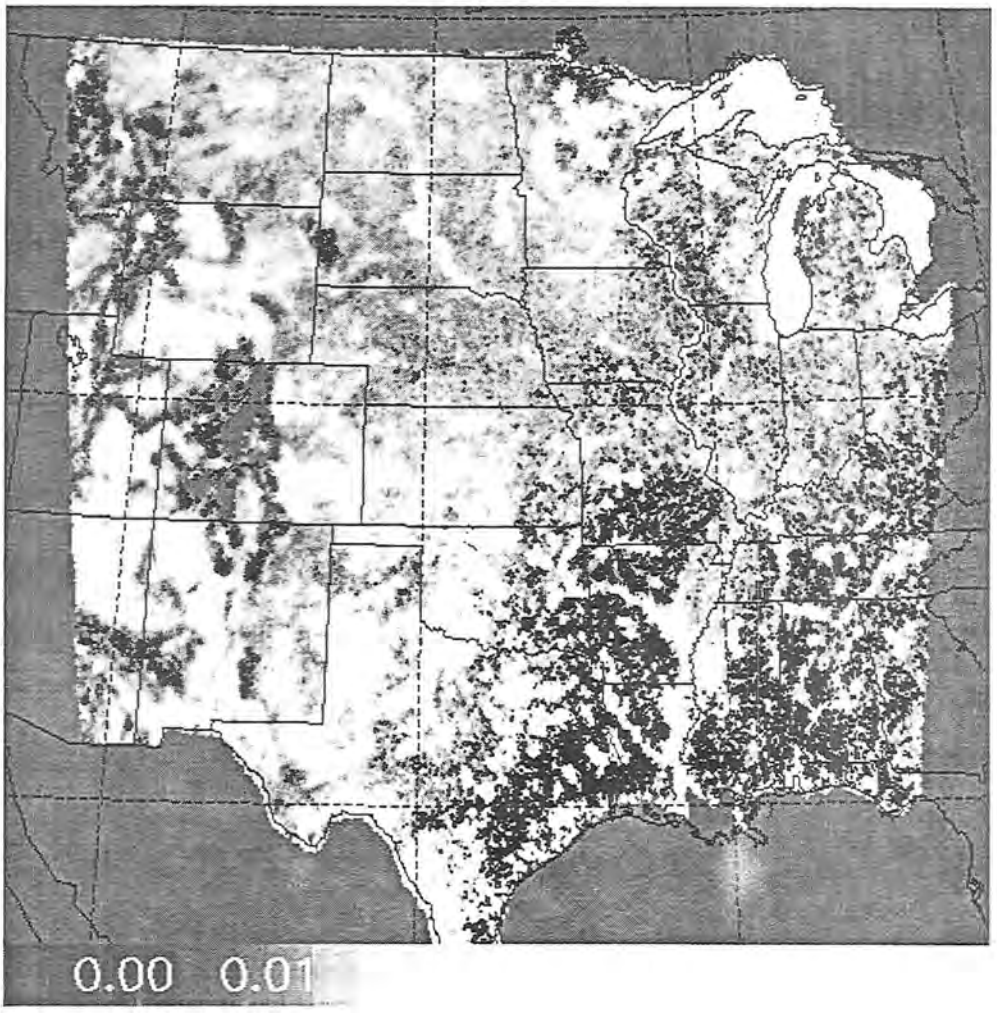

Figure 4.45 Same as Figure 4.41, except that mean 85.5 GHz surface emittance polarization difference values that are less than the measured standard deviation (see Figure 4.44) are shaded black. Values that remain are signals that are 1 standard deviation above the natural background variability.

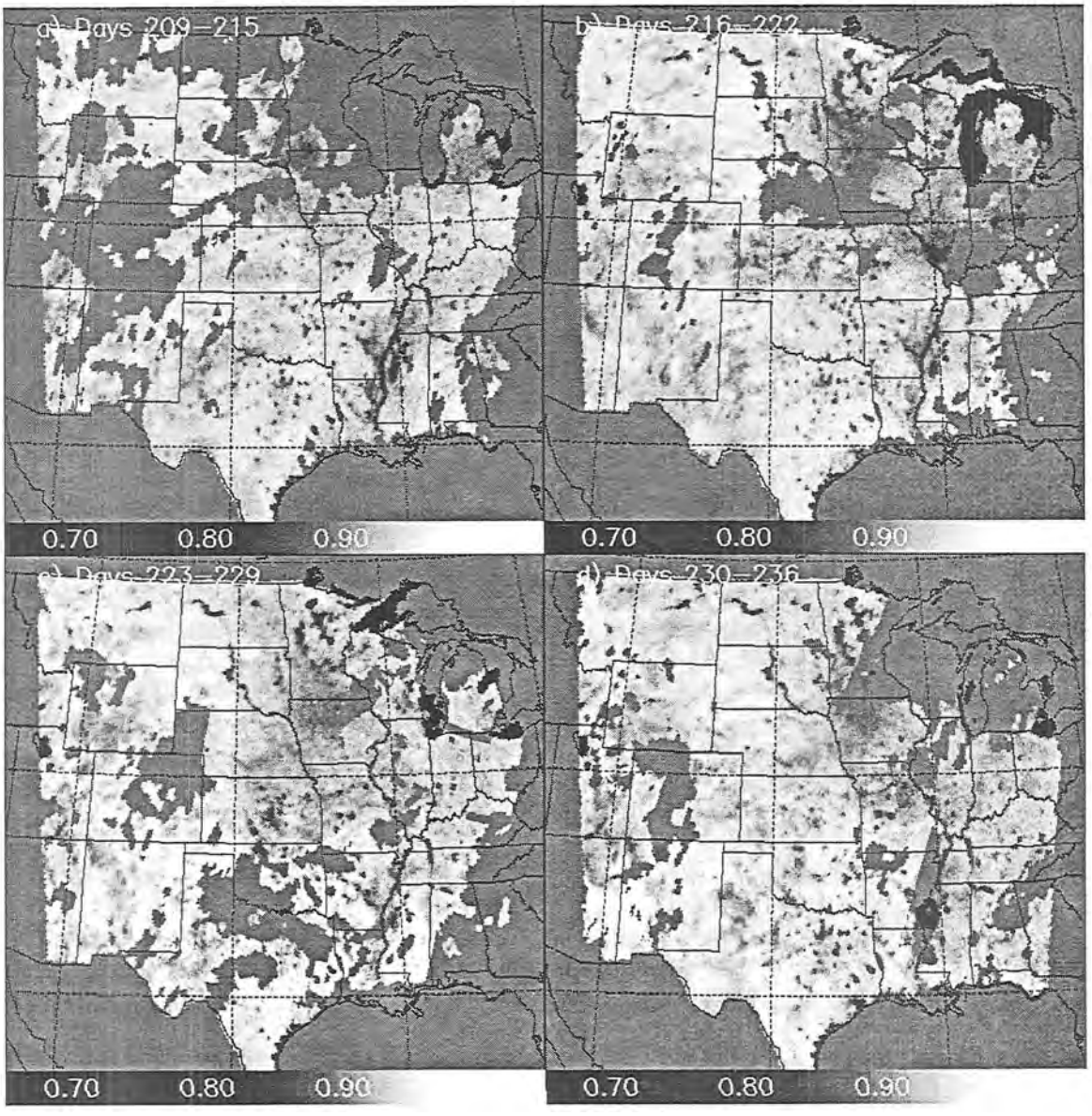

Figure 4.46: Weekly composite mean 85.5H GHz surface emittance derived using DMSP F-10 SSM/I data for Julian days a) 209-215, b) 216-222, c) 223-229, and d) 230-236.

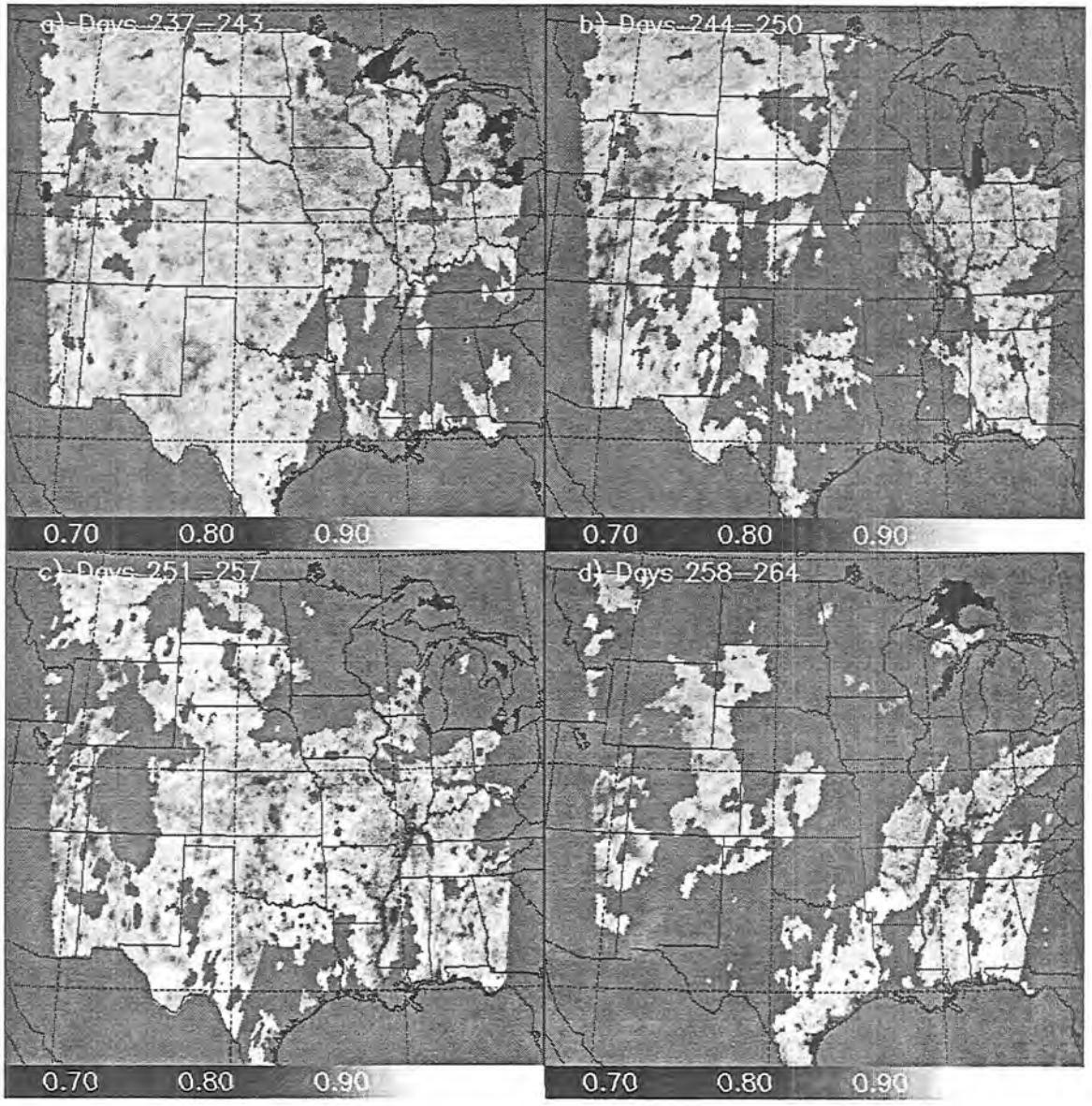

Figure 4.47: Same as Figure 4.46, except for days a) 237-243, b) 244-250, c) 251-257, d) 258-264.

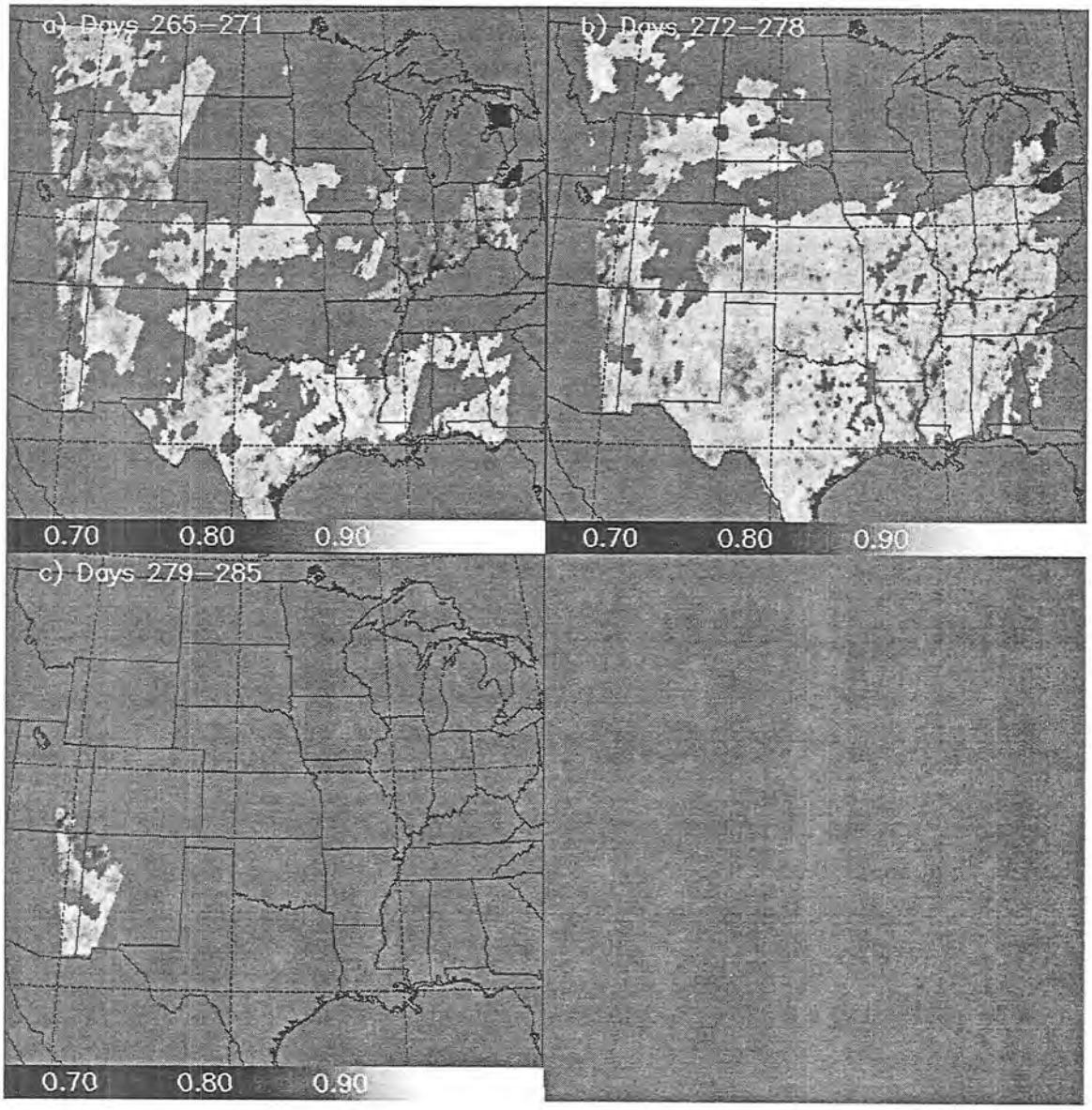

Figure 4.48: Same as Figure 4.46, except for days a) 265-271, b) 272-278, and c) 279-285.

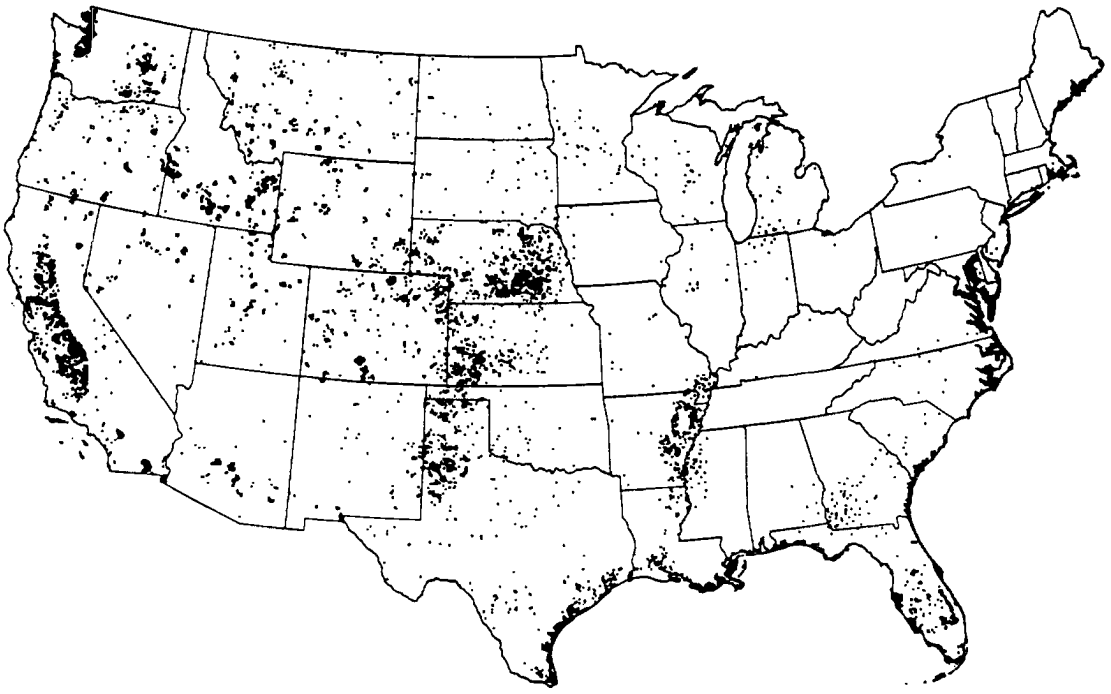

Figure 4.49: Irrigated land in farms, 1982 (Bajwa et al. 1987).

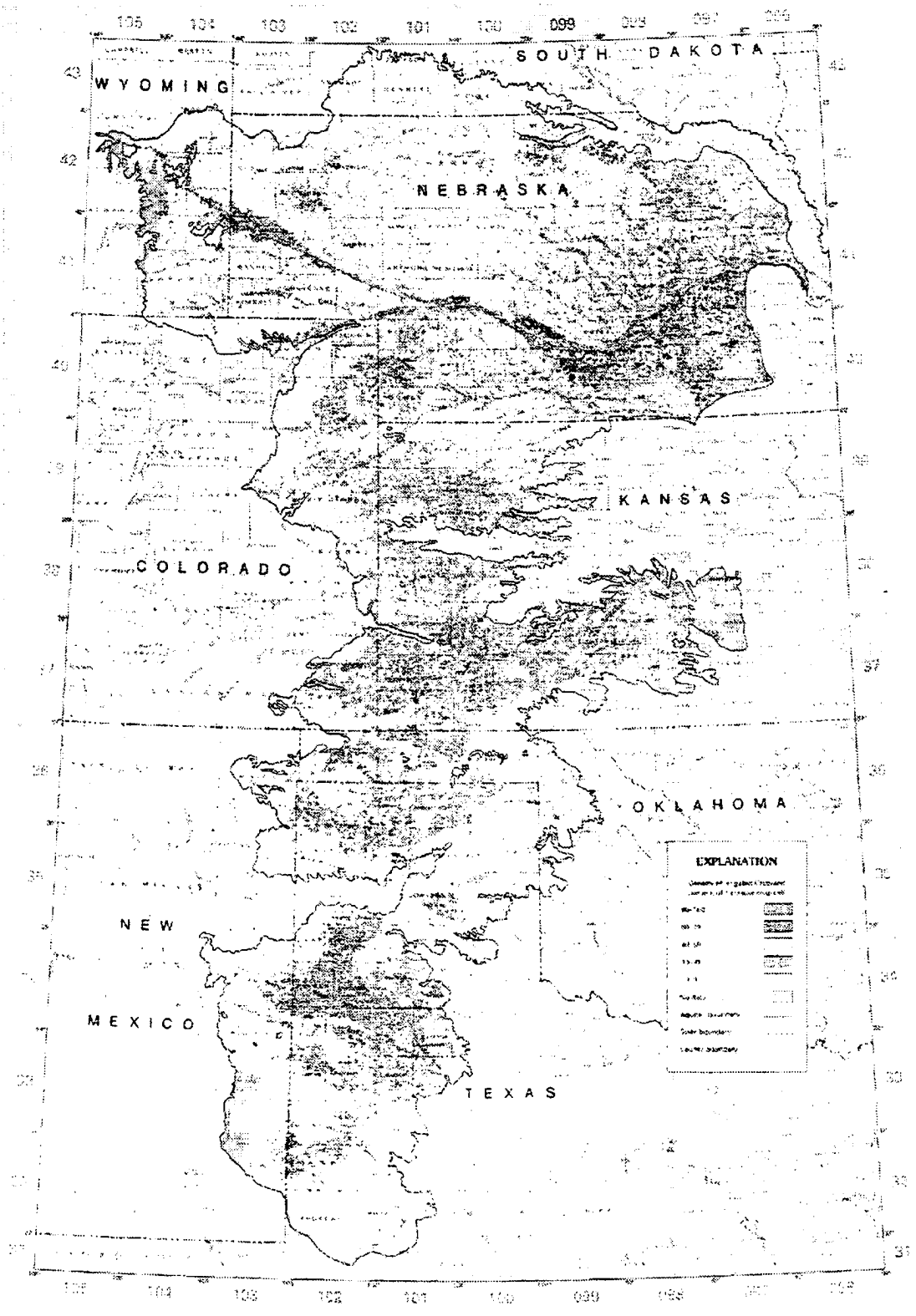

Figure 4.50: Irrigated cropland in the High Plains Aquifer Region as derived from Landsat data, 1980 (adapted from Thelin et al. 1987). The colors blue, dark green, light green, brown, and yellow denote regions with 80-100, 60-79, 40-59, 10-39, and 0-9 percent densities. Gray regions are areas with no data available.

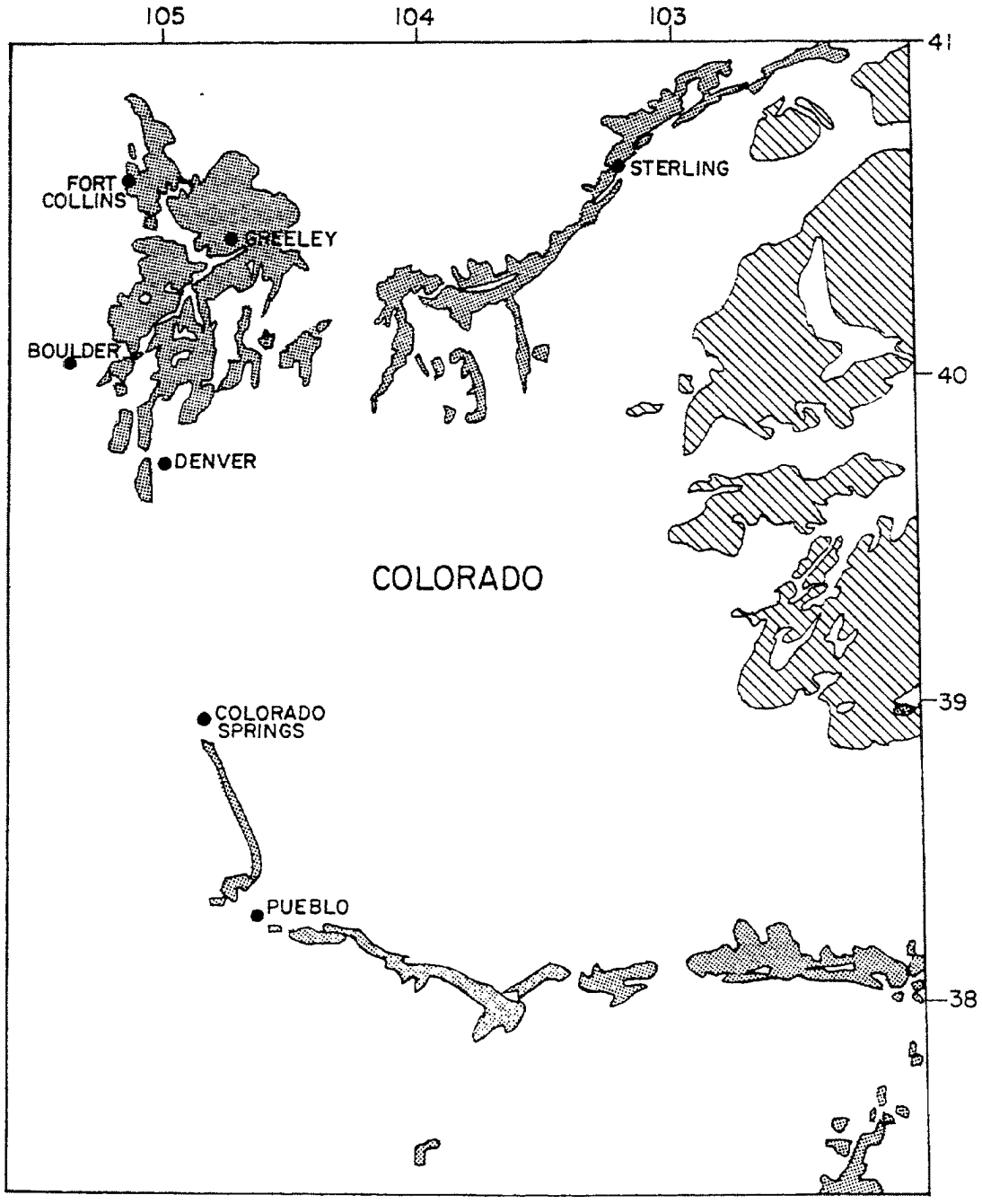

Figure 4.51: Irrigation areas of eastern Colorado (reproduced from the map of Important Farmlands of Colorado, prepared by USDA Soil Conservation Service and Colorado State University Experiment Station, 1980).

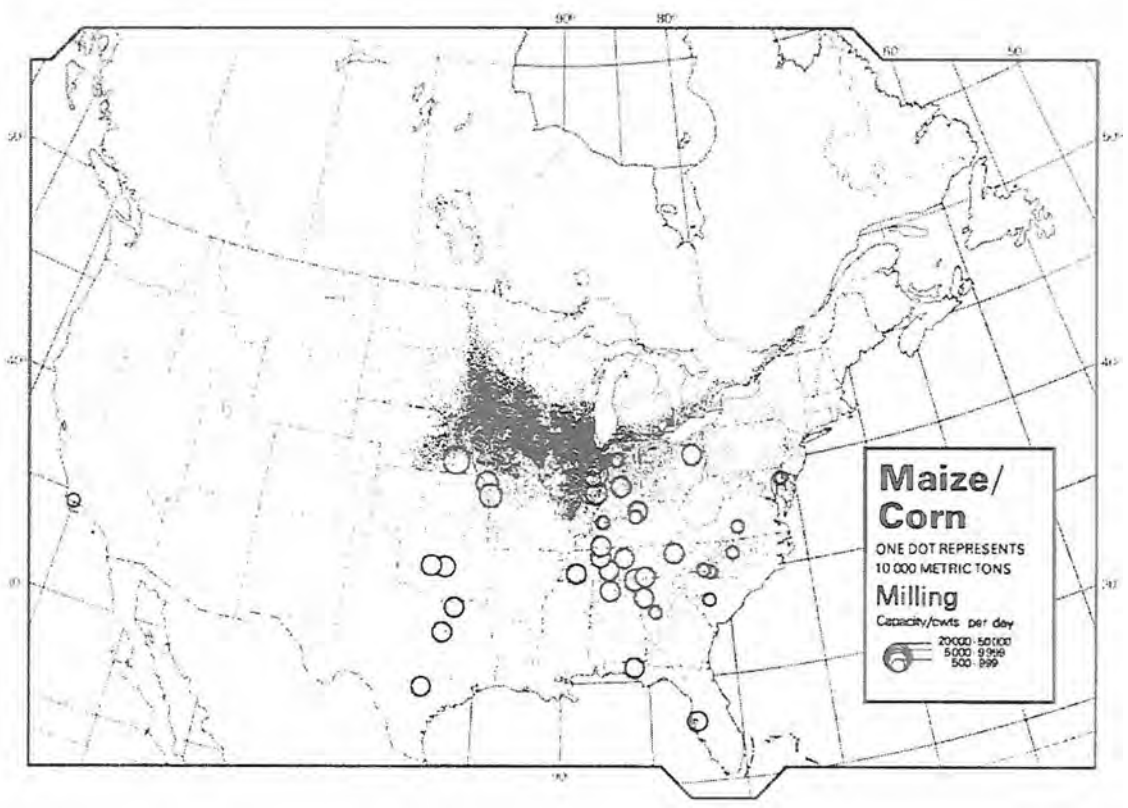

Figure 4.52: Density of corn crop production and milling capacities (Chapman and Sherman 1982).

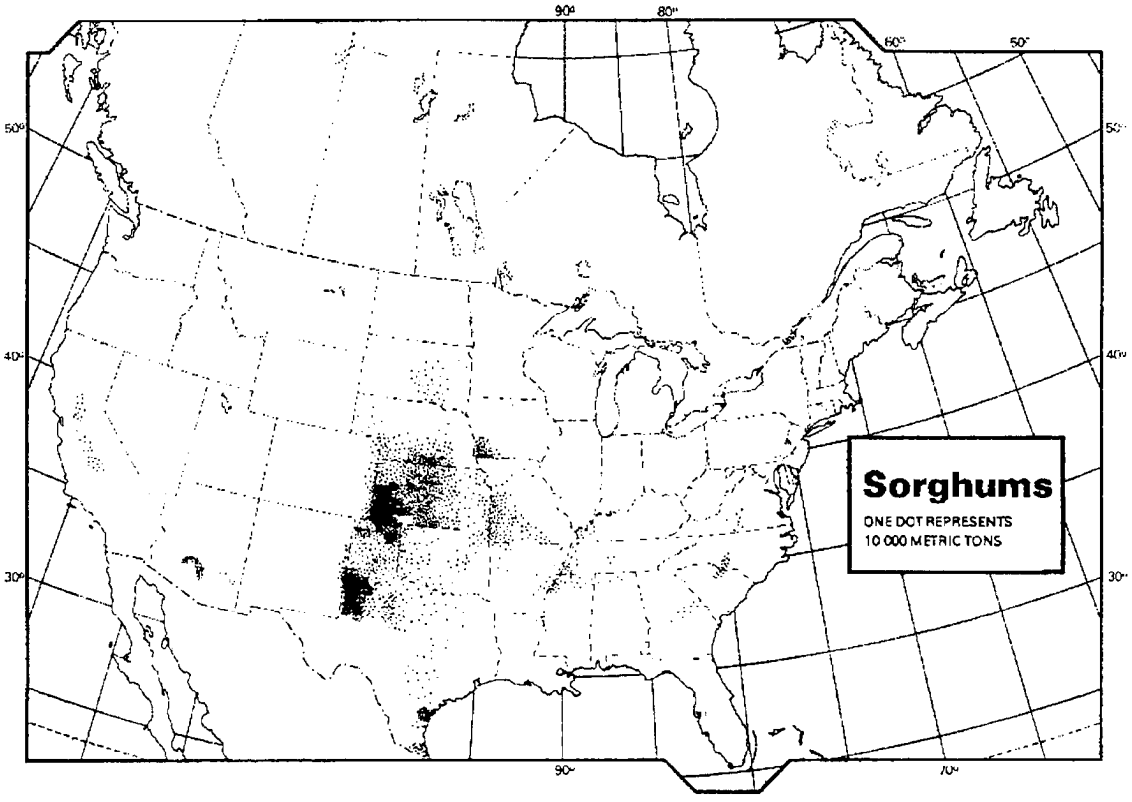

Figure 4.53: Density of sorghum production (adapted from Chapman and Sherman 1982).

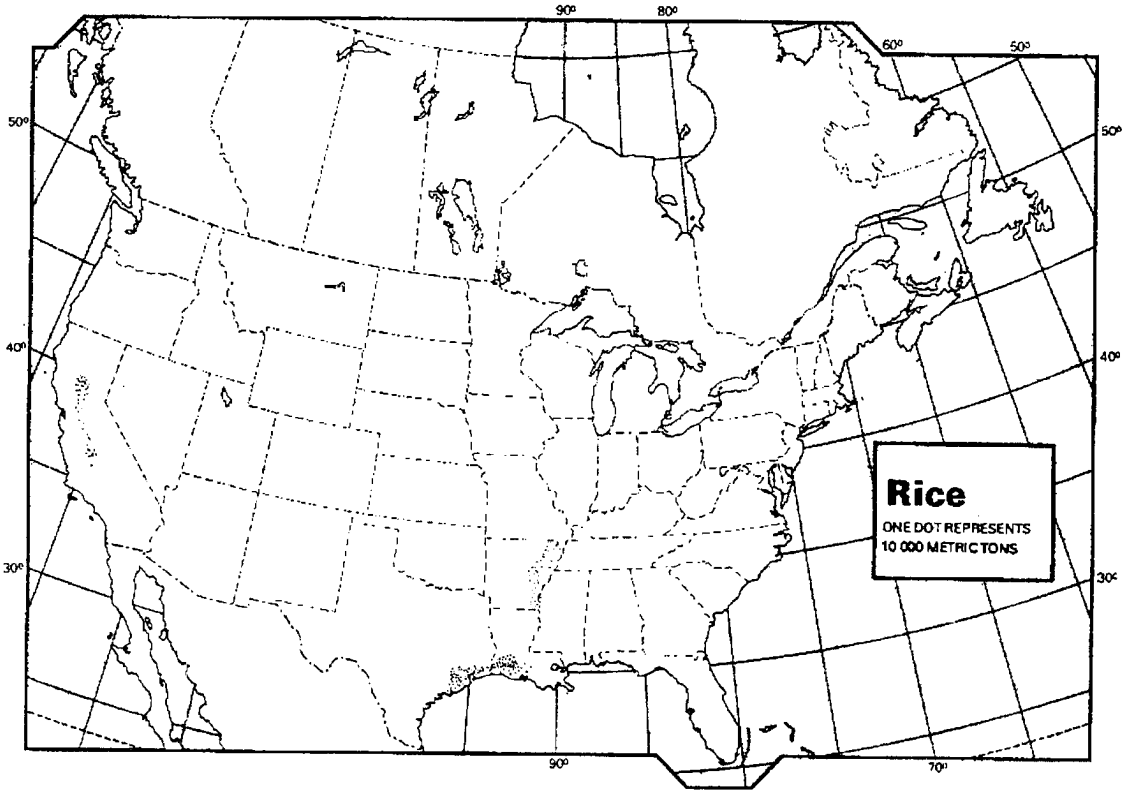

Figure 4.54: Density of rice production (adapted from Chapman and Sherman 1982).

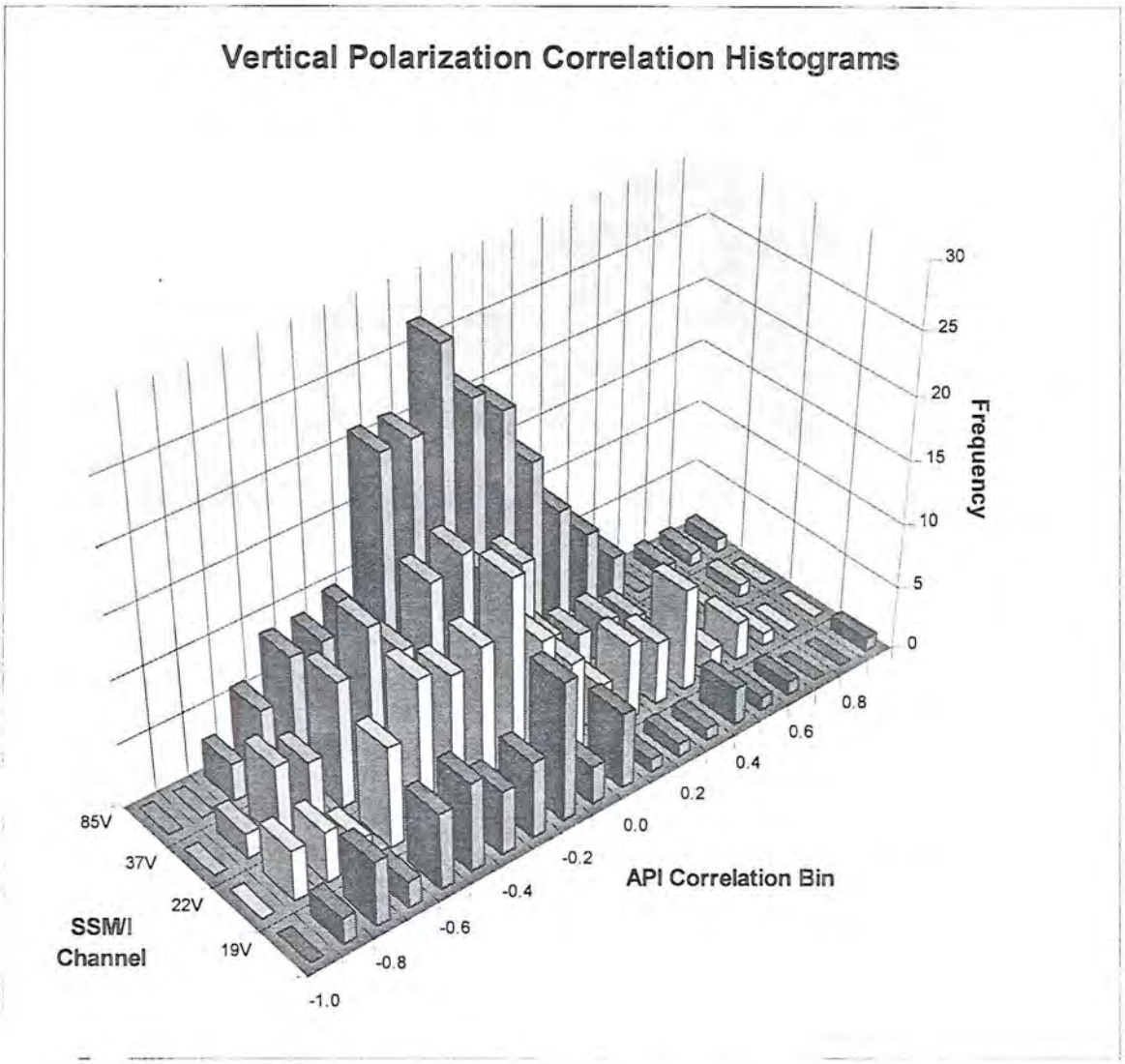

Figure 4.55: Histograms of the microwave surface emittance versus API correlation distribution for the SSM/I vertical polarization channels (19V, 22V, 37V, 85V).

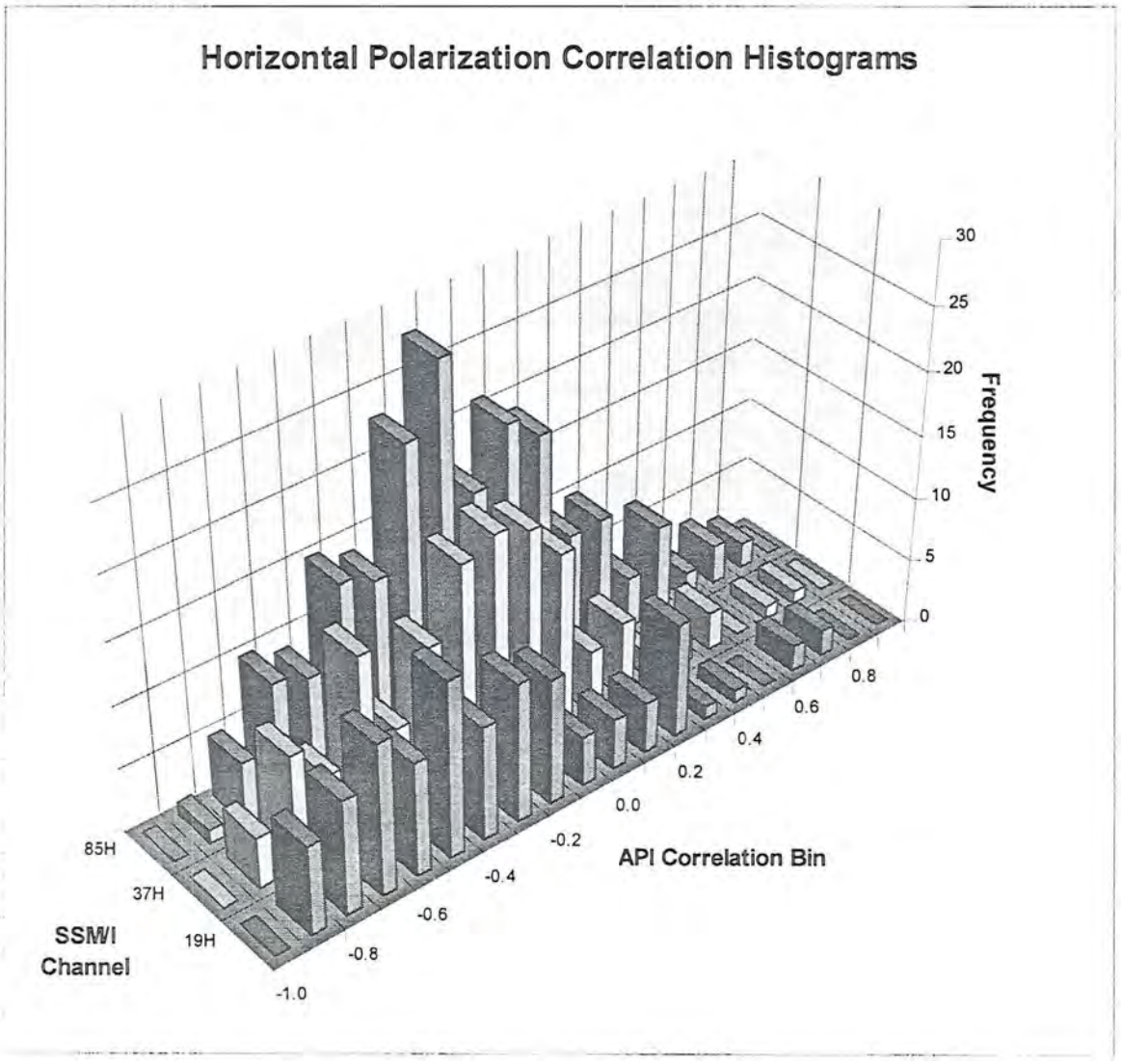

Figure 4.56: Same as Figure 4.55, except for the SSM/I horizontal polarization channels (19H, 37H, 85H).

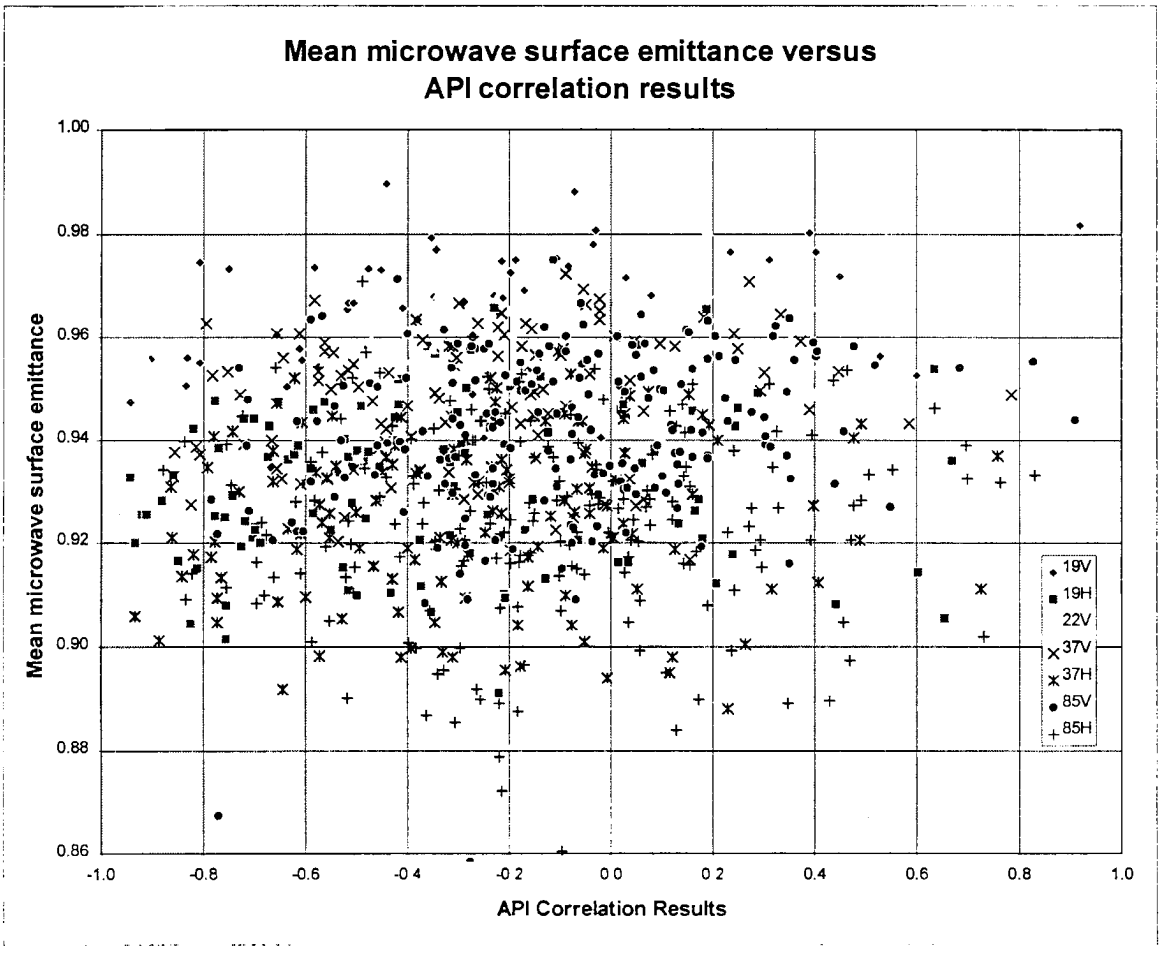

Figure 4.57: Mean microwave surface emittance versus API correlation results. Each SSM/I channel has a unique symbol (see the figure legend).

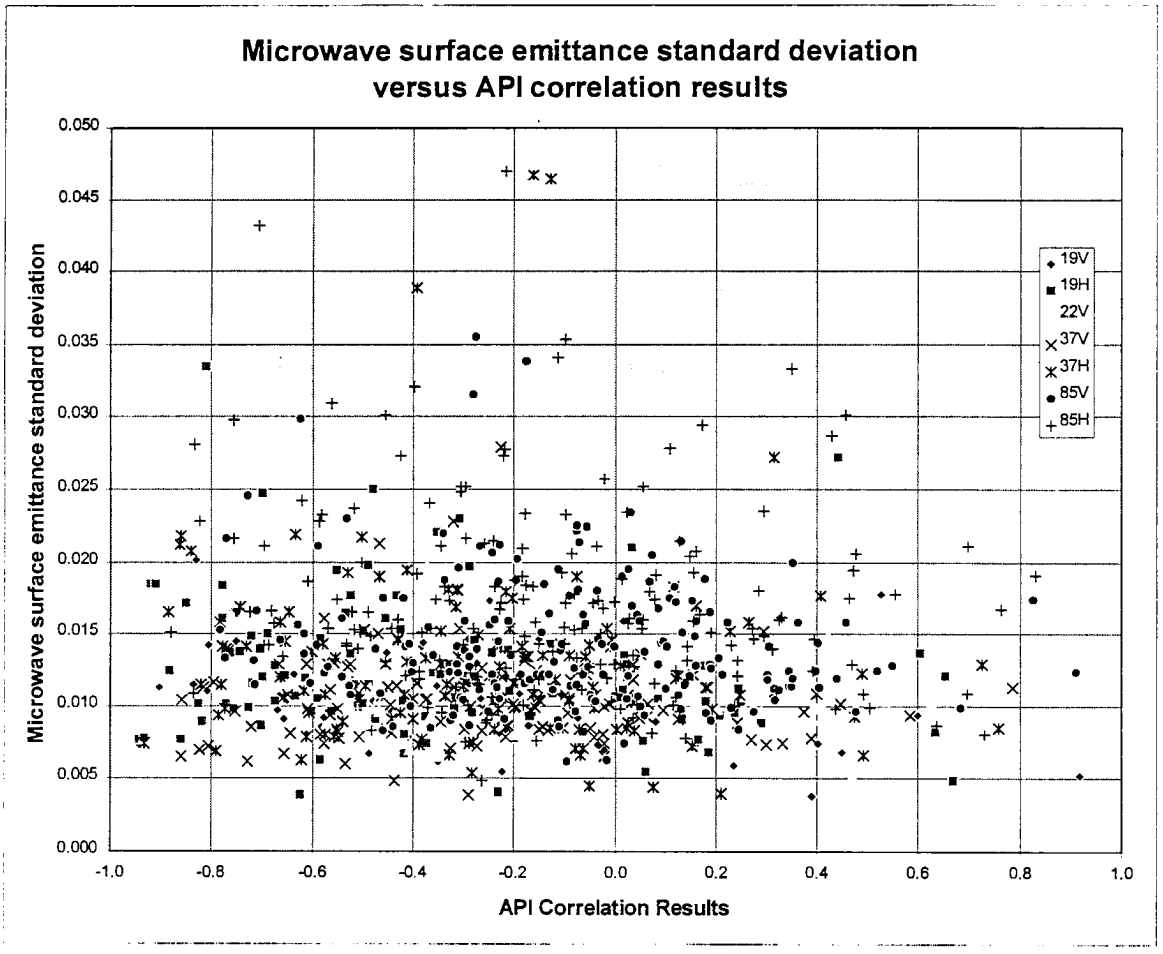

Figure 4.58: Same as Figure 4.57, except for the microwave surface emittance standard deviation versus the API correlation results.

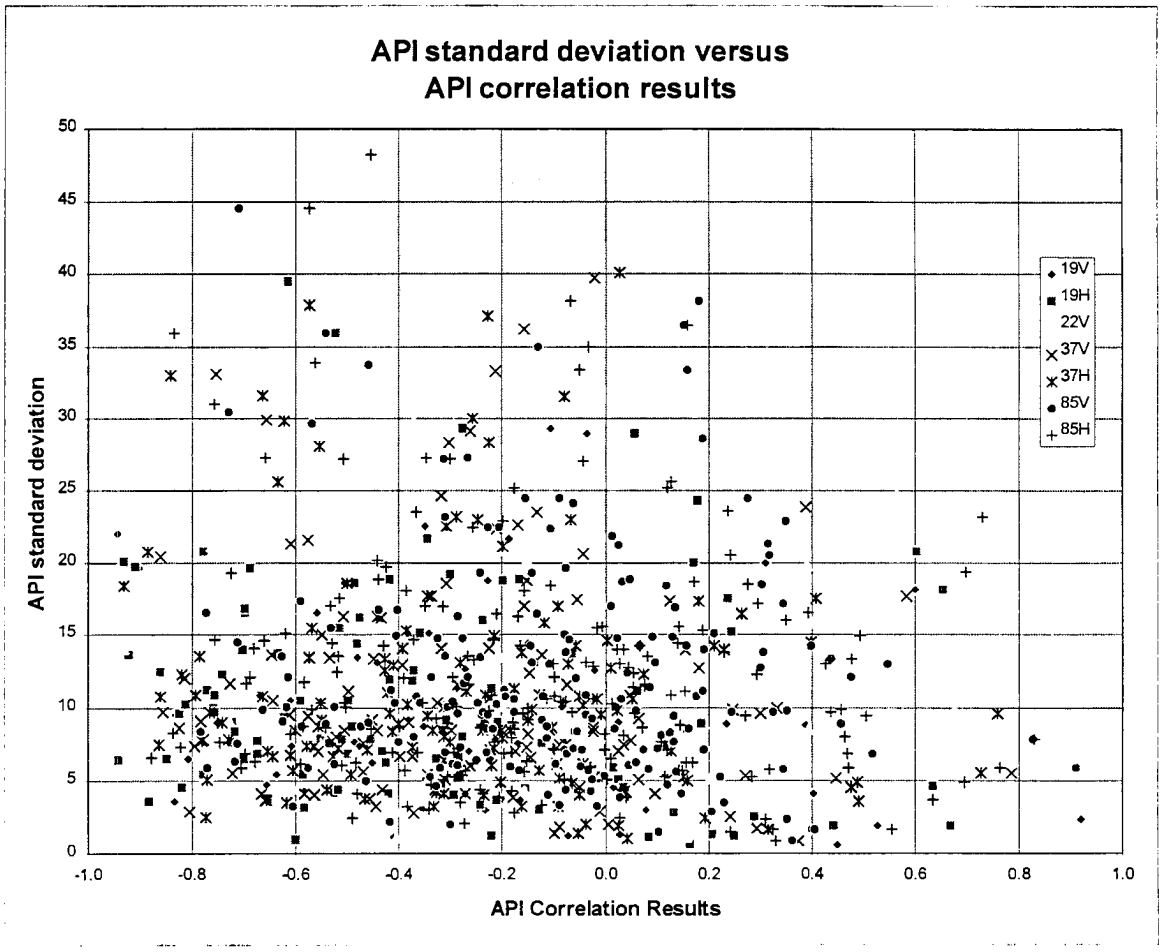

Figure 4.59: Same as Figure 4.57, except for the API standard deviation versus the API correlation results.

Figure 4.60: Station locations where the 85.5H GHz surface emittance versus API correlation values are less than -0.5.

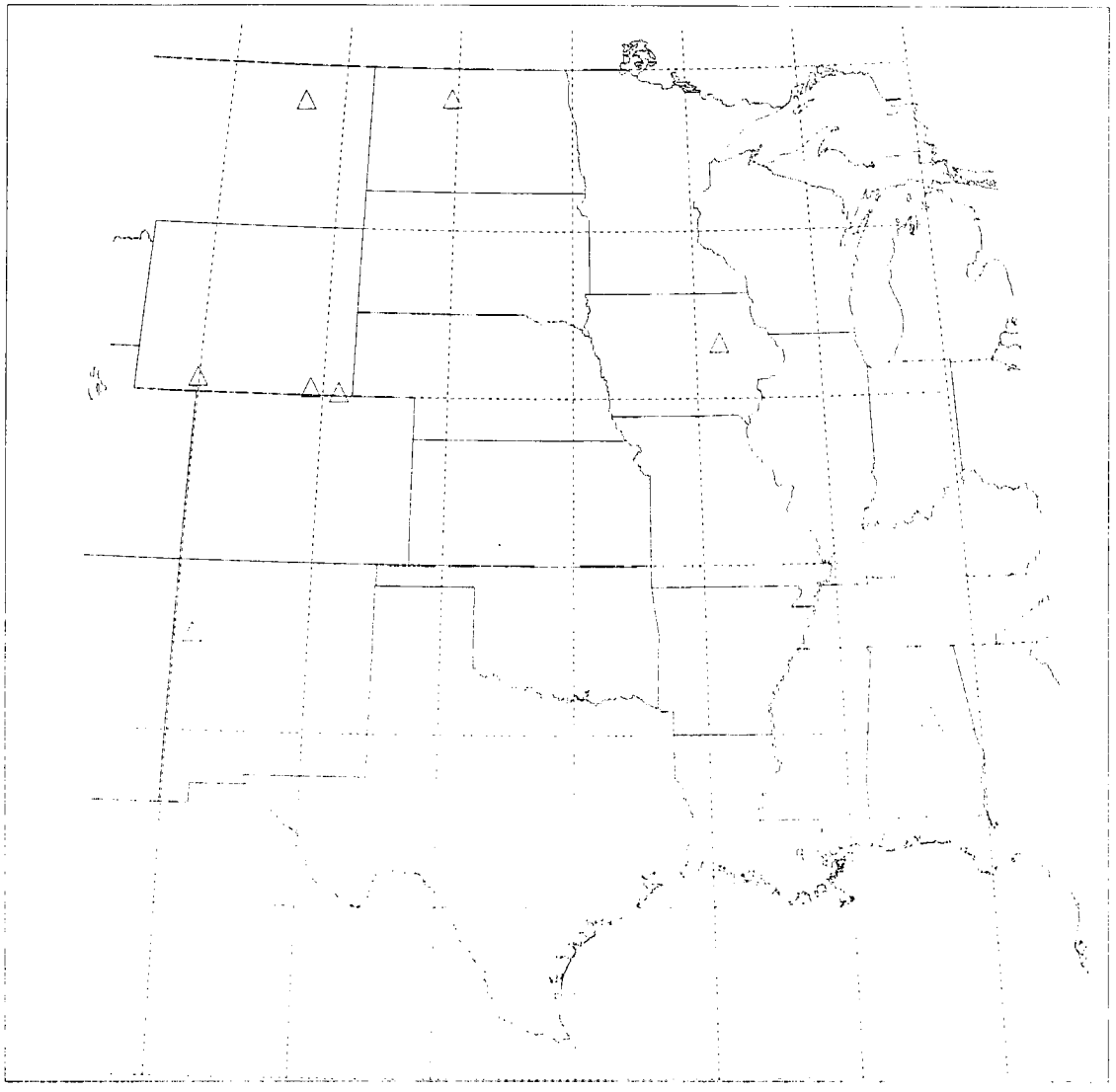

Figure 4.61: Same as Figure 5.60, except for correlation values greater than 0.5.

Figure 4.62: Same as Figure 4.60, except for all SSM/I channels.

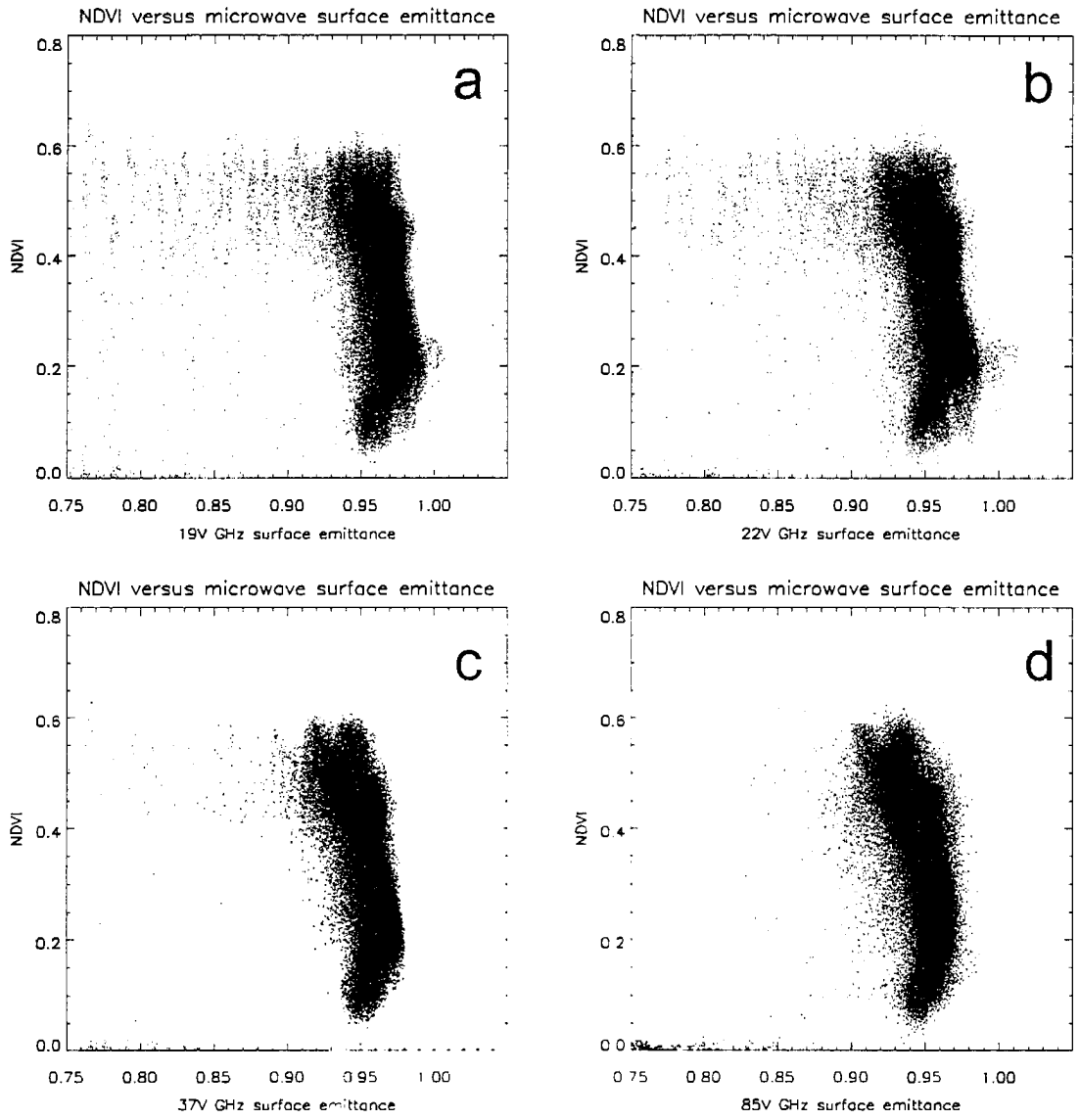

Figure 4.63: Mean NDVI values versus a) 19V GHz, b) 22V GHz, c) 37V GHz, and d) 85V GHz mean surface emittance for 30 July - 7 October 1991.

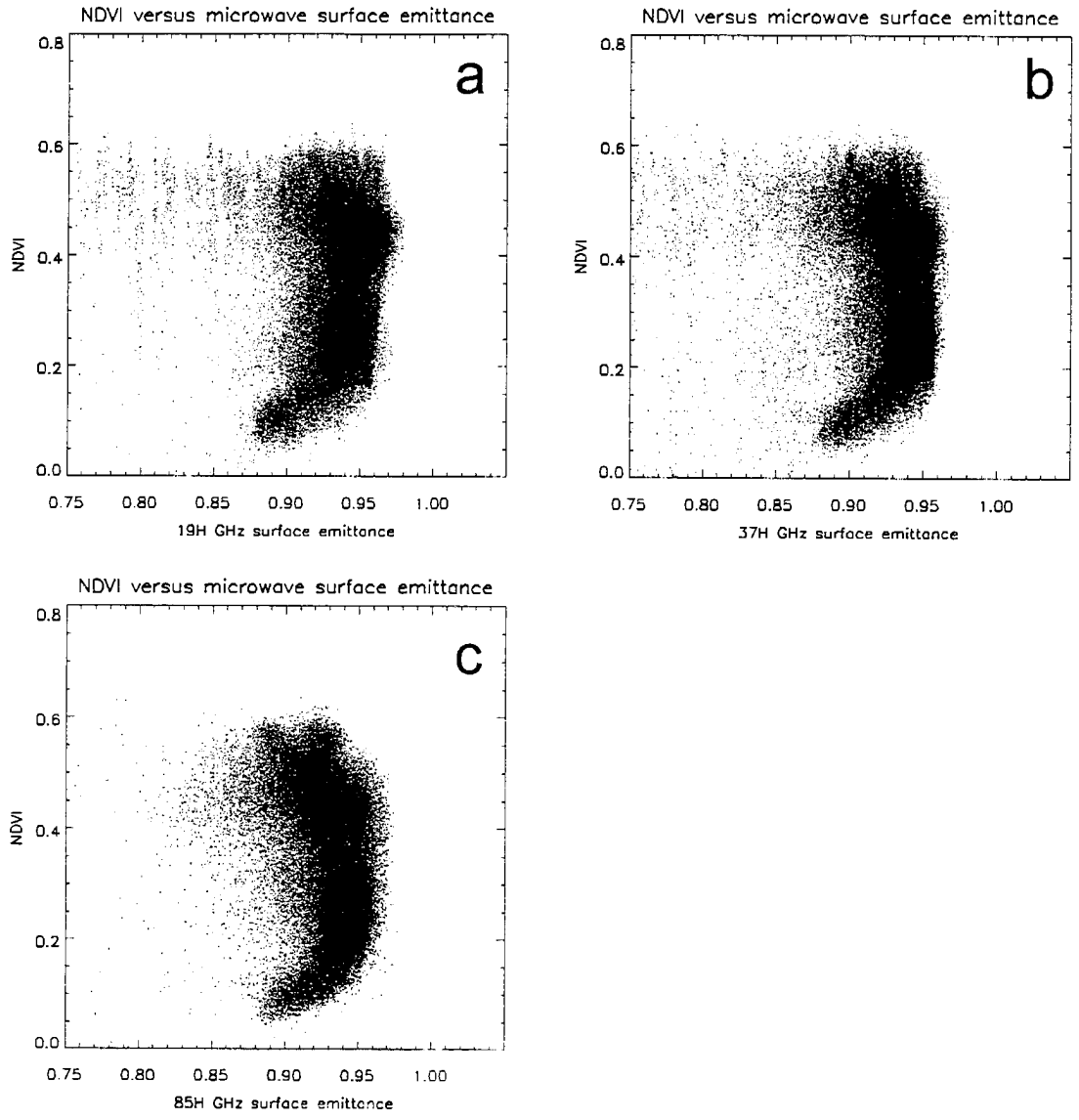

Figure 4.64: Same as Figure 4.63, except for mean NDVI values versus a) 19H GHz, b) 37H GHz, and c) 85H GHz mean surface emittance.

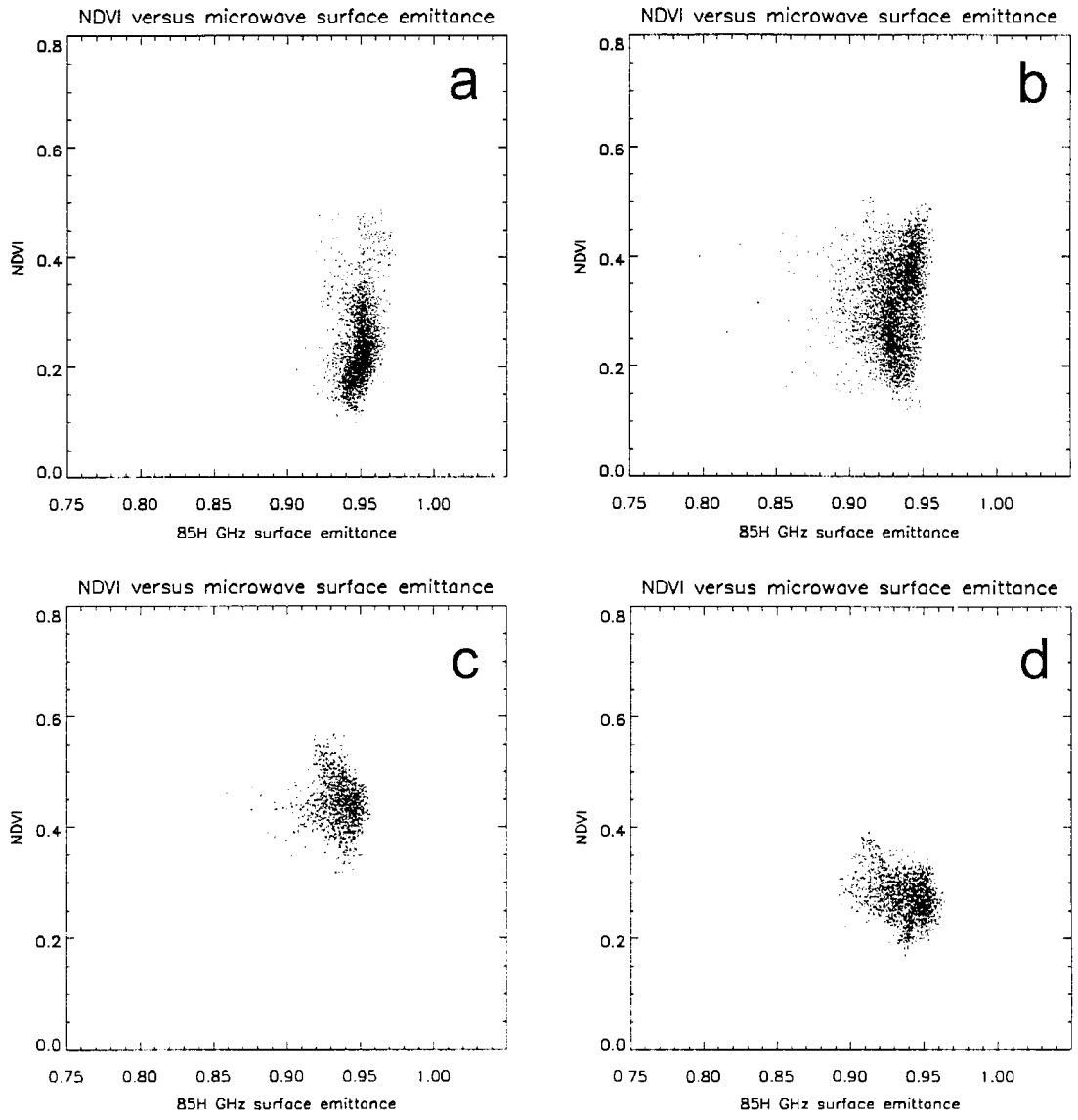

Figure 4.65: Same as Figure 4.63, except for mean NDVI values versus 85H GHz mean surface emittance for areas a) A, b) B, c) C, and d) D.

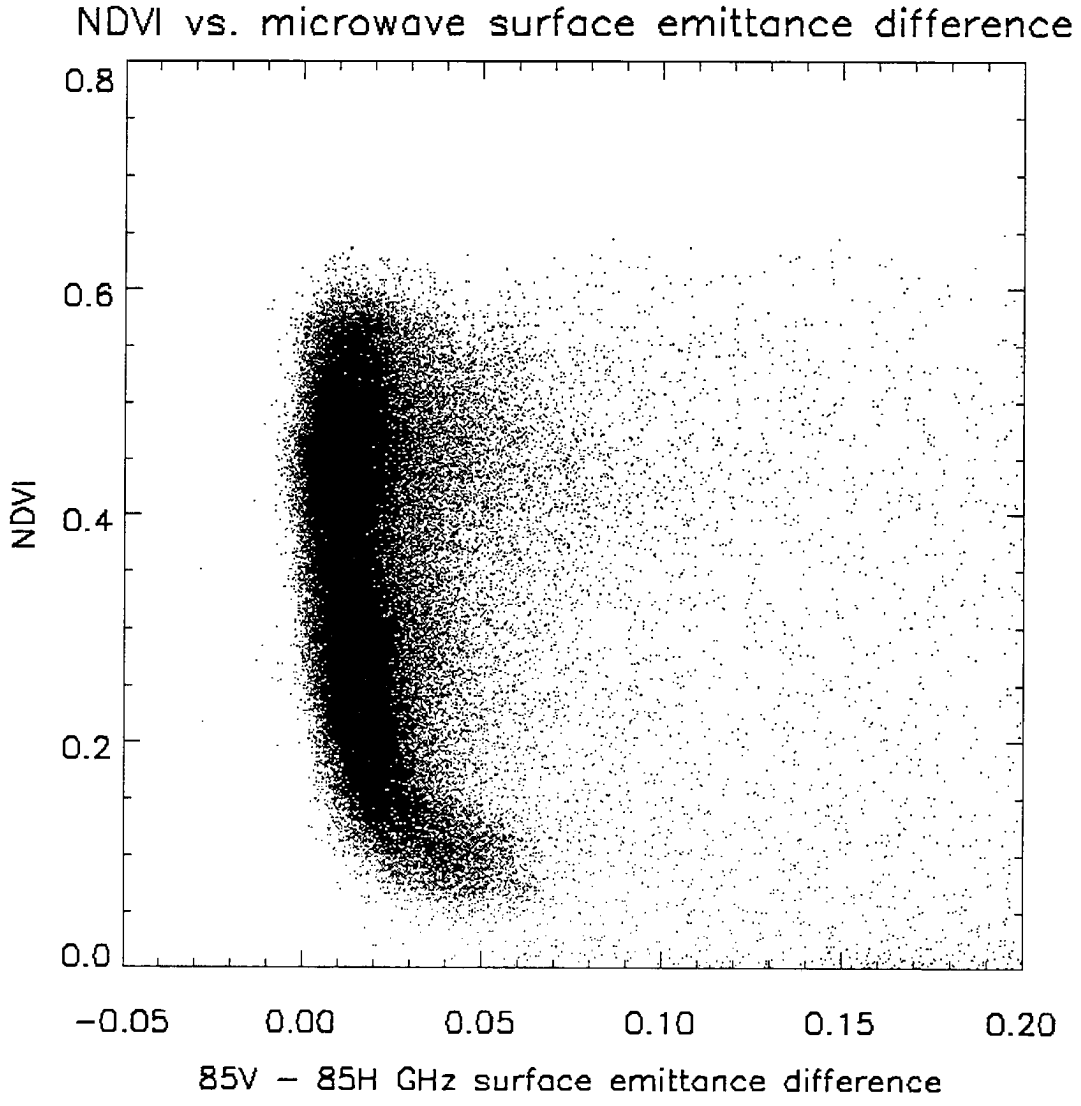

Figure 4.66: Same as Figure 4.63, except for mean NDVI values versus 85V - 85H GHz surface emittance polarization difference.

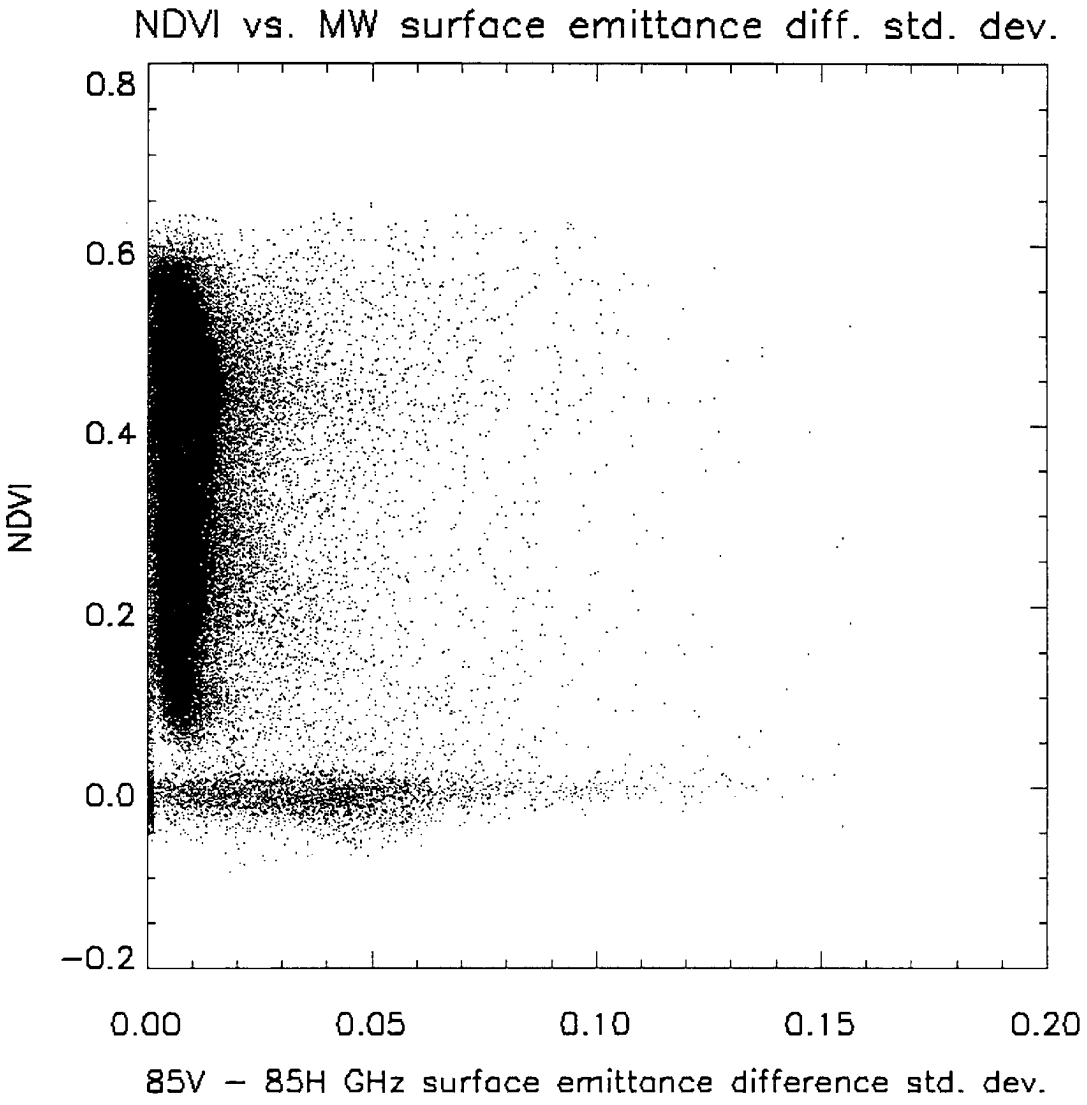

Figure 4.67: Same as Figure 4.63, except for mean NDVI values versus the standard deviation of the 85V - 85H GHz surface emittance polarization difference.

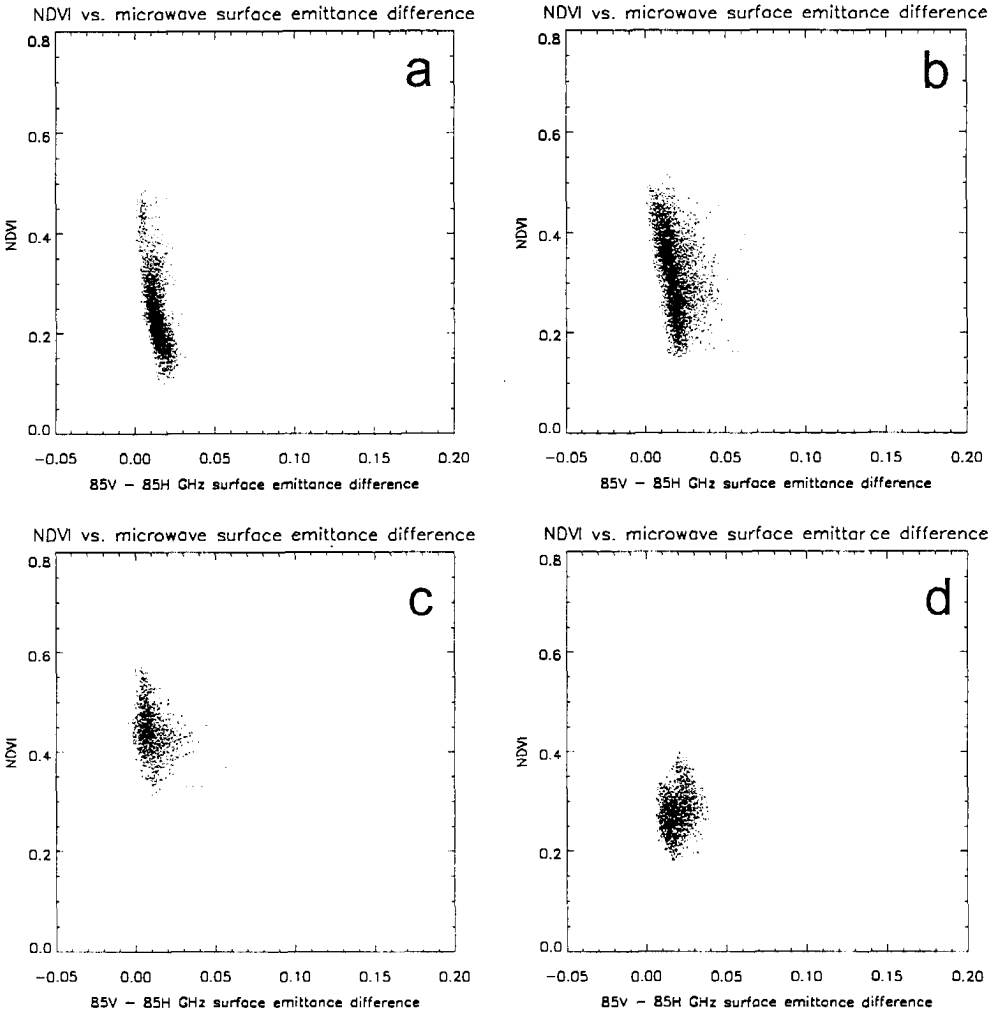

Figure 4.68: Same as Figure 4.66, except for areas a) A, b) B, c) C, and d) D.

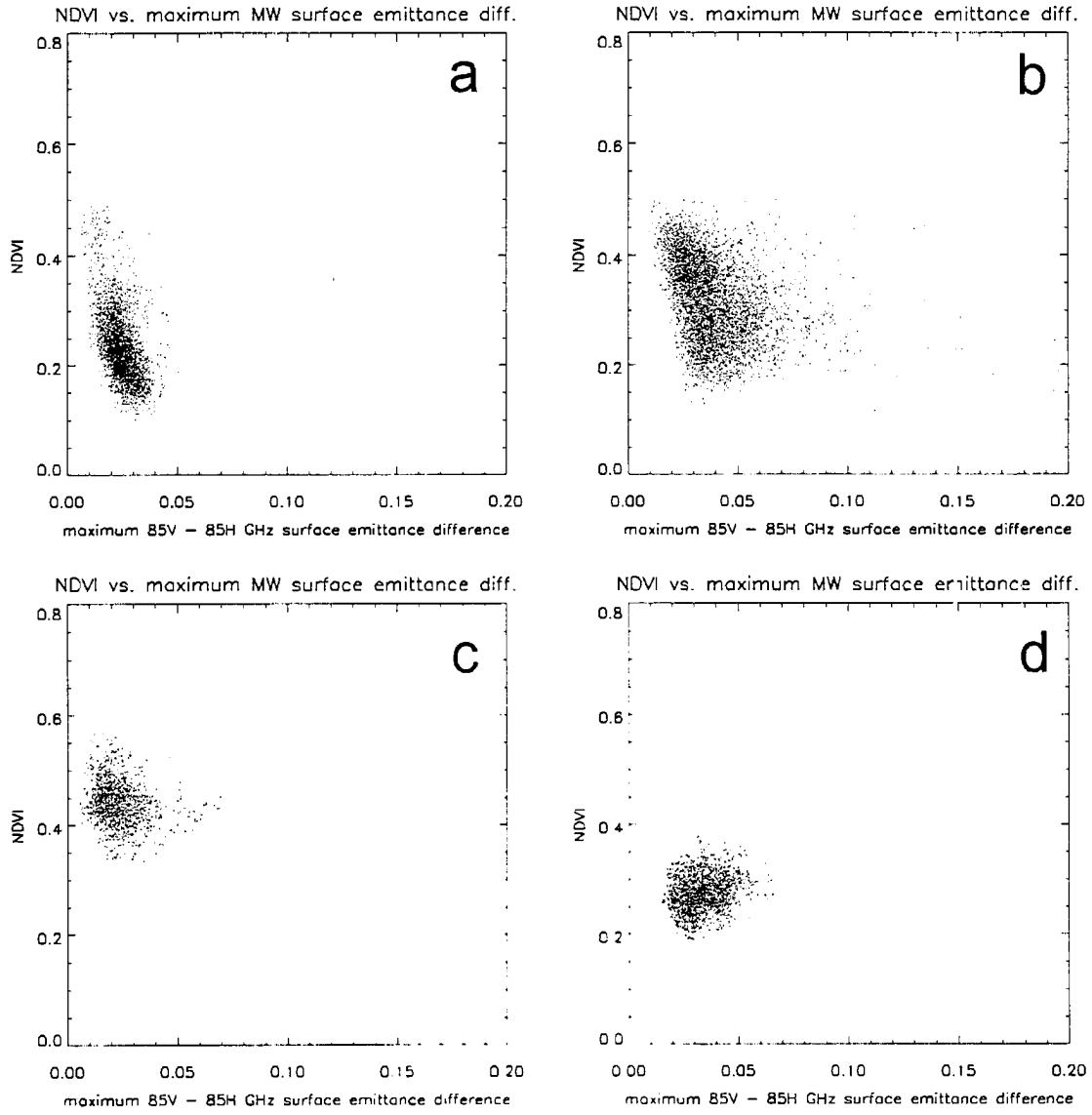

Figure 4.69: Same as Figure 4.63, except for mean NDVI values versus the maximum 85V - 85H GHz surface emittance polarization difference for areas a) A, b) B, c) C, and d) D.

Chapter 5

DATA ASSIMILATION OF SATELLITE-DERIVED SURFACE SOIL MOISTURE INTO AN ATMOSPHERIC MESOSCALE MODEL

This chapter presents the development and testing of a satellite-model coupled data assimilation system for incorporating satellite-derived surface soil moisture into an atmospheric mesoscale model. The method is based on the McNider technique discussed in section 2.4, with extensions added to account for vegetation effects using a simple "big leaf" vegetation parameterization scheme. The method is derived in section 5.1, and tested in a 1D sensitivity test and a 3D case study in sections 5.2 and 5.3, respectively. A simple noise experiment is performed in section 5.3.3. The data assimilation results are summarized in section 5.4.

5.1 SATELLITE DATA ASSIMILATION METHOD

The satellite data assimilation method is based on using satellite measured heating rates as an estimate of the surface latent heat flux in a manner similar to McNider et al.'s work (1994). Major differences include the inclusion of a prognostic soil model, and a vegetation parameterization. The Colorado State University (CSU) Regional Atmospheric Modeling System (RAMS) was selected as the atmospheric mesoscale model to implement the data assimilation method due to its capabilities to perform variable initialization from observations, and its long history as a research-quality mesoscale atmospheric model including an emphasis on land surface parameterization (Pielke et al. 1992).

5.1.1 CSU-RAMS Land Surface Parameterization Scheme

The standard vegetation/land surface parameterization scheme used in RAMS is based on a series of papers (McCumber 1980; Avissar and Mahrer 1982; Avissar and Mahrer 1988; Avissar and Pielke 1989), each incrementally improving upon the original scheme. The basic overall capabilities of the model are described in Pielke et al. (1992), while a review of the current specific vegetation scheme is reported in Lee (1992). The basic components of the bare soil prognostic model (Tremback and Kessler 1985) have already been discussed in sections 2.1.2 and 2.1.3.

Several features of the vegetation/land surface parameterization scheme are relevant to this work. The model is composed of 4 parts: the bare soil, shaded soil, vegetation, and water surfaces. The bare soil and shaded soil models use basically the same physical parameterization except with different boundary conditions due to the overlaying vegetation. The water surface has a relatively simple parameterization in which the water temperature is assumed to have a seasonally specified temperature that is constant during the simulated period of the model run, and water vapor is evaporated freely from its surface as a function of temperature, atmospheric humidity and wind speed. The vegetation parameterization is a modified "big leaf" vegetation scheme in which all vegetation is assumed to exist as one constant slab of plant material over the shaded soil surface. Horizontal variations in the vegetation are accounted for by defining several vegetation classes that specify appropriate model parameters (e.g., albedo, roughness length, and leaf area index (LAI)) for the particular classification category. The RAMS vegetation categories are based on the Biosphere-Atmosphere Transfer Scheme (BATS) (Dickinson et al. 1986). Additionally, USGS land classification categories based on NDVI measurements (Loveland et al. 1991) are used to realistically distribute the various land classification categories at a 1 km grid interval scale. Examples of the vegetation classification used for this work are shown in section 5.3.2.1.

5.1.2 Satellite Data Assimilation Method Derivation

The aggregate model heating rate (i.e. the heating rate that is equivalent to a single-FOV satellite heating rate) is composed of 3 parts: the heating rate fraction due to the bare soil, vegetation, and standing water. Although a shaded-soil heating rate component is calculated within the land surface parameterization scheme, it is not used in the following derivation since the vegetation would shield the shaded soil temperatures from satellite observation. Thus,

$$\left(\frac{dT}{dt}\right)_m = f_L\left(\frac{dT_L}{dt}\right)_m + f_V\left(\frac{dT_V}{dt}\right)_m + f_W\left(\frac{dT_W}{dt}\right)_m, \tag{5.1}$$

represents the aggregate model heating rate that would be comparable to a satellite observed heating rate. Each component is determined from the individual model heating rates,

$$\left(\frac{dT_L}{dt}\right)_m, \quad \left(\frac{dT_V}{dt}\right)_m, \quad \left(\frac{dT_W}{dt}\right)_m, \tag{5.2}$$

and is multiplied by its respective fractional area coverage, f_L, f_V, f_W, where the subscripts, L, V, and W denote the land, vegetation, and water components, respectively. To distinguish satellite variables from model variables, the subscripts m and s are used, where m refers to model quantities, and s, to satellite quantities. The combination of all fractional area coverage is defined such that,

$$f_L + f_V + f_W = 1. \tag{5.3}$$

Following the technique of McNider et al. (1994), the aggregate model heating rate is perturbed to force agreement between the model and observed satellite heating rates. This yields

$$\left(\frac{dT}{dt}\right)_{m'} = f_L\left(\frac{dT_L}{dt}\right)_{m'} + f_V\left(\frac{dT_V}{dt}\right)_{m'} + f_W\left(\frac{dT_W}{dt}\right)_{m'} = \left(\frac{dT}{dt}\right)_s, \tag{5.4}$$

where the subscript m' is used to denote the new perturbed model variables. Within the CSU-RAMS land surface parameterization scheme, Equations 5.1 and 5.4 can be simplified since water surface temperatures are assumed to be constant, i.e.,

$$\left(\frac{dT_W}{dt}\right)_m = \left(\frac{dT_W}{dt}\right)_{m'} = 0. \tag{5.5}$$

Further usage of these equations requires that additional assumptions be introduced to reduce the degrees of freedom in the equation set, since only an aggregate heating rate is available from the satellite platform. Section 5.1.2.1 continues the data assimilation method derivation, focusing on the derivation of the bare soil component, while section 5.1.2.2 derives the solution for the vegetation equation set.

5.1.2.1 Bare Soil Component

The heating rate of the bare soil component is not directly measured by the satellite, thus an assumption is introduced that the current bare soil and vegetation model heating rates are proportional to the new perturbed model heating rates which are to be calculated,

$$\frac{\left(\frac{dT_L}{dt}\right)_{m'}}{\left(\frac{dT_{l'}}{dt}\right)_{m'}} = \frac{\left(\frac{dT_L}{dt}\right)_m}{\left(\frac{dT_{l'}}{dt}\right)_m}. \tag{5.6}$$

This assumes that the model is sufficiently capable of determining the relative magnitudes of the component heating rates. It also has a side benefit, in that it ensures that the new perturbed model heating rates will not abruptly alter the energy partitioning between the bare soil and vegetation surface components. Inserting Equation 5.6 into Equation 5.4, and solving for the perturbed model heating rate over bare soil, produces the following relationship,

$$\left(\frac{dT_L}{dt}\right)_{m'} = \left[\frac{\left(\frac{dT}{dt}\right)_s}{f_L + f_V\left(\frac{dT_V}{dt}\right)_m\left(\frac{dT_L}{dt}\right)_m^{-1}}\right], \tag{5.7}$$

which can be used to estimate the new model heating rate over bare soil as a function of the satellite-derived heating rate.

From Equation 2.4, introduced in section 2.1.2, the soil heat flux is also related to the bare soil heating rate, such that (in finite difference form),

$$\left(\frac{dT_L}{dt}\right)_{m'} = \frac{Q'_{nzg} - Q'_{(nzg-1)}}{\Delta z \rho' c'}, \tag{5.8}$$

where Q'_{nzg} and $Q'_{(nzg-1)}$ are the perturbed model soil heat fluxes at the ground surface, $z_{nzg} = 0\,\text{cm}$, and at the model level immediately below the ground surface (which was 3 cm below the ground surface for the model configuration used in these runs). Δz is the depth of the surface soil layer (3 cm), while ρ' and c' are the moisture-dependent soil density and soil specific heat capacity of the perturbed model (see section 2.1.2). Equation 5.8 is then solved for the perturbed model soil heat flux,

$$Q'_{nzg} = Q'_{(nzg-1)} + \left(\frac{dT_L}{dt}\right)_{m'} \Delta z \rho' c'. \tag{5.9}$$

Proceeding beyond this point requires the second major assumption, which (after McNider) is the assumption that all the terms in the model's surface energy budget are the same as the actual energy budget except for the latent energy term E (McNider et al. 1994). Thus the new perturbed surface soil heat flux can be written as,

$$Q'_{nzg} = Q_{nzg} + \Delta E = Q_{nzg} + L_v \rho_a u_{*_L} \Delta q_{*_L}, \tag{5.10}$$

where ΔE is the latent energy term adjustment required to bring the model into balance with the satellite observations. From similarity theory, the latent heat flux is also related to the surface friction velocity, u_*, and friction humidity, q_* (see section 2.1.1), which allows ΔE to be expanded in Equation 5.10. By combining Equations 5.9 and 5.10, the satellite-derived heating rate forcing can then be reduced to a relationship involving a friction humidity perturbation,

$$\Delta q_{*_L} = \left[\frac{Q'_{(nzg-1)} - Q_{nzg} + \left(\frac{dT_L}{dt} \right)_{m'} \Delta z \rho' c'}{L_v \rho_a u_{*_L}} \right], \tag{5.11}$$

where the subscript L denotes *bare soil* friction velocity and humidity values. As you can see, we are working our way downward into the land surface parameterization scheme.

The next derivation phase involves inverting the similarity relationship that connects the surface friction velocity and friction humidity values to the surface specific humidity value, q_G. CSU-RAMS implements the Louis (1979) stability adjustment functions since the method is non-iterative. This means a direct inversion is possible. The surface flux term is given by,

$$u_{*_l} q_{*_l} = C_1 f_h \left(q_a - q_G \right), \tag{5.12}$$

where

$$C_1 = \beta \bar{l} \left[\frac{k}{\ln(z / z_0)} \right]^2, \tag{5.13}$$

and

$$f_h = \begin{cases} (1+4.7\,\mathrm{Ri})^{-2} & \theta > \theta_G \\ 1-9.4\,\mathrm{Ri}\left\{1+5.3\left[\dfrac{k}{\ln(z/z_0)}\right]^2\sqrt{|\mathrm{Ri}|}\right\}^{-1} & \theta \le \theta_G \end{cases}, \tag{5.14}$$

where Ri is the Richardson number (see section 2.1.4 for further details). Equation 5.12 therefore relates the surface specific humidity perturbation, Δq_G, to the surface friction humidity, Δq_{*_L}, and can be expressed as

$$\Delta q_G = -\frac{\Delta q_{*_L} u_{*_L}}{C_1 f_h}. \tag{5.15}$$

Combining Equations 5.11 and 5.15 produces a relationship for Δq_G,

$$\Delta q_G = \left[\frac{Q_{nzg} - Q'_{(nzg-1)} - \left(\dfrac{dT_L}{dt}\right)_{m'} \Delta z \rho' c'}{L_v \rho_a C_1 f_h}\right], \tag{5.16}$$

where Equations 5.7, 5.13 and 5.14 are used to complete the equation set.

The soil surface specific humidity parameterization scheme of Lee and Pielke (1992) is used to relate the surface specific humidity to the surface soil moisture value, η. This particular parameterization scheme was found to have the smallest variations of six methods compared by Mihailovic et al. (1995) against observed latent heat fluxes. The surface specific humidity is a function of the surface ground temperature, T_G, and atmospheric humidity above the ground surface, q_a. Additional parameters α and β are introduced to control the performance of the method,

$$q_G = \alpha\beta q_s(T_G) + (1-\beta) q_a, \tag{5.17}$$

where,

$$\alpha = \exp\left(\frac{g\Psi}{RT_G}\right), \tag{5.18}$$

$$\beta = \begin{cases} \frac{1}{4}\left[1-\cos\left(\frac{\eta\pi}{\eta_{fc}}\right)\right]^2, & \eta \le \eta_{fc} \\ 1, & \eta > \eta_{fc} \end{cases}, \tag{5.19}$$

and $q_s(T)$ is the saturation specific humidity at a given temperature T, η_{fc} is the volumetric soil water content at the field capacity of the soil, g is the acceleration due to gravity, Ψ is the soil water potential at the surface, and R is the gas constant for water vapor (Lee and Pielke 1992). Therefore, the perturbation form of Equation 5.17 can be written as

$$\Delta q_G = q'_G - q_G = \alpha\beta\big|_{\eta'} q_s(T_G) - \beta\big|_{\eta'} q_a - \alpha\beta\big|_{\eta} q_s(T_G) + \beta\big|_{\eta} q_a, \tag{5.20}$$

where the α and β terms are evaluated at their appropriate surface soil moisture values.

Therefore, the combination of Equations 5.16 and 5.20, in addition to their associated equations (Equations 5.7, 5.13 and 5.14) is the solution for the bare soil surface soil moisture in the presence of the satellite observed heating rates. An iterative numerical solution technique is required to solve Equations 5.16 and 5.20. Equations 5.16 and 5.20 are subtracted so that a new function, ΔF, is defined,

$$\Delta F = \left[\frac{Q_{nzg} - Q'_{(nzg-1)} - \left(\frac{dT_L}{dt}\right)_{m'} \Delta z \rho' c'}{L_v \rho_a C_1 f_h}\right] + \left[\alpha\beta\big|_{\eta} - \alpha\beta\big|_{\eta'}\right] q_s(T_G) - \left[\beta\big|_{\eta} - \beta\big|_{\eta'}\right] q_a . \tag{5.21}$$

Using Newton's method (Conte and de Boor 1980), the iterative solution is then

$$\eta_{i+1} = \eta_i - \frac{\Delta F_i\left(\eta_i - \eta_{i-1}\right)}{\left(\Delta F_i - \Delta F_{i-1}\right)}. \tag{5.22}$$

To initialize the method, η_{-1} and η_0 are assumed to be

$$\eta_{-1} = \eta^{t-1} + 0.01, \tag{5.23}$$

and

$$\eta_0 = \eta^{t-1}, \tag{5.24}$$

where η^{t-1} is the surface soil moisture of the bare soil from the preceding time step of the model.

Since improperly initialized soil heat fluxes may for some cases prevent convergence of the method, the surface soil temperature gradient is reinitialized at the beginning of the soil moisture data assimilation period, so that $Q'_{(nzg-1)}$ is initially in balance with the satellite observations (i.e. $\Delta q_G = 0$). From Equations 2.4 and 5.16, the perturbed soil heat flux at the level immediately below the surface layer is

$$Q'_{(nzg-1)} = \left(\frac{\nu'_{nzg} + \nu_{(nzg-1)}}{2}\right)\left(\frac{\theta_{nzg} - \theta_{(nzg-1)}}{z_{nzg} - z_{(nzg-1)}}\right) = Q_{nzg} - \left(\frac{dT_L}{dt}\right)_{m'} \Delta z \rho' c'. \tag{5.25}$$

Thus the revised sub-surface soil temperature, $\theta_{(nzg-1)}$, is then,

$$\theta_{(nzg-1)} = \theta_{nzg} - 2\left[Q_{nzg} - \left(\frac{dT_L}{dt}\right)_{m'} \Delta z \rho c\right]\left(\frac{z_{nzg} - z_{(nzg-1)}}{\nu_{nzg} + \nu_{(nzg-1)}}\right), \tag{5.26}$$

where ρ and c are used as approximations for ρ' and c'. The adjustment is propagated downward into the soil model. It is weighted linearly with depth so that the top levels are affected

the most with the lowest soil temperature remaining unchanged. The model's deep soil vertical heat fluxes are then recalculated using the revised sub-surface temperatures. The deep soil temperature adjustment procedure eliminates the initial soil temperature gradient information from having an initial impact on the soil moisture retrieval results, but at the same time, allows for later soil model feedback into the system. No further soil temperature reinitialization adjustments are made during the remainder of the model run.

5.1.2.2 Vegetation Component

The vegetation surface parameterization of the CSU-RAMS model is based on a "big leaf" vegetation parameterization scheme (McCumber 1980; Avissar and Mahrer 1982; Avissar and Mahrer 1988; Avissar and Pielke 1989). The history and details of the vegetation parameterization scheme are discussed in Lee (1992). The focus of this work was not to improve the vegetation parameterization method but to assimilate the satellite-derived heating rates into the current vegetation parameterization scheme. Additional efforts are currently underway to include an improved vegetation parameterization method (Lee 1992; Walko et al. 1996) within the standard distribution of RAMS.

Recalling where the bare soil and vegetation components parted ways in the satellite data assimilation method derivation (section 5.1.2), the satellite heating rate has two parts; due to the bare soil heating rate, and due to the vegetation heating rate. For the vegetation satellite data assimilation component, the previous bare soil heating rate from the bare soil data assimilation results is used, since the actual assimilated heating rate may differ from the requested bare soil heating rate. This allows the vegetation component to compensate for any model restrictions or limitations affecting the bare soil component (this will be discussed futher in section 5.2). The satellite-derived heating rate is then simply the sum of the component heating rates,

$$\left(\frac{dT}{dt}\right)_s = f_L\left(\frac{dT_L}{dt}\right)_{m'} + f_V\left(\frac{dT_V}{dt}\right)_{m'}, \tag{5.27}$$

bearing in mind that the water covered regions were assumed in section 5.1.2 to be of constant temperature. The vegetation heating rate is given by a simple heat equation,

$$C_{veg}\left(\frac{dT_V}{dt}\right)_m = Q_{veg} \tag{5.28}$$

where the effective heat capacity of the vegetation is related to the heat capacity of water, c_w, the density of water, ρ_w, and the leaf area index (LAI),

$$C_{veg} = 0.006\, c_w \rho_w \mathrm{LAI}. \tag{5.29}$$

Combining Equations 5.27 and 5.28, an expression is obtained relating the vegetation heat flux to the satellite-derived heating rate and the previously retrieved bare soil heating rate,

$$Q'_{veg} = C_{veg}\left[\left(\frac{dT}{dt}\right)_s - f_L\left(\frac{dT_L}{dt}\right)_{m'}\right] f_V^{-1}. \tag{5.30}$$

Making the identical assumption as before in section 5.1.2.1, all the terms in the model's surface energy budget are assumed to be the same except for the latent energy term. Thus,

$$Q'_{veg} = Q_{veg} + \Delta E = Q_{veg} + L_v \rho_a u_{*_V} \Delta q_{*_V} \mathrm{LAI}, \tag{5.31}$$

represents the perturbed vegetation heat flux, where the subscript V denotes the *vegetation* friction velocity and friction humidity terms. Equations 5.30 and 5.31 are then solved for Δq_{*_V}, which results in the following,

$$\Delta q_{*_V} = \left\{ \frac{C_{veg}\left[\left(\frac{dT}{dt}\right)_s - f_L\left(\frac{dT_L}{dt}\right)_{m'}\right] f_V^{-1} - Q_{veg}}{L_v \rho_a u_{*_V} \mathrm{LAI}} \right\}. \tag{5.32}$$

Again as in section 5.1.2.1 regarding the bare soil surface similarity equations, the Louis (1979) stability adjustment functions are used to relate the surface friction humidity perturbation to the vegetation specific humidity perturbation,

$$\Delta q_{veg} = -\frac{\Delta q_{*_V} u_{*_V}}{C_1 f_h}. \tag{5.33}$$

Combining Equations 5.32 and 5.33,

$$\Delta q_{veg} = \left\{ \frac{Q_{veg} - C_{veg}\left[\left(\frac{dT}{dt}\right)_s - f_L\left(\frac{dT_L}{dt}\right)_{m'}\right] f_V^{-1}}{L_v \rho_a C_1 f_h \mathrm{LAI}} \right\}, \tag{5.34}$$

the vegetation specific humidity perturbation is related to the satellite-derived heating rate and the previously retrieved bare soil heating rate.

The vegetation specific humidity is related to the vegetation stomatal function that determines the vegetation's physical response to its environmental conditions. This controls the vegetation transpiration rate and thus is a key factor to the vegetation heating rate. The specific humidity at the leaf-air interface is computed following a procedure suggested by Avissar et al. (1985),

$$q_{veg} = q_s\left(T_{veg}\right)\left(1 - d_{stom}\right) + d_{stom} q_a, \tag{5.35}$$

where d_{stom} is the dimensionless relative stomatal conductance and is defined as,

$$d_{stom} = 1 - \left[d_c + \left(d_m - d_c \right) \frac{F_R}{\mathrm{LAI}} \prod_i f_i \right] \tag{5.36}$$

where d_c is the minimal stomatal conductance that occurs through the leaf cuticle when the stomata are closed, d_m is the maximal stomatal conductance that occurs when the stomata are completely opened, and F_R is the incident solar radiation. The environmental functions, f_i, are given by

$$f_i = \left\{ 1 + \exp\left[-S_i \left(x_i - x_{b_i} \right) \right] \right\}^{-1}, \tag{5.37}$$

where the subscript *i* represents a specific environmental factor (the subscript R represents the solar radiation , T for leaf temperature, V for vapor pressure difference between leaf and ambient air, C for ambient carbon dioxide concentration, and Ψ for soil water potential in the root zone).

Determining the vegetation specific humidity perturbation from Equation 5.35,

$$\Delta q_{veg} = q'_{veg} - q_{veg} = \Delta d_{stom} \left[q_a - q_s \left(T_{veg} \right) \right], \tag{5.38}$$

and solving for the stomatal conductance perturbation, yields

$$\Delta d_{stom} = d'_{stom} - d_{stom} = \Delta q_{veg} \left[q_a - q_s \left(T_{veg} \right) \right]^{-1}, \tag{5.39}$$

which when combined with Equation 5.34,

$$\Delta d_{stom} = \left\{ \frac{Q_{veg} - C_{veg} \left[\left(\frac{dT}{dt} \right)_s - f_L \left(\frac{dT_L}{dt} \right)_{m'} \right] f_V^{-1}}{\left[q_a - q_s \left(T_{veg} \right) \right] L_v \rho_a C_1 f_h \mathrm{LAI}} \right\}, \tag{5.40}$$

produces an expression relating the stomatal conductance perturbation to the satellite-derived heating rate and to the previously derived bare soil heating rate.

Therefore, the perturbed stomatal conductance can be determined using Equation 5.40, since

$$d'_{stom} = d_{stom} + \Delta d_{stom} . \tag{5.41}$$

Solving Equation 5.36 for the environmental factors,

$$\prod_i f_i = \frac{\left(1 - d_{stom} - d_c\right)\mathrm{LAI}}{\left(d_m - d_c\right)F_R}, \tag{5.42}$$

and then inverting the soil moisture environmental factor for the both the perturbed and nonperturbed soil moisture values yields the following equations,

$$\Psi \equiv x_\Psi = x_{b\Psi} - \frac{1}{S_\Psi}\ln\left\{\left[\frac{\left(d_m - d_c\right)F_R}{\left(1 - d_{stom} - d_c\right)\mathrm{LAI}}\right]\prod_{i\neq\Psi} f_i - 1\right\}, \tag{5.43}$$

and

$$\Psi' \equiv x'_\Psi = x_{b\Psi} - \frac{1}{S_\Psi}\ln\left\{\left[\frac{\left(d_m - d_c\right)F_R}{\left(1 - d'_{stom} - d_c\right)\mathrm{LAI}}\right]\prod_{i\neq\Psi} f'_i - 1\right\}. \tag{5.44}$$

where the product of the environmental factors is over all environmental terms except for the root zone soil moisture potential environmental factor, and

$$\Psi = \sum_i root_i \Psi_s \left(\frac{\eta_s}{\eta_i}\right)^b, \tag{5.45}$$

and

$$\Psi' = \sum_i root_i \Psi_s \left(\frac{\eta_s}{\eta'_i}\right)^b, \tag{5.46}$$

are the root zone soil moisture potentials for the non-perturbed and perturbed soil moisture profiles.

Since no observational data exists for the actual distribution of the soil moisture profile, a constant vertical soil moisture profile is assumed, so that

$$\eta_i = \eta_{i+1} \tag{5.47},$$

where i represents the soil model level. Therefore, the perturbed soil moisture profile is then

$$\eta_i' = \eta_i + \Delta\eta\,. \tag{5.48}$$

From the definition of the perturbation root zone soil moisture potential,

$$\Delta\Psi = \Psi' - \Psi\,, \tag{5.49}$$

and Equations 5.45 and 5.46, an equation relating the perturbed vegetated soil moisture to the root zone soil moisture potential perturbation is derived,

$$\eta' = \left[\frac{\left(\frac{\Delta\Psi}{\Psi_s \eta_s^b}\right) + \sum_i root_i \eta_i^{-b}}{\sum_i root_i}\right]^{-1/b}\,. \tag{5.50}$$

Thus for the satellite data assimilation method, Equations 5.29,5.36, 5.37, 5.40, 5.41, 5.43, 5.44, 5.49 and 5.50 constitute the solution for the vegetation component once the bare soil component of the data assimilation method has been previously solved.

5.1.3 Satellite Data Assimilation Method Procedure Summary

The satellite data assimilation procedure is graphically depicted in Figure 5.1. The satellite data is preprocessed to clear cloud contaminated FOVs using the dynamic infrared threshold technique that was previously described in section 4.2.2. After cloud clearing, the satellite skin

surface temperature heating rates are determined using unadjusted infrared skin temperatures for each available satellite time period and are weighted linearly in time for input into the data assimilation method. The satellite skin temperature heating rate is then first used in the bare soil component soil moisture retrieval. The target model heating rate is estimated from the previous unadjusted model component heating rates and the satellite-derived heating rate using Equation 5.7. The subsurface ground soil heat flux is then adjusted using Equation 5.26 to balance the satellite-derived heating rates and subsurface ground soil heat flux as described previously in section 5.1.2.1. Based on the satellite-derived forcing value, ΔF_{-1} and ΔF_0 are determined using Equations 5.21, 5.23, and 5.24. Similarly, the iteration loop calculates ΔF_i using Equation 5.21, and a new surface soil moisture value is estimated from Equation 5.22. The iteration is loop is exited when the soil moisture value converges to a solution, i.e., when

$$\left| \frac{\eta_i - \eta_{i-1}}{\eta_i} \right| < 10^{-5}. \tag{5.51}$$

The loop typically converges within 3-5 iterations. The target model heating rate is then recalculated using the retrieved bare-soil soil moisture and is used as input into the vegetation component soil moisture retrieval method. The vegetation soil moisture is retrieved by simply solving a series of analytical equations (Equations 5.29, 5.36, 5.37, 5.40, 5.41, 5.43, 5.44, 5.49 and 5.50). Figure 5.1 shows a simplified functional view of the vegetation-soil moisture retrieval process.

In summary, the satellite data assimilation method, has two major parts, the bare soil and vegetation components. The bare-soil soil moisture is retrieved first using an iterative method, while the vegetation soil moisture is a series of analytical solutions. The vegetation soil moisture requires as input both the satellite-derived heating rates and the retrieved bare-soil soil moisture values. Based on the RAMS model configuration that was used for this study, the satellite data

assimilation method adds approximately 8% to the overall computational time of the model. The RAMS model configuration that was used is described later in section 5.3.2.1.

5.2 1D SENSITIVITY TESTS

A one-dimensional test of the method was performed by inserting a 1D version of the satellite data assimilation method which used simulated satellite heating rates, into a small 3D version (10×10 horizontal grid with 30 grid intervals in the vertical for the atmospheric variables and 11 soil model levels) of the RAMS model. The host model's 3D boundary conditions were forced by the RAMS variable initialization procedure which is explained in more detail in section 5.3.2.1. Several tests were performed in an attempt to access the validity of the equation set derived in section 5.1.2. In this section, results are shown from a control run in which the satellite data assimilation method is turned off, and a run that was forced with a constant simulated satellite heating rate of 1 K/h. While the constant satellite heating rate is unrealistic (especially in the late afternoon, when the surface should be cooling), it exhibits several features of the data assimilation method worth noting, and thus serves as a pedagogical example.

The surface energy budget over bare soil is shown for both the control run and forced run in Figure 5.2. In the figures to be shown (Figures 5.2-5.8), time is measured in hours since the start of the simulation which began at 600 local time. Therefore, 6 hours into the simulation is roughly noon. The major features of the surface energy budget over bare soil for the control run are the large diurnal cycle of the net radiation, the small impact of the surface soil heat fluxes, and the comparable magnitudes of the latent and sensible heat fluxes. In the control run the latent and sensible heat fluxes are slightly out of phase with each other since the model was relatively wet initially (40% soil moisture). In contrast to the control run, the 1 K/hr forcing run (see Figure 5.2) has a much diminished sensible heat flux, and a correspondingly greater latent heat flux. Thus it is expected that the soil moisture for each run is rather different with presumably the 1 K/hr run

having retrieved wetter soil. The control run surface energy budget for the vegetation (Figure 5.3) shows similar features to the bare soil surface energy budget (Figure 5.2), in that the magnitude of the sensible heat flux is low while the transpiration is high. However, the forcing run surface energy budget for the vegetation shows that the sensible heat flux increases in magnitude over the course of the 1 K/h constant forcing run simulation, suggesting that the vegetation is being forced to dry out in the afternoon.

The volumetric soil moisture for the bare soil component is shown for both runs in Figure 5.4. The control run soil moisture values show that the surface model level gradually dries with time, while the lower soil moisture levels (levels 9 and 10) maintain the initial soil water content. The model effectively decoupled the bare soil surface layer from the underlying soil model levels. The forced run using a constant 1 K/h simulated satellite heating rate, shows that the data assimilation method initially moistens the surface and then saturates a little after 2 hours into the simulation (early morning). Thus the simulated satellite heating rate is too low for this early morning time period, and to maintain a balance the assimilation method adjusts the soil moisture in an attempt to reduce the bare soil heating rate to match the specified satellite heating rate of 1 K/h. After 3 hours into the simulation, the model begins to rapidly dry out, and is able to maintain a soil moisture level of approximately 0.20-0.25 for almost 5 more additional hours. Eventually, the bare soil is forced to dry out completely after 11 hours since the positive 1 K/hr heating rate is unrealistic for this time period, when in fact the model should normally be cooling the surface at this point in the simulation. To counter this natural tendency the data assimilation method completely dries the surface layer. The lower model levels of the bare soil (e.g., levels 9 and 10) lag the surface soil moisture due to diffusion of water between the model soil layers. Thus the bare soil surface energy budget partitioning mentioned previously was caused by an increase in the bare-soil soil moisture. The soil moisture limits of approximately 0.42 and 0.06 in

Figure 5.4 are due to the physical soil model properties, which for the case shown is for a sandy-clay-loam soil.

Correspondingly, the bare soil temperatures are suppressed for the data assimilation method run (Figure 5.5), since the soil moisture for the bare soil was increased initially to reduce the heating rate of the model. Thus the bare soil temperatures were most suppressed during their normal period of maximum heating. Since the bare soil temperature heating rate is reduced from the control run, the forced run soil temperatures also tend to be more closely coupled and exhibit less of a pronounced phase shift with time.

The shaded soil moisture for the control run (Figure 5.6) shows a reduced soil moisture value range than does the bare soil control run results (Figure 5.4). A unique feature of the shaded soil moisture is that the surface lags the lower soil levels throughout the day. This is because the vegetation soil moisture is primarily influenced by the vegetation transpiration and its associated depletion of the soil moisture in its root zone. Less drying occurs for the surface layer since very few roots are found in this layer and also because the canopy humidity is higher which inhibits evaporation from the surface. The data assimilation results show that initially the shaded soil is dried out to increase the vegetation heating rate, but that the method saturates after 2 hours into the simulation. A key feature to note is that the shaded vegetation saturates at a relatively low soil moisture value of 0.177 that corresponds roughly to a 50% soil moisture value, rather than 100% as the bare-soil soil moisture case did. This is due to the extreme sensitivity of the vegetation parameterization to the soil moisture potential in the root zone. From section 5.1.2.2, the environmental factors are modeled as exponential functions, thus additional moisture above 0.177 is not used and produces the same transpiration effect as does soil with a soil moisture value of 0.177. Rather than retrieve soil moisture values of 100% in the extreme cases, the data

assimilation method was restricted to retrieve soil moisture values from which a definite functional relationship existed. Thus values above or below the steep soil moisture transitional regions,

$$0.016 < \eta < 0.177 \tag{5.52}$$

are truncated to their respective limits. This prevents the erroneous retrieval of extremely high shaded soil moisture values that might persist after initialization by the satellite data assimilation method. Thus the vegetation component of the satellite data assimilation method is more sensitive to the satellite-derived heating rate than the bare soil component. However, it must also be remembered that for this case the cropland land cover classification type was used and it implicitly assumes that the vegetation fraction, f_V, is 85%. Thus for the constant satellite forcing used here, the vegetation component will shoulder a disproportionate amount of the satellite forcing burden. However, this should not be made into a generalization, in that the amount of forcing is also time dependent in the real world, while for the simplified test case the forcing was assumed fixed in time.

The vegetation and shaded soil temperatures (Figure 5.7) show an approximately linear upward trend with time for the control run case. This is due to the vegetation's ability to transpire which effectively integrates the day's heating. The forced run shows a similar temperature profile, with the main exception being the stronger linear relationship with time which is due to the constant forced heating rate imposed on the data assimilation method for that case.

The main question remains, is the satellite data assimilation method described in section 5.1.2 able to successfully assimilate the satellite heating rates? Figure 5.8 plots the satellite-equivalent model heating rate, which from Equation 5.4 is

$$\left(\frac{dT}{dt}\right)_{m'} = \left[f_L \left(\frac{dT_L}{dt}\right)_{m'} + f_V \left(\frac{dT_V}{dt}\right)_{m'} \right]. \tag{5.53}$$

The model heating rate has a significant negative spike at approximately 20 minutes into the simulation that is due to the sun rising and waking the plants up which immediately begin transpiring, thus cooling the surface. This early behavior of the vegetation parameterization is overcome quickly (within minutes) once the vegetation and surface boundary layer parameters adjust to the transpiring vegetation. The heating rate is greatest at 2.5 hours into the simulation with heating rates approaching 2 K/h (about double the forced run's 1 K/h heating rate). The dip in the heating rate at 3 hours is associated with an increase of the surface boundary layer wind speeds. Thus the grid element represented by this plot receives a cooling shock from which it recovers in about 30-45 minutes. The remainder of the day has relatively uniform heating rates which hover around 1 K/h, until late afternoon when the model begins to cool again. The forced run with a 1 K/h simulated satellite heating rate, shows similar features in early morning. This is because the satellite data assimilation method is not turned on until the sun rises and the model heating rate becomes positive. The method is started later to allow the vegetation to begin transpiring so that the vegetation component of the data assimilation method can converge to a valid solution, otherwise the vegetation environmental factors (particularly the shortwave radiation factor) effectively cause the vegetation component to be inactive. The satellite data assimilation method is able to quickly reach the desired 1 K/h heating rate specified for the forcing run. This is successfully maintained throughout an 8.5 h period. Only two instances occur where the satellite data assimilation method is unable to keep the model's heating rate at 1 K/h. The region from 2-3 hours into the simulation corresponds to the flooded conditions of the soil for both the bare and shaded soil (see Figures 5.4 and 5.6). The model is unable to make the model any wetter and thus continues to heat at a rate above the 1 K/h target rate. The lower heating rates after 9.5 hours into

the simulation for the forced run are associated with the vegetation drying out completely (see Figure 5.6). Thus the model can not dry the soil any further to maintain the high heating rates. The satellite data assimilation method does converge to a reasonable solution for all conditions that are not too wet or too dry for the model to handle. Thus the satellite data assimilation method performs only as well as the land surface parameterization allows it.

5.3 CASE STUDY RESULTS

The satellite data assimilation method was used in a 3D case study over the central United States. A day was selected from the intensive satellite data analysis during the late summer of 1991 which was previously discussed in Chapter 4. In particular, the case of 8 September 1991 was selected due to the mostly clear morning conditions over the central Great Plains, the development of an afternoon dryline, and the relatively high spatial contrast of the microwave surface emittance results indicating heterogeneous surface wetness conditions. The synoptic situation for the day is discussed in section 3.6.2. Additional surface observations are compared with the case study model run results later in section 5.3.2.

5.3.1 Remote Sensing Data

5.3.1.1 Visible and Infrared Imagery

A selected time series from the available 30 minute interval data set of the GOES-7 VISSR visible and infrared imagery for 8 September 1991 is shown in Figures 5.9-5.11. The morning begins with clear skies over the western part of Kansas and Oklahoma, and low stratus and ground fog over the eastern half of the region (Figure 5.9). The main region of ground fog is in the south central part of Kansas. Broken fog conditions lingered in this region past local noon (Figure 5.10). Brightness temperatures over the fog at 1501 UTC and 1601 UTC showed infrared temperatures of approximately 297 K (or 75° F), which are within 2 K of the surface shelter

temperatures observed at this time. The low stratus deck in the extreme northeast quadrant of the sector and throughout most of Oklahoma moves slowly eastward with time as observed in a 30 minute interval time loop of the imagery. The stratus deck was most persistent in the Oklahoma region, but became more broken in nature as time elapsed (Figures 5.9-5.11).

Convection along the dryline near the east part of the Oklahoma panhandle begins to form by 1801 UTC (Figure 5.10). Within 2 hours, 3 small thunderstorms have formed along a dryline that is oriented southwest to northeast. An hour later at 2101 UTC (Figure 5.11), the storms have dissipated, with their anvil remains drifting northeastward. The infrared imagery (Figure 5.11a) depicts the anvil remains more clearly than does the visible imagery (Figure 5.11b). Also at 2101 UTC the dryline cumulus field begins to broaden spatially, and the most significant convection begins to form on the west and east edges of the cumulus field by 2201 UTC (Figures 5.11c and d). This convection also dies out within the next couple of hours. The most significant storm on this day occurred much later in the evening and in the extreme northeast portion of the sector shown in Figures 5.9-5.11. The overall motion of the dryline was stagnant with little east-west propagation observed. However, the dryline continually reformed over the course of the day with the most recent convection initiating westward of the older convection and then advecting eastward until it dissipated to again be formed west of its current location. Thus the overall motion of the dryline was confined to a nearly stationary position due to its redevelopment.

5.3.1.2 Radar Summaries

The National Weather Service (NWS) radar summary reports for the case study region (Figures 5.12 and 5.13) show that on the previous day this region experienced widespread rain over the eastern portion of Kansas and most of Oklahoma, while the western portion of the region did not experience any significant rainfall events. The general pattern of the rain was associated

with a line of precipitation oriented north-south slowly propagating eastward as mentioned in section 3.6.2. Within this line individual storms were moving to the north or northeast. Thus precipitation fields produced by this rainfall pattern tend to be oriented north-south following the track of the individual storms. Most of the precipitation had moved out of the Kansas/Oklahoma region by 8 September 1991 at 600 UTC.

The convection that developed on 8 September 1991 is first indicated on the radar summaries at 2135 UTC, which corresponds to the second round of convective activity on the dryline. The severe thunderstorm watch box (valid from 1951-0200 UTC) issued for central Kansas is indicated by the dashed lines in Figures 5.13d, e, and f. A second severe thunderstorm watch box (valid from 2018-0300 UTC) was issued for a large part of the Texas panhandle (Figures 5.13e, and f). Most convective activity on 8 September in the Kansas/Oklahoma region was light, except for one hail producing storm that developed near sunset in north central Kansas which formed on the north part of the dryline observed in Figures 5.9-5.11.

5.3.1.3 Microwave Surface Emittance Results

Atmospheric-corrected microwave surface emittance results for 8 September 1991 1529 UTC (Figure 5.14) indicate a strong depression of the microwave surface emittance values in south central Kansas and for a small region in north Oklahoma (microwave surface emittance statistics for the entire 70 day dataset are shown in Figures 4.30-4.34 and in Appendix E). The region of low microwave surface emittance values is apparent in both the vertical and horizontal polarizations. However, the horizontal polarization is most affected by the rain event from the previous day. The resolution dependence of the microwave surface emittance results is also obvious from the results shown in Figure 5.14. From this data, surface flooding and generally wet soil conditions are expected for the regions where $\varepsilon_V < 0.92$ (denoted by green areas in Figure 5.14), and $\varepsilon_H < 0.85$ (denoted by blue areas in Figure 5.14). The microwave surface emittance horizontal

polarization results at the frequencies of 19H, 37H and 85H GHz are comparable in magnitude, but with a noticeable refinement in the resolution with higher frequency. The reduction of the spatial extent of the areas where $\varepsilon_H < 0.85$ is related to the reduced sensitivity of the 85 GHz channel to the soil features (see results from section 4.3.5). However, for regions which have standing water or extremely wet conditions, the 85H GHz frequency might be used to locate regions of surface flooding, whereas the low frequency microwave surface emittance results would be more indicative of less severely flooded conditions, and would have a wet soil categorization that is broader in scope. The vertical polarization results show a similar frequency dependency as did the horizontal polarization results, except that the low frequency results (19V and 37V GHz) appear to be less sensitive to vegetation and/or microwave surface roughness features (see also the discussion in Appendix sections A.3.5 and A.3.6). Thus the lower 85V GHz microwave surface emittances in western Kansas, and to a lesser extent the 37V GHz microwave surface emittances, appear to be related to the vegetation and microwave surface roughness effects. This exemplifies the complexity and difficulties involved with using the microwave surface emittances as a direct measurement of surface wetness conditions. This was the motivational source for using the infrared surface skin temperature heating rates as a preferred method over the microwave surface emittance for direct coupling of the satellite-derived surface wetness information and the atmospheric model.

5.3.1.4 Diurnal Surface Skin Temperature Results

Cloud-cleared GOES VISSR infrared brightness temperatures were used to produce non-atmospheric-corrected surface skin temperature heating rates for 8 September 1991 at 1501, 1531, and 1601 UTC for input into the satellite data assimilation method (Figure 5.15). In Figure 5.15, high satellite-derived heating rates are shown as light shades of gray, while darker shades represent low heating rates. The spatial distribution of heating rates indicates that the

western half of the sector shown in Figure 5.15 experienced relatively high heating rates (up to 5 K/h) compared to the eastern portions of Kansas and most of Oklahoma that had some locations with heating rates of nearly 0 K/h. As mentioned previously (section 5.3.1.1), broken ground fog did exist in south-central Kansas during this period. Consequently, the heating rates are actually ground fog cloud top temperature heating rates, but when the satellite-derived heating rates are compared with surface observations in this region, they are found to be comparable to the shelter temperature heating rates (see Figures 5.16 and 5.17). Therefore the satellite-derived heating rates are not seriously in error for the ground fog conditions. However, the model's solar heat fluxes would almost certainly be over estimated by the model's solar radiation parameterization under such conditions, since the solar parameterization does not allow for cloudy conditions. The satellite-derived heating rates shown in Figure 5.15 are also relatively stable in appearance between the 30 minute sampling intervals. In addition, the linear time sampling performed by the satellite data assimilation method also tends to smooth out some of the instrument noise.

Since the satellite-derived heating rates are produced from two different VISSR images, the satellite navigation can change between images and produces a rather noisy appearance in the satellite heating rates shown in Figure 5.15. The noise is particularly noticeable with streaks in the east-west direction since the VISSR instrument has a rectangular FOV that over samples in the east-west direction. Therefore, any north-south satellite navigation adjustments between image times are more noticeable, since over sampling does not occur in the north-south direction and instead produces east-west streaks in the dataset. The instrument noise of the GOES-7 VISSR channel 8 sensor has been estimated to be approximately 0.2 K (see Table 3.1). This provides a signal to noise ratio of about 25:1 (5 K / 0.2 K). A noise sensitivity experiment using the satellite data assimilation method is performed later in section 5.3.3.

5.3.2 Model Runs

Three 12 h 3D model runs using variable initialization forcing from observed synoptic conditions were performed to test the satellite data assimilation method. The first was a controlrun (CONTROL) in which no satellite-derived heating rates were used to force the surface land vegetation parameterization scheme. The second model run (SAT) was with the satellite data assimilation method turned on between 1500 and 1600 UTC, with the remainder of the SAT run being the same as CONTROL, but with the satellite soil moisture as derived from the 1500 to 1600 UTC forcing period. The third run (DRY) was performed as a sanity check in which the model soil was initialized as completely dry to assist in determining the relative importance of the day's synoptic environment to that of the surface conditions. The model configuration and initialization are described in section 5.3.2.1, while the model results are presented and discussed in subsequent subsections.

5.3.2.1 Model Configuration

The CSU-RAMS, Version 3a, atmospheric mesoscale model (Pielke et al. 1992) was configured to run as a three-dimensional, non-hydrostatic, compressible, primitive equation model. The surface layer parameterization has already been described in section 5.1.1 and will not be repeated here. The model was run in a nested grid configuration with 2 grids initially, with a 3rd grid added after 1000 LST (i.e., 4 hours after the start of the model simulations). The model grid specifications are listed in Table 5.1. The model had 30 vertical levels and 11 soil model levels in each grid, with horizontal grid intervals of 40 km, 10 km, and 5 km on grids 1, 2, and 3, respectively. The vertical coordinate is a terrain following sigma coordinate system that had a minimum vertical spacing of 100 m at the surface and was stretched by a factor of 1.15 to a 1 km maximum vertical interval. The model top was a rigid lid at 17.5 km with nudging toward observations at the top 5 boundary points to dampen gravity waves. The soil model depths and initial soil

temperature offsets from the lowest atmospheric temperature are specified in Table 5.2. The soil layers nearest the surface were 3 cm in depth, with lower levels becoming progressively thicker, up to a 10 cm thick slab for the lowest soil model layer. The location of the first two grids was centered on 38° N, -99° E (see Figure 5.18), while grid 3 was offset slightly to the west and had center coordinates of 38° N, -100° E (see Figure 5.19).

The model option input list used to specifiy the numerics and physical parameterizations is given in its entireity in Appendix H. A few of the model parameterization options are highlighted.

- A hybrid timestep scheme was used. A centered difference scheme was used on momentum variables, while a forward in time difference scheme was used on scalar variables. Both methods used second order advection.

- A Smagorinsky deformation-based K (Smagorinsky 1963) with stability modifications (Lilly 1962) was used for vertical and horizontal turbulence above the surface layer.

- Water vapor advection and cloud water condensation microphysics was turned on in the model (RAMS level 2 microphysics). No ice species or other more advanced conversion processes were allowed. This saves a considerable amount of processing time. Thus the primary focus from the model results should be the water vapor fields and the initial location of the cloud fields. Subsequent convective development is beyond the scope of this work and due to this model option setting should not be expected to perform realistically.

- The Mahrer-Pielke (Mahrer and Pielke 1977) longwave and shortwave radiation parameterization was used. This parameterization does not include cloud effects. It was activated every 60 s and was coincident with the grid 1 model timestep. Usually the radiation tendencies can be calculated at longer timestep intervals, however updated radiation parameters were required for each time step in which the satellite-derived heating rates were ingested.

5.3.2.2 Model Initialization

The BATS land classification categories (see section 5.1.1) for grid 2 are shown as an example of the vegetation heterogeneity in the model initialization that was provided by the USGS NDVI vegetation database (Loveland et al. 1991) (Figure 5.20). The major vegetation classification is cropland, followed by evergreen shrub. The vegetation classifications are from a 1 km resolution database that is interpolated to the respective grids of the model, in a manner very similar to that of the topographic data. Constant LAI values are used to represent their entire respective vegetation classification category. Following Shaw (1995) and Grasso (1996), the LAI values for each vegetation classification were modified to limit the maximum LAI index to a value of 3. This prevents unrealistically large surface fluxes in the model due to incorrect specification of this parameter. The resulting LAI values conform more reasonably to the LAI values derived by Lee (1992) using a method based directly on the NDVI.

The model was nudged by surface and sounding observations from 8 September 1991 1200 UTC and 9 September 1991 0000 UTC archived synoptic data on grid 1. The synoptic data is described in more detail in section 3.3.1. The zone of nudging was 5 lateral boundary grid elements, with nudging also specified for the top 5 grid levels of the model. The nudging is weighted so that the outer-most grid elements are weighted the heaviest with decreasing weights toward the model center (only up to 5 grid points into the model). Over 80% of grid 1 experiences no direct forcing from the observations, and grids 2 and 3 experience no direct observational lateral boundary condition forcing at all.

5.3.2.3 CONTROL Results

As previously mentioned in section 5.3.2, the CONTROL run used no satellite-derived heating rates to force the surface land vegetation parameterization scheme. Initial soil moisture was initialized homogeneously throughout the model domain at 25% of soil capacity. Results of that

simulation at 1200, 1600, 2000, and 0000 UTC are shown in Figures 5.21-5.24, where quadrant a) is a plot of the surface air temperature, b) is the bare-soil soil temperature, c) is the mixing ratio, and d) is the grid 1 surface wind speed with vectors indicating wind direction and relative magnitude based on the size of the vector arrows. Grid 1 winds are shown due to the extremely small font of the grid 2 wind vectors; however, the wind speeds and directions are nearly identical with the nested grid results, with exceptions noted below.

The 1200 UTC results (Figure 5.21) are from the model's objective analysis of the archived surface observations and thus represent the atmospheric conditions at 1200 UTC interpolated to the model's grid configuration. The dryline feature described earlier in section 5.3.1 is located in western Kansas (Figure 5.21c) at this time. Strong southerly and southwesterly winds are prevalent over a wide portion of the grid 2 domain. A wind speed maxima exists in central Kansas with winds reaching over 7 m s^{-1}. As will be shown later, the strong winds in this particular case study hampered the overall performance of the satellite data assimilation method. A region of rather calm wind conditions exists over western Nebraska and the High Plains of Colorado. This feature persisted throughout the simulation (see Figures 5.21d-5.24d), and was in good agreement with the surface observations during the period, in that extremely weak upslope (east winds) conditions began in late afternoon in the Colorado High Plains. Peak winds were slightly less in the model simulation than in the real world by about 1-2 m s^{-1}. Winds were slightly higher on the nested grids (0.5 to 1.0 m s^{-1}) which had smaller grid intervals, thus suggesting that higher model resolution would increase the maximum winds in the model. The model was also able to successfully propagate the water vapor mixing ratio gradient contrast eastward in time (see Figures 5.21c-5.24c). The orientation of the dryline and its placement in the afternoon is nearly identical to the satellite observations (Figures 5.9-5.11). Thus the model simulated the actual wind fields rather well during the period.

The dryline water vapor mixing ratio gradient was very weak throughout the simulation, except for a small region in the Oklahoma panhandle during 2300-2400 UTC (Figures 5.21c-5.24c). This model behavior is expected from earlier work with homogeneous soil moisture simulations by Shaw (1995) and Ziegler et al. (1995). The tightening of the water vapor mixing ratio gradient in the Oklahoma panhandle region was traced to the formation of convection along the dryline feature that began at approximately 2300 UTC (Figure 5.25). Thus the sharpening of the water vapor mixing ratio gradient appears to be connected to the microphysical parameterization of the model and its associated latent heat release that provides a feedback mechanism between the local circulations and the convection on the dryline. This effect will be readdressed in the analysis of the SAT simulation results in section 5.3.2.4. The dryline convection was also reduced in overall magnitude compared to the satellite observations (Figures 5.9-5.11), suggesting a lack of sufficient surface heating, or other convective initiation mechanism in this region, or possibly a need for cloud ice microphysics. The cloud features in eastern Colorado in Figure 5.25 occur in a region that experienced scattered thunderstorms as seen from the radar dataset (Figures 5.12-5.13); however, the actual placement of the High Plains convection appears to be slightly incorrect, but again this is within the performance capabilities that can be expected of this homogeneously initialized simulation.

Maximum surface air temperatures reached 34° C (93° F) in Kansas and Oklahoma. Observations reported highs of 97° F and 99° F for Hill City, KS (HCL) and Dodge City, KS (DDC) (see Figures 5.26-5.27). Thus the model under-estimated the maximum air temperatures for the day by approximately 3 K.

Figures 5.21e-5.24e and 5.21f-5.24f depict the model's surface latent and sensible heat fluxes. The general pattern is of an east-west gradient, with regions to the east having higher latent heat fluxes and lower sensible heat fluxes than the western regions. Since an initial soil

moisture gradient was not imposed, this pattern is primarily produced by the vegetation parameterization that relies on the statically defined vegetation categories (Figure 5.20). Surface radiative cooling dominates the sensible heat flux by late afternoon (0000 UTC) and produces negative sensible heat fluxes (Figure 5.24f).

Overall the CONTROL simulation does a remarkable job at simulating the location and orientation of the dryline. Some deficiencies were noted in lower than expected maximum surface air temperatures, but all-in-all the CONTROL simulation produced very respectable results.

5.3.2.4 SAT Results

The satellite data assimilation method consists of 4 basic steps (see Figure 5.28). The microwave surface emittance dataset discussed in Chapter 4 is used as a subjective filter to select case study days that have significant surface soil moisture heterogeneity (Step 1). As shown in Chapter 5, the microwave surface emittance does not exhibit an obvious direct relationship with the vegetation, or a consistently strong antecedent precipitation signal. Thus for implementing a quantitative satellite data assimilation technique, the infrared satellite dataset from GOES is used in conjunction with the satellite data assimilation method derived in section 5.1. The standard RAMS initialization procedure is then performed using a static vegetation classification database (Step 2). Atmospheric variable initialization from archived surface and upper air data sets is then performed and creates a dataset from which the model is nudged on its grid 1 boundaries (Step 3) (see section 5.3.2.2). The satellite derived heating rates are then used as input for the satellite data assimilation method during a selected period of the model simulation (preferably in the morning when the surface soil and vegetation temperature response is the strongest). For the 8 September case study, the satellite data assimilation method was turned on between 1500 and 1600 UTC due to unfavorable cloudy conditions during the remainder of the morning hours. If optimal morning clear-sky conditions existed, the satellite data assimilation method could have easily been

implemented for longer period (e.g., 4 h) with minimal modifications. After the initial satellite data assimilation period, the satellite data assimilation method is turned off, and the model continues execution using the standard surface parameterization scheme (see section 5.1.1).

Results from the SAT simulation are shown in Figures 5.29-5.33. Apart from the surface soil temperature field, and latent and sensible heat flux fields, the SAT simulation results are very similar to the CONTROL run results shown in Figures 5.22-5.24. The surface air temperatures are generally within 1 K of the previous results and surface wind speed and directions are nearly the same. However, a slight strengthening of the winds is seen in the SAT simulation results, especially at 1800 UTC (Figure 5.30d) with winds exceeding 10 m s^{-1} in eastern Kansas. These winds are in slightly better agreement with the surface observations of up to 25 knot (10 m s^{-1}) surface winds, but the overall difference between the CONTROL and SAT wind fields is small. The wind minimum in western Nebraska and eastern Colorado appears in the SAT simulation as it did in the CONTROL simulation results and no significant differences are noticeable.

The surface water vapor mixing ratio field does exhibit a notable difference between the CONTROL and SAT simulation results. The water vapor mixing ratio gradient sharpens throughout most of the length of the dryline in Kansas and Oklahoma. Previously only a tight gradient existed in the Oklahoma panhandle region, and it was found to be associated with convection along the dryline. The cloud field of the SAT simulation results shows no model convection along the dryline feature in Kansas or Oklahoma (Figure 5.34). Thus the weak satellite-derived surface water vapor mixing ratio gradient tightening is not caused by convection and related latent heat release due to the cloud microphysics. However, the convection in the High Plains of Colorado is similar to that of the CONTROL simulation results (see Figure 5.25). West to east water vapor mixing ratio cross sections located in the middle of grid 3 (Figure 5.35) show the intensification of the dryline gradient for the SAT simulation results as compared with the

CONTROL simulation results. The SAT simulation results also indicate that the west part of grid 3 is drier than the control run simulation results. Even accounting for the tightening of the water vapor mixing ratio gradient, the overall differences between the simulations are rather small. The location and orientation of the dryline were unchanged between the simulations.

The extra structure contained in the surface soil temperature field, and the latent and sensible heat flux fields (see Figures 5.29b-5.33b, 5.29e-5.33e, and 5.29f-5.33f) can be attributed to the altered soil moisture assimilated into the model surface parameterization scheme. The surface bare-soil soil moisture expressed as a percentage of the field capacity of the soil for grid 2 is shown for both the CONTROL and SAT simulations for 1600, 1800, 2100, and 0000 UTC in Figures 5.36 and 5.37. Quadrants a) and c) represent the CONTROL run results, and quadrants b) and d) represent the SAT simulation results. In Figures 5.36-5.39, the east part of the domain, the lower Texas panhandle, and the northwest corner, are cloud covered during the data assimilation period and thus have soil moisture values that are equivalent to the CONTROL simulation results. The bare-soil soil moisture results show that the satellite data assimilation method retrieved very dry conditions for western Kansas and wetter conditions farther east. It is interesting that the orientation of the bare-soil soil moisture discontinuity in central Kansas is the same as that of the dryline which forms later that day. However, little can be drawn from this fact since it appears simply fortuitous, in that the CONTROL simulation results appear to be quite able to form the dryline in the correct location without the additional satellite information. The bare-soil soil moisture dries down quite rapidly in the model, until at 0000 UTC there is little structure left of the heterogeneous soil moisture field. The shaded-soil soil moisture results (Figures 5.38 and 5.39) exhibit similar spatial features as the bare-soil soil moisture fields, except that the contrast between the wet and dry soils is reduced and additional horizontal variability exists in the shaded-soil soil moisture fields. The enhanced shaded-soil soil moisture variability is due in part to the

surface vegetation parameterization scheme, since different vegetation classification types transpire differently in the model. Additionally, the vegetation can have a strong sensitivity to the environmental forcing functions that are used to control the stomatal conductance of the vegetation, so small relative changes in environmental conditions can produce significantly different plant evapotranspiration rates.

West to east cross sections of the surface bare-soil and shaded-soil soil moisture fields from grid 3 for both the CONTROL and SAT simulations are plotted at 1600, 2000, 0000 UTC in Figures 5.40 and 5.41. From Figure 5.40, an obvious contrast can be made between the homogeneously initialized CONTROL results versus the SAT results. The CONTROL simulation results show that over the entire domain drying is occurring, with slightly more drying in the west portion of the grid domain. The satellite data assimilation results indicate that additional soil moisture has been added in the east, however the absolute soil moisture amount added is relatively small. The maximum soil moisture amounts approach 30% of the soil moisture capacity of the soil which is contrasted with 23% soil moisture in the CONTROL simulation results. The 7% soil moisture increase is rather disappointing, especially given the microwave surface emittance results that suggest surface flooding conditions for the same region (Figure 5.14). Drying over the western half of grid 3 appears to be limited by the model's sensitivity to low soil moisture values, thus forcing the data assimilation method to rely upon the dry threshold limit for the soil moisture calculations (see section 5.1.2.1). However, the relative spatial contrast of the soil moisture values however appears to be excellent at 1600 UTC, with the region of maximum rainfall from the radar summary reports (Figures 5.12 and 5.13) and API results (Figure 5.42), correlating well with the retrieved bare-soil soil moisture results. Another notable feature of the bare-soil soil moisture results is the rapid drying that occurs after 1600 UTC. Within 4 hours, the soil moisture has been reduced to within 2% of its 0000 UTC soil moisture value. This significantly hampers

any eventual effect the satellite data assimilation method can have on the atmospheric phenomena during the afternoon, since the soil moisture has already been removed at this point by strong bare-soil evaporation in the model. The shaded-soil soil moisture cross section shows a pattern that is similar (in a gross sense) to the bare-soil soil moisture cross section, in that regions that are wet in the bare-soil soil moisture field are also wet in the shaded-soil soil moisture field. The main differences between the shaded-soil and bare-soil soil moisture fields are the enhanced variability in the shaded-soil results that was noted earlier in the horizontal surface plots, and that the drying rate of the shaded-soil is more uniform as a function of time. The uniformity of the drying rate is associated with the data assimilation method's initialization of the entire root zone of the vegetation. Thus a larger reservoir is available to draw upon throughout the simulation. Another factor is that if the vegetation is sufficiently wet, the transpiration rate is relatively constant. Thus changes to the soil moisture of wet vegetation would occur at a nearly constant rate, until the vegetation reaches its wilting point, or an environmental factor (other than the root zone soil moisture potential environmental factor) changes to a new regime (e.g., sunset).

The similarities of the CONTROL and SAT simulations also extend vertically into the atmospheric model. A west to east vertical cross section of the water vapor mixing ratio at 2000, and 0000 UTC is shown for the CONTROL and SAT simulation results in Figures 5.43 and 5.44. An active boundary layer is seen in both simulations at 0000 UTC, with a more stratified boundary layer earlier in the day. Only small differences are apprent in a comparison between the results. The differences which do exist are mainly related to the surface water vapor mixing ratio field which has been discussed previously.

5.3.2.5 DRY Results

A DRY simulation run was performed to examine the effect of the rapid dry down of the model's surface soil moisture and its impact specifically on the initiation of the dryline. The soil

moisture (both bare and shaded) in the DRY simulation was initialized at 4% soil moisture, which is the minimum soil moisture allowed in the model soil, but otherwise it was allowed to run with the same conditions as the CONTROL simulation. The DRY simulation results at 1800, and 0000 UTC are shown in Figures 5.45 and 5.46. The main differences from the CONTROL and SAT simulation results are the slightly increased surface air temperature (about 0.5 K), increased bare-soil surface temperature (approximately 2-4 K warmer), and the corresponding increase and decrease in the sensible and latent heat flux values, respectively. The wind field pattern is not significantly different. The water vapor mixing ratio field shows that the dryline is stronger for the DRY simulation than for either the CONTROL or SAT simulations, but of the two it is more similar to the CONTROL simulation concerning the location of the gradient tightening. However, upon examination of the vertically integrated cloud water field (Figure 5.47), it is seen that the convection along the dryline in the Oklahoma panhandle is stronger in the DRY simulation results than for the CONTROL results (Figure 5.25). Thus the enhanced surface temperatures of the DRY simulation were able to strengthen the surface circulations by adding energy into the system. The timing of the initial dryline formation was the same (within 10 minutes) for the CONTROL and DRY simulation results. This suggests that the extremely sharp water vapor mixing ratio gradient tightening (described by Shaw (1995), Ziegler et al. (1995), and Grasso (1996) for example) is associated with initial convection and the microphysical latent heat release. A more general and less extreme water vapor gradient tightening is associated with the soil moisture initialization, which in turn may provide a focusing mechanism for initial convective formation along the dryline. The modeling results from this single case study were not sufficient to confirm this hypothesis.

5.3.3 Noise Sensitivity

A NOISE simulation was performed to determine the sensitivity of the method to noise. The simulation added 0.2 K of Gaussian noise to the satellite infrared brightness temperatures. This effectively doubles the instrument noise in the retrieval system (see Table 3.1). The soil moisture retrieval results (Figure 5.48) were found to be nearly the same as the SAT simulation soil moisture results (Figures 5.36-5.39). The same spatial features are evident in both simulations with generally dry conditions in western Kansas and wetter conditions in the east. The orientation and position of the soil moisture discontinuity are the same in both simulations. A west to east cross sectional view (Figure 5.49) shows that the magnitudes of soil moisture values at 1600 UTC (the end of the satellite data assimilation period) are also very similar to the previous SAT simulation results (Figure 5.40 and 5.41). Some small variability can be noticed in the bare-soil soil moisture results, but the overall differences are very small. The shaded-soil soil moisture appears to have slightly more variability due to the added noise compared to the bare-soil soil moisture. However, again the effect is small. The NOISE soil moisture retrievals are not significantly different from the SAT simulation results. This shows that sensor instrument noise is not a significant factor in the soil moisture retrieval accuracy, given the other static model inputs (e.g., vegetation classification). Since small differences were found in the 1600 UTC soil moisture fields, it is expected that the atmospheric model results at later model integration times would also be very similar to the SAT simulation results. This is what is found (Figure 5.50). Nearly identical atmospheric fields are found in the NOISE simulations results as compared to the SAT simulation results. The noise sensitivity experiment has shown that the satellite data assimilation method is not highly sensitive to the satellite instrument noise characteristics.

5.4 SUMMARY

In this chapter, a satellite-coupled data assimilation method using GOES infrared heating rates has been developed and tested. The satellite data assimilation method is an extension of McNider et al.'s method (1994). The data assimilation is separated into two parts, a bare soil component and a vegetation component. The addition of a vegetation component in satellite data assimilation is a new concept. The major assumptions of the method are, 1) that the discrepancies between the model's heating rate and the satellite-derived heating rates are related exclusively to the model's evaporation and transpiration rates which are then adjusted into balance with the satellite observations (McNider's assumption), and 2) that the model adequately predicts the relative heating rates of the bare soil and vegetation components (a new assumption introduced in this work). Also, an inherent assumption is that the model's surface parameterization is adequate to explain the physical features observed by the satellite. The satellite data assimilation method is developed as a two part solution, with an iterative solution for the bare soil component, and an analytical solution for the vegetation component (Figure 5.1). An advantage over the McNider et al. (1994) method is that the problematic C_b term in the McNider method is removed (see section 2.4). Thus the satellite data assimilation method is entirely objective and not subject to possible tuning parameters that may be highly variable or non-physical. The method was found to add about 8% to the overall computational time of the model simulation during the model integration period in which the satellite data is assimilated.

1D tests were used to explore the characteristics of the satellite data assimilation method. Physical limitations of the current RAMS surface parameterization were found to constrain the ability of the satellite data assimilation method retrievals of soil moisture. The physical limitations include the environmental stomatal control functions, specification of the soil type with its associated soil heat capacities and field capacities, and a constant surface albedo, among other

model surface parameters which are assumed to have known initial values. Limits were imposed within the satellite data assimilation method to prevent over forcing of the soil moisture due to indeterminate model conditions. This limits the satellite data assimilation method to retrieving relatively low soil moisture values, since high soil moisture values have a minimal sensitivity to the vegetation transpiration rates due to the particular environmental root zone soil moisture factor implemented in the RAMS vegetation parameterization. In addition, the 1D tests confirmed that the data assimilation method is able to correctly force the model component heating rates to match the satellite observations.

A case study was selected to apply the method to a period with known surface soil moisture heterogeneity. The focus of the study was on a weak dryline feature in western Kansas and the Oklahoma panhandle. The CONTROL simulation performed very well for the period selected with a few deficiencies noted such as slightly cooler surface air temperatures west of the dryline. The corresponding SAT simulation that used the satellite data assimilation method was able to successfully retrieve wetter soil conditions east of the dryline feature and dry conditions west of the dryline. The orientation and placement of the retrieved heterogeneous soil moisture field corresponded to the dryline orientation and placement. However, the CONTROL simulation was also able to correctly place the dryline feature. thus it seems that no firm conclusion can be made about the data assimilation method's impact on changing the location of the dryline, since the dryline feature did not change locations between the simulations. The SAT simulation increased the water vapor mixing ratio gradient throughout the length of the dryline in central Kansas; however, convection was suppressed in the SAT simulation results compared to the CONTROL. To test the cause of the dryline convection, a DRY simulation run was performed with 4% homogeneous soil moisture. This run was also able to form convection along the dryline in the panhandle of Oklahoma. The extreme tightening of the water vapor gradient in the panhandle region

appears to have been caused by the latent heat release due to convection. Since the SAT simulation did not develop the convection, the extreme tightening of the water vapor gradient shown by authors such as Shaw (1995), Ziegler et al. (1995), and Grasso (1996), did not appear in the SAT simulation results. Regions in the SAT simulation where the data assimilation method initialized the bare-soil soil moisture as being wet were found to dry out too quickly. Thus the influence of the heterogeneous soil moisture initialization was rather temporary in its effect. Differences in the atmospheric fields between the SAT and CONTROL runs at the end of the 12 h simulation were rather small.

A simple noise sensitivity test was also performed which doubled the GOES infrared sensor instrument noise. The impact of the extra noise on the satellite data assimilation method was found to be minimal. The retrieved soil moisture values were nearly identical to the previous SAT simulation results, and correspondingly the atmospheric fields were also not significantly affected by the extra noise in the data assimilation method. Thus the satellite data assimilation method is not highly sensitive to instrument sensor noise.

Overall, the satellite data assimilation method was able to successfully retrieve realistic heterogeneous surface soil moisture fields for assimilation into the model's surface parameterization scheme. While internally consistent with the model's surface parameterization scheme, and thus correct from the model's perspective, the range of soil moisture values appeared to be somewhat smaller than what the atmospheric conditions in the late afternoon implied were needed to initiate the convection along the dryline. So in this sense, other than improving the water vapor gradient of the model in general, the satellite data assimilation method failed to improve the final forecast of the model. The satellite data assimilation method proved in this case to be more useful as a tool for the analysis and tuning of the model's surface parameterization scheme. Suggestions for future work along these lines are mentioned in section 6.5.

Table 5.1: RAMS model grid specifications.

	grid 1	grid 2	grid 3
x grid intervals	68	118	100
y grid intervals	68	130	100
z grid intervals	30	30	30
soil grid intervals	11	11	11
Δx (km)	40	10	5
Δy (km)	40	10	5
Δt (s)	60	20	10

Table 5.2: RAMS soil model grid specifications.

Soil level	Depth (cm)	Initial soil temperature offset from lowest atmospheric level (K)
1	50	5.0
2	40	5.0
3	30	5.0
4	25	5.0
5	20	3.5
6	16	2.0
7	12	0.5
8	9	-1.0
9	6	-1.5
10	3	-1.8
11	0	-2.0

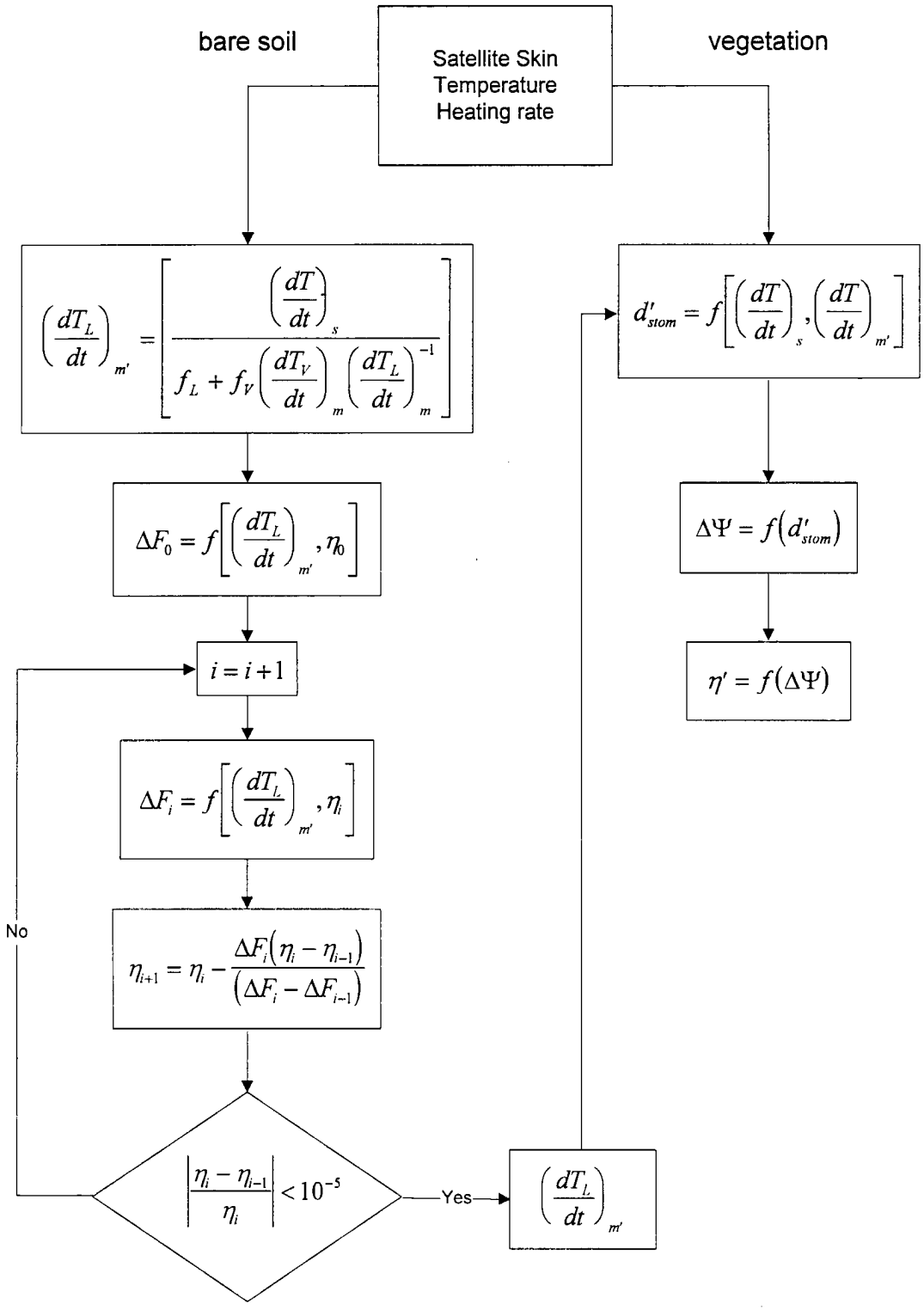

Figure 5.1: Flowchart of the satellite data assimilation process. The procedure is discussed in the text.

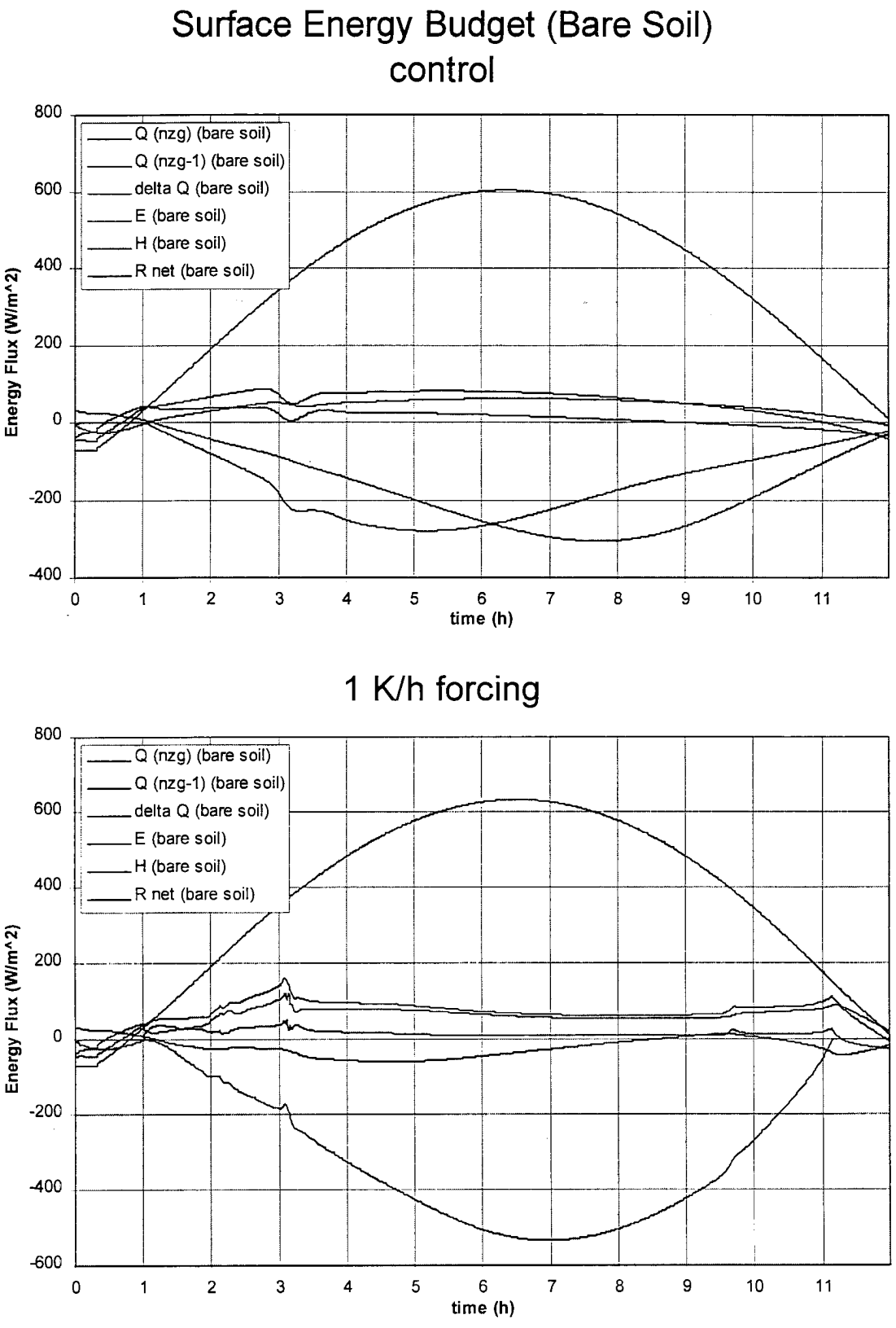

Figure 5.2: Bare soil surface energy budget for the control and for 1.0 K/h constant forcing.

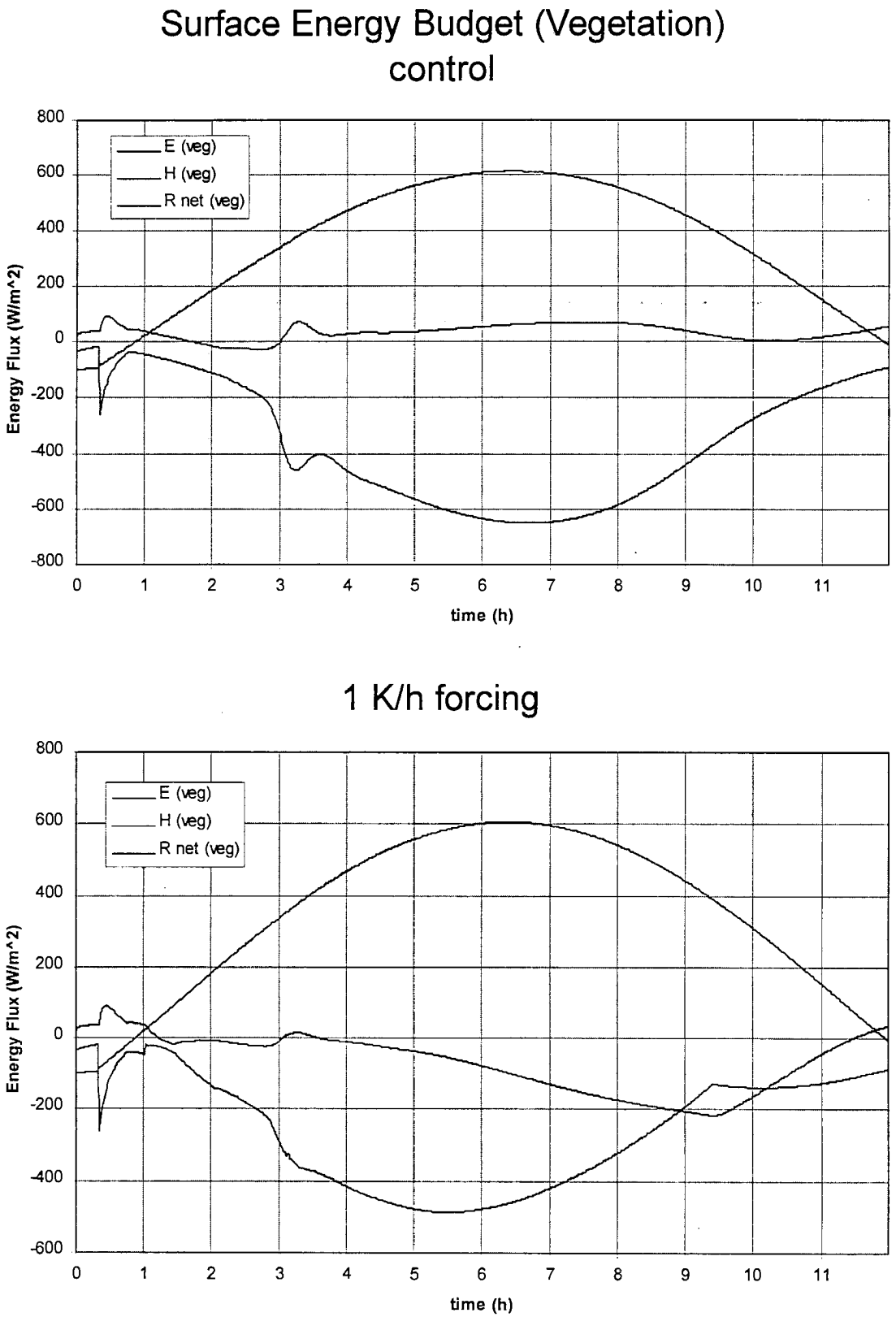

Figure 5.3: Same as Figure 5.2, except for vegetation surface energy budget.

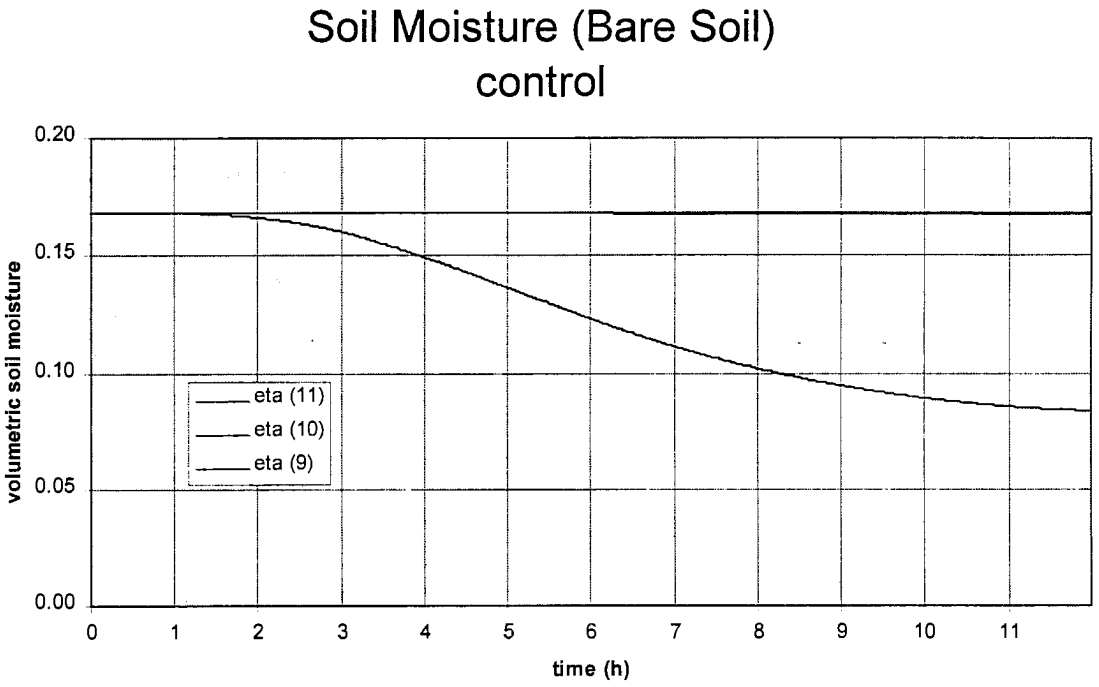

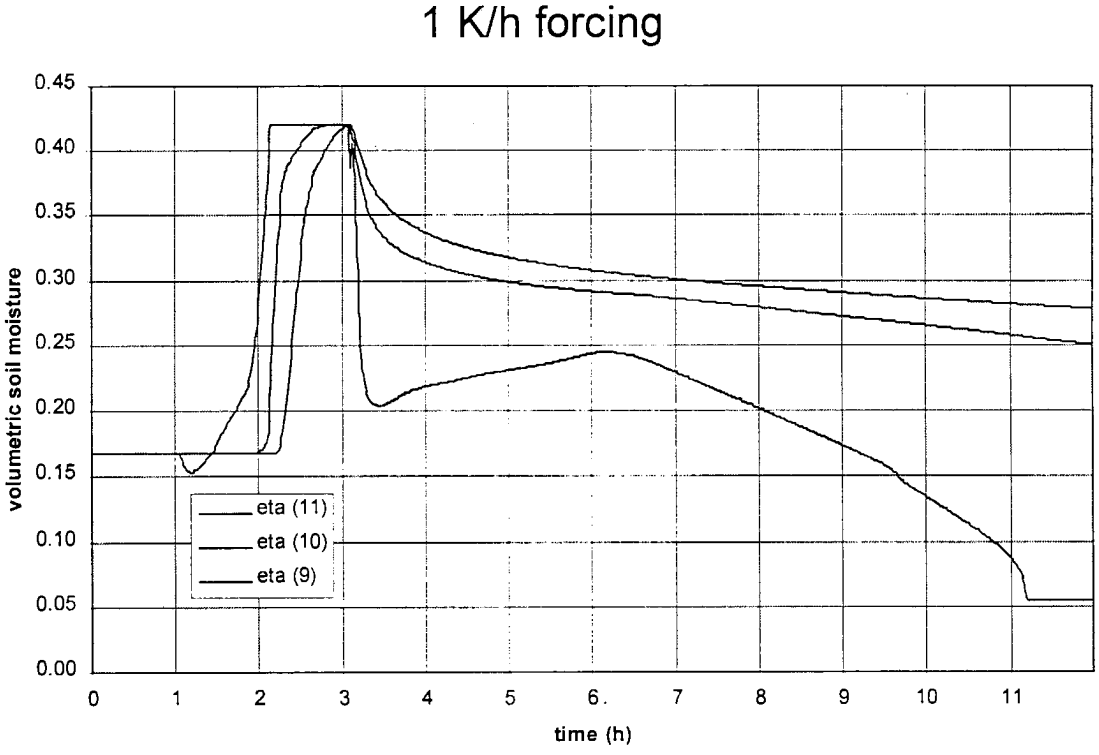

Figure 5.4: Same as Figure 5.2, except for soil moisture (bare soil) (eta) for soil model levels 9-11 (soil depths 6 cm, 3 cm, and 0 cm, respectively).

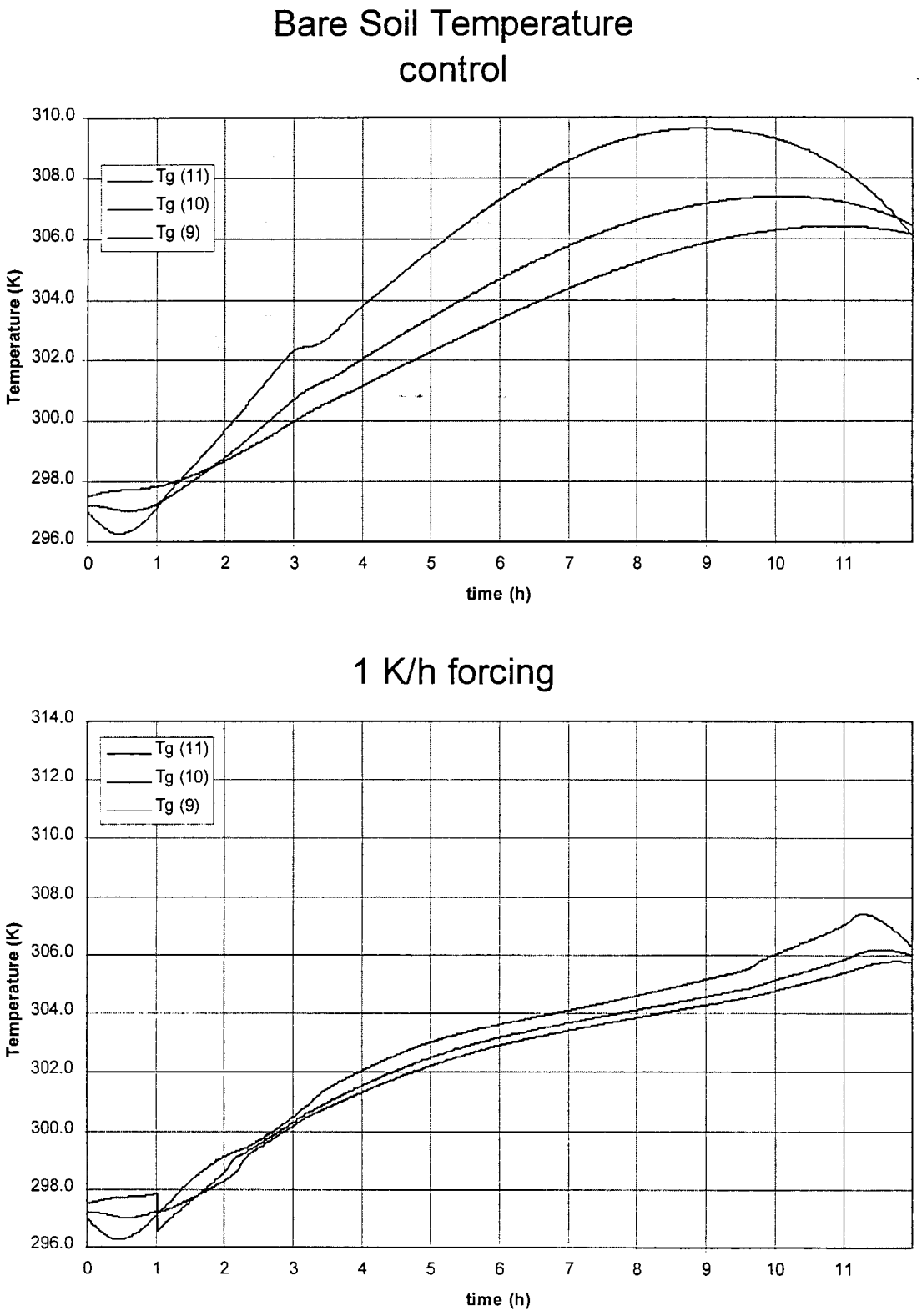

Figure 5.5: Same as Figure 5.4, except for bare soil temperature.

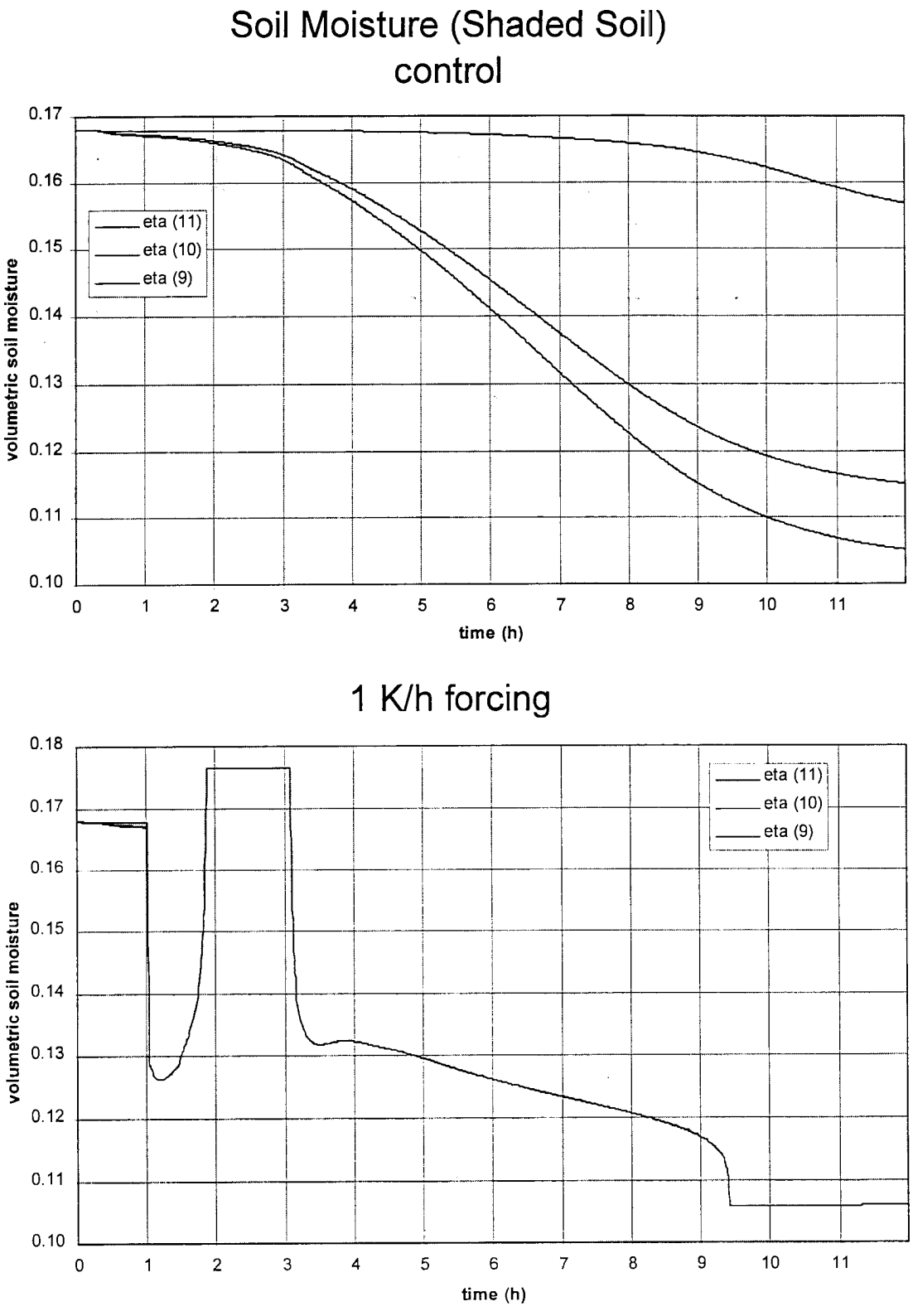

Figure 5.6: Same as Figure 5.4, except for soil moisture (shaded soil).

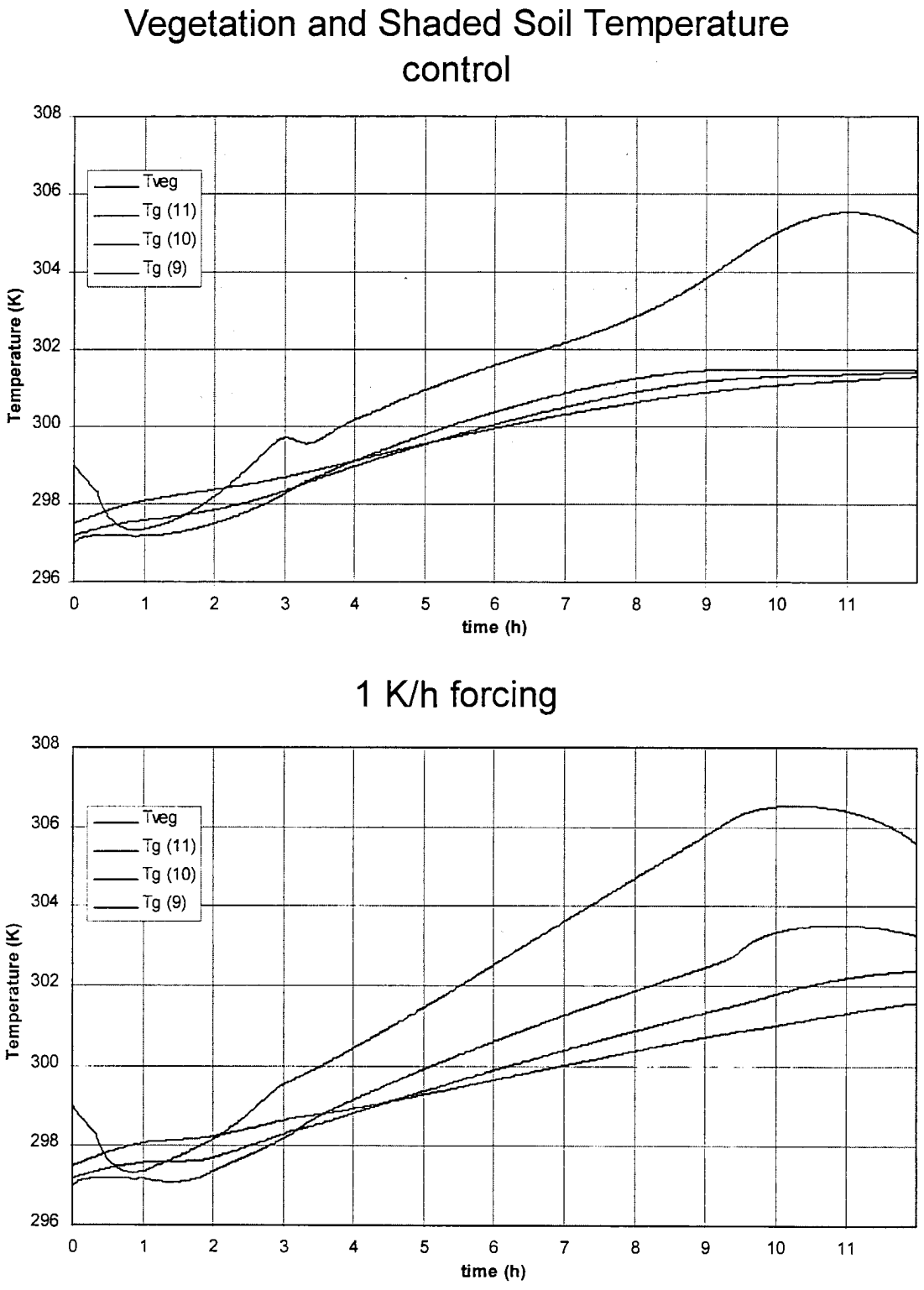

Figure 5.7: Same as Figure 5.4, except for vegetation canopy temperature and shaded soil temperature.

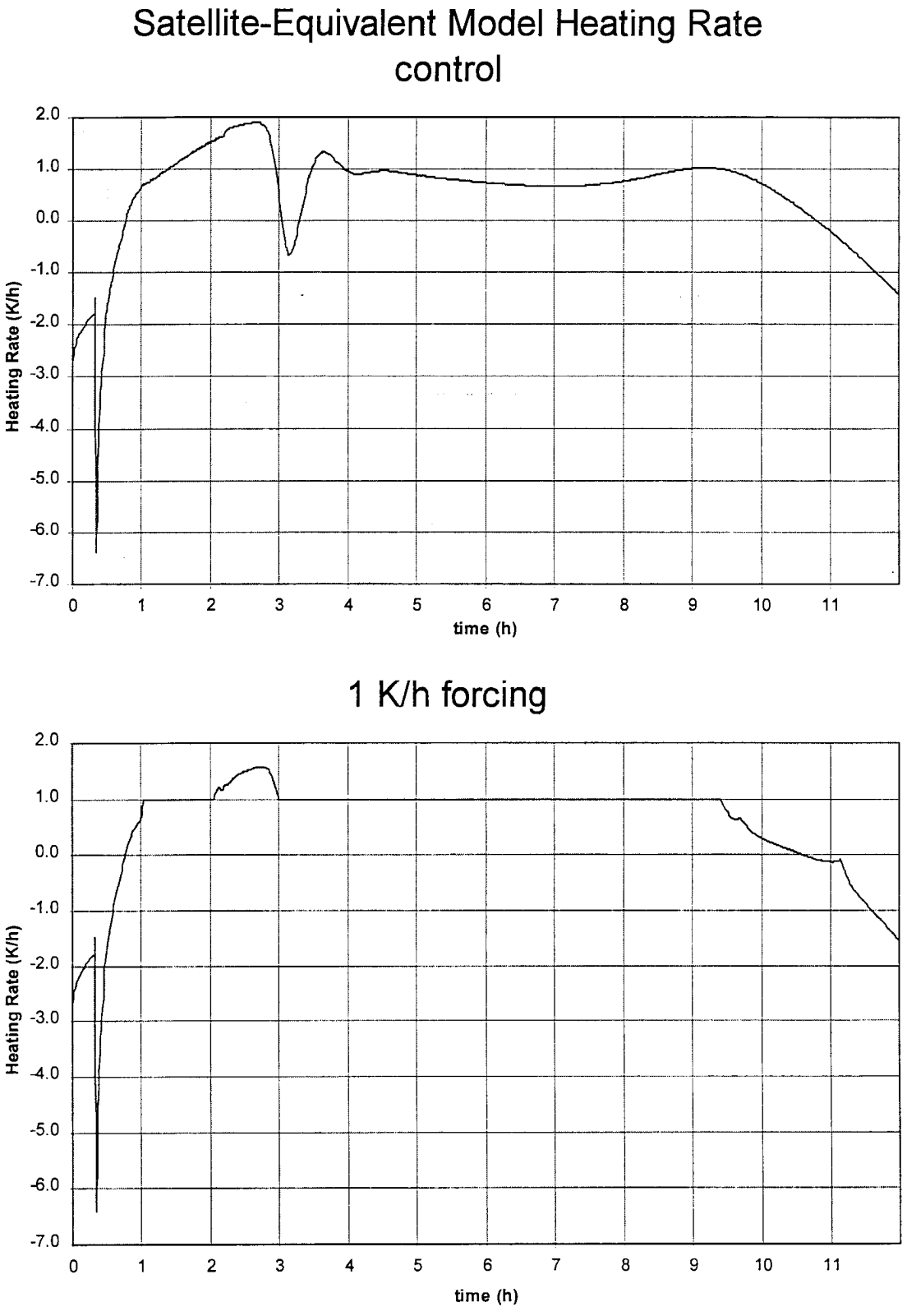

Figure 5.8: Same as Figure 5.2, except for satellite-equivalent model surface heating rate.

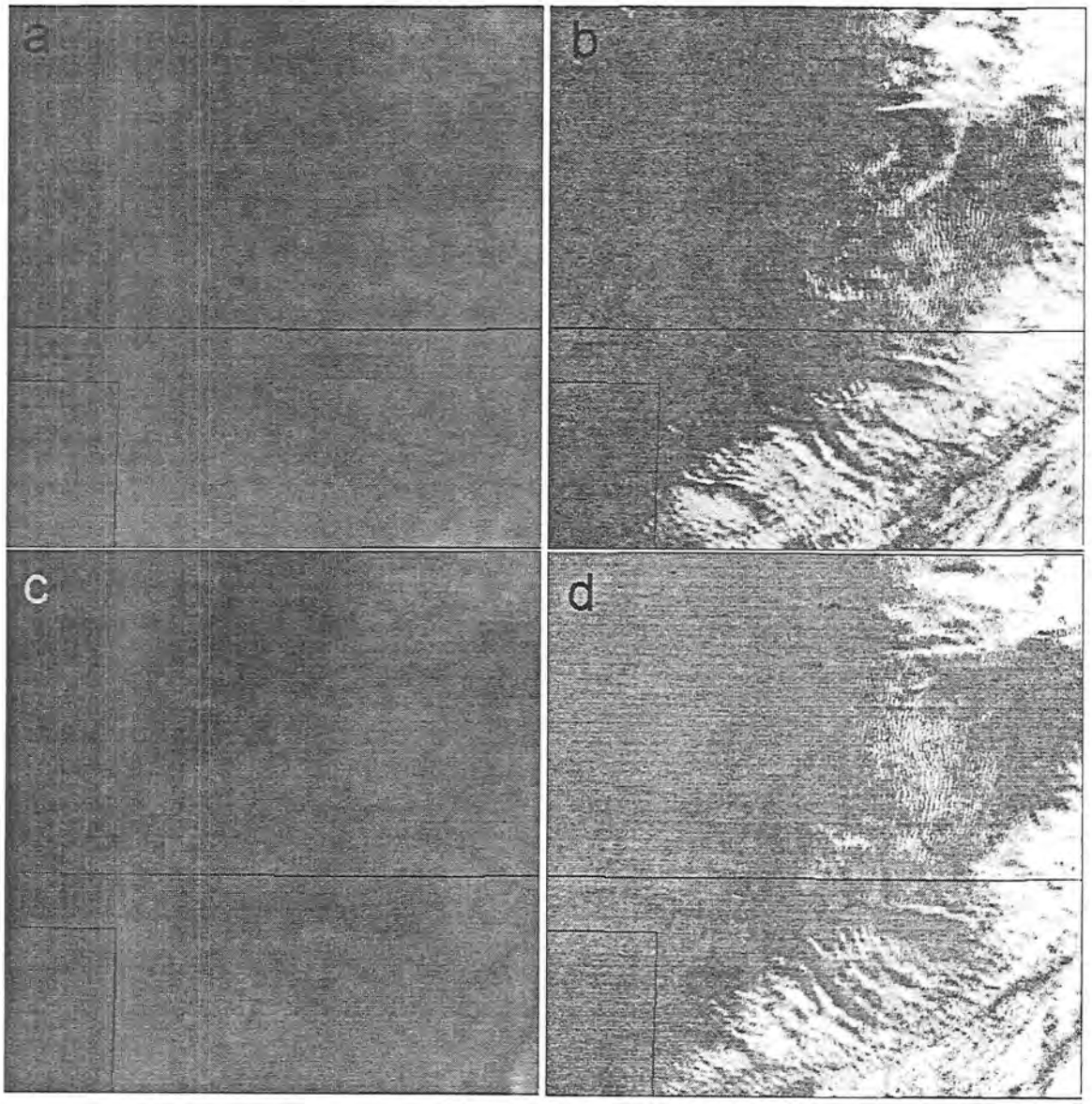

Figure 5.9: Time series of GOES VISSR infrared and visible satellite imagery for the Kansas/Oklahoma case study region for 8 September 1991 1501 UTC (a and b), and 1601 UTC (c and d). Infrared data is shown in a) and c), while visible imagery is shown in b) and d). Dark values in the infrared imagery indicate warm temperatures, while lighter shades represent colder temperatures.

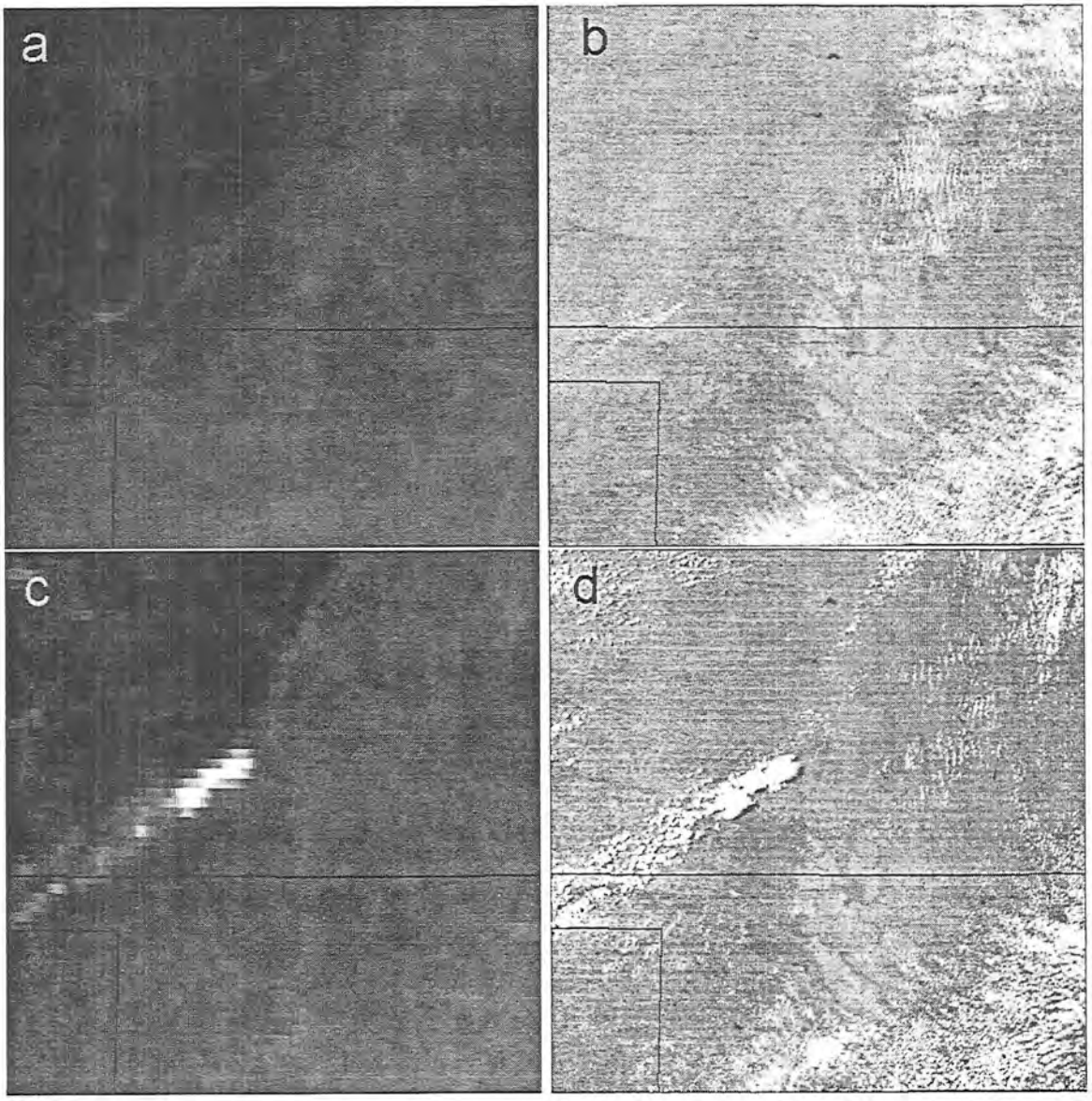

Figure 5.10: Same as Figure 5.9, except for 1801 UTC (a and b), and 2001 UTC (c and d).

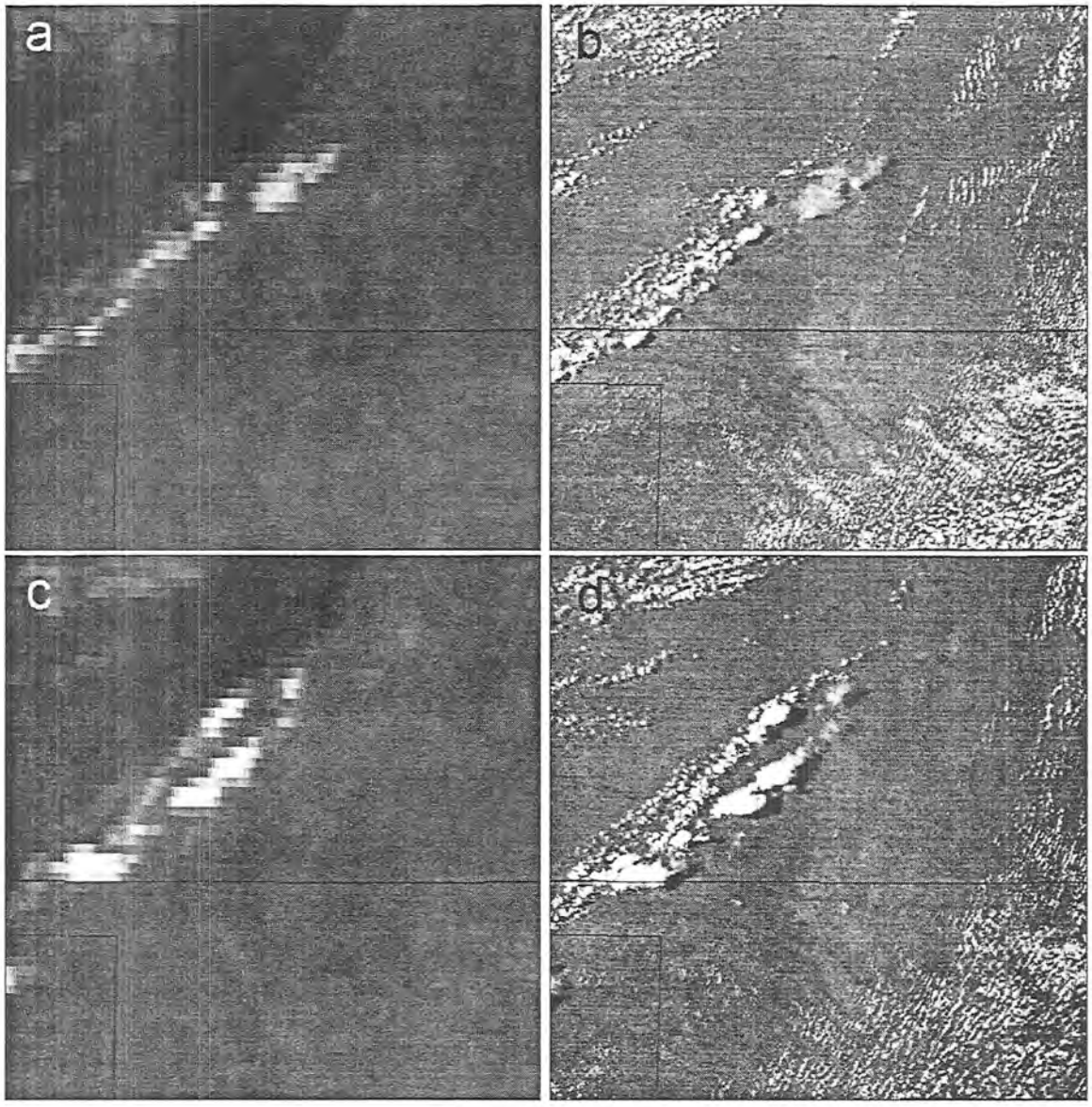

Figure 5.11: Same as Figure 5.9, except for 2101 UTC (a and b), and 2201 UTC (c and d).

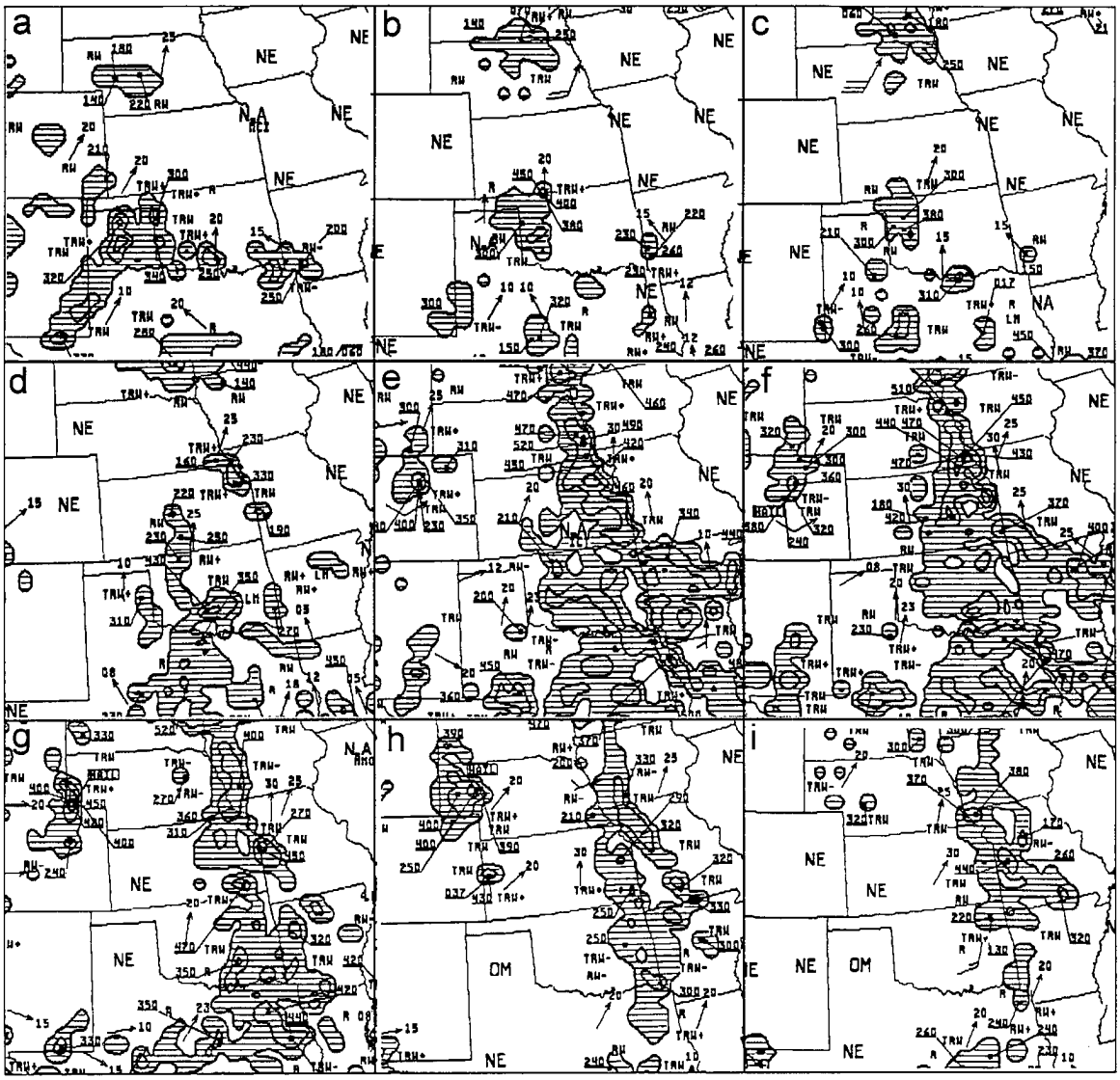

Figure 5.12: Radar summaries for 7 September 1991 at a) 0635, b) 1035, c) 1235, d) 1635, e) 2135, and f) 2235 UTC; and for 8 September 1991 at g) 0035, h) 0335, and i) 0635 UTC.

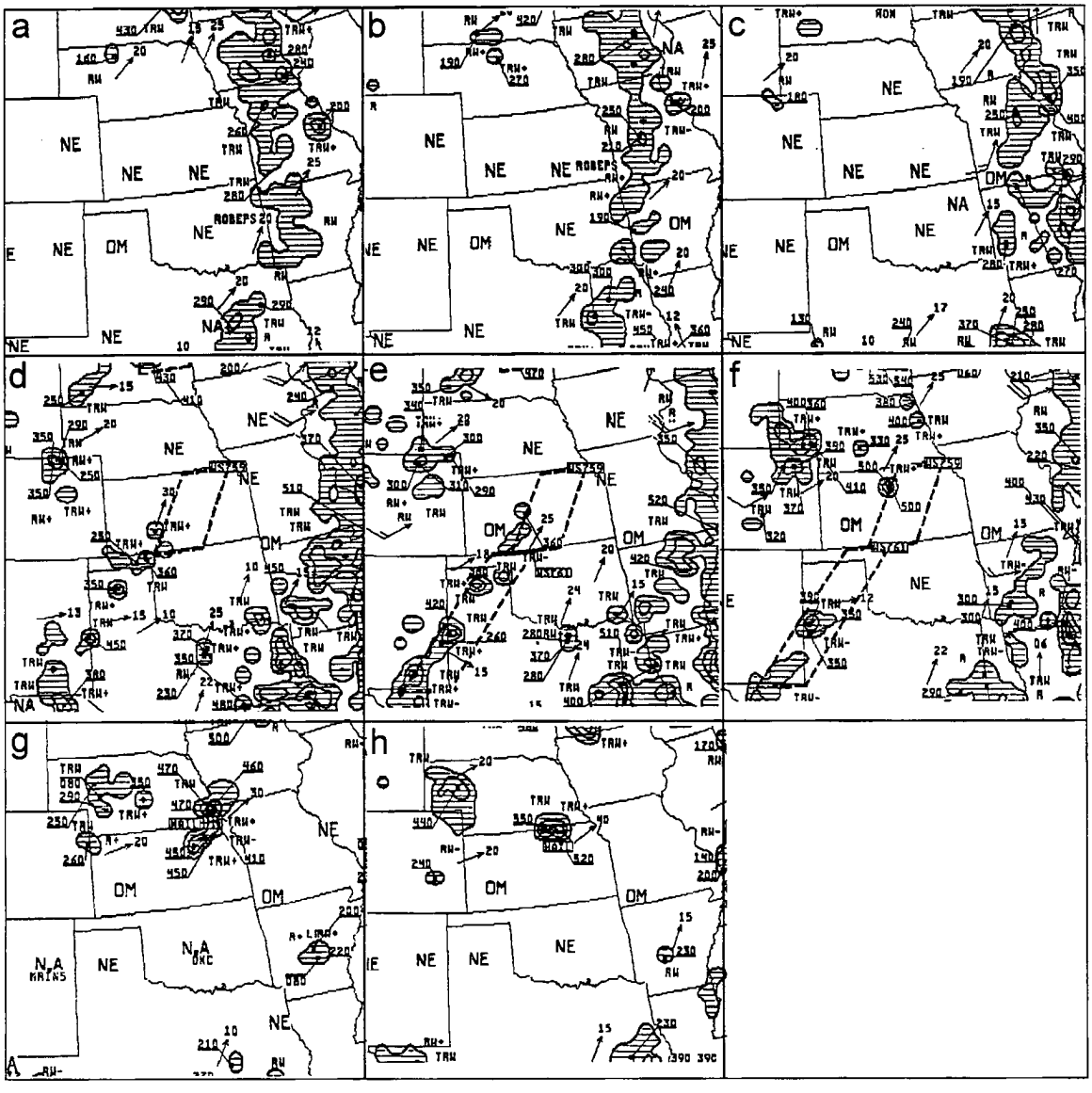

Figure 5.13: Same as Figure 5.12 , except for 8 September 1991 at a) 1035, b) 1235, c) 1635, d) 2135, e) 2235 UTC; and for 9 September 1991 at f) 0035, g) 0335, and h) 0635 UTC.

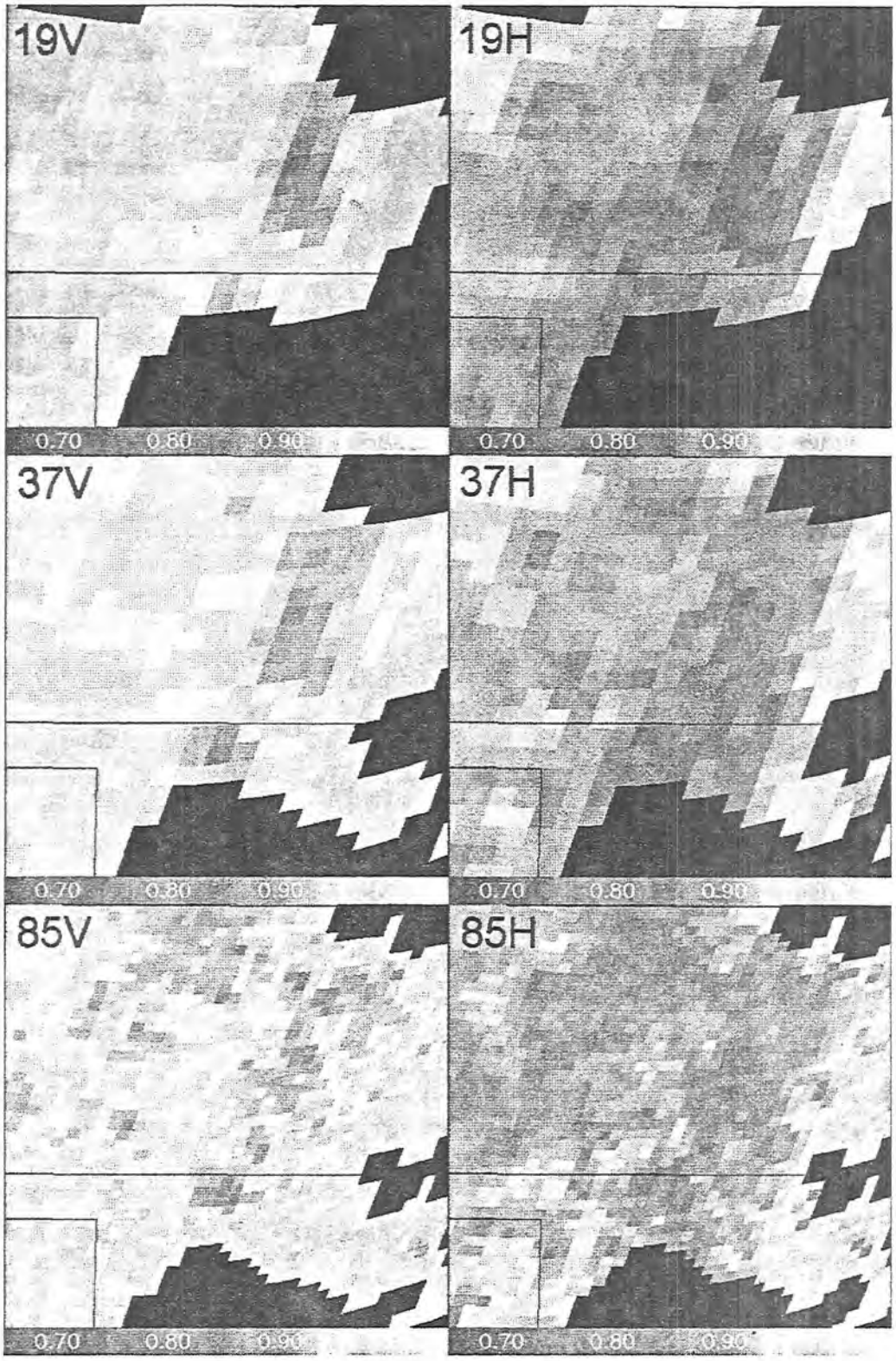

Figure 5.14: Atmospheric-corrected microwave surface emittance for 8 September 1991 1529 UTC for the Kansas/Oklahoma region. Results from vertical and horizontal polarizations at the SSM/I frequencies of 19, 37 and 85.5 GHz are shown. Reds and pinks denote high microwave emittance, while greens and blues represent low microwave surface emittance.

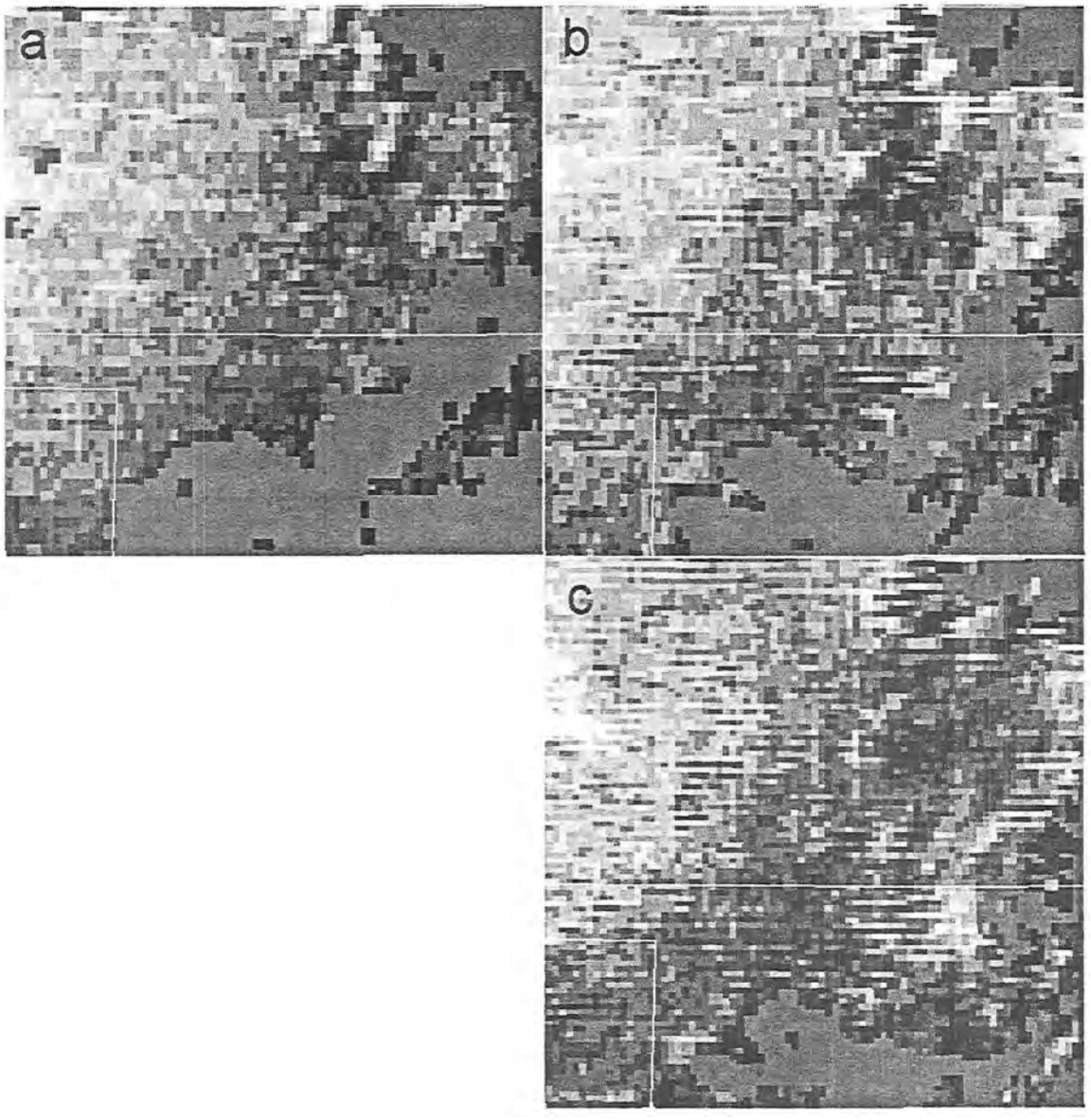

Figure 5.15: Satellite-derived surface skin temperature heating rates for 8 September 1991 a) 1501 UTC, b) 1531 UTC, and c) 1601 UTC, for the Kansas/Oklahoma region. Dark regions represent low heating rates (nearly 0 K/h for the darkest regions), while lighter regions denote high heating rates (approaching 5 K/h for the lightest areas).

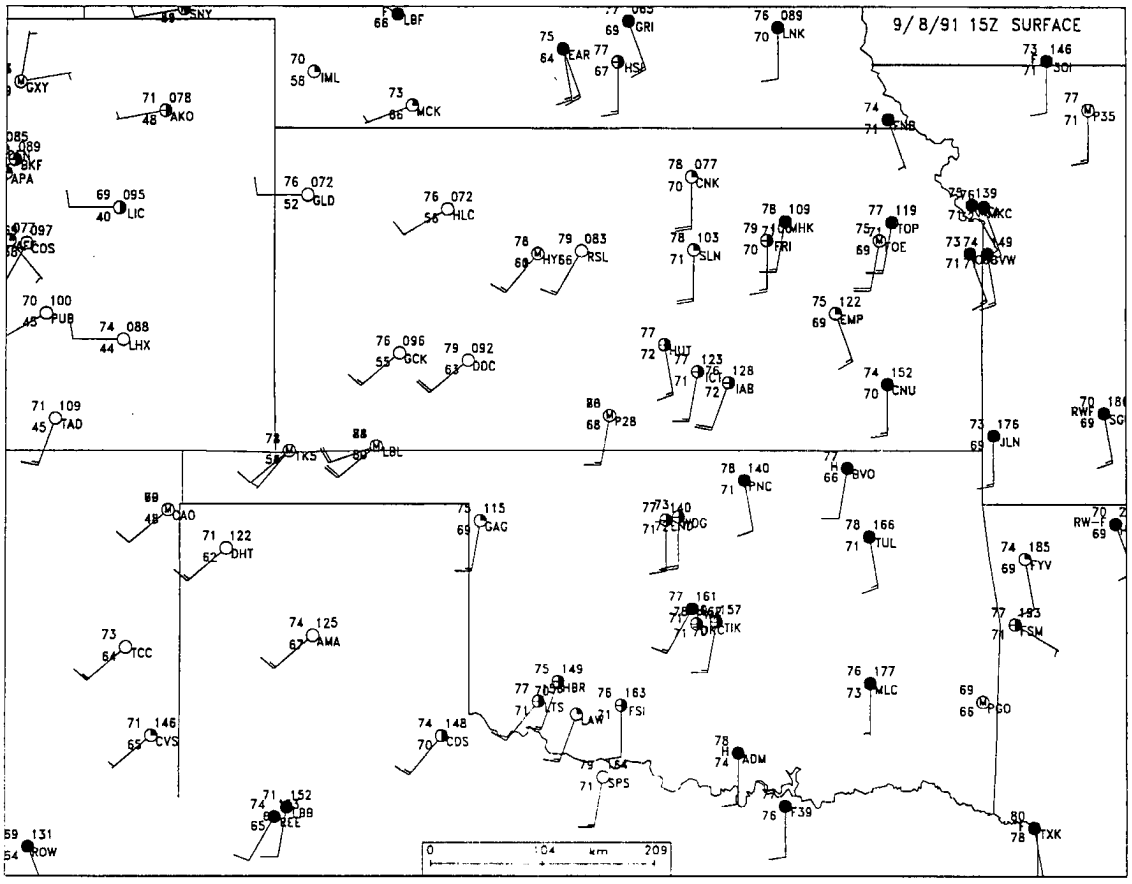

Figure 5.16: Surface observations for 8 September 1991 1500 UTC for the Kansas/Oklahoma region.

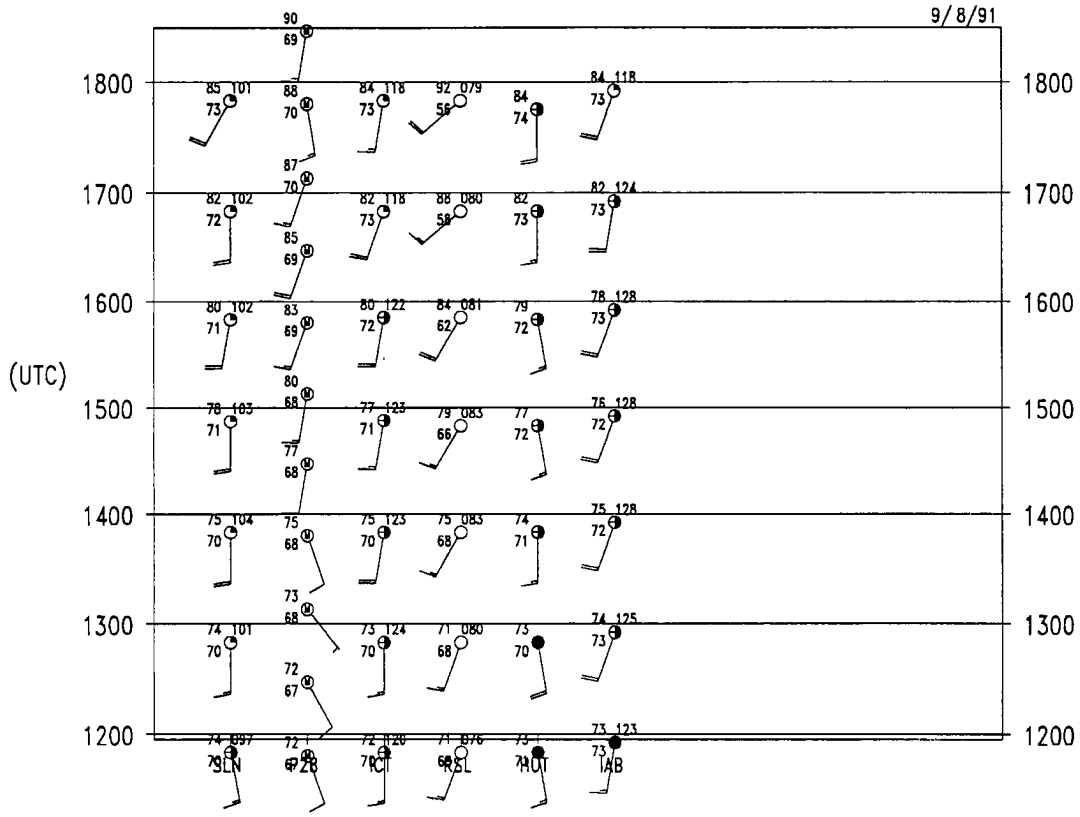

Figure 5.17: Time series plot of surface observations for 8 September 1991 from 1200 to 1800 UTC for central Kansas. Station locations are shown in Figure 5.16.

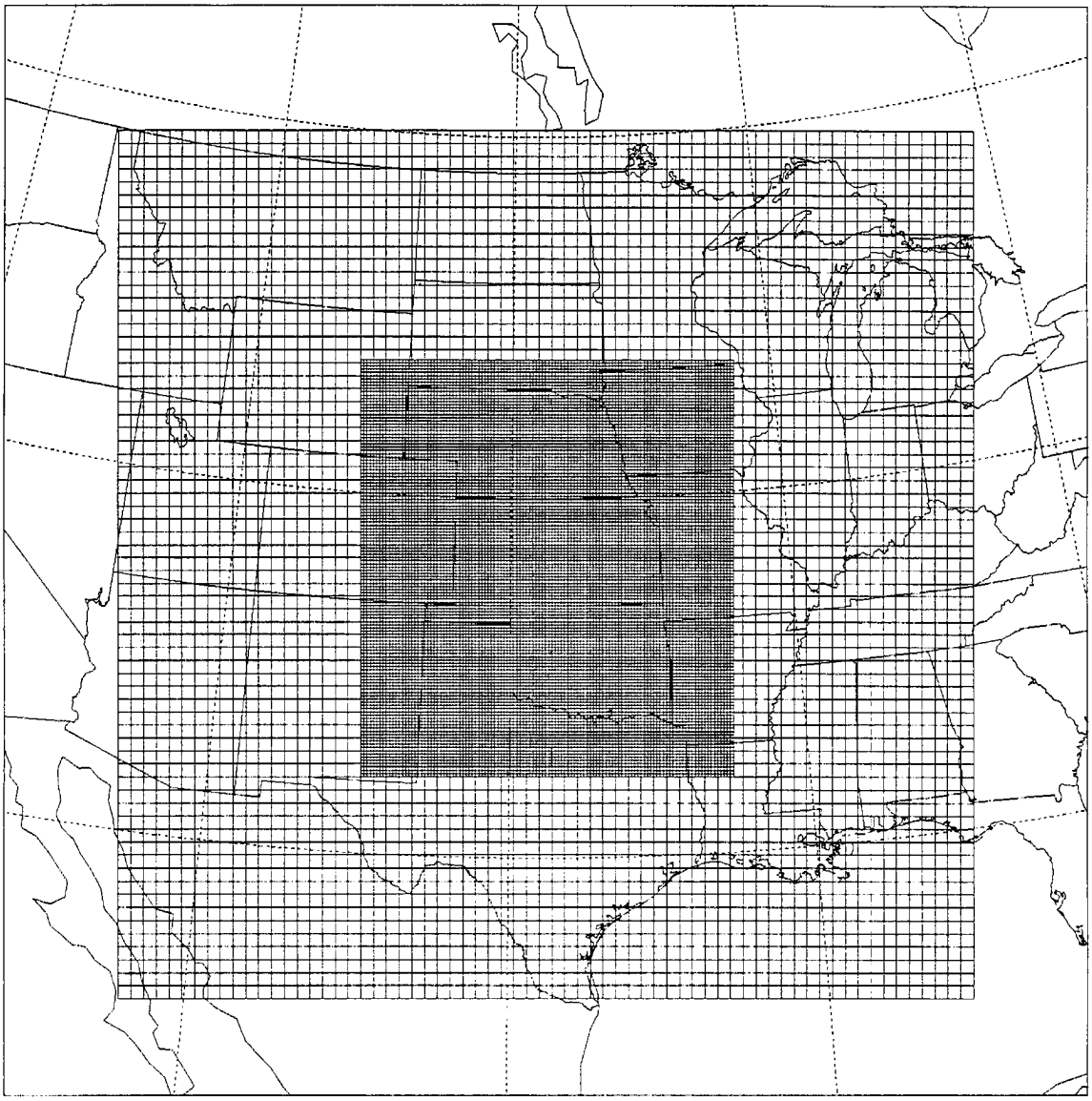

Figure 5.18: RAMS nested grid configuration for grids 1 and 2.

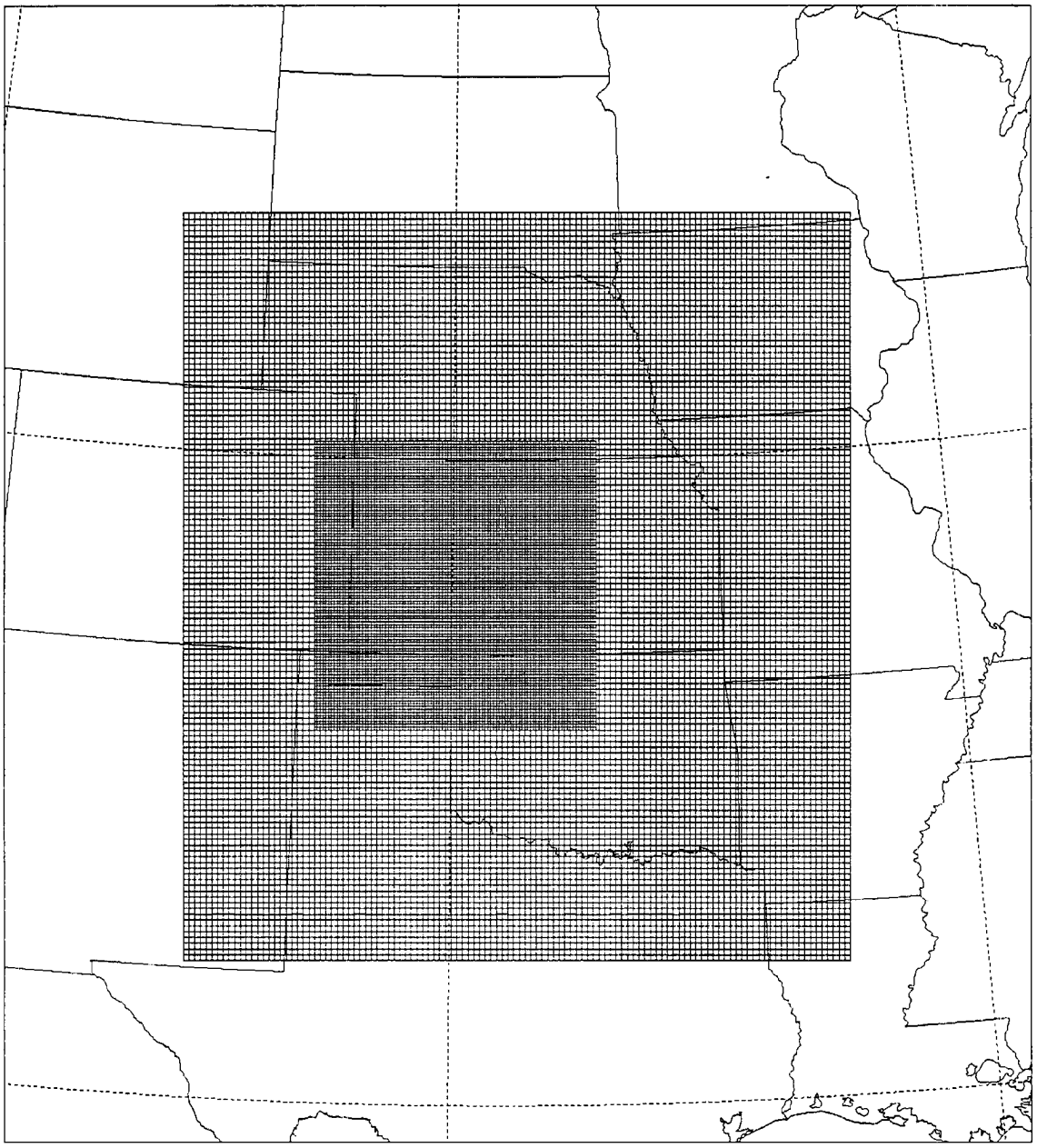

Figure 5.19: RAMS nested grid configuration for grids 2 and 3.

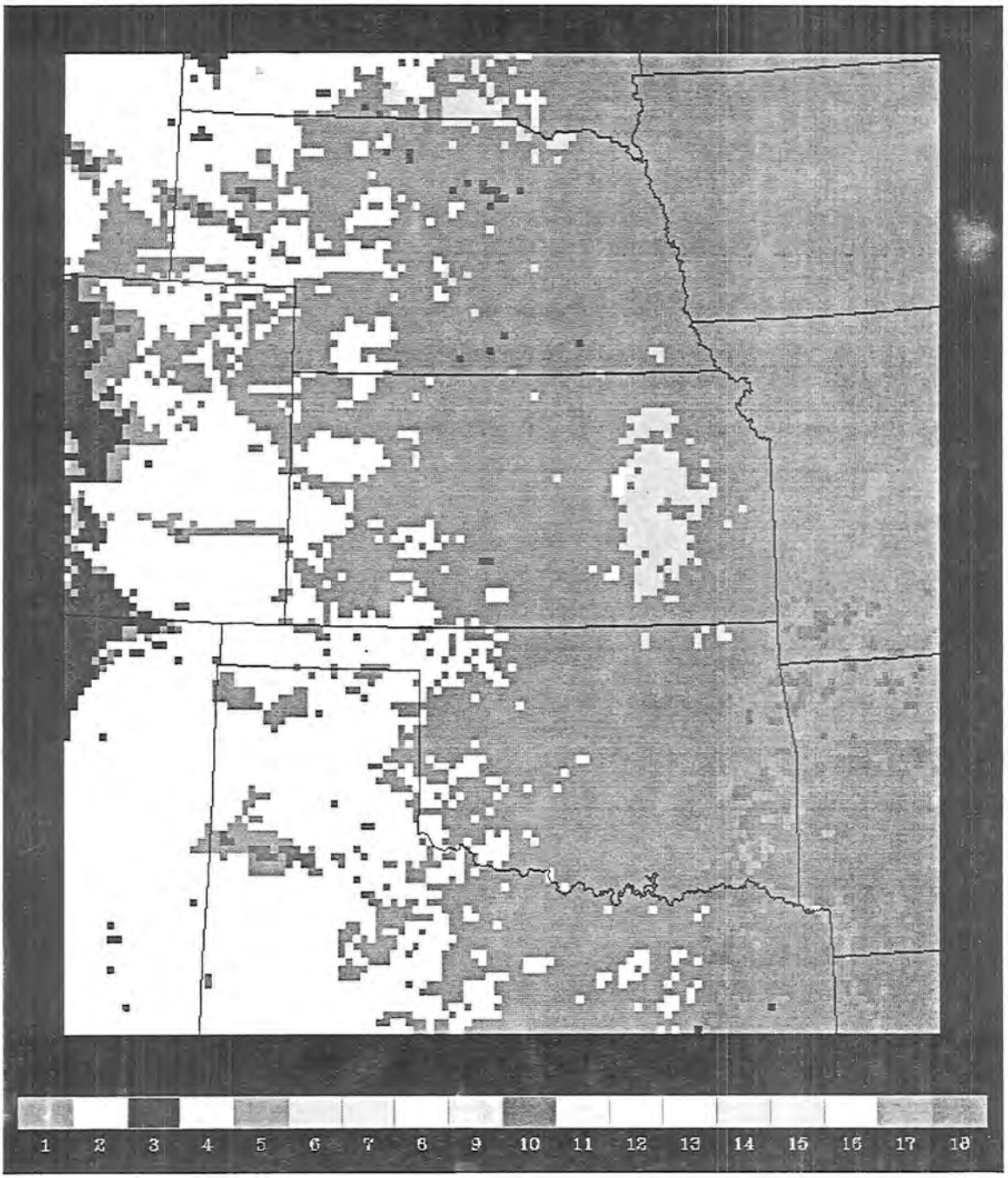

Figure 5.20: BATS land cover and vegetation classification categories for grid 2. Main vegetation types are (1) crop/mixed farming; (2) short grass prairie; (3) evergreen needleleaf tree; (5) deciduous broadleaf tree; (7) tall grass prairie; (10) irrigated crop; (16) evergreen shrub; and (18) mixed woodland.

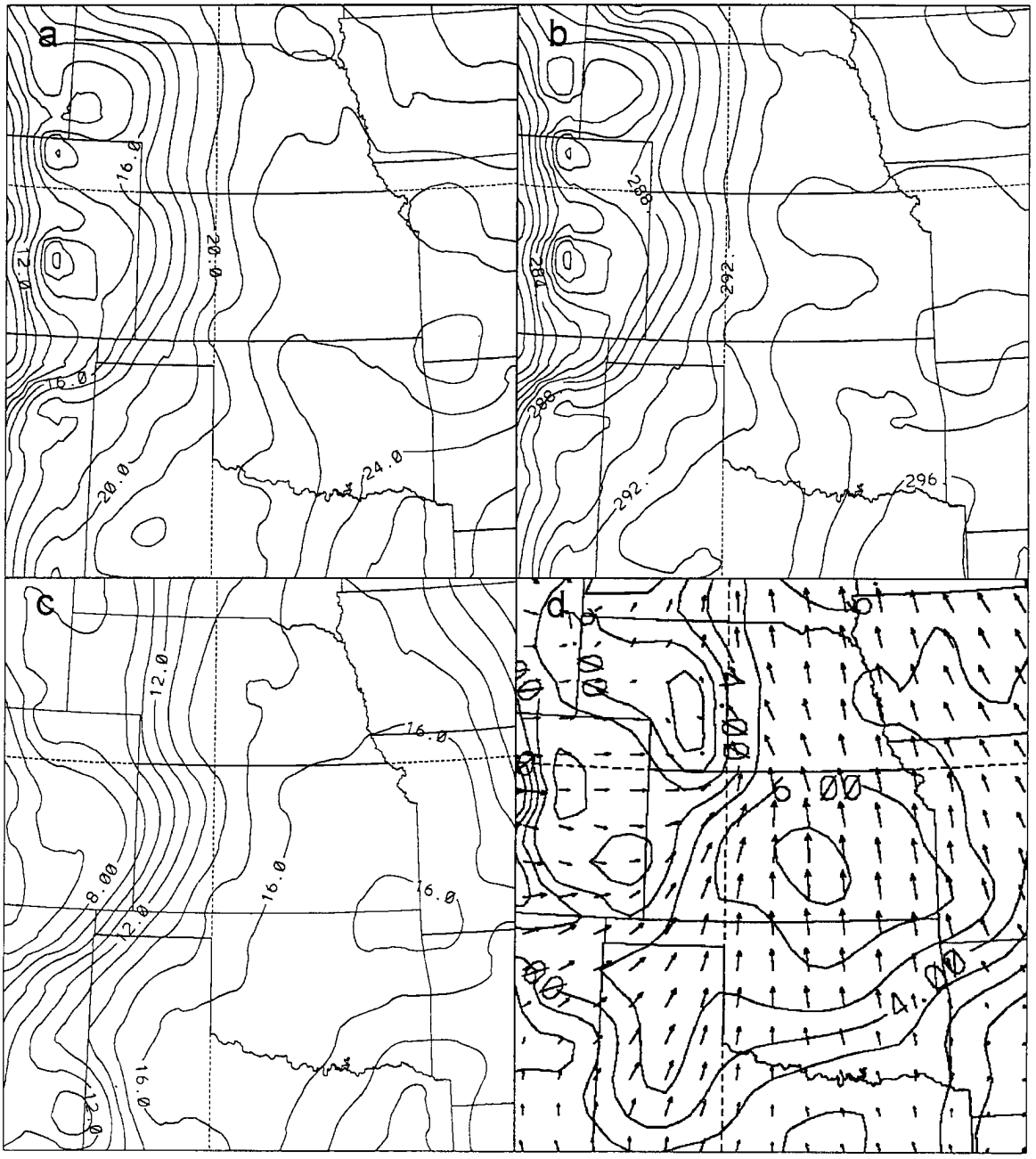

Figure 5.21: RAMS CONTROL run results from the lowest atmospheric level for grid 2 at 1200 UTC, where a) is the surface air temperature (°C) contoured in 1 °C intervals, b) is the bare-soil soil temperature (K) contoured in 1 K intervals, c) is the mixing ratio (g kg^{-1}) contoured in 1 g kg^{-1} intervals, and d) is the grid 1 surface wind speed (m s^{-1}) contoured in 1 m s^{-1} intervals with vectors indicating wind direction and relative magnitude based on the size of the vector arrows.

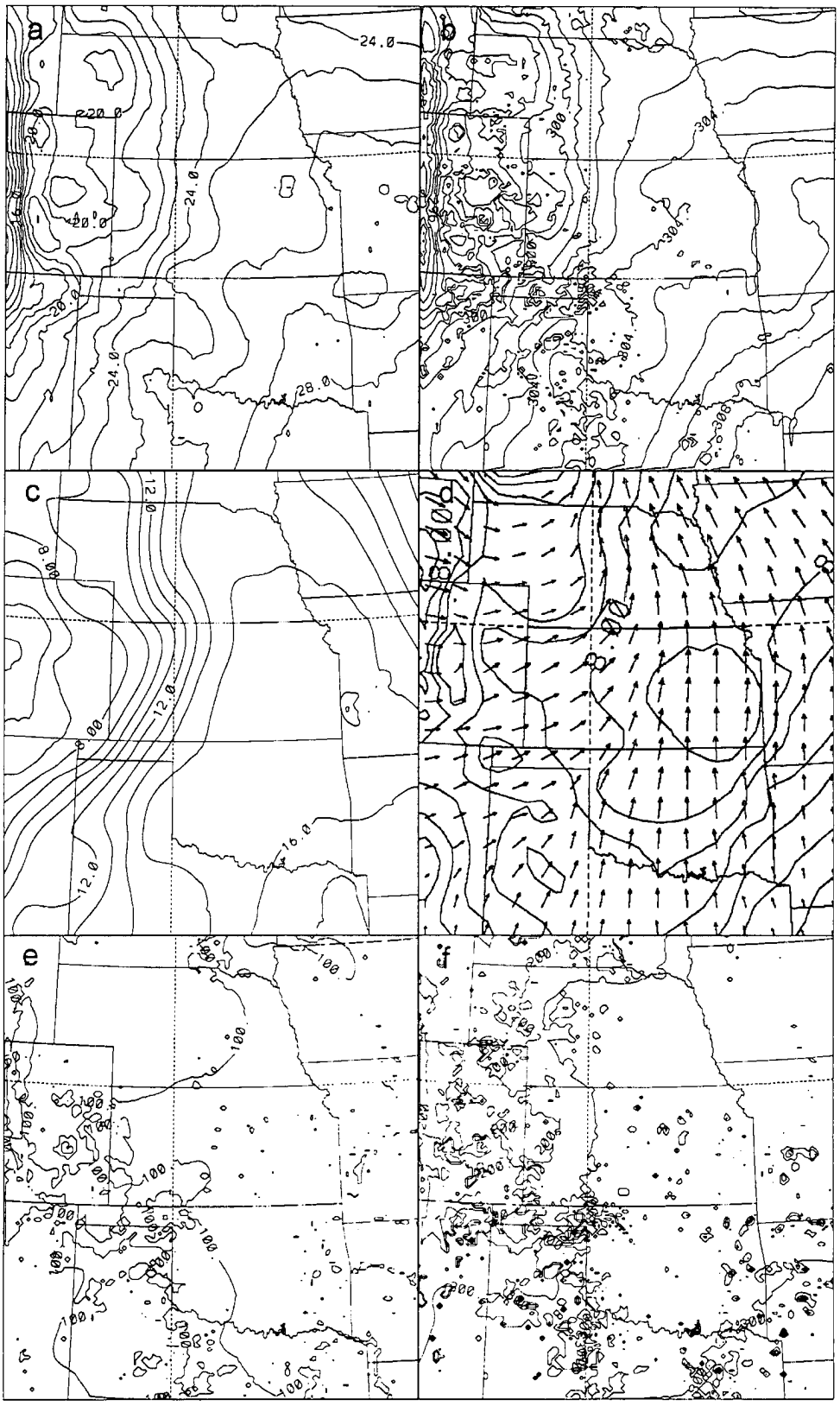

Figure 5.22: Same as Figure 5.21, except at 1600 UTC, and that e) and f) are the surface latent and sensible heat fluxes (W m^{-2}) contoured in 50 W m^{-2} intervals.

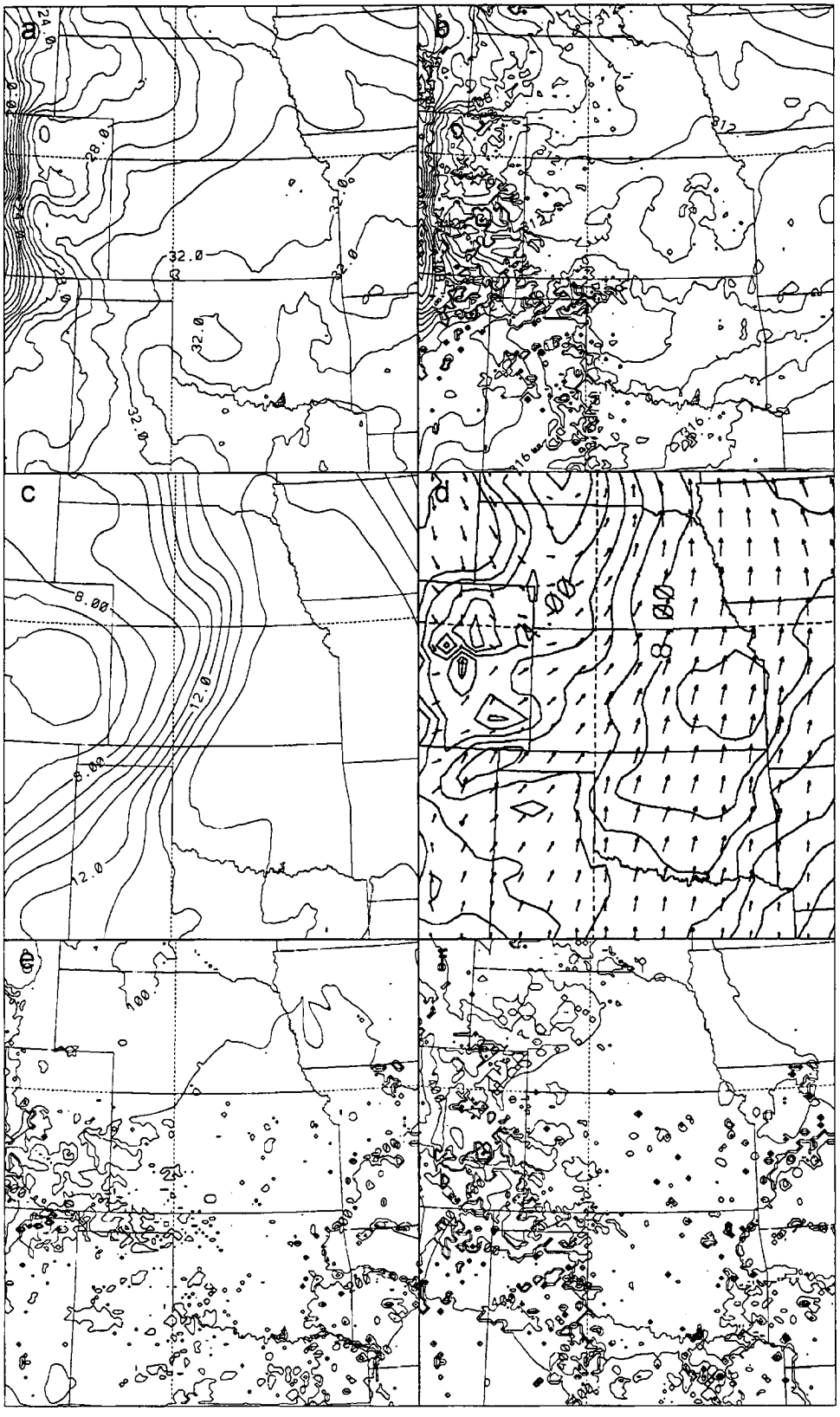

Figure 5.23: Same as Figure 5.22, except at 2000 UTC.

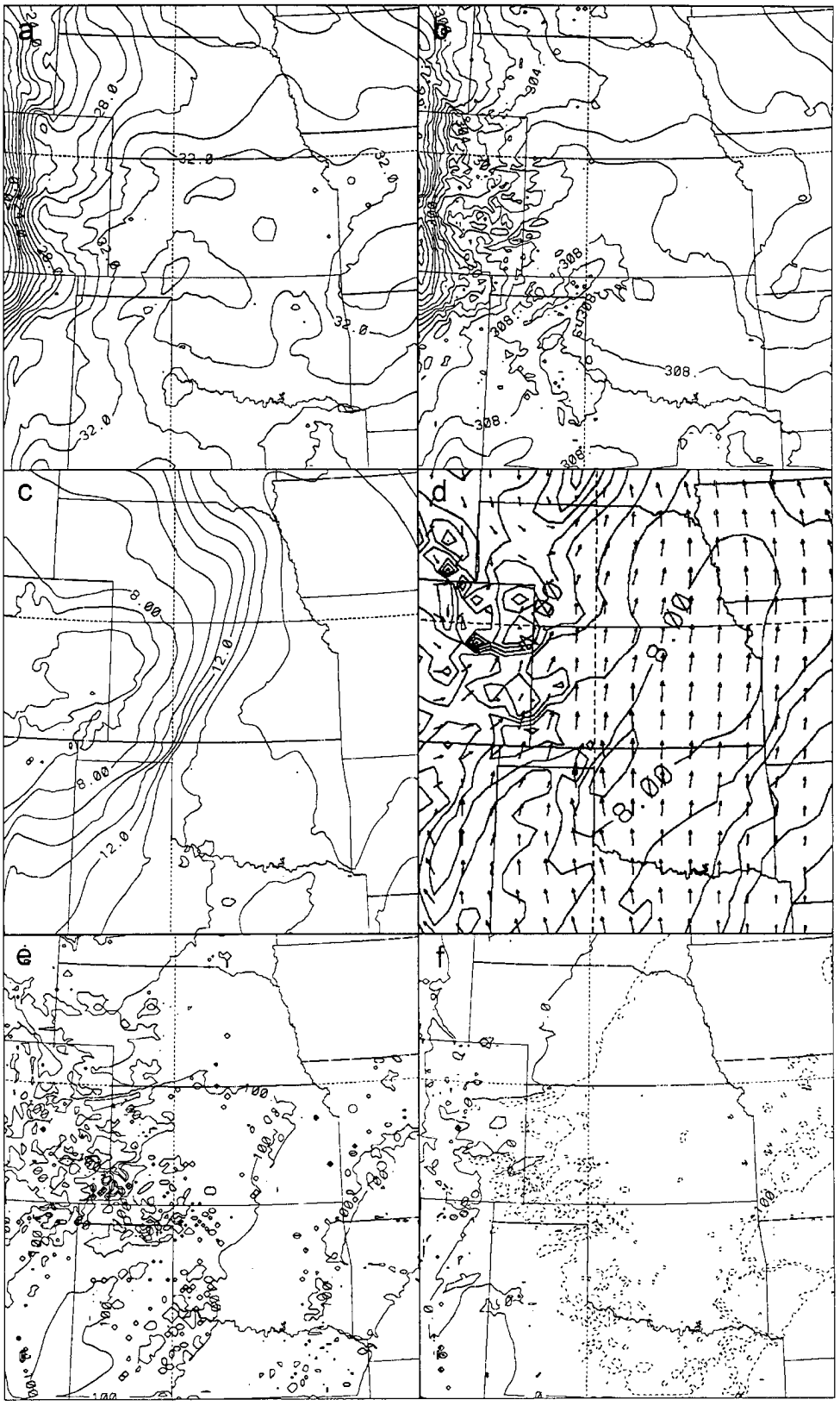

Figure 5.24: Same as Figure 5.22, except at 0000 UTC.

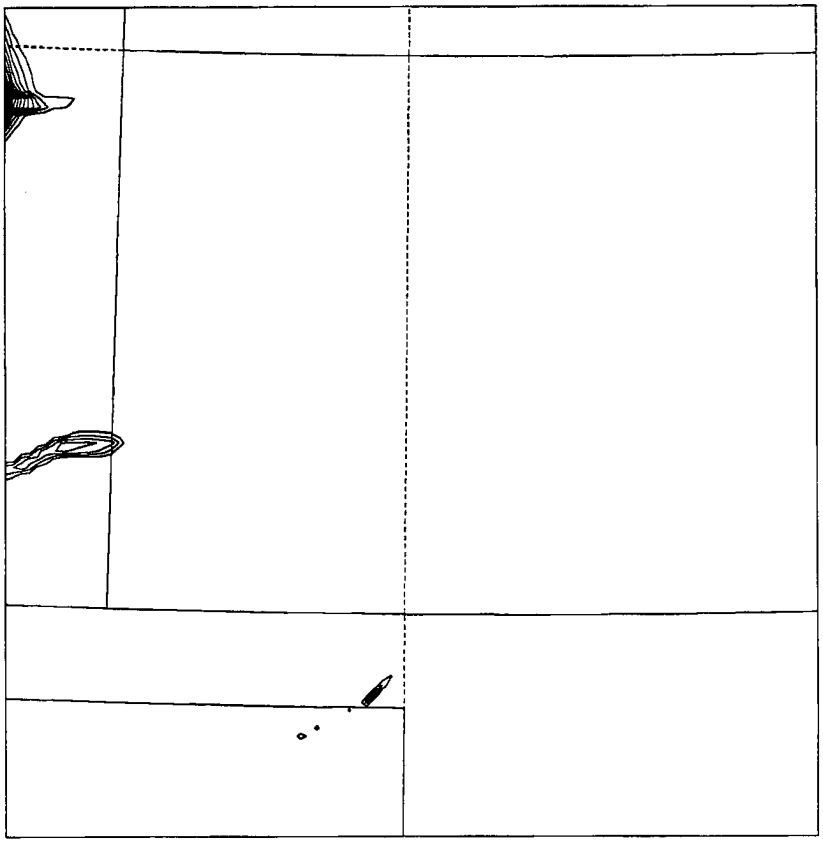

Figure 5.25: RAMS CONTROL run vertically integrated cloud water results (kg m^{-2}) for grid 3 at 0000 UTC.

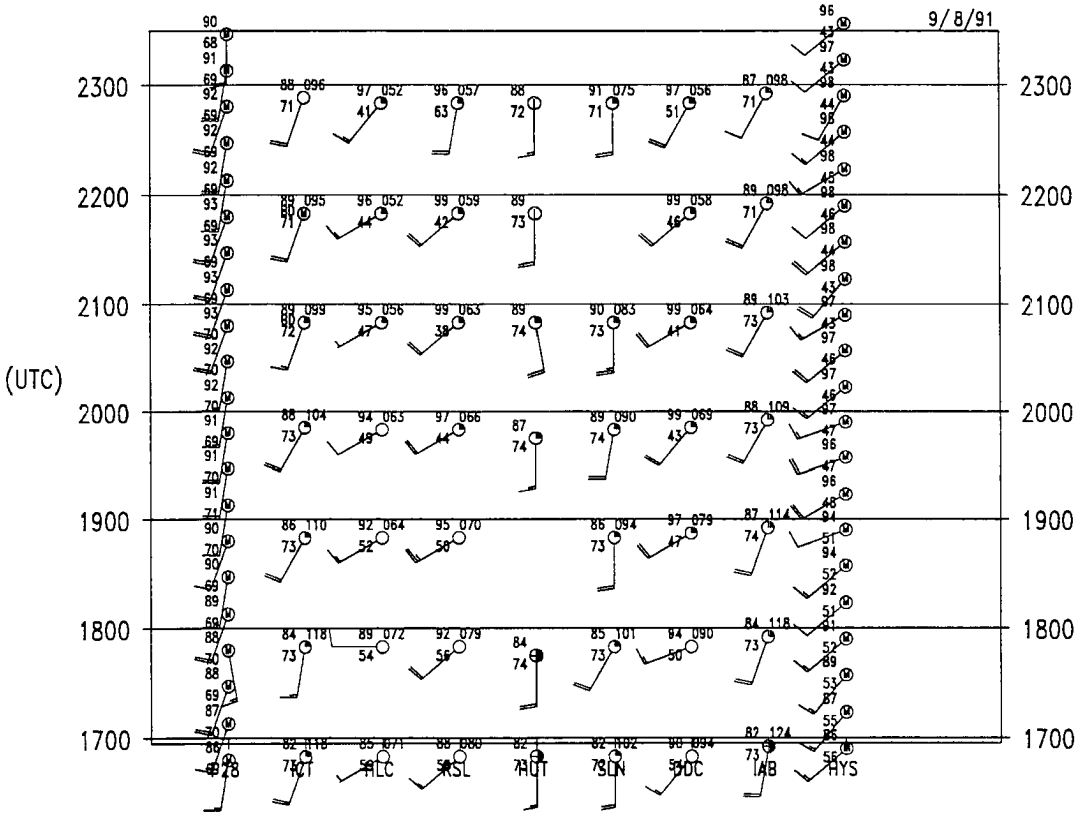

Figure 5.26: Time series plot of surface observations for 8 September 1991 from 1700 to 0000 UTC for central Kansas. Station locations are shown in Figure 5.16.

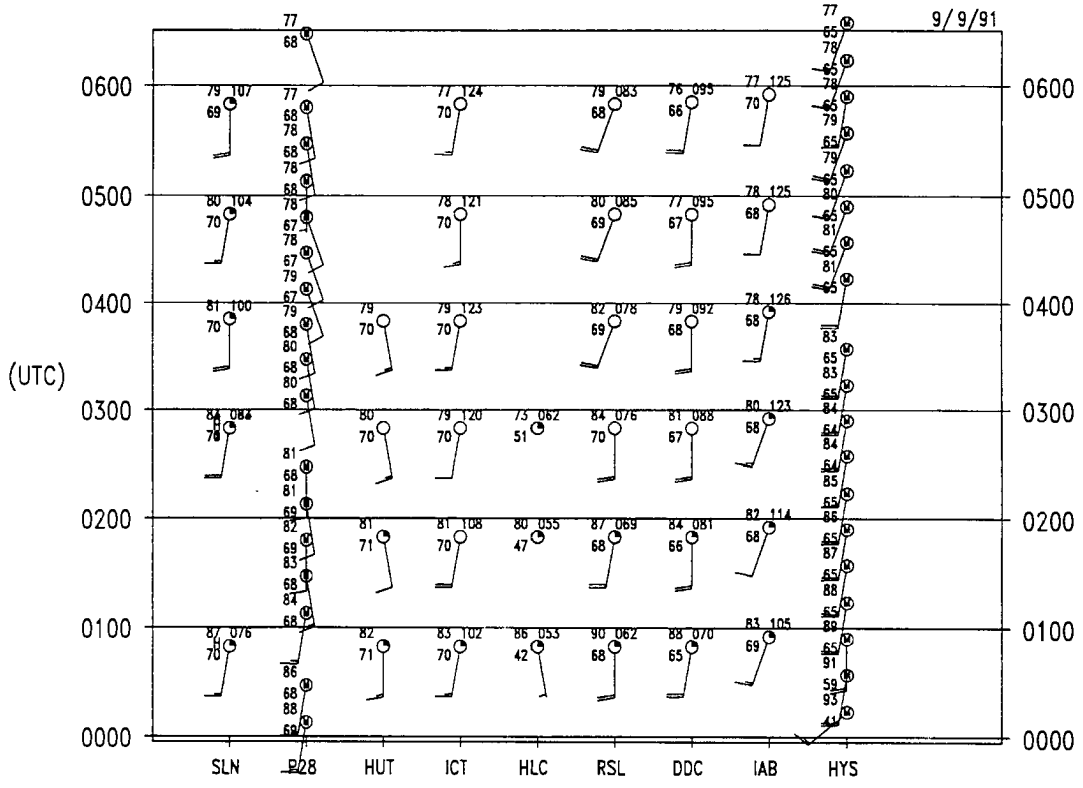

Figure 5.27: Time series plot of surface observations for 9 September 1991 from 0000 to 0600 UTC for central Kansas. Station locations are shown in Figure 5.16.

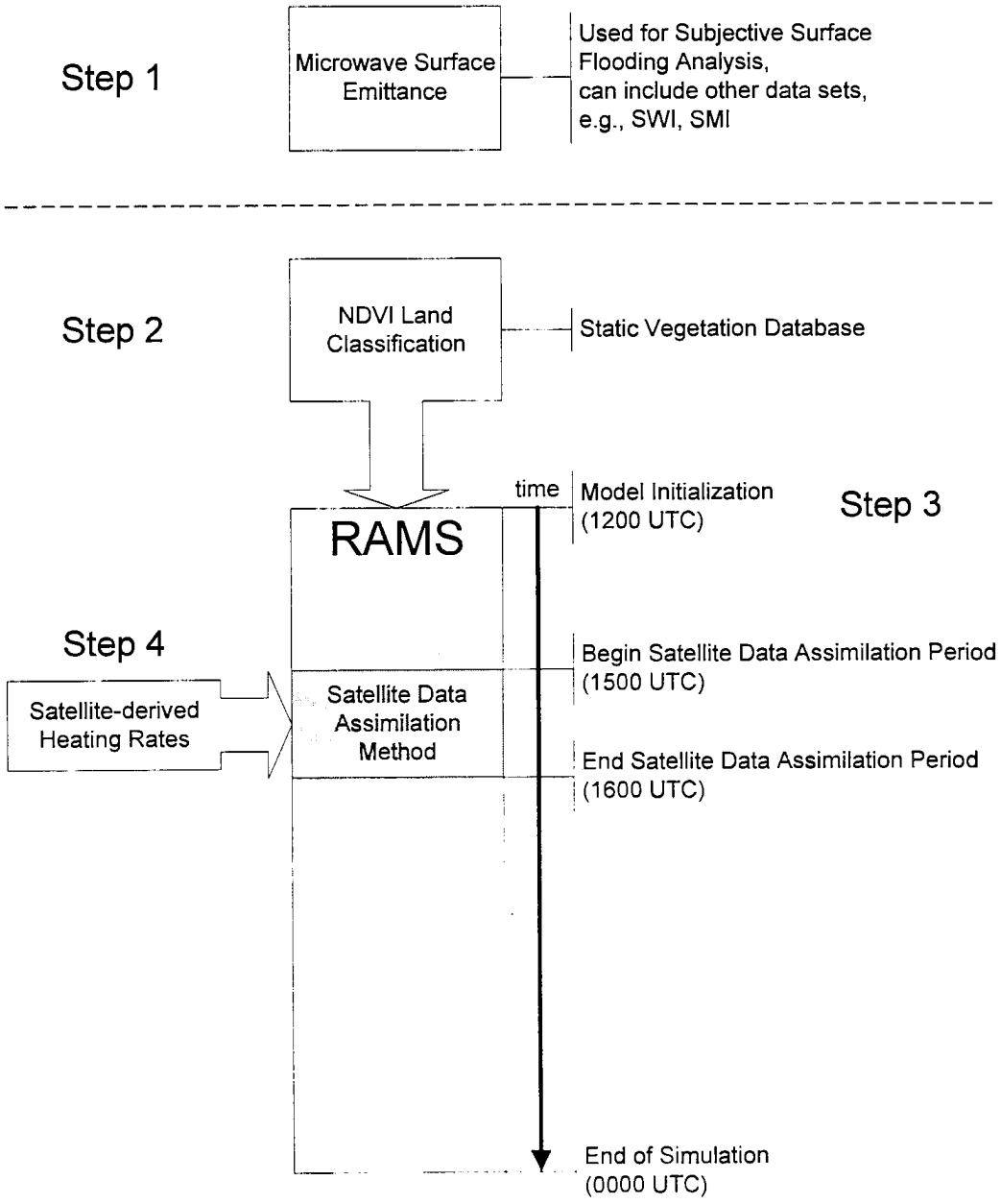

Figure 5.28: The satellite data assimilation method's processing steps.

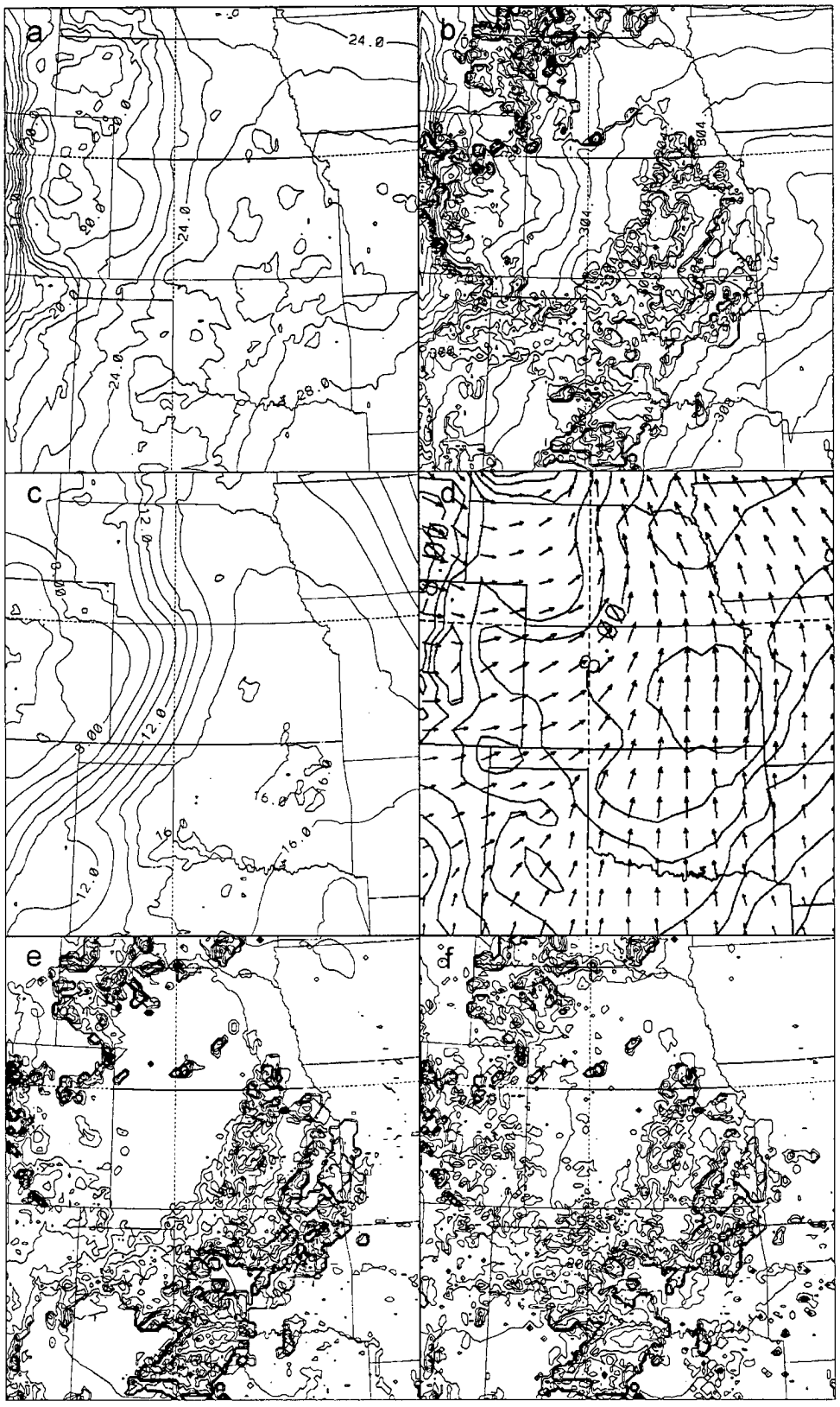

Figure 5.29: Same as Figure 5.22, except for the SAT simulation results at 1600 UTC.

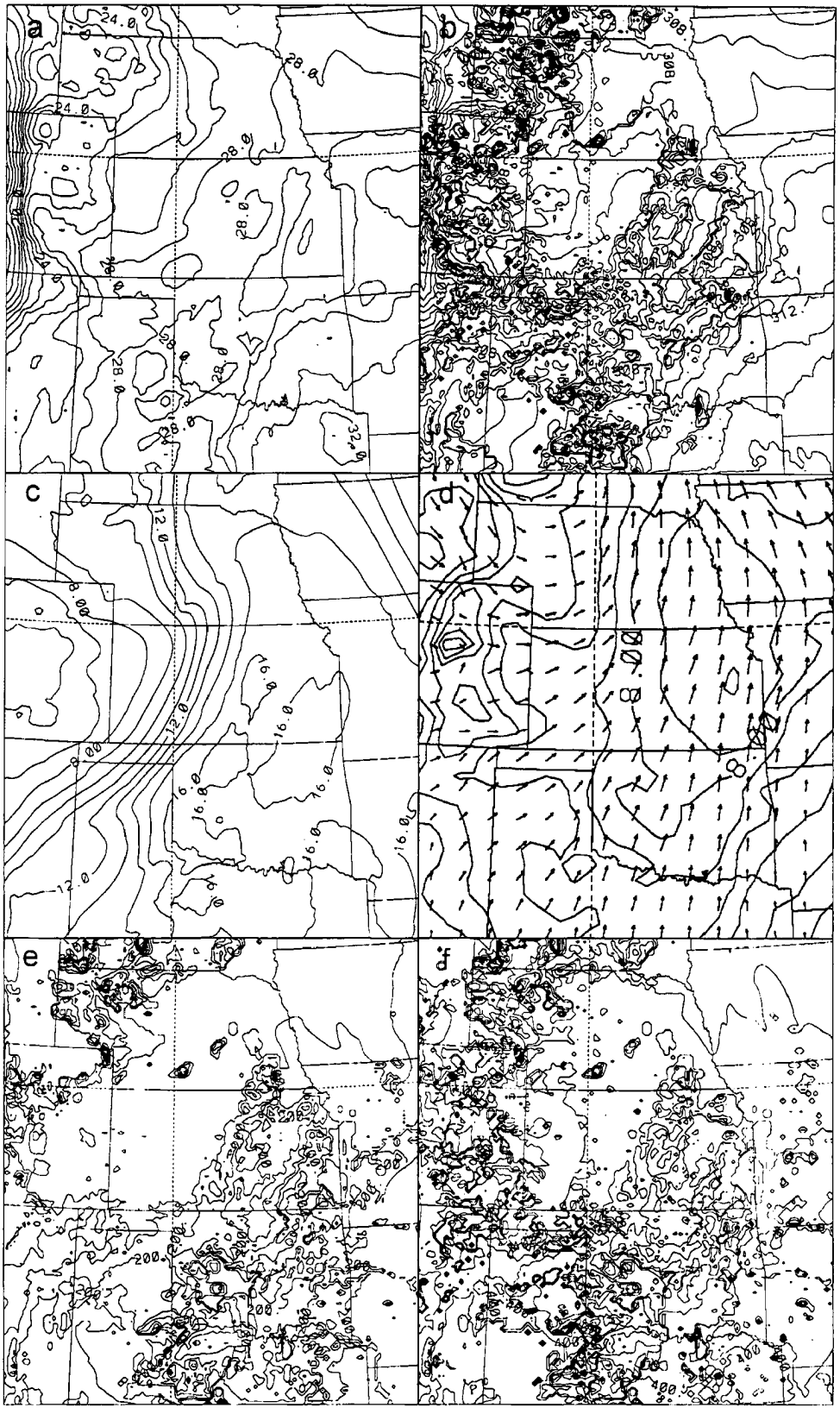

Figure 5.30: Same as Figure 5.22, except for the SAT simulation results at 1800 UTC.

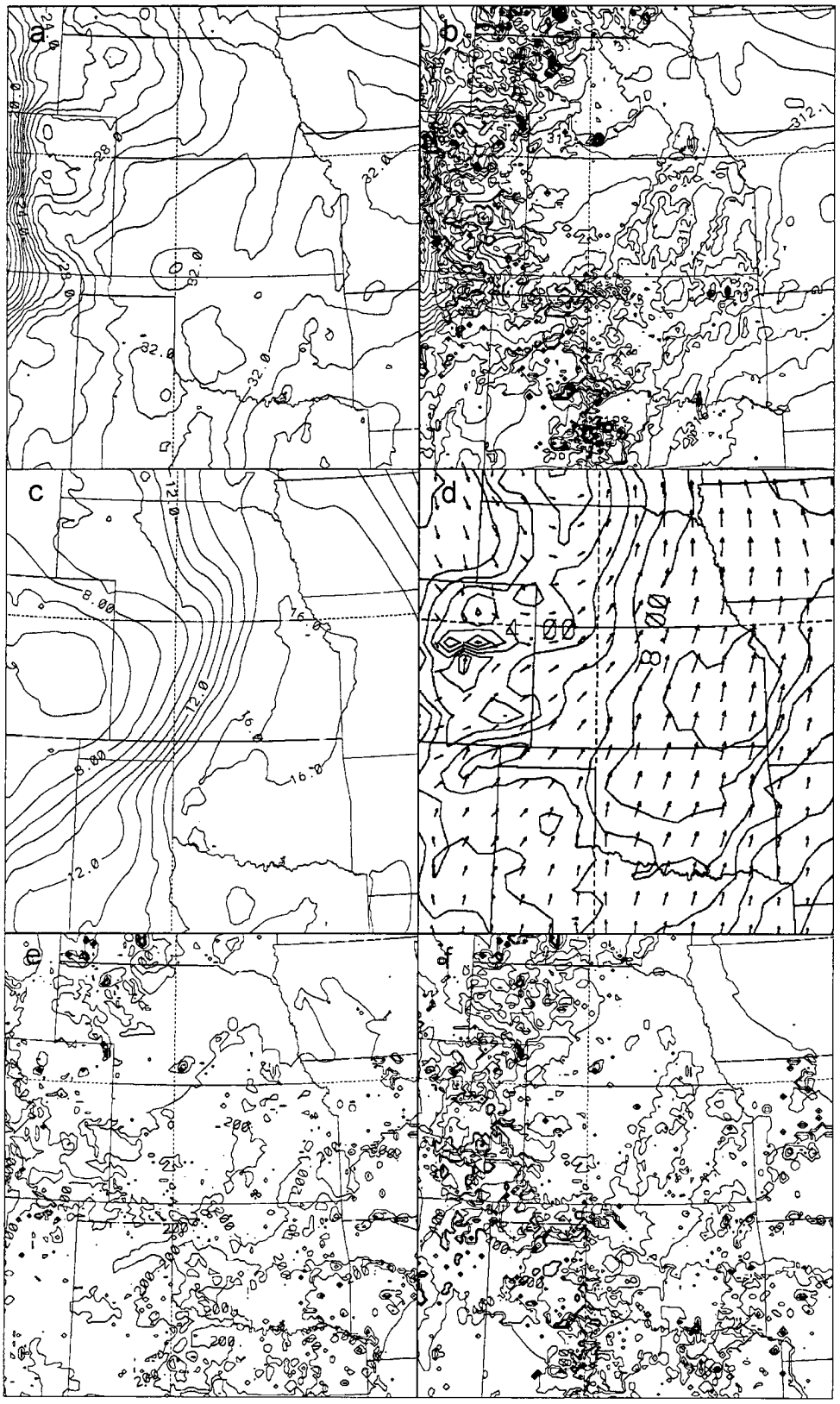

Figure 5.31: Same as Figure 5.22, except for the SAT simulation results at 2000 UTC.

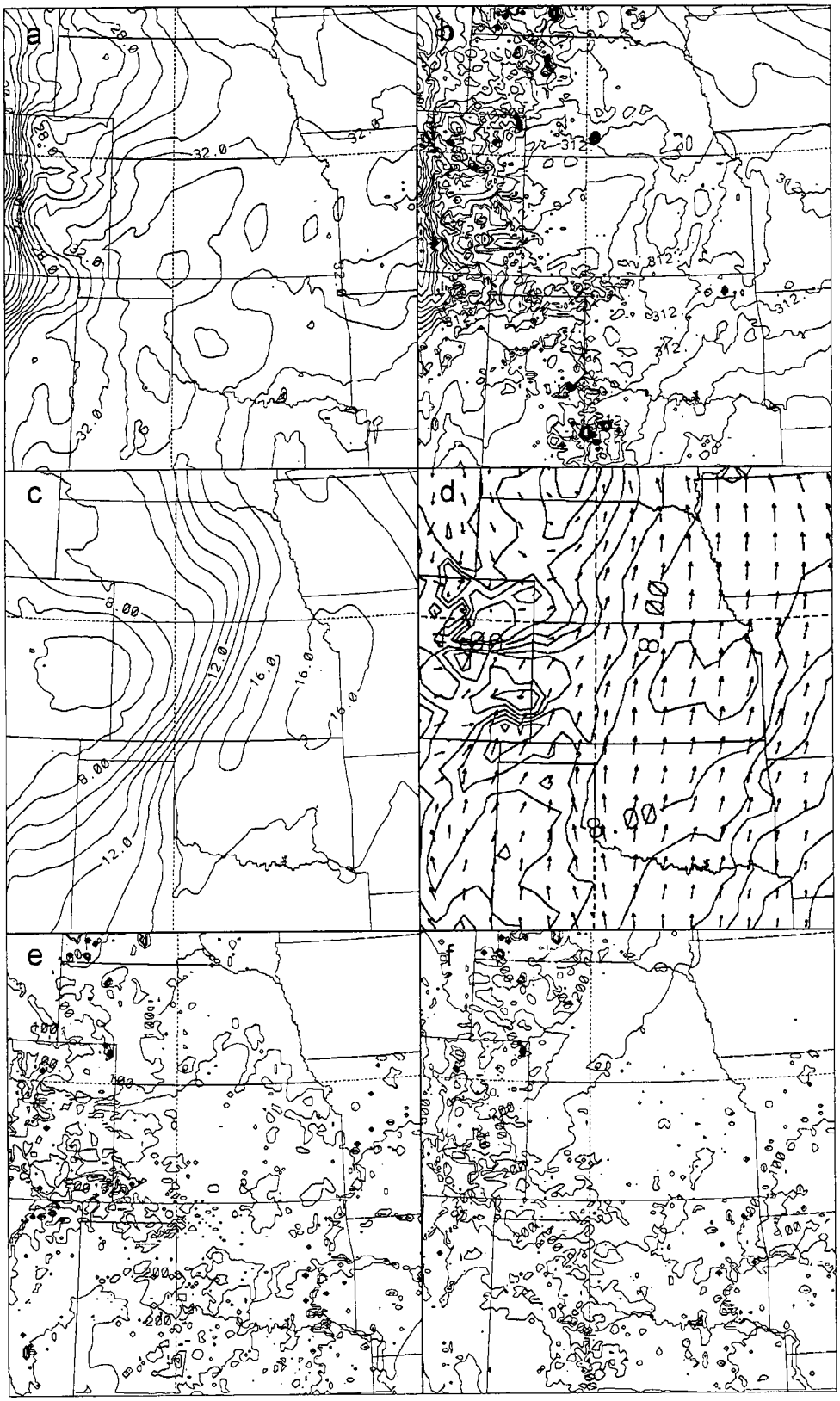

Figure 5.32: Same as Figure 5.22, except for the SAT simulation results at 2200 UTC.

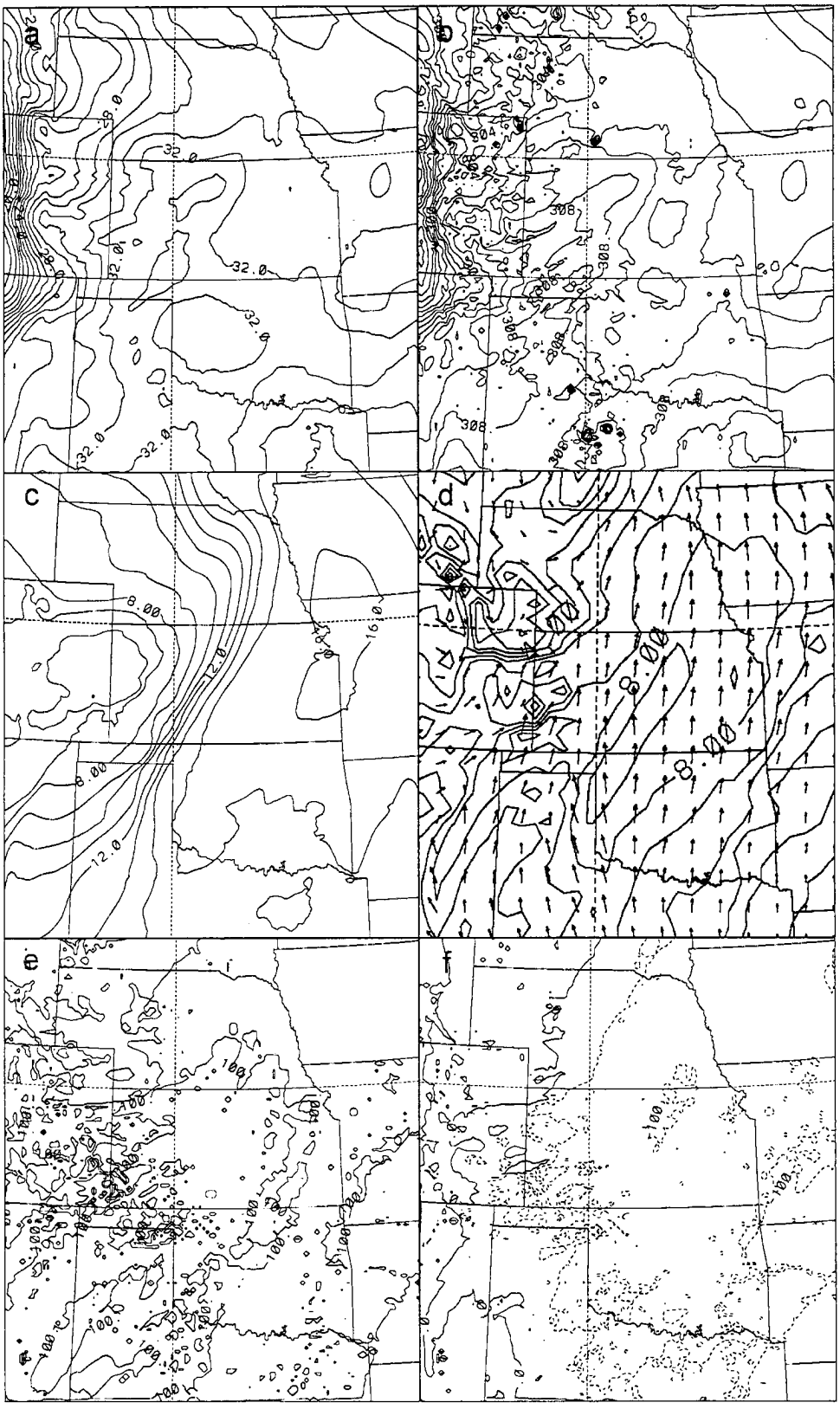

Figure 5.33: Same as Figure 5.22, except for the SAT simulation results at 0000 UTC.

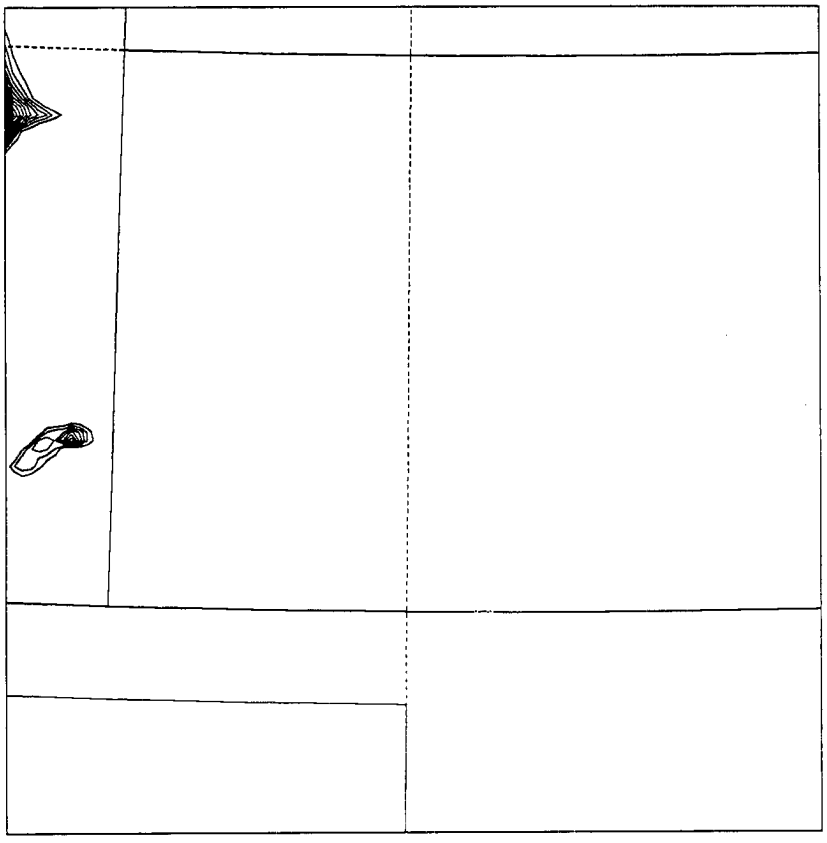

Figure 5.34: Same as Figure 5.25, except for the SAT simulation results.

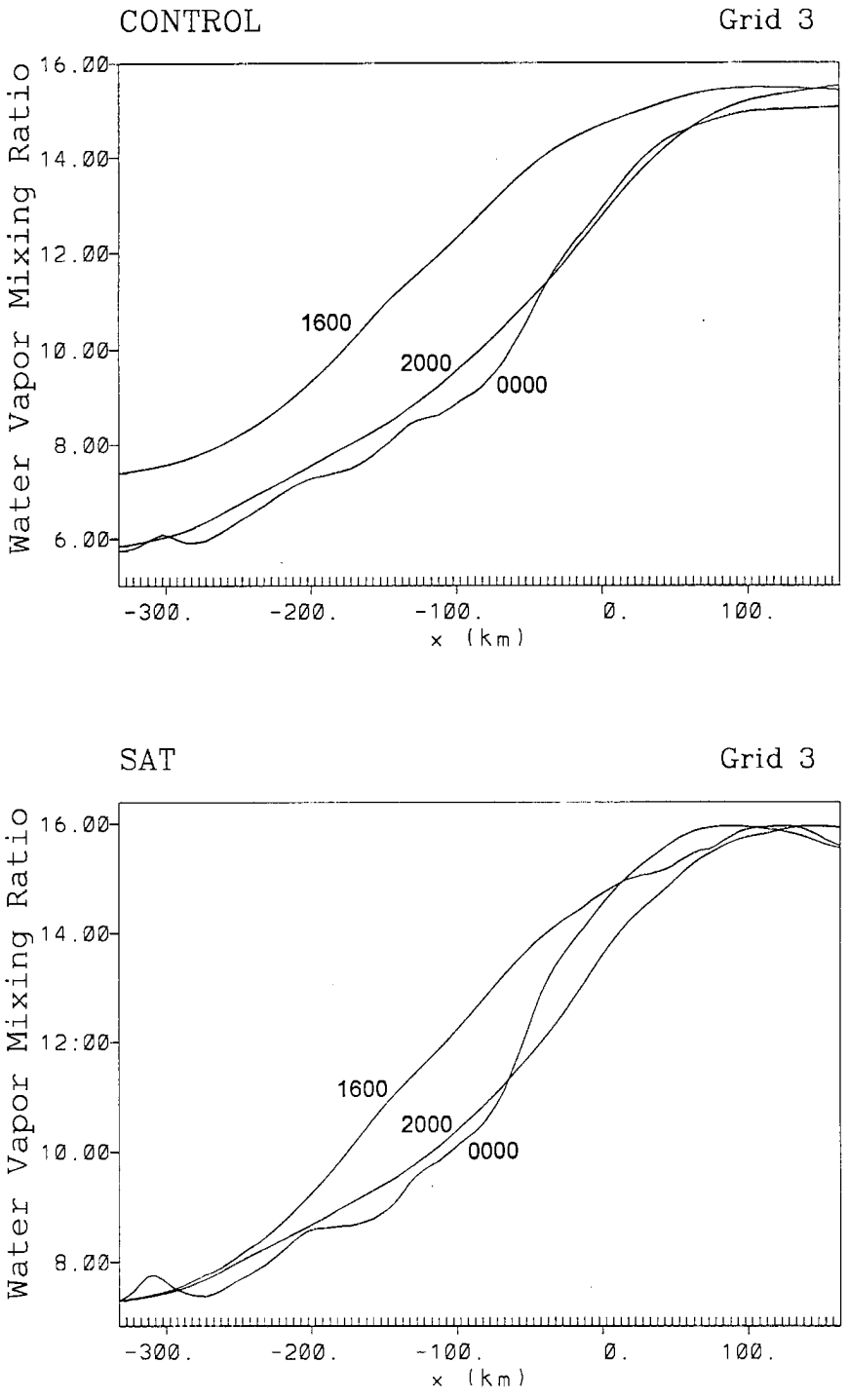

Figure 5.35: West to east cross section of water vapor mixing ratio (g kg^{-1}) at 1600, 2000, and 0000 UTC for the CONTROL and SAT simulations. The cross section is through the middle of grid 3, averaged over 7 grid points in the north-south direction (elements 47 to 53).

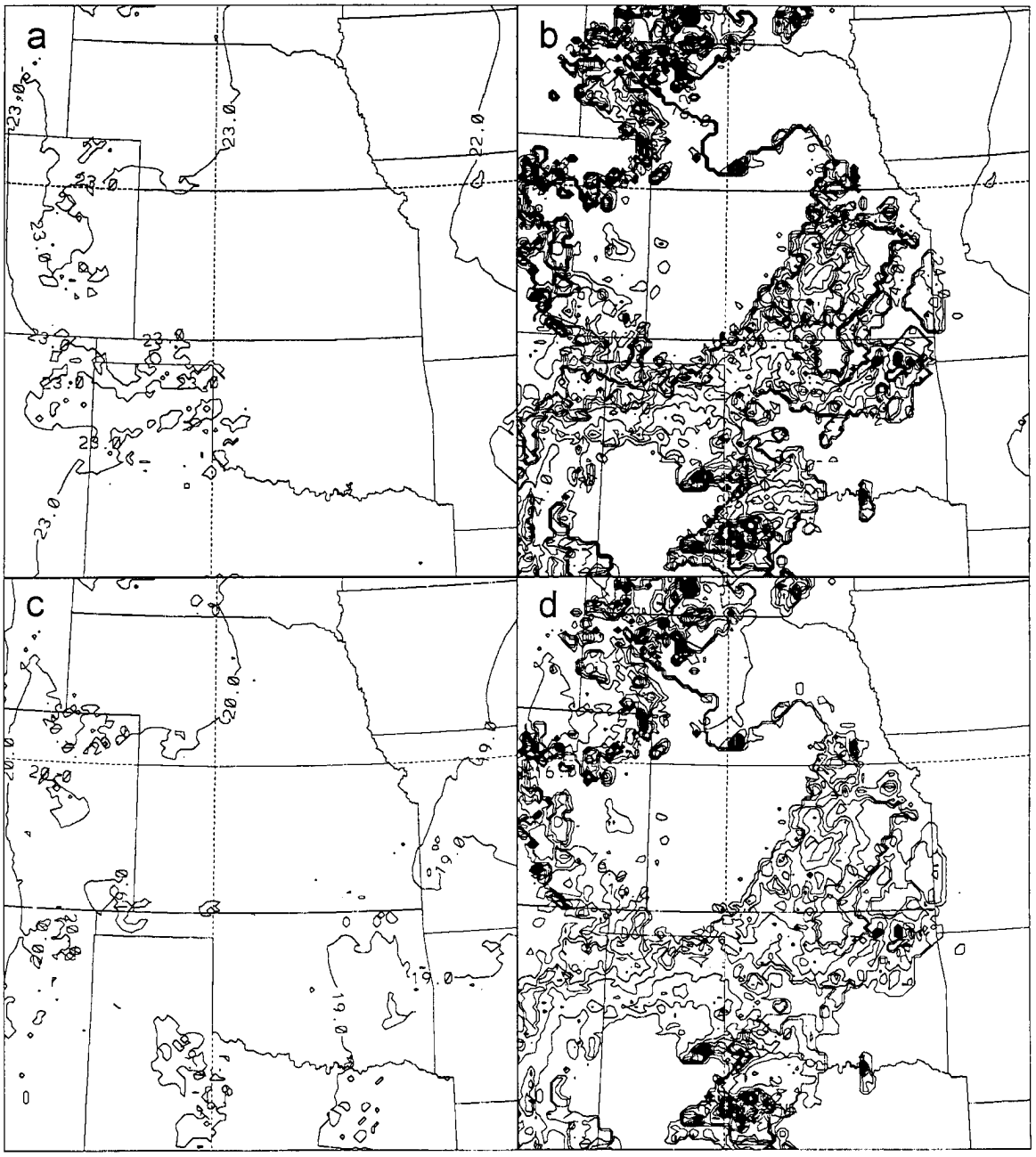

Figure 5.36: Surface bare-soil soil moisture expressed as a percentage of field capacity for a) the CONTROL run at 1600 UTC, b) the SAT run at 1600 UTC, c) the CONTROL run at 1800 UTC, and d) the SAT run at 1800 UTC.

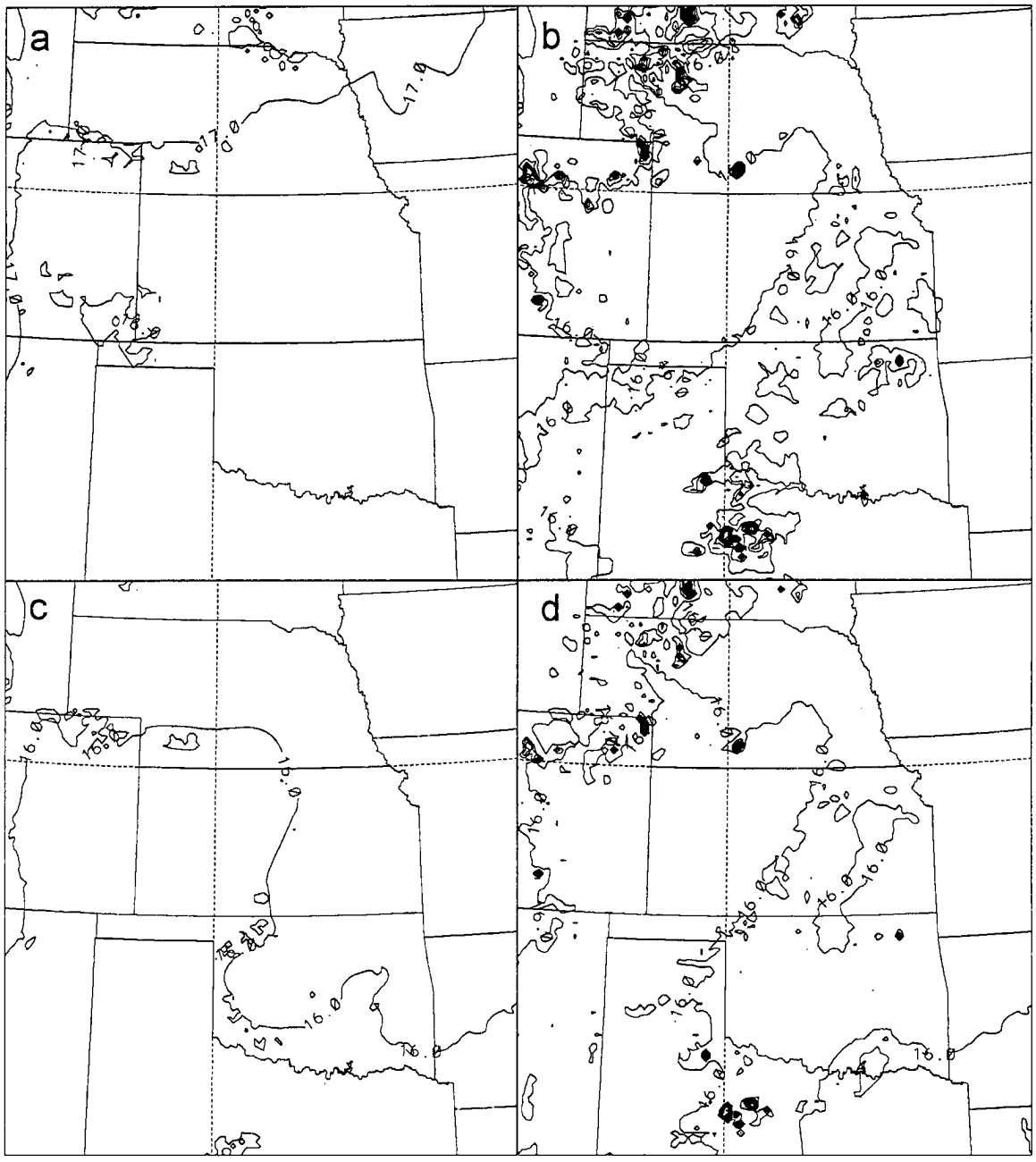

Figure 5.37: Same as Figure 5.36, except for a) the CONTROL run at 2100 UTC, b) the SAT run at 2100 UTC, c) the CONTROL run at 0000 UTC, and d) the SAT run at 0000 UTC.

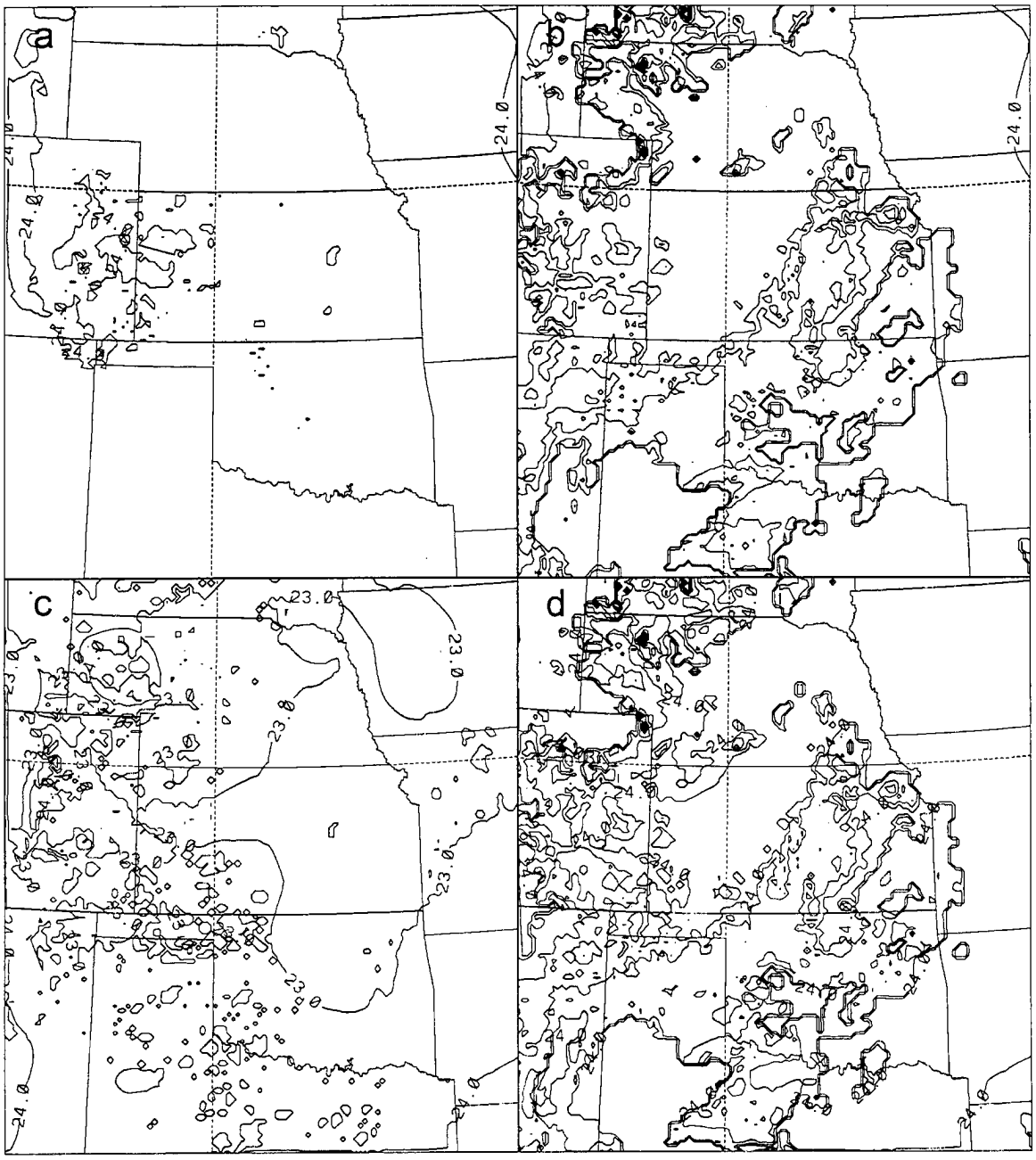

Figure 5.38: Surface shaded-soil soil moisture expressed as a percentage of field capacity for a) the CONTROL run at 1600 UTC, b) the SAT run at 1600 UTC, c) the CONTROL run at 1800 UTC, and d) the SAT run at 1800 UTC.

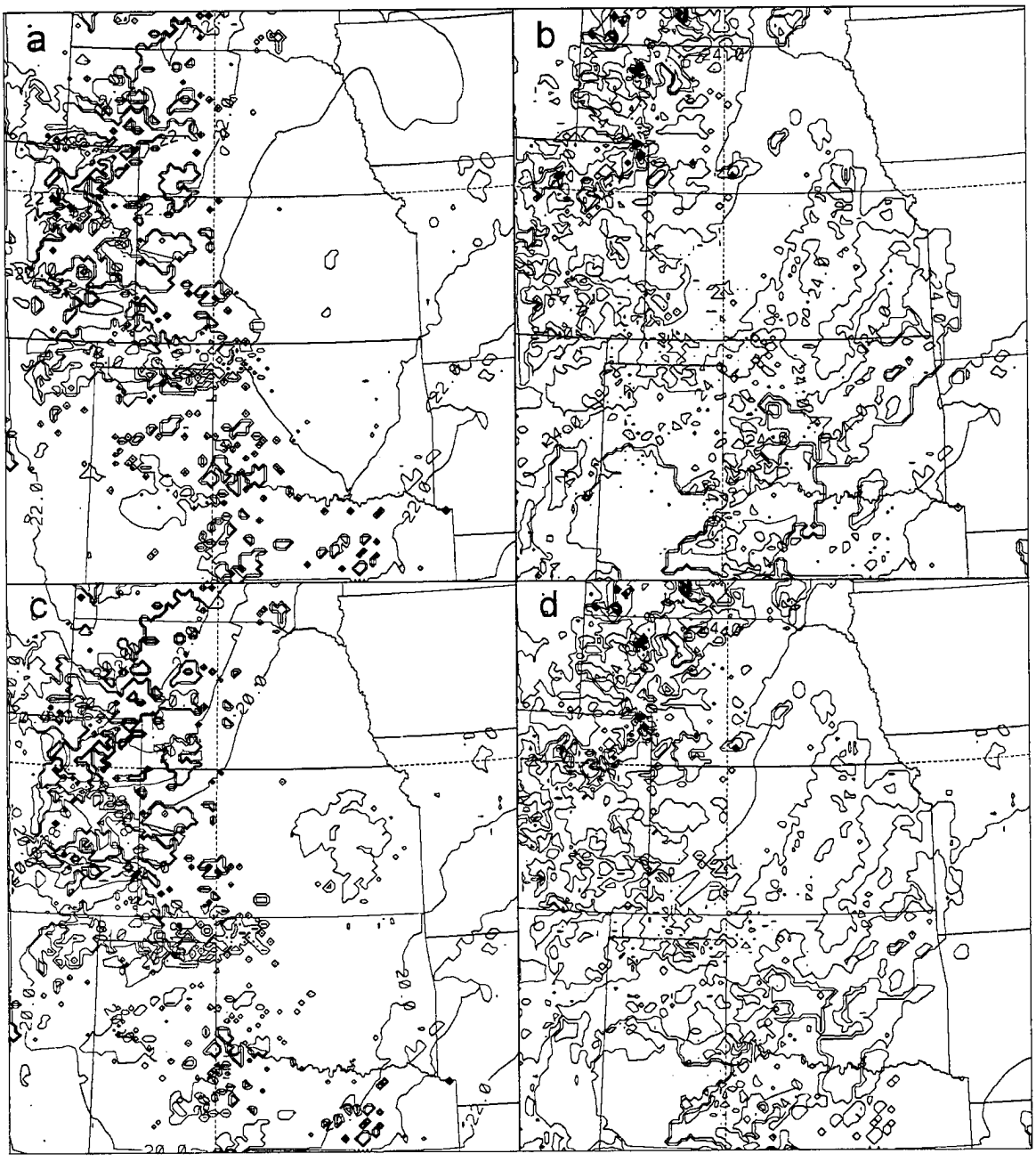

Figure 5.39: Same as Figure 5.38, except for a) the CONTROL run at 2100 UTC, b) the SAT run at 2100 UTC, c) the CONTROL run at 0000 UTC, and d) the SAT run at 0000 UTC.

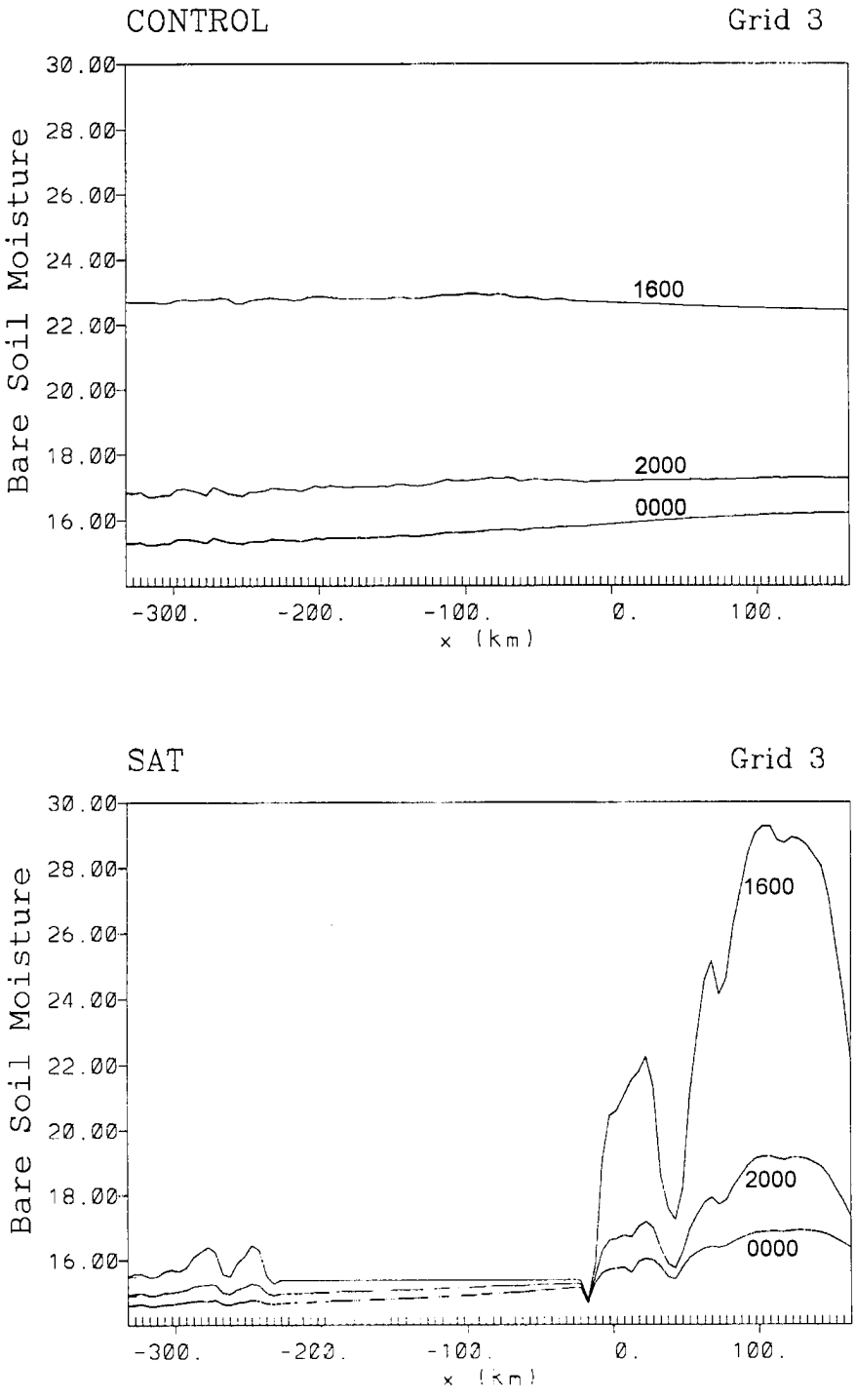

Figure 5.40: Same as Figure 5.35, except for bare-soil soil moisture (%).

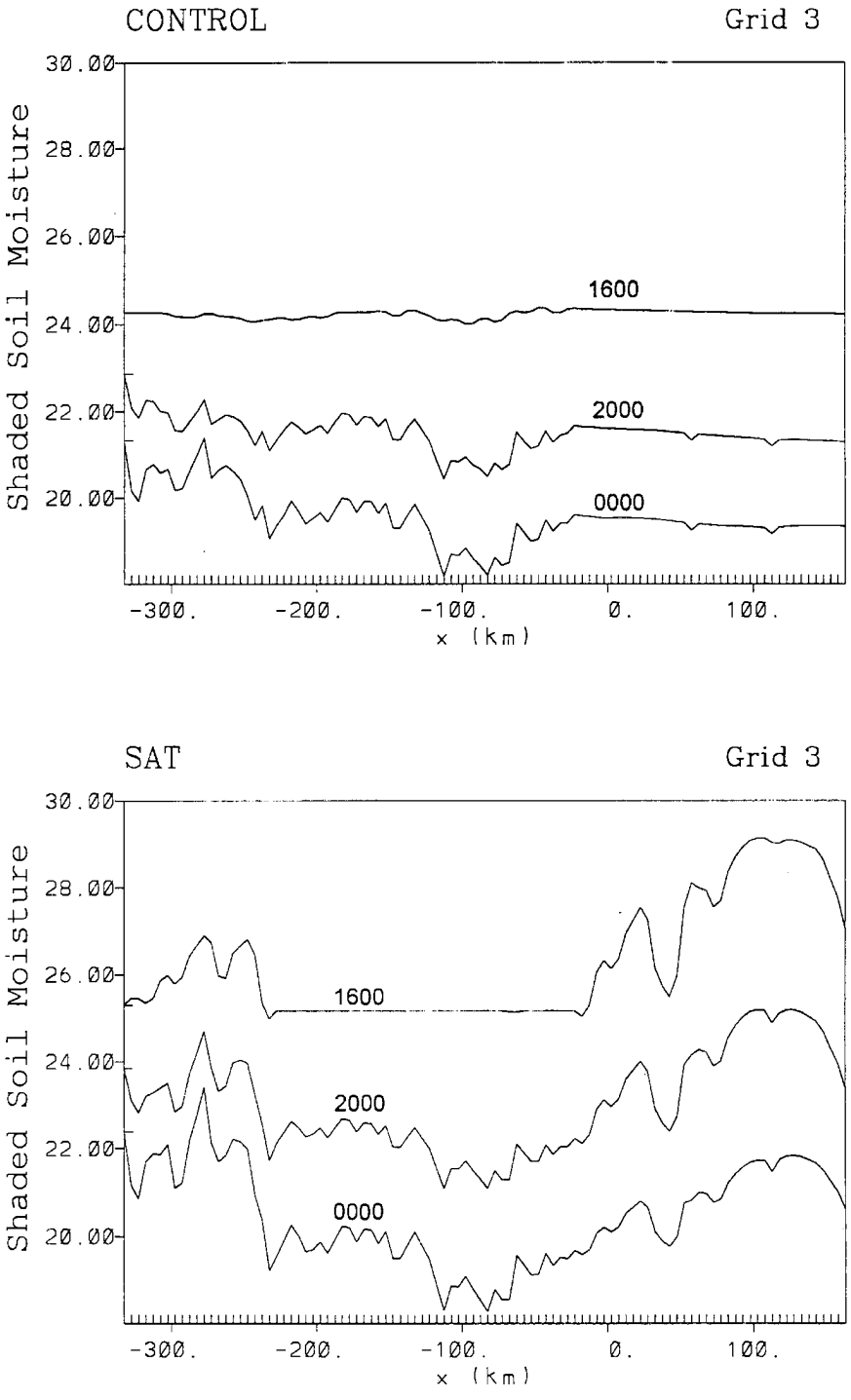

Figure 5.41: Same as Figure 5.35, except for shaded-soil soil moisture (%).

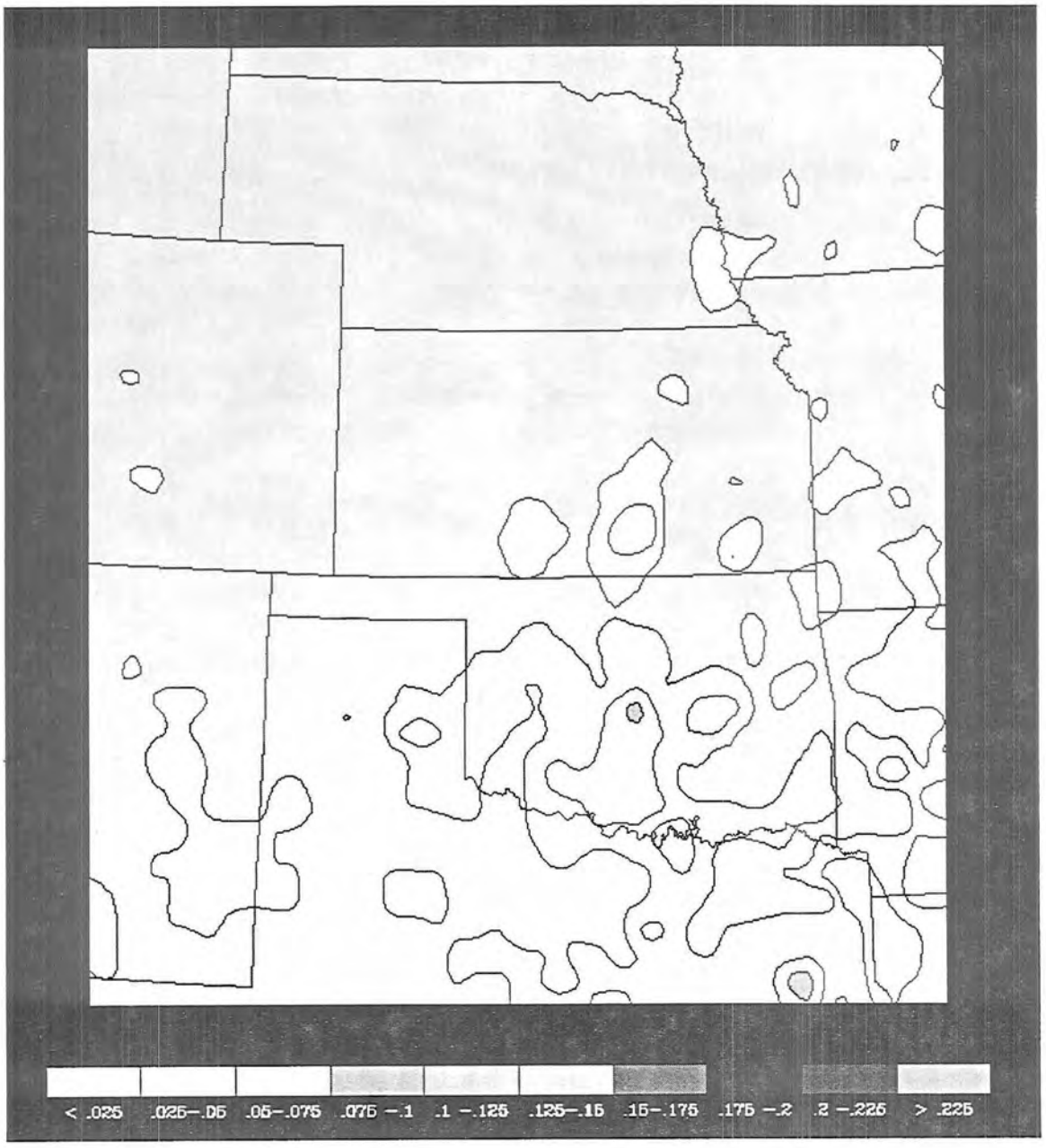

Figure 5.42: API for grid 2 at 8 September 1991 1200 UTC.

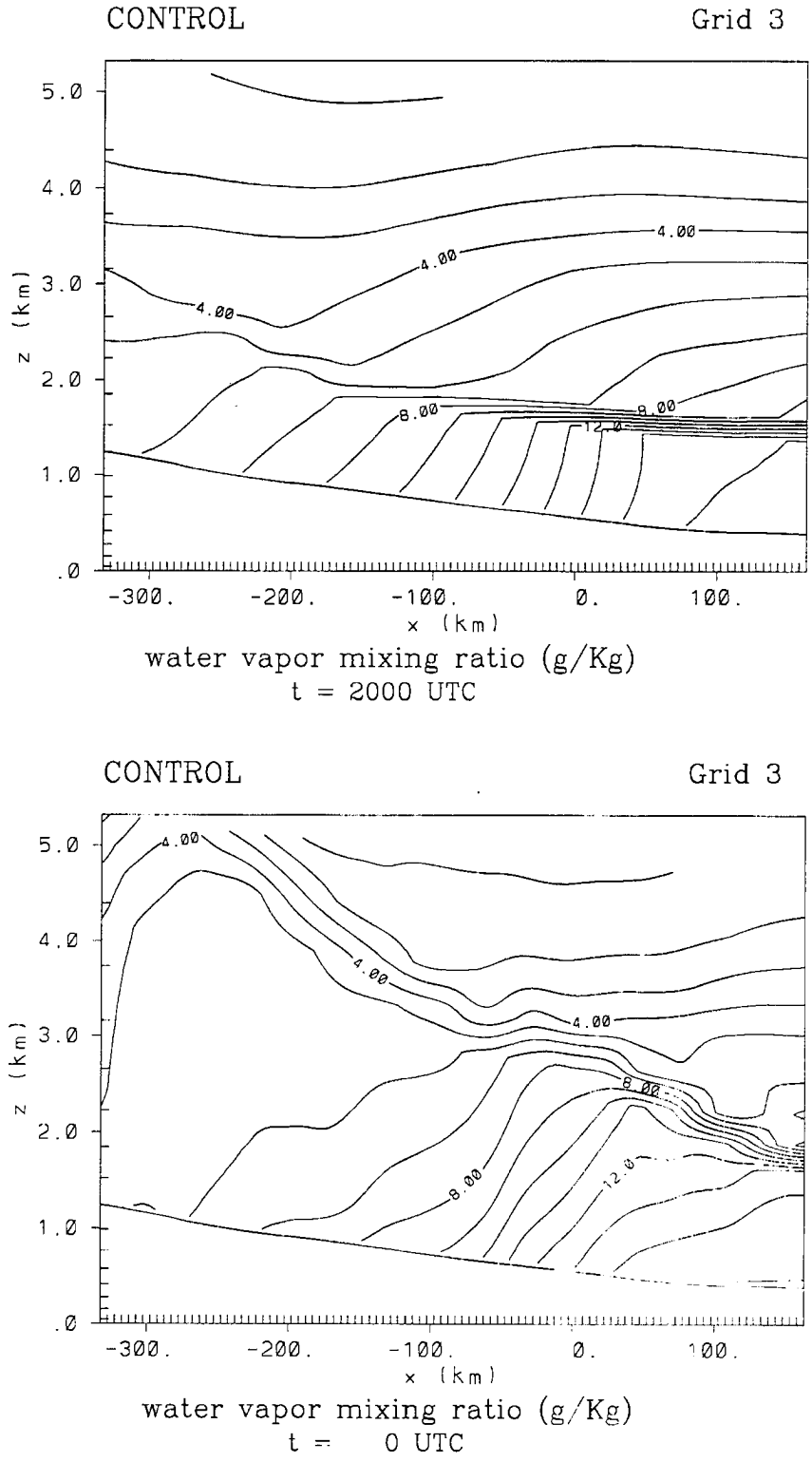

Figure 5.43: West to east vertical cross section of water vapor mixing ratio (g kg^{-1}) at 2000, and 0000 UTC for the CONTROL simulation. The cross section is through the middle of grid 3, averaged over 7 grid points in the north-south direction (elements 47 to 53).

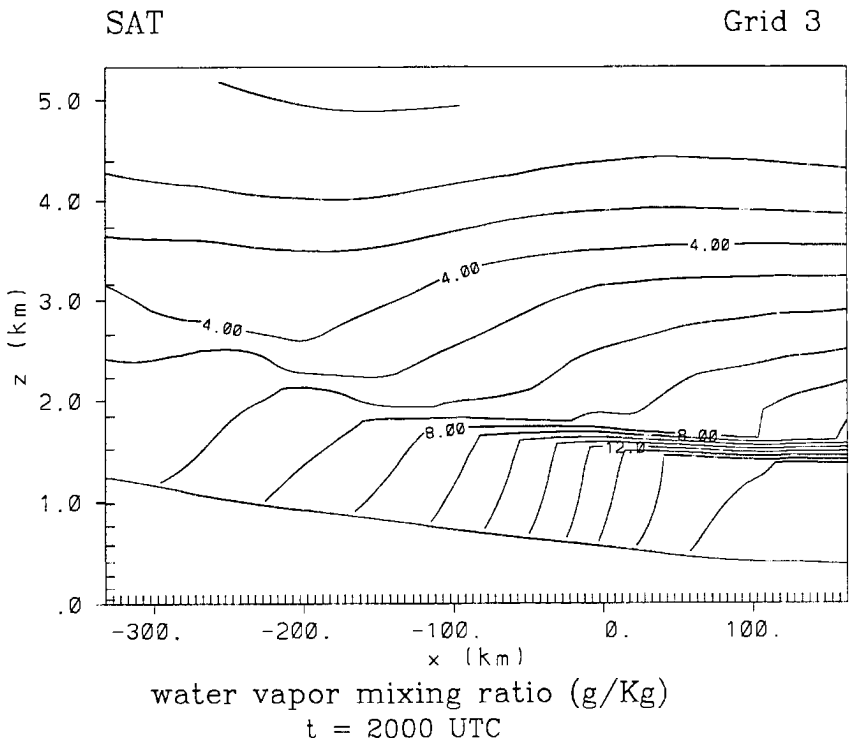

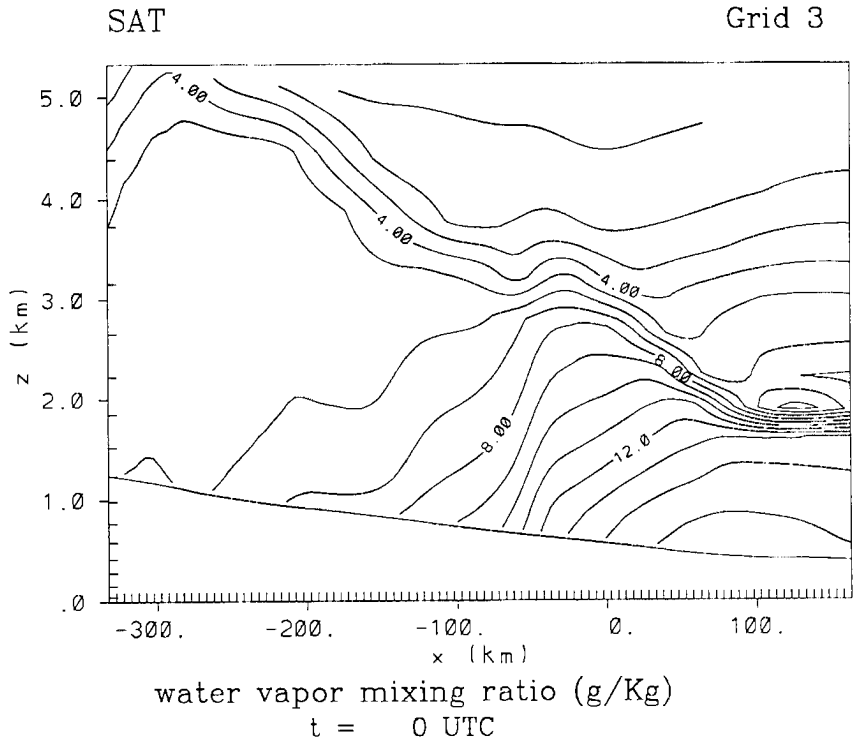

Figure 5.44: Same as Figure 5.43, except for the SAT simulation results.

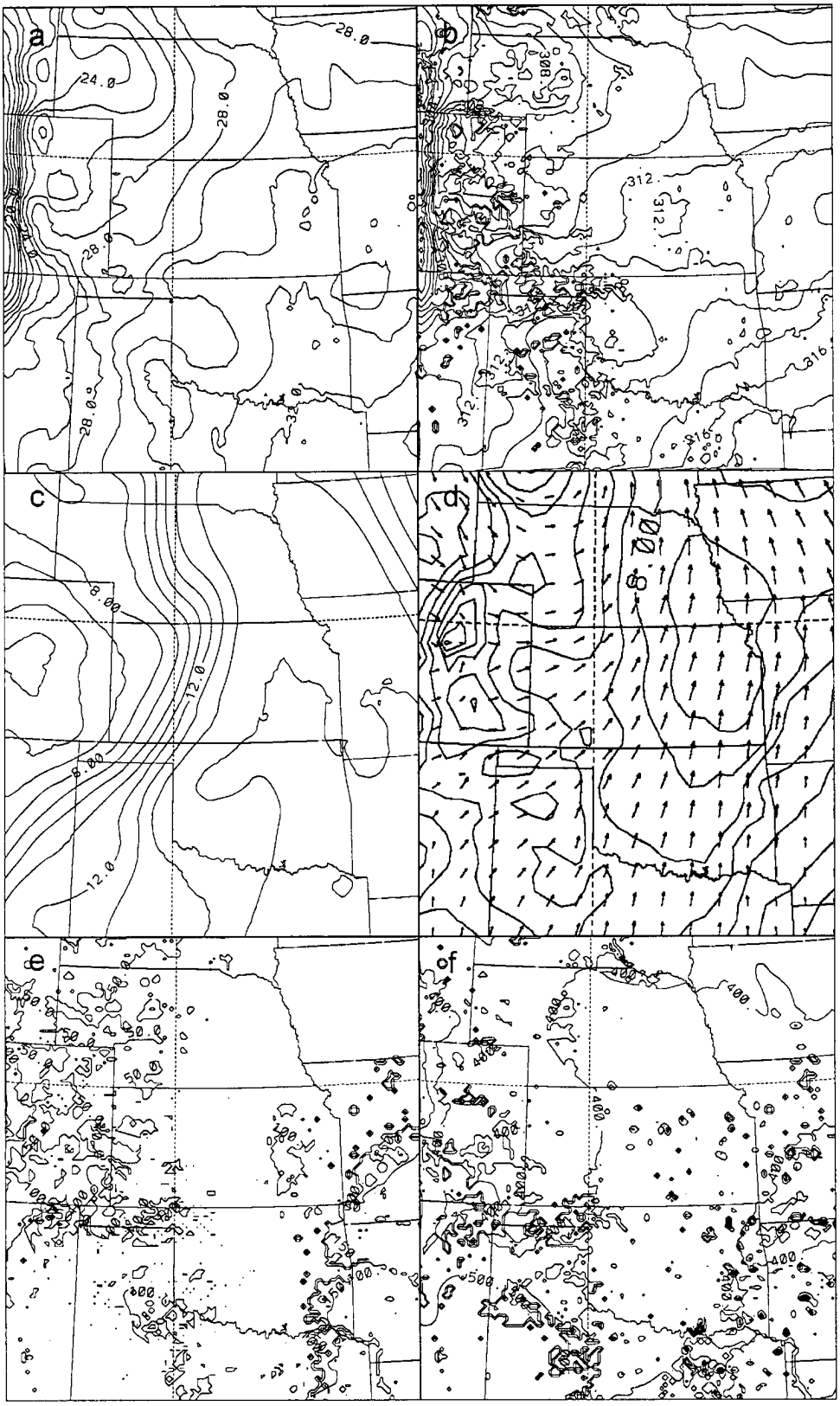

Figure 5.45: Same as Figure 5.22, except for the DRY simulation results at 1800 UTC.

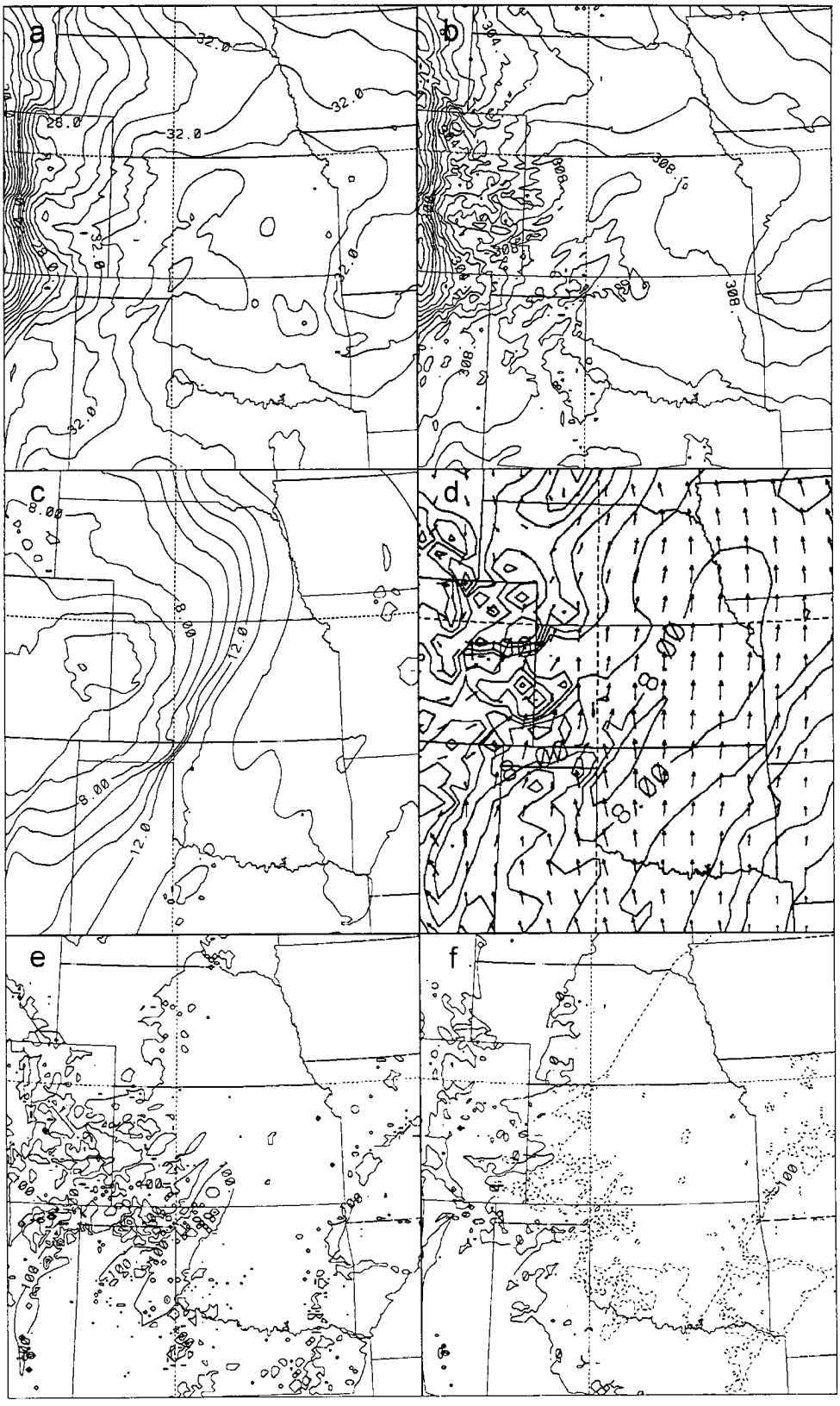

Figure 5.46: Same as Figure 5.22, except for the DRY simulation results at 0000 UTC.

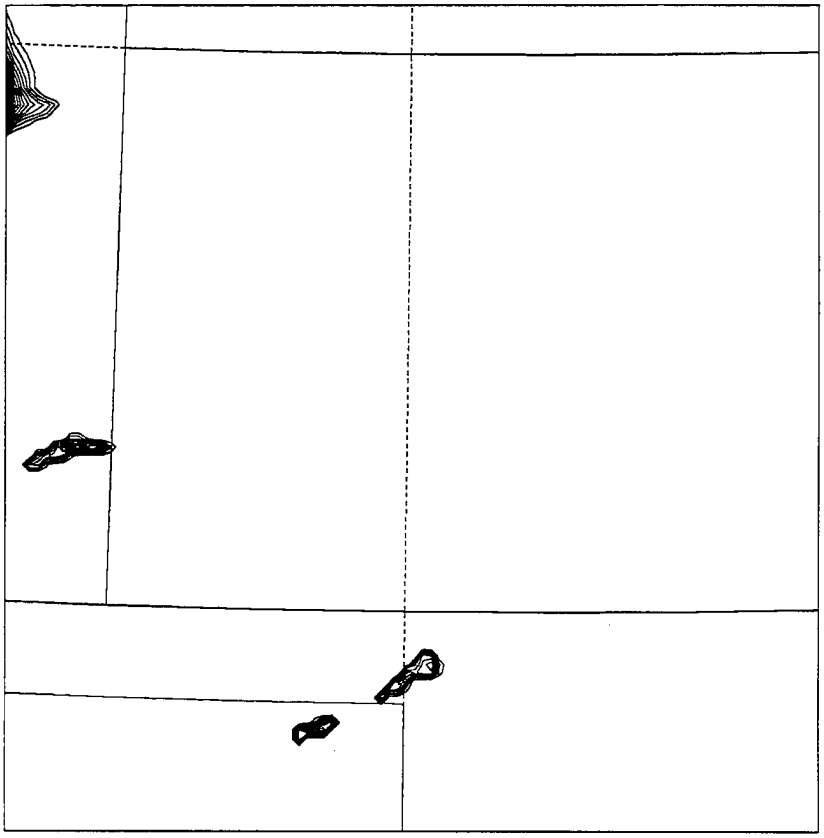

Figure 5.47: Same as Figure 5.25, except for the DRY simulation results at 0000 UTC.

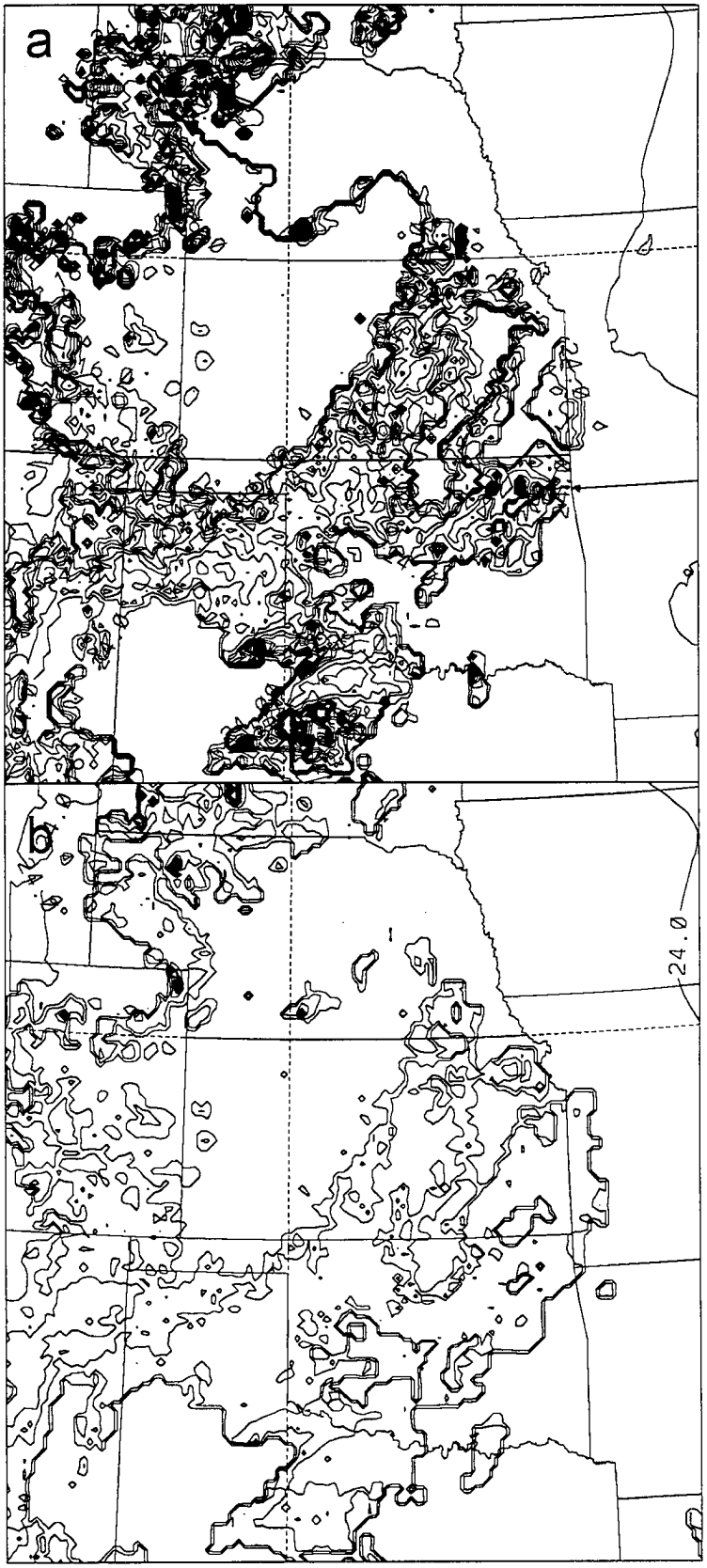

Figure 5.48: Same as Figure 5.36, except for the NOISE simulation soil moisture results at 1600 UTC for a) bare soil, and b) shaded soil.

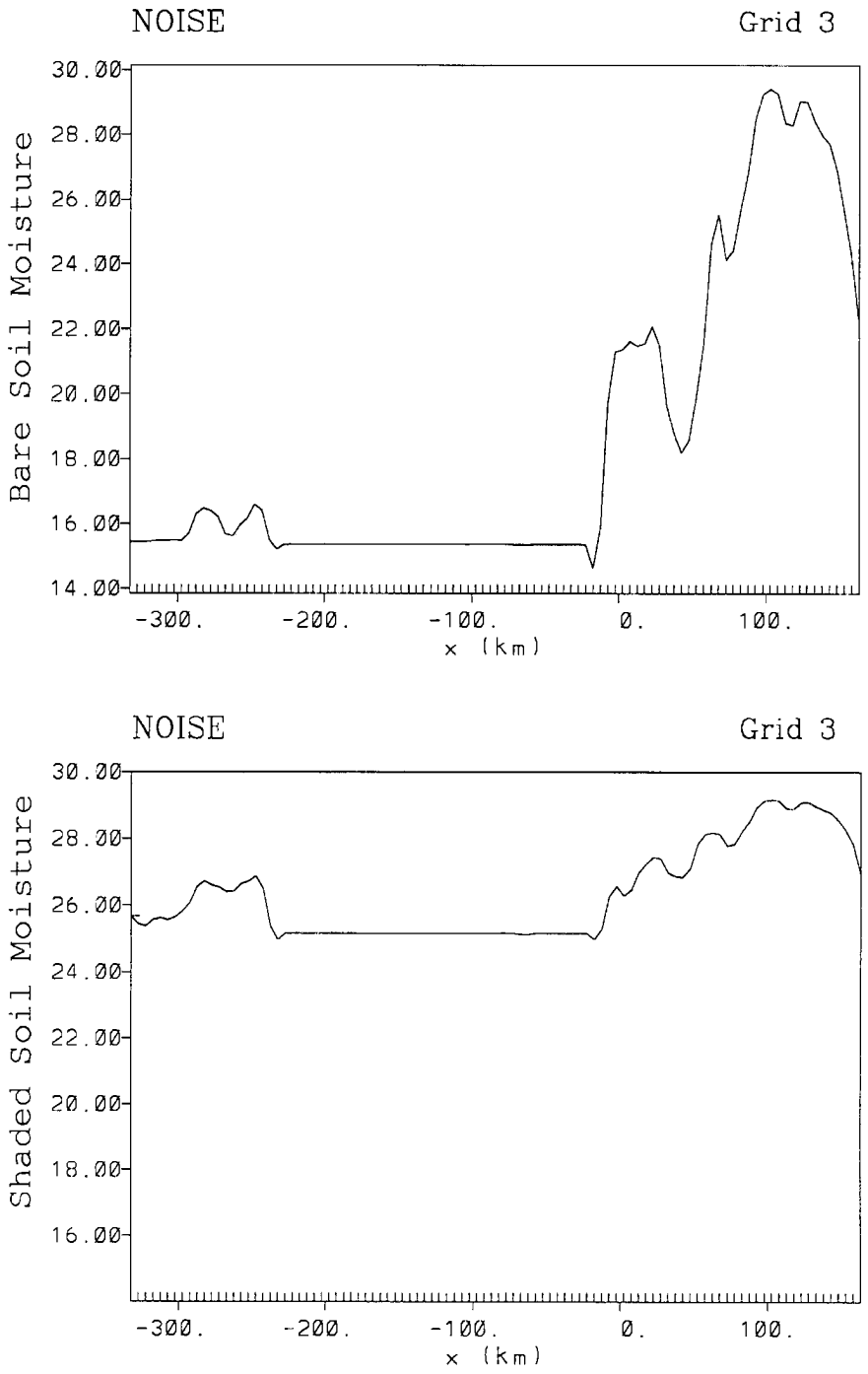

Figure 5.49: Same as Figure 5.40, except for the NOISE simulation soil moisture results at 1600 UTC for a) bare soil, and b) shaded soil.

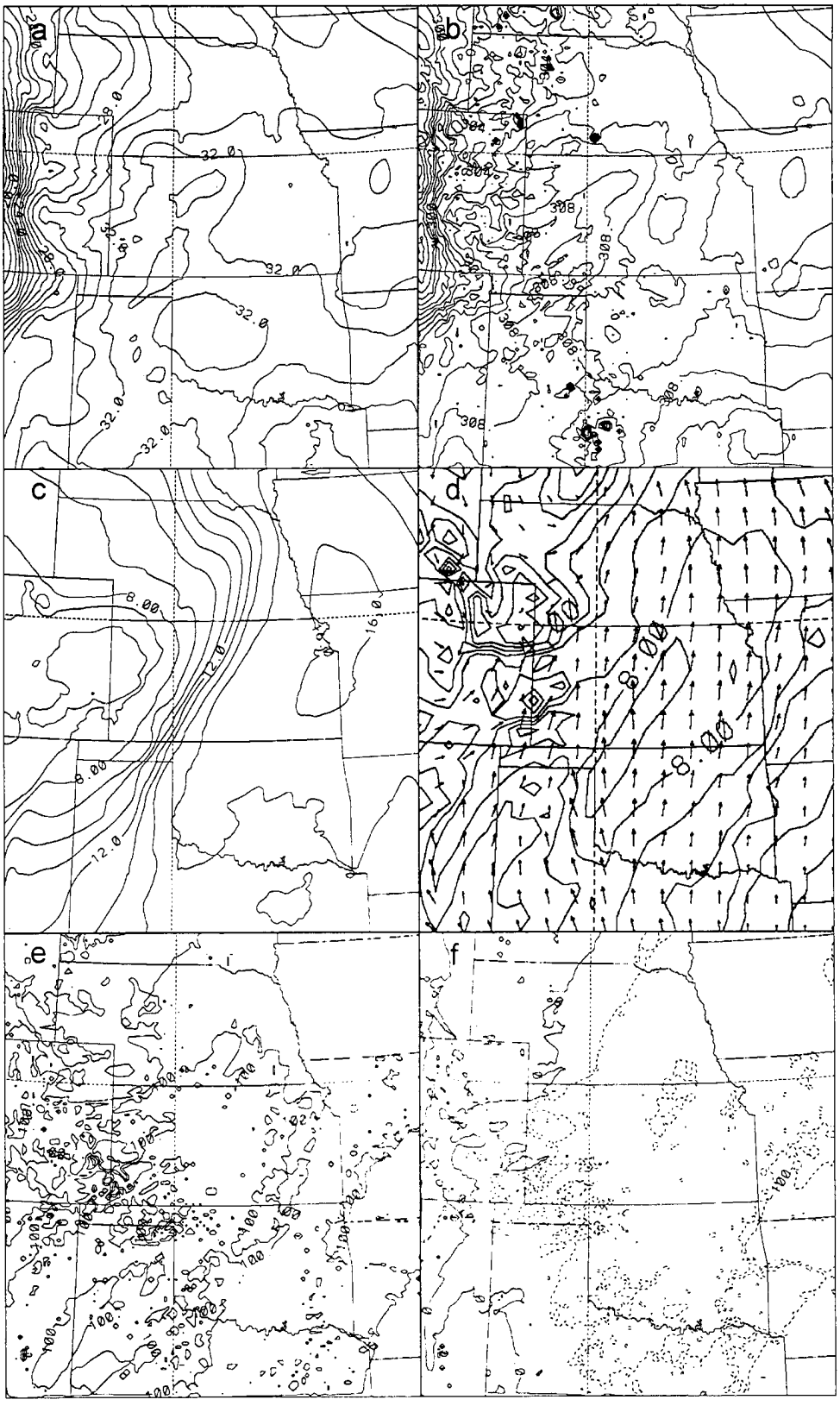

Figure 5.50: Same as Figure 5.22, except for the NOISE simulation results at 0000 UTC.

Chapter 6

SUMMARY AND CONCLUSIONS

Principal results of this dissertation fall into three categories as related to the scientific objectives noted in section 1.2.

6.1 MICROWAVE SURFACE EMITTANCE RESULTS

Microwave surface emittance is an important fundamental radiometric surface parameter. The results shown in Chapter 4 are unique in their spatial extent, and time covered in the microwave surface emittance composites. Extensive analysis was performed comparing the microwave surface emittance results other related datasets. Key findings of this work include the following:

- The microwave surface emittance is sensitive to temporal surface wetness features, irrigation regions, and some vegetation types. Weekly composites of the microwave surface emittance graphically show the temporal nature of the microwave surface emittance fields, and thus their potential for retrieval of temporal surface features such as surface wetness.

- Not all rain events appear in the microwave surface emittance data set, especially in the forested regions of the East; however, significant features related to rainfall were also found in some highly vegetated regions such as Illinois and west Mississippi. The microwave surface emittance is thus spatially inconsistent as an indicator of all precipitation events.

- The atmospheric correction applied during the retrieval of the microwave surface emittance tended to normalize the frequency dependence of the microwave surface emittance statistics and

thus would benefit remote sensing applications that need accurate radiometric surface boundary conditions.

- A small negative gradient with frequency is found with retrieved microwave surface emittance, which is opposite of the expected frequency dependence due to water. A non-uniform sampling size due to a frequency dependent FOV-size is suggested as the cause of this frequency dependent feature.

- Only limited diurnal effects were found in the microwave surface emittance data set, this suggests that the frequency penetration depth has little effect, since the penetration depth should experience a diurnal cycle due to an out-of-phase vertical heating profile for the surface and near-surface layers.

- Desert regions with different surface properties did not exhibit a noticeable difference in their microwave surface emittance values. This suggests that the low microwave emittance of desert regions is primarily related to the dielectric constant of the surface material and not the size and shape of the desert surface properties as has been suggested in earlier literature (e.g., Grody 1991). Further work is needed to confirm this hypothesis, since the desert regions examined in this study were rather small.

- Examination of the microwave polarization difference showed that most land surfaces are polarized to some extent. These results indicate the possibility of exploiting this parameter for the determination of cloud liquid water over land. A particular cloud liquid water retrieval method is suggested in this work.

- The NDVI comparisons showed little correspondence to the microwave surface emittance, except at very low NDVI values (< 0.2). This work highlights the inappropriateness of using the annualized MPDT versus NDVI relationship for generalizations about the sensitivity of the

microwave surface emittance to vegetation greenness as measured by the NDVI. This has serious implications regarding recent attempts to use generalized SVAT models (Olioso et al. 1995) which require a deterministic NDVI versus MPDT relationship that is simply not observed at the SSM/I frequencies. The microwave data is not responsive to vegetation in the same manner as NDVI except on a regional basis and at extremely low NDVI values. Irrigation effects are thus a substantial source of noise in the MPDT versus NDVI relationship.

- In a comparison of SSM/I-only semi-operational surface wetness indices, spatial filtering methods used in the methods were examined, and suggestions are made regarding the source of their underlying physical mechanisms as seen in light of the microwave surface emittance results.

6.2 SATELLITE DATA ASSIMILATION RESULTS

A new satellite-coupled data assimilation method using GOES infrared heating rates has been developed and tested. The method is an extension of the McNider et al. (1994) data assimilation method, and improves upon it by including a prognostic soil model, and an explicit vegetation representation. One of the most significant improvements over the McNider method is the removal the McNider method's problematic and highly variable C_h term. The data assimilation method was found to perform well in 1D tests using simulated observations. The RAMS surface parameterization scheme was found to impose physical constraints on the soil moisture retrievals, specifically for the driest and wettest conditions. This hampers the overall performance of the method, in that extreme events can not be successfully retrieved, since the satellite observations do not have the same limitations as the model's surface parameterization. However, analysis of a 3D case study showed the method was able to successfully retrieve realistic heterogeneous distributions (but not absolute magnitudes) of surface soil moisture conditions. The microwave surface wetness datasets, radar summaries, and API data corroborate the retrieved surface soil moisture fields of the satellite data assimilation method.

Because of the lack of response to the extremes, the new method had difficulty in significantly affecting the atmospheric model's forecast. While the surface water vapor gradient was increased slightly in the region of greatest soil moisture contrast, the effect was not long lasting in the model due to rapid surface evaporation in the model surface parameterization scheme. The location and orientation of the surface soil moisture field discontinuity were found to be coincident with that of a dryline which formed in the afternoon of the case study; however, since the CONTROL simulation results also placed the dryline in the same position, the satellite data assimilation results appear to be simply fortuitous. Another model simulation with dry soil moisture conditions showed that some of the intense water vapor gradient tightening in the Oklahoma panhandle is associated with convection in the region. This implies that the latent heat release due to the convection may be the cause of the sharp tightening of the water vapor gradient in previous related work [e.g., Shaw (1995), Ziegler et al. (1995), and Grasso (1996)]. Since only one 3D case study was simulated in the present work, this hypothesis requires additional testing. A simple noise sensitivity test was also performed which doubled the instrument noise, and found that the satellite data assimilation method produced nearly identical results. Thus instrument noise does not appear to be a major factor in the performance of the method.

6.3 DATA FUSION METHOD PERFORMANCE

A data fusion method is developed that is general enough for use with any scan-line-based datasets (satellite and ground based) and enables multisensor-multispectral datasets to be merged on a routine basis. The PORTAL system is able to combine data from sensors that have radically different earth scan patterns and ground resolutions. A self-describing generalized data format is used to modularize the data processing flow and obtain significant improvements in terms of flexibility, extensibility, and generality of application. Computational efficiencies are compared between this data fusion method and that of conventional remapping methods. While comparable

processing times are needed to physically merge the datasets, results show significant performance gains on any subsequent analysis of the merged datasets since scientific algorithms operate within the original satellite projection space.

6.4 CONCLUSIONS

A suite of satellite methodologies has been examined related to the problem of surface wetness retrievals. Atmospheric-corrected microwave surface emittance results were shown to enhance the use of the microwave datasets for land surface characteristics, especially in regards to analysis of the data's frequency dependencies. Several problems that affect the use of the microwave brightness temperature data were examined, including sub-FOV effects, and the natural characteristics of spatial and temporal variability of the microwave background signature. Use of datasets such as this can significantly improve and expand the work of microwave remote sensing over land regions. Much of the current microwave remote sensing work is limited over land surfaces due to uncertainties in the microwave surface properties. Land surface regions have been traditionally treated as beyond the reach of current remote sensing technologies. This limitation has resulted in the application of land masks to remote sensing techniques that omit data if it is over land. An immediate application of this work could be to improve the SSM/T-2 lower tropospheric water vapor retrievals (Felde and Pickle 1995). This study lays the scientific foundation to help extend current remote sensing technologies to fill this data-void region for microwave remote sensing techniques.

Specifically regarding the surface wetness remote sensing problem, the microwave surface emittance was found to be sensitive to numerous rain events captured in the dataset. However, the relationship of the microwave surface emittance to the NDVI was shown to be highly variable when analyzed at high spatial resolutions, and for all but the sparsest vegetation amounts. The additional complexity that was observed in the microwave surface emittance versus vegetation

relationship limits any future quantitative use of the microwave surface emittance for direct soil moisture retrieval. It also casts doubt on current methods that suppose a generalized instantaneous MPDT versus NDVI relationship that is simply not in the observations except at extremely low NDVI values. In addition to the previously mentioned enhancement of microwave retrieval methods over land surfaces, the microwave surface emittance may serve as a better indicator for selecting obviously flooded regions in a gross subjective manner. Thus, the potential application of the microwave surface emittance for flooding monitoring purposes and trafficability indices is high for non-forested regions. In fact, some of the highest API correlations were found in regions east of the Mississippi River, in Illinois and west Mississippi. The observational characteristics of the microwave surface emittance from its current observational platform makes continual observation of all surface wetness events unlikely. Thus, if routine monitoring of soil wetness is implemented from the current DMSP platforms, temporal performance expectations should be readjusted to the more sporadic nature of the microwave products.

The satellite data assimilation method developed in this work shows that GOES infrared heating rates can monitor heterogeneous surface wetness fields in a gross sense. Limitations were found regarding the ability to retrieve extreme dry or wet events. This has implications on the ability of the retrieved soil moisture values to affect the atmospheric model's forecast. As an example, extremely wet events that are retrieved with not enough soil moisture can not persist in the model as long as they should in the real world (assuming that the model's surface parameterization is realistic). Likewise, retrieved dry conditions that are not dry enough, reduce the model's predicted surface heating and can delay the onset of convection in the model (as occurred in the simulation of this study). From the noise sensitivity experiment results, instrument noise does not appear to be a major factor in the performance of the satellite data assimilation method. Overall,

this work shows the viability of the approach of assimilating satellite heating rates into a mesoscale model to improve atmospheric numerical weather prediction model initialization.

A note should added that the ability to successfully monitor soil moisture has far reaching benefits beyond atmospheric weather prediction. For example, several agricultural uses are mentioned by Engman (1991) and includes such diverse uses as crop yield prediction, irrigation management, and pest control. The potential economic ramifications of reliably determining soil moisture content are enormous, and thus it deserves a significant expenditure of our scientific resources.

6.5 SUGGESTIONS FOR FUTURE RESEARCH

6.5.1 Coupled Satellite-Model Remote Sensing of Surface Wetness

The satellite data assimilation method has been shown to be a viable method for incorporating infrared remote sensing data into an atmospheric mesoscale model. It is suggested that further work is needed to explore additional case studies to test the method under a variety of environmental conditions to determine other possible limitations of the method. This should include additional datasets from other periods to explore possible seasonally related performance variability. To improve the ability of the data assimilation method to sufficiently impact the atmospheric simulation later in the afternoon, longer data assimilation periods should be investigated to determine optimal satellite ingest periods, or possibly thicker surface soil levels should be used to increase the prognostic soil model's effect on subsequent model weather features.

An alternative to extensive tuning of the current method is to explore the possibility of assimilating the satellite heating rates in an adjoint version of the atmospheric model that would simultaneously adjust other parameters in addition to the soil moisture fields. Such a method could possibly overcome the limitations imposed on the method used in this study by allowing

perhaps the bare-soil/vegetation/water fraction to freely adjust to the satellite conditions. Such a method would allow extreme flooding events to be captured in the model in a more physical way than the current method. For example, an adjoint method may be able to retrieve a surface flooding fraction that would extend the ability of the model to duplicate observations in the real world. Albedo factors that were fixed in this study could also be incorporated in such a scheme. Advanced work could also include incorporating more realistic cloud fields into the model's radiation code. Thus cloud shading effects might be able to account for some differences in the surface energy budget of the model [e.g., see Lipton (1993)].

Soil moisture validation datasets are also needed. Previous programs focused on rather small regions that were relatively insignificant in size compared the microwave satellite FOVs (e.g., FIFE). In situ soil moisture data from larger domains has only recently become more freely available. In particular, the Atmospheric Radiation Measurement (ARM) Programs's Cloud and Radiation Test Bed (CART) field site will provide additional high quality surface measurements of soil temperature and soil moisture which would assist in the validation efforts of similar work (Stokes and Schwartz 1994). Future work should strongly focus on making the most of what soil moisture data is available.

Another general area of future research would be the coupling of a hydrological model to an atmospheric mesoscale model (Dabberdt and Schlatter 1996). Runoff processes and channel flow are not represented in the current RAMS atmospheric model. The addition of satellite-derived soil moisture information could help initialize the hydrological processes and provide better flooding forecasts. A pilot research project should be initiated to test the feasibility of performing such a threefold coupling of hydrologic and atmospheric modeling systems with satellite data.

6.5.2 Data Fusion Methodologies

PORTAL is just an initial step toward developing a more comprehensive data fusion methodology. There is a need for further development of data fusion software so that multisensor remote sensing can become more routine in the research community. This would allow all the calibration, scale, format, projections, etc., problems to be more transparent to the scientists, thereby permitting them to be more productive (Engman 1991). This should include a more robust data model that can account for the effects of possible data errors that are currently ignored in the present system. Many factors, such as inaccurate satellite navigation, and calibration errors could be better handled in a revised system. Software standardization should be a key goal in any further work in this area. Simply developing a highly customized system specific to your current needs and computing environment is not sufficient. It does not allow the researcher or scientific management to take advantage of the many possible alternatives and developments that are not locally created. Any future data fusion systems should be created with adherence to software standardization as a high priority. As outlined in Jones et al. (1995), error propagation analysis in the data fusion process can be automated, thus substantially enhancing the scientific value of the merged datasets. Future work should be undertaken to implement such a data system based on the PORTAL data fusion paradigm.

REFERENCES

Achutuni, R., J. G. LaDue, R. Scofield, N. Grody, and R. Ferraro, 1994: A soil wetness index for monitoring The Great Flood of 1993. *Seventh Conference on Satellite Meteorology and Oceanography,* Monterey, CA, Amer. Meteor. Soc., 580–583.

Allen, K. C., and H. J. Liebe, 1983: Tropospheric absorption and dispersion of millimeter and submillimeter waves. *IEEE Trans. Antennas Propag.,* **AP-31,** 221–223.

Allison, L., T. J. Schmugge, and G. Byrne, 1979: A hydrologic analysis of East Australian floods using Nimbus-5 Electrically Scanning Radiometer data. *Bull. Amer. Meteor. Soc.*, **60,** 1414–1427.

Avissar, R., and Y. Mahrer, 1982: Verificiation study of a numerical greenhouse microclimate model. *Trans. Amer. Soc. Agric. Eng.,* **25,** 1711–1720.

Avissar, R., and Y. Mahrer, 1988: Mapping frost-sensitive areas with a three-dimensional local-scale numerical model. Part I: Physical and numerical aspects. *J. Appl. Meteor.,* **27,** 400–413.

Avissar, R., and R. A. Pielke, 1989: A parameterization of heterogeneous land surface for atmospheric numerical models and its impact on regional meteorology. *Mon. Wea. Rev.*, **117,** 2113–2136.

Avissar, R., P. Avissar, Y. Mahrer, and B. A. Bravado, 1985: A model to simulate response of plant stomata to environmental conditions. *Agric. For. Meteor.,* **34,** 21–29.

Bajwa, R. S., W. M. Crosswhite, and J. E. Hostetler, 1987: *Agricultural Irrigation and Water Supply.* AIB-532, USDA, 109 pp.

Barnes, S. L., 1964: A technique for maximizing details in numerical weather map analysis. *J. Appl. Meteor.,* **3,** 396–409.

Barnes, S. L., 1980: SESAME news. *Bull. Amer. Meteor. Soc.,* **61,** 1401–1404.

Barton, I. J., 1978: A case study comparison of microwave radiometer measurements over bare and vegetated surfaces. *J. Geophys. Res.*, **83,** 3513–3517.

Basist, A., D. Garrett, R. Ferraro, N. Grody, and K. Mitchell, 1996: A comparison between snow cover products derived from visible and microwave satellite observations. J. Appl. Meteor., 35, 163–177.

Becker, F., 1987: The impact of spectral emissivity on the measurement of land surface temperature from a satellite. *Int. J. Remote Sens.,* **8,** 1509–1522.

Becker, F., and B. J. Choudhury, 1988: Relative sensitivity of Normalized Difference Vegetation Index (NDVI) and Microwave Polarization Difference Index (MPDI) for vegetation and desertification monitoring. *Remote Sens. Environ.*, **24,** 297–311.

Beers, Y., 1957: *Introduction to the Theory of Error.* Addison-Wesley Publishing Co., 66 pp.

Benjamin, S. G., and T. N. Carlson, 1986: Some effects of surface heating and topography on the regional severe storm environment. Part I: Three-dimensional simulations. *Mon. Wea. Rev.*, **114,** 307–329.

Benoit, A., 1968: Signal attenuation due to neutral oxygen and water vapor, rain, and clouds. *Microwave J.*, **11,** 73–80.

Bernard, R. M., J. V. Soares, and D. Vidal-Madjar, 1986: Differential bare field drainage properties from airborne microwave observation. *Water Resources Res.*, **22,** 869–875.

Bernard, R. M., M. Vauclin, and D. Vidal-Madjar, 1981: Possible use of active microwave remote sensing for prediction of regional evaporation by numerical simulation of water movement in the unsaturated zone. *Water Resources Res.*, **17,** 1603–1610.

Bernstein, R., C. Colby, S W. Murphey, and J. P. Snyder, 1983: Image geometry and rectification. Vol. 1, *Manual of Remote Sensing,* 2d ed. R. N. Colwell, Ed., American Society of Photogrammetry, 873–922.

Betts, A. K., J. B. Ball, A. C. M. Beljaars, M. J. Miller, and P. A. Viterbo, 1996: The land surface-atmosphere interaction: A review based on observational and global modeling perspectives. *J. Geophys. Res.*, **101,** 7209–7225.

Black, T. L., 1994: The new NMC mesoscale Eta model: Description and forecast examples. *Wea. Forecasting,* **9,** 265–278.

Blackadar, A. K., 1979: High resolution models of the planetary boundary layer. *Adv. Environ. Sci. Eng.*, **1,** 50–85.

Blume, H.-J. C., B. M. Kendall, and J. C. Fedors, 1978: Measurements of ocean temperature and salinity via microwave radiometry. *Boundary-Layer Meteor.*, **13,** 295–308.

Botts, M. E., 1992: The state of scientific visualization with regard to the NASA EOS Mission to Planet Earth. *Applied Information Systems Reseach Progam (AISRP) Workshop II Meeting Proc.*, Boulder, CO, Laboratory for Atmospheric and Space Physics, University of Colorado, E132-E139. [Available from Information Systems Banch, Flight Systems Division, Office of Space Science and Applications, NASA Headquarters.]

Bruckler, L., and H. Witono, 1989: Use of remotely sensed soil moisture content as boundary conditions in soil-atmosphere water transport modeling, Part 2: Estimating soil water balance. *Water Resources Res.*, **25,** 2437.

Burke, W. J., T. J. Schmugge, and J. F. Paris, 1979: Comparisons of 2.8- and 21-cm microwave radiometer observations over soils with emission model calculations. *J. Geophys. Res.*, **84,** 287–294.

Businger, J. A., 1973: Turbulent transfer in the atmosphere surface layer. *Workshop in Micrometeorlogy*, Chapter 2, Amer. Meteor. Soc., Boston, MA.

Businger, J. A., J. C. Wangaard, Y. Izumi, and E. F. Bradley, 1971: Flux profile relationships in the atmospheric surface layer. *J. Atmos. Sci.*, **28,** 181–189.

Campbell, W. J., and R. F. Cromp, 1990: Evolution of an intelligent information fusion system. *Photogram. Eng. Remote Sens.*, **56,** 867–870.

Campbell, W. J., N. M. Short Jr., and L. A. Teinish, 1989: Adding intelligence to scientific data management. *Comput. Phys.*, **3,** 26–32.

Cardone, V., T. Chester, and R. Lipes, 1983: Evaluation of SEASAT SMMR wind measurements. *J. Geophys. Res.*, **88,** 1709–1726.

Carlson, T. N., 1986: Regional scale estimates of surface moisture availability and thermal inertia using remote thermal measurements. *Remote Sens. Reviews*, **1,** 197–246.

Carlson, T. N., J. K. Dodd, S. G. Benjamin, and J. N. Cooper, 1981: Satellite estimation of the surface energy balance, moisture availability and thermal inertia. *J. Appl. Meteor.*, **20,** 67–87.

Carlson, T. N., E. M. Perry, and T. J. Schumugge, 1990: Remote estimation of soil moisture availability and fractional vegetation cover for agricultural fields. *Agric. For. Meteor.*, **52,** 45–69.

Carlson, T. N., F. G. Rose, and E. M. Perry, 1984: Regional-scale estimates of surface moisture availability from GOES infrared satellite measurements. *Agronomy J.*, **76,** 972–979.

Chandrasekhar, S., 1960: *Radiative Transfer*. Dover Publications, Inc., New York, 393 pp.

Chang, A. T. C., J. L. Foster, and D. K. Hall, 1987: Nimbus-7 SMMR derived global snow cover parameters. *Annuals of Glaciology*, **9,** 39–55.

Chang, A. T. C., J. L. Foster, D. K. Hall, A. Rango, and B. K. Hartline, 1982: Snow water equivalent estimation by microwave radiometry. *Cold Regions Science and Technology*, **5,** 259–267.

Chang, J.-T., and P. J. Wetzel, 1991: Effects of spatial variations of soil moisture and vegetation on the evolution of a prestorm environment: A numerical case study. *Mon. Wea. Rev.*, **119,** 1368–1390.

Chapman, J. D., and J. C. Sherman, editors, 1982: *Oxford Regional Economic Atlas, The United States and Canada, 2nd Edition*. Oxford University Press, 128 pp.

Chen, F., and R. Avissar, 1994a: Impact of land-surface moisture variability on local shallow convective cumulus and precipitation in large-scale models. *J. Appl. Meteor.*, **33,** 1382–1401.

Chen, F., and R. Avissar, 1994b: The impact of land-surface wetness heterogeneity on mesoscale heat fluxes. *J. Appl. Meteor.*, **33,** 1323–1340.

Chesters, D., and W. D. Robinson, 1983: *Performance appraisal of VAS radiometry for GOES-4, -5, and -6*. NASA Tech. Memo. 85125 [NTIS Ref: N84-18781], 55 pp.

Choudhury, B. J., 1990: A comparative analysis of satellite-observed visible reflectance and 37 GHz polarization difference to assess land surface change over the Sahel zone, 1982-1986. *Climatic Change*, **17,** 193–208.

Choudhury, B. J., 1991a: Multispectral satellite data in the context of land surface heat balance. *Rev. of Geophys.*, **29,** 217–236.

Choudhury, B. J., 1991b: Passive microwave remote sensing contribution to hydrological variables. *Surveys in Geophysics*, **12,** 63–84.

Choudhury, B. J., 1992: Multispectral satellite observations for arid land studies. *ISPRS J. of Photogrammetry and Remote Sensing*, **47,** 101–126.

Choudhury, B. J., and B. J. Blanchard, 1983: Simulating soil water recession coefficients for agricultural watersheds. *Water Resources Bull.*, **19,** 241–248.

Choudhury, B. J., and J. L. Monteith, 1988: A four-layer model for the heat budget of homogeneous land surfaces. *Quart. J. Royal Meteor. Soc.*, **114,** 373–398.

Choudhury, B. J., T. J. Schmugge, A. Chang, and R. W. Newton, 1979: Effect of surface roughness on the microwave emission from soils. *J. Geophys. Res.*, **84,** 5699–5706.

Choudhury, B. J., T. J. Schmugge, and T. Mo, 1982: A parameterization of effective soil temperature for microwave emission. *J. Geophys. Res.*, **87,** 1301–1304.

Choudhury, B. J., J. R. Wang, A. Y. Hsu, and Y. L. Chien, 1990: Simulated and observed 37 GHz emission over Africa. *Int. J. Remote Sens.*, **11,** 1837.

Clark, C. A., and R. W. Arritt, 1995: Numerical simulations of the effect of soil moisture and vegetation cover on the development of deep convection. *J. Appl. Meteor.*, **34,** 2029–2045.

Clark, J. D., 1983: *GOES User's Guide*. U.S. Dept. of Commerce, Washington, D.C.

Coates, G. D., V. C. Wong, J. W. Zack, and M. L. Kaplan, 1984: A numerical investigation of the effect of soil moisture gradients on the regional severe storm environment. Preprints, *Tenth Conference on Weather Forecasting and Analysis*, Clearwater Beach, FL, Amer. Meteor. Soc., 506–512.

Comiso, J. C., 1983: Sea ice effective microwave emissivities from satellite passive microwave and infrared observations. *J. Geophys. Res.*, **88,** 7686–7704.

Comiso, J. C., 1985: Remote sensing of sea ice using multispectral microwave satellite data. Deepak, A., Fleming, H. E., and Chahine, M. T., editors, *Advances in Remote Sensing Retrieval Methods*, pages 349–369, A. Deepak Publishing.

Comiso, J. C., 1990: Arctic multiyear ice classification and summer ice cover using passive microwave satellite data. *J. Geophys. Res.*, **95,** 13411–13422.

Comiso, J. C., P. Wadhams, W. B. Krabill, R. N. Swift, J. P. Crawford, and W. B. Tucker III, 1991: Top/bottom multisensor remote sensing of arctic sea ice. *J. Geophys. Res.*, **96,** 2693–2709.

Conte, S. D., and C. de Boor, 1980: *Elementary Numerical Analysis.* McGraw-Hill, New York, 432 pp.

Cooper, H. J., E. A. Smith, and W. L. Crosson, 1995: Limitations in estimating surface sensible heat fluxes from surface and satellite radiometric skin temperatures. *J. Geophys. Res.*, **100,** 25419–25427.

Crago, R., M. Sugita, and W. Brutsaert, 1995: Satellite-derived surface temperatures with boundary layer temperatures and geostrophic winds to estimate surface energy fluxes. *J. Geophys. Res.*, **100,** 25447–25451.

Dabberdt, W. F., and T. W. Schlatter, 1996: Research opportunities from emerging atmospheric observing and modeling capabilities. *Bull. Amer. Meteor. Soc.*, **77,** 305–323.

Davis, F. W., D. A. Quattrochi, M. K. Ridd, N. S.-L. Lam, S. J. Walsh, J. C. Michaelsen, J. Franklin, D. A. Stow, C. J. Johannsen, and C. A. Johnston, 1991: Environmental analysis using integrated GIS and remotely sensed data: Some research needs and priorities. *Photogram. Eng. Remote Sens.*, **57,** 689–697.

Deardorff, J. W., 1974: Three-dimensional numerical study of the height and mean structure of a heated planetary boundary layer. *Boundary-Layer Meteor.*, **7,** 81–106.

Deardorff, J. W., 1978: Efficient prediction of ground surface temperature and moisture, with inclusion of a layer of vegetation. *J. Geophys. Res.*, **83,** 1889–1903.

Deirmendjain, D., 1963: *Complete Microwave Scattering and Extinction Properties of Polydispersed Cloud and Rain Elements.* Rep. 12-422-PR, Rand Corp., Santa Monica, CA, 54 pp.

Delage, Y., and D. Verseghy, 1995: Testing the effects of a new land surface scheme and of initial soil moisture conditions in the Canadian global forecast model. *Mon. Wea. Rev.*, **123,** 3305–3317.

Diak, G. R., and M. S. Whipple, 1995: Note on estimating surface sensible heat fluxes using surface temperatures measured from a geostationary satellite during FIFE 1989. *J. Geophys. Res.*, **100,** 25453–25461.

Diak, G., S. Heikkinen, and J. Bates, 1986: The influence of variations in surface treatment on 24-h forecasts with a limited area model, including a comparison of modeled and satellite-measured surface temperatures. *Mon. Wea. Rev.*, **114,** 215–232.

Diak, G. R., R. M. Rabin, K. P. Gallo, and C. M. Neale, 1995: Regional-scale comparisons of vegetation and soil wetness with surface energy budget properties from satellite and in-situ observations. *Remote Sens. Reviews,* **12,** 355–382.

Dickinson, R. E., 1994: Land atmosphere interaction. *U.S. Natl. Rep. Int. Union Geod. Geophys. 1991-1994, Rev. Geophys.* submitted.

Dickinson, R. E., A. Henderson-Sellers, P. J. Kennedy, and M. F. Wilson, 1986: *Biosphere-Atmosphere Transfere Scheme for the NCAR community climate model.* Technical Report NCAR/TN-275+STR, NCAR, Boulder, CO, 69 pp.

Dobson, M. C., F. T. Ulaby, M. T. Hallikainen, and M. A. El-Rayes, 1985: Microwave dielectric behavior of wet soil — Part II: Dielectric mixing models. *IEEE Trans. Geosci, and Remote Sensing,* **GE-23,** 35–46.

Dombrovskiy, L. A., and V. Y. Rayzer, 1992: Microwave model of a two-phase medium at the ocean surface. *Izvestiia, Atmospheric and Oceanic Physics*, **28,** 650–656.

Ehlers, M., 1991: Multisensor image fusion techniques in remote sensing. *ISPRS J. Photogram. Remote Sens.,* **46,** 19–30.

Emery, W. J., J. Brown, and Z. P. Nowak, 1989: AVHRR image navigation: Summay and review. *Photogram. Eng. Remote Sens.,* **55,** 1175–1183.

England, A. W., J. F. Galantowicz, and M. S. Schretter, 1992: The radiobrightness thermal inertia measure of soil moisture. *IEEE Trans. Geosci. and Remote Sensing,* **30,** 132–139.

Engman, E. T., 1990: Progress in microwave remote sensing of soil moisture. *Canadian J. of Remote Sens.*, **16**(3), 6–14.

Engman, E. T., 1991: Applications of microwave remote sensing of soil moisture for water resources and agriculture. *Remote Sens. Environ.*, **35,** 213–226.

Entekhabi, D., H. Nakamura, and E. G. Njoku, 1994: Solving the inverse problem for soil moisture and temperature profiles by sequential assimilation of multifrequency remotely sensed observations. *IEEE Trans. Geosci. and Remote Sensing,* **32,** 438–448.

Evans, K. F., 1993: *Microwave Remote Sensing Algorithms for Cirrus Clouds and Precipitation.* PhD dissertation, Colorado State University, 232 pp.

Eyre, J., and A. C. Lorenc, 1989: Direct use of satellite sounding radiances in numerical weather prediction. *The Meteor. Mag.*, **118,** 13–15.

Falcone, V. J., M. K. Griffin, R. G. Isaacs, J. D. Pickle, J. F. Morrissey, A. J. Jackson, A. Bussey, R. Kakar, J. Wang, P. Racette, D. J. Boucher, B. H. Thomas, and A. M. Kishi, 1992: *SSM/T-2 Calibration and Validation Data Analysis.* Technical Report PL-TR-92-2293, Environ. Res. Papers, No. 1111, Phillips Lab., Hanscom AFB, MA.

Fast, J. D., and M. D. McCorcle, 1991: The effect of heterogeneous soil moisture on a summer baroclinic circulation in the central United States. *Mon. Wea. Rev.*, **119,** 2140–2167.

Felde, G. W., and J. D. Pickle, 1995: Retrieval of 91 and 150 GHz Earth surface emissivities. *J. Geophys. Res.,* **100,** 20855–20866.

Ferraro, Jr., R. R., N. C. Grody, and J. A. Kogut, 1986: Classification of geophysical parameters using passive microwave satellite measurements. *IEEE Tran. Geosci. and Remote Sensing,* **GE-24,** 1008–1013.

Fleming, H. E., and L. M. McMillin, 1977: Atmospheric transmittance of an absorbing gas 2: A computationally fast and accurate transmittance model for slant paths at different zenith angles. *Appl. Opt.*, **16,** 1366–1370.

Frank, A. U., M. J. Egenhofer, and W. Kuhn, 1991: A perspective on GIS technology in the nineties. *Photogram. Eng. Remote Sens.*, **57,** 1431–1436.

Franklin, S. E., and C. F. Blodgett, 1993: An example of satellite data fusion. *Comput. Geosci.*, **19,** 577–583.

Freeland, R. S., 1989: Review of soil moisture sensing using soil electrical conductivity. *Trans. ASAE*, **32,** 2190.

Friedl, M. A., 1995: Modeling land surface fluxes using a sparse canopy model and radiometric surface temperature measurements. *J. Geophys. Res.*, **100,** 25435–25446.

Fung, A. K., and M. F. Chen, 1981: Emission from an inhomogeneous layer with irregular interfaces. *Radio Sci.*, **16,** 289–298.

Fung, A. K., and H. J. Eom, 1981: Emission from a Rayleigh layer with irregular boundaries. *J. Quant. Spectr. Radiative Transfer*, **26,** 397–409.

Gibson, H. M., and T. H. Vonder Haar, 1990: Cloud and convection frequency over the southeast United States as related to small-scale geographic features. *Mon. Wea. Rev.*, **118,** 2215–2227.

Giddings, L., and B. J. Choudhury, 1989: Observation of hydrological features with Nimbus-7 37 GHz data, applied to South Africa. *Int. J. Remote Sens.*, **10**(10), 1673–1686.

Gilbert, J. R., C. Moler, and R. Schreiber, 1992: Sparse matrices in MATLAB: Design and implementation. *SIAM J. Matix Anal.*, **13,** 333–356.

Gillies, R. R., and T. N. Carlson, 1995: Thermal remote sensing of surface soil water content with partial vegetation cover for incorporation into climate models. *J. Appl. Meteor.*, **34,** 745–756.

Gloersen, P., and J. K. Larabee, 1981: *An optical model for the microwave properties of sea ice.* NASA Tech. Memo. 83865, 25 pp.

Gloersen, P., H. J. Zwally, A. T. C. Chang, D. K. Hall, W. J. Campbell, and R. O. Ramseier, 1978: Time dependence of sea ice concentration and multiyear ice fraction in the arctic basin. *Boundary-Layer Meteor.*, **13,** 339–359.

Goodberlet, M. A., C. T. Swift, and J. C. Wilkerson, 1989: Remote sensing of ocean surface winds with the Special Sensor Microwave/Imager. *J. Geophys. Res.*, **94,** 14547–14555.

Grasso, L. D., 1996: *Numerical Simulation of the May 15 and April 26, 1991 Thunderstorms.* PhD dissertation, Colorado State University, 151 pp. [Available as Atmospheric Science Paper No. 596]

Grody, N. C., 1976: Remote sensing of atmospheric water content from satellites using microwave radiometry. *IEEE Trans. Antennas Propag.*, **AP-24,** 155–162.

Grody, N. C., 1983: Severe storm observations using the Microwave Sounding Unit. *J. Climate and Appl. Meteor.*, **22,** 609–625.

Grody, N. C., 1991: Classification of snow cover and precipitation using the Special Sensor Microwave Imager. *J. Geophys. Res.*, **96,** 7423–7435.

Grody, N. C., and A. Basist, 1995: Global identification of snowcover using SSM/I measurements. IEEE Trans. Geosci. Remote Sens., in press.

Guissard, A., and P. Sobieski, 1987: An approximate model for the microwave brightness temperature of the sea. *Int. J. Remote Sens.*, **8,** 1607–1627.

Gunn, K. L. S., and T. W. R. East, 1954: The microwave properties of precipitation particles. *Quart. J. Royal Meteor. Soc.*, **80,** 522–545.

Guo, Y., and P. H. Schuepp, 1994: On surface energy balance over the northern wetlands 1. The effects of small-scale temperature and wetness heterogeneity. *J. Geophys. Res.*, **99,** 1601–1612.

Gutman, G. G., 1990: Review of the workshop on the use of satellite-derived vegetation indices in weather and climate prediction model. *Bull. Amer. Meteor. Soc.*, **71,** 1458–1463.

Gutman, G. G., 1991: Vegetation indices from AVHRR: An update and future prospects. *Remote Sens. Environ.*, **35,** 121–136.

Gutman, G. G., D. Tarpley, A. Ignatov, and S. Olson, 1995: The enhanced NOAA global land dataset from the Advanced Very High Resolution Radiometer. *Bull. Amer. Meteor. Soc.*, **76,** 1141–1156.

Hall, F. G., and P. J. Sellers, 1995: First International Satellite Land Surface Climatology Project (ISLSCP) Field Experiment (FIFE) in 1995. *J. Geophys. Res.*, **100,** 25383–25395.

Hallikainen, M., and P. Jolma, 1992: Comparison of algorithms for retrieval of snow water equivalent from Nimbus-7 SMMR data in Finland. *IEEE Trans. Geosci. and Remote Sens.*, **30,** 124–131.

Henderson-Sellers, A., and A. J. Pitman, 1992: Land-surface schemes for future climate models: Specification, aggregation, and heterogeneity. *J. Geophys. Res.*, **97,** 2687–2696.

Henderson-Sellers, A., A. J. Pitman, P. K. Love, P. Irannejad, and T. H. Chen, 1995: The Project for Intercomparison of Land Surface Parameterization Schemes (PILPS): Phases 2 and 3. *Bull. Amer. Meteor.*, **76,** 489–503.

Herzburg, G., 1950: *Molecular Spectra and Molecular Structure*, Vol. 1: Spectra of Diatomic Molecules. D. Van Nostrand Co., Princeton, NJ.

Heymsfield, G. M., and R. Fulton, 1992: Modulation of SSM/I microwave soil radiances by rainfall. *Remote Sens. Environ.*, **39,** 187–202.

Heymsfield, G. M., K. K. Gnosh, and L. C. Chen, 1983: An interactive system for compositing digital radar and satellite data. *J. Climate Appl. Meteor.*, **22,** 705–713.

Hibbard, W., and D. Satek, 1989: Visualizing large data sets in the earth sciences. *Computer,* **22,** 53–57.

Hillger, D. W., J. F. W. Purdom, and D. A. Molenar, 1993: A noise level analysis of special multiple-spin VAS data during STORM-FEST. NOAA Tech. Rep., NESDIS 65, NOAA/NESDIS/ RAMM Branch, Fort Collins, CO, 30 pp.

Ho, D., and A. Asem, 1986: NOAA AVHRR image referencing. *Int. J. Remote Sens.,* **7,** 895–904.

Hoekstra, P., and A. Delaney, 1974: Dielectric properties of soils at UHF and microwave frequencies. *J. Geophys. Res.*, **76,** 4922–4931.

Hollinger, J. P., 1971: Passive microwave measurements of sea surface roughness. *IEEE Tran. Geosci. Electron.,* **GE-9,** 165–169.

Hollinger, J. P., 1974: *The determination of oil slick thickness by means of multifrequency passive microwave techniques.* Rep. 2953, Naval Research Laboratory, Washington, D.C.

Hollinger, J. P., and R. A. Mennella, 1973: Oil spills: Measurements of their distributions and volumes by multifrequency microwave radiometry. *Science*, **181,** 54–56.

Hollinger, J., R. Lo, G. Poe, R. Savage, and J. Peirce, 1987: *Special Sensor Microwave/Imager User's Guide.* Naval Research Laboratory, Washington, DC, 120 pp.

Hollinger, J. P., J. L. Peirce, and G. A. Poe, 1990: SSM/I instrument evaluation. *IEEE Tran. Geosci. and Remote Sensing,* **28,** 781–790.

Holton, J. R., 1979: *An Introduction to Dynamic Meteorology.* Academic Press Inc., 391 pp.

Huete, A. R., 1988: A soil-adjusted vegetation index (SAVI). *Remote Sens. Environ.*, **27,** 47–57.

Humes, K. S., W. P. Kustas, M. S. Moran, W. D. Nichols, and M. A. Weltz, 1994: Variability of emissivity and surface temperature over a sparsely vegetated surface. *Water Resources Res.*, **30,** 1299–1310.

IAMAP, 1978: *Terminology and Units of Radiation Quantities and Measurements.* International Association of Meteorology and Atmospheric Physics (IAMAP) Radiation Commission, Boulder, CO, 17 pp.

Idso, S. B., T. J. Schmugge, R. D. Jackson, and R. J. Reginato, 1975: The utility of surface temperature measurements for the remote sensing of soil water status. *J. Geophys. Res.*, **80,** 3044–3049.

Il'in, V. A., V. G. Irisov, S. S. Kasymov, and V. S. Etkin, 1992: Spectral investigations of millimeter-range radiation emission from a periodically uneven water surface. *Izvestiya, Atmospheric and Oceanic Physics*, **28,** 669–670.

Isaacs, R. G., Y.-Q. Jin, R. D. Worsham, G. Deblonde, and V. J. Falcone, Jr., 1989: The RAD-TRAN microwave surface emission models. *IEEE Tran. Geosci. and Remote Sensing,* **27,** 433–440.

Jackson, T. J., 1993: Measuring surface soil moisture using passive microwave remote sensing. *Hydrological Processes*, **7,** 139–152.

Jackson, T. J., and T. J. Schmugge, 1989: Passive microwave remote sensing system for soil moisture: Some supporting research. *IEEE Tran. Geosci. and Remote Sensing,* **27,** 225–235.

Jackson, T. J., and T. J. Schmugge, 1991: Vegetation effects on the microwave emission of soils. *Remote Sens. Environ.*, **36,** 203–212.

Jackson, T. J., T. J. Schmugge, and J. R. Wang, 1982: Passive microwave sensing of soil moisture under vegetation canopies. *Water Resources Res.*, **18,** 1137–1142.

Jasinski, M. F., and P. S. Eagleson, 1990: Estimation of subpixel vegetation cover using red infrared scattergrams. *IEEE Tran. Geosci. and Remote Sensing,* **28,** 253–267.

Jones, A. S., and T. H. Vonder Haar, 1990: Passive microwave remote sensing of cloud liquid water over land regions. *J. Geophys. Res.*, **95,** 16673–16683.

Jones, A. S., and T. H. Vonder Haar, 1992: PORTAL - A satellite remap/fusion system. Preprints, *Sixth Conf. on Satellite Meteorology and Oceanography and Eighth Int. Conf. on Interactive Information and Processing Systems for Meteorology, Oceanography and Hydrology,* Atlanta, GA, Amer. Meteor. Soc., J98–J101.

Jones, A. S., K. E. Eis, and T. H. Vonder Haar, 1993: Measurement of high resolution microwave surface emittance using advanced multisensor data fusion techniques. Preprints, *Topical Symp. on Combined Optical-Microwave Earth and Atmosphere Sensing,* Albuquerque, NM, IEEE/LEOS, 248–251.

Jones, A. S., K. E. Eis, and T. H. Vonder Haar, 1995: A method for multisensor-multispectral satellite data fusion. *J. Atmos. Oceanic Technol.*, **12,** 739–754.

Justice, C. O., J. R. G. Townshend, B. N. Holben, and C. J. Tucker, 1985: Analysis of the phenology of global vegetation using meteorological satellite data. *Int. J. Remote Sens.*, **6,** 1271–1318.

Kahn, R., R. D. Haskins, J. E. Knighton, A. Pursch, and S. Granger-Gallegos, 1991: Validating a large geophysical data set: Experiences with satellite-derived cloud parameters. *Proc. 23d Symp. on the Interface,* Computing Science and Statistics, 133–140.

Kairu, E. N., 1991: A review of methods for estimating evapotranspiration. *GeoJournal,* **25,** 371–376.

Kakar, R. K., 1983: Retrieval of clear sky moisture profiles using the 183 GHz water vapor line. *J. Climate and Appl. Meteor.*, **22,** 1282–1289.

Kalb, V. L., 1991: Representation of vegetation by continental data sets derived from NOAA-AVHRR data. *Int. J. Remote Sens.*, **12,** 999–1022.

Kaufman, Y. J. and B. N. Holden, 1993: Calibration of AVHRR visible and near-IR bands by atmospheric scattering, ocean glint and desert reflection. *Int. J. Remote Sens.*, **14,** 21–52.

Kerr, Y. H., and E. G. Njoku, 1990: A semiempirical model for interpreting microwave emission from semiarid land surfaces as seen from space. *IEEE Tran. Geosci. and Remote Sensing,* **28,** 384–393.

Kidder, S. Q., 1979: *Determination of Tropical Cyclone Surface Pressure and Winds from Satellite Microwave Data.* Atmos. Sci. Paper 307, Colorado State University, Fort Collins, CO, 87 pp.

Kidwell, K., 1994: *Polar Orbiter Data User's Guide.* U.S. Dept. of Commerce, NOAA/NESDIS, National Climatic Data Center, Satellite Data Services Division, 126 pp.

King, M., 1992: Editor's comer. *The Earth Observer,* **4,** EOS Project Office, Code 900, NASA Goddard Space Flight Center, 1-2.

Kirdiashev, K. P., A. A. Chukhlantsev, and A. M. Shutko, 1979: Microwave radiation on the Earth's surface in the presence of vegetation cover. *Radio Eng. Electron.*, **24,** 256–264.

Klein, L. A., and C. T. Swift, 1977: An improved model for the dielectric constant of sea water at microwave frequencies. *IEEE Trans. Antennas Propag.*, **AP-25,** 104–111.

Koch, S. E., M. desJardins, P. J. Kocin, 1983: An interactive Barnes objective map analysis scheme for use with satellite and conventional data. *J. Climate and Appl. Meteor.*, **22,** 1487–1503.

Kohn, N. M., A. L. Johnston, and C. G. Mohr, 1978: MUDRAS—Multiple Doppler Radar Analysis System. NOAA Tech. Memo. ERL/WPL-35, Wave Propagation Lab, Boulder, 170 pp.

Kummerow, C., and J. A. Weinman, 1988: Determining microwave brightness temperatures from precipitating horizontally finite and vertically structured clouds. *J. Geophys. Res.*, **93,** 3720–3728.

Kunzi, K. F., S. Patil, and H. Rott, 1982: Snowcover parameters retrieved from Nimbus-7 Scanning Multichannel Microwave Radiometer (SMMR) data. *IEEE Tran. Geosci. and Remote Sensing,* **GE-20,** 452–467.

Kustas, W. P., 1990: Estimates of evapotranspiration with a one- and two-layer model of heat transfer over partial canopy cover. *J. Appl. Meteor.*, **29,** 704–715.

Kustas, W. P., 1993: Relationships between evaporative fraction and remotely sensed vegetation index and microwave brightness temperature for semiarid rangelands. *J. Appl. Meteor.*, **32,** 1781–1790.

Kustas, W. P., D. C. Goodrich, M. S. Moran, S. Amer, L. B. Bach, J. Blanford, A. Chehbouni, H. Classen, W. E. Clements, P. C. Doraiswamy, P. Dubois, T. R. Clarke, C. S. T. Daughtry, D. Gellman, T. A. Grant, L. E. Hipps, A. R. Huete, K. S. Humes, T. J. Jackson, T. O. Keffer, W. D. Nichols, R. Parry, E. Perry, R. T. Pinker, P. J. Pinter, J. Qi, A. C. Riggs, T. J. Schmugge, A. M. Shutko, D. Stannard, E. Swiatek, J. D. Van Leeuwen, J. Van Zyl, A. Vidal, J. Washburne, and M. A. Weltz, 1991: An interdisciplinary study of the energy and water fluxes in the atmosphere-biosphere system over semiarid rangelands: Description and some preliminary results. *Bull. Amer. Meteor. Soc.*, **72,** 1683–1705.

Kustas, W. P., K. S. Humes, J. M. Norman, and M. S. Moran, 1996: Single- and dual-source modeling of surface energy fluxes with radiometric surface temperature. *J. Appl. Meteor.*, **35,** 110–121.

Lanicci, J. M., T. N. Carlson, and T. T. Warner, 1987: Sensitivity of the Great Plains severe-storm environment to soil-moisture distribution. *Mon. Wea. Rev.*, **115,** 2660–2673.

Lee, A. C. L., 1994: Filtering, sampling, and information content within satellite-derived multispectral or mixed-resolution imagery. *J Atmos. Oceanic Technol.*, **11,** 401–421.

Lee, T. J., 1992: *The Impact of Vegetation on the Atmospheric Boundary Layer and Convective Storms*. PhD dissertation, Colorado State University, 137 pp. [Available as Atmospheric Science Paper No. 509].

Lee, T. J., and R. A. Pielke, 1992: Estimating the soil surface specific humidity. *J. Appl. Meteor.*, **31,** 480–484.

Liebe, H. J., 1981: Modeling attenuation and phase of radio waves in air at frequencies below 1000 GHz. *Radio Sci.*, **16,** 1183–1199.

Liebe, H. J., 1985: An updated model for millimeter wave propagation in moist air. *Radio Sci.*, **20,** 1069–1089.

Liebe, H. J., 1989: MPM — An atmospheric millimeter-wave propagation model. *Int. J. of Infrared and Millimeter Waves*, **10,** 631–650.

Liebe, H. J., and G. G. Gimmestad, 1978: Calculation of clear air EHF refractivity. *Radio Sci.*, **13,** 245–251.

Liebe, H. J., and D. H. Layton, 1987: *Millimeter-wave properties of the atmosphere: Laboratory studies and propagation modeling.* NTIA Report 87-224, NTIA/ITS, Boulder, CO, 74 pp.

Liebe, H. J., G. G. Gimmestad, and J. D. Hopponen, 1977: Atmospheric oxygen microwave spectrum — experiment versus theory. *IEEE Trans. Antennas Propag.*, **AP-25,** 327–355.

Liebe, H. J., G. A. Hufford, and T. Manabe, 1991: A model for the complex permittivity of water at frequencies below 1 THz. *Int. J. of Infrared and Millimeter Waves*, **12,** 659–675.

Lilly, D. K., 1962: On the numerical simulation of buoyant convection. *Tellus,* **14,** 148–172.

Liou, K., 1980: *An Introduction to Atmospheric Radiation.* Academic Press Inc., Orlando, FL, 392 pp.

Lipes, R. G., R. L. Bernstein, V. J. Cardone, K. B. Katsaros, E. J. Njoku, A. L. Riley, D. B. Ross, C. T. Swift, and F. J. Wentz, 1979: Seasat scanning multichannel microwave radiometer: Results of the Gulf of Alaska workshop. *Science*, **204,** 1415–1417.

Lipton, A. E., 1988: *Mesoscale Analysis by Numerical Modeling Coupled with Satellite-based Sounding.* PhD dissertation, Colorado State University [Available as CIRA report ISSN No. 0737-5352-13].

Lipton, A. E., 1993: Cloud shading retrieval and assimilation in a satellite-model coupled mesoscale analysis system. *Mon. Wea. Rev.*, **121,** 3062–3081.

Lipton, A. E., and T. H. Vonder Haar, 1990a: Mesoscale analysis by numerical modeling coupled with sounding retrieval from satellites. *Mon. Wea. Rev.*, **118,** 1308–1329.

Lipton, A. E., and T. H. Vonder Haar, 1990b: Preconvective mesoscale analysis over irregular terrain with a satellite-model coupled system. *Mon. Wea. Rev.*, **118,** 1330–1358.

Lipton, A. E., G. D. Modica, S. T. Heckman, and A. J. Jackson, 1995: Satellite-model coupled analysis of convective potential in Florida with VAS water vapor and surface temperature data. *Mon. Wea. Rev.*, **123,** 3292–3304.

Louis, J.-F., 1979: A parametric model of vertical eddy fluxes in the atmosphere. *Boundary-Layer Meteor.*, **17,** 187–202.

Lovejoy, S., and D. Schertzer, 1988: Meeting reports: Scaling, fractals, and nonlinear variability in geophysics. *EOS Trans.*, Amer. Geophysical Union, **69,** 143–145.

Lovejoy, S., D. Schertzer, and A. A. Tsonis, 1987: Functional box-counting and multiple elliptical dimensions in rain. *Science*, **235,** 1036–1038.

Loveland, T. R., J. W. Merchant, and D. Ohlen, 1991: Development of a land-cover characteristics database for the conterminous U.S. *Photogrammetric Eng. and Remote Sens.*, **57,** 1453–1463.

Lunetta, R. S., R. G. Congalton, L. K. Fenstermaker, J. R. Jensen, K. C. McGwire, and L. R. Tinney, 1991: Remote sensing and geographic information system integration: Error sources and research issues. *Photogram. Eng. Remote Sens.*, **57,** 677–687.

Mahfouf, J.-F., 1991: Analysis of soil moisture from near-surface parameters: A feasibility study. *J. Appl. Meteor.*, **30,** 1534–1547.

Mahrer, Y., and R. A. Pielke, 1977: A numerical study of the airflow over irregular terrain. *Beitr. Phys. Atmos.*, **50,** 98–113.

Manabe, T. J., R. O. DeBolt, and H. J. Liebe, 1989: Moist-air attenuation at 96 GHz over a 21-km line-of-sight path. *IEEE Trans. Antennas Propag.*, **37,** 262–266.

Massman, W. J., 1992: A surface energy balance method for partitioning evapotranspiration data into plant and soil components for a surface with partial canopy cover. *Water Resources Res.*, **28,** 1723–1732.

Mather, J. C., E. S. Cheng, and R. E. Eplee, 1990: A preliminary measurement of the cosmic microwave background spectrum by the Cosmic Background Explorer satellite. *The Astrophysical J.*, **354,** L37–L40.

Matsushima, D., and J. Kondo, 1995: An estimation of the bulk transfer coeffficients for a bare soil surface using a linear model. *J. Appl. Meteor.*, **34,** 927–940.

McCumber, M. C., 1980: *A numerical simulation of the influence of heat and moisture fluxes upon mesoscale circulations*. PhD dissertation, Univ. of Virginia, Charlottesville.

McCumber, M. C., and R. A. Pielke, 1981: Simulation of the effects of surface fluxes of heat and moisture in a mesoscale numerical model. Part I: Soil layer. *J. Geophys. Res.*, **86,** 9929–9938.

McFarland, M. J., 1976: The correlation of Skylab L-band brightness temperatures with antecedent precipitation. Preprints, *Conf. Hydrometeorology,* Fort Worth, TX, Amer. Meteor. Soc., 60–65.

McFarland, M. J., and B. J. Blanchard, 1977: Temporal correlations of antecedent precipitation with Nimbus 5 ESMR brightness temperatures. Preprints, *Second Conf. Hydrometeorology,* Toronto, Amer. Meteor. Soc., 311–315.

McFarland, M. J., and C. M. U. Neale, 1991: *DMSP Special Sensor Microwave/Imager Calibration/validation, Section 9, Land parameter algorithm validation and calibration.* Final Report, Vol. 2, Naval Research Laboratory, Washington DC, pp. 108.

McFarland, M. J., P. H. Harder III, G. D. Wilke, and G. L. Huebner, Jr., 1984: *Crop Moisture Estimation over the Southern Great Plains with Dual Polarization 1.66 Centimeter Passive Microwave Data from Nimbus 7.* Final Rep. RSC-4854, Remote Sensing Center, Texas A&M University, 142 pp.

McMillin, L. M., and H. E. Fleming, 1976: Atmospheric transmittance of an absorbing gas: A computationally fast and accurate transmittance model for absorbing gases with constant mixing ratios in inhomogeneous atmospheres. *Appl. Opt.*, **15,** 358–363.

McNider, R. T., A. J. Song, D. M. Casey, P. J. Wetzel, W. L. Crosson, and R. M. Rabin, 1994: Toward a dynamic-thermodynamic assimilation of satellite surface temperature in numerical atmospheric models. *Mon. Wea. Rev.*, **122,** 2784–2803.

Menzel, W. P., and J. F. W. Purdom, 1994: Introducing GOES-I the first generation of a new generation of geostationary operational environmental satellites. *Bull. Amer. Meteor. Soc.*, **75,** 757–781.

Mie, G., 1908: Beitrage zur optik truber median, speziell kolloidaler metallosungen.*Annalen der Physik*, **25,** 377–445.

Mihailovic, D. T., B. Rajkovic, B. Lalic, L. Dekic, 1995: Schemes for parameterizing evaporation from a non-plant covered surface and their impact on partioning the surface energy in land-air exchange parameterization. *J. Appl. Meteor.*, **34,** 2462–2475.

Mo, T., B. J. Choudhury, T. J. Schmugge, J. R. Wang, and T. J. Jackson, 1982: A model for microwave emission from vegetation-covered fields. *J. Geophys. Res.*, **87,** 11229–11237.

Mohr, C. G., L. J. Miller, R. L. Vaughan, and H. W. Frank, 1986: The merger of mesoscale datasets into a common Cartesian format for efficient and systematic analyses.*J. Atmos. Oceanic Technol.*, **3,** 143–161.

Montgomery, H. E., and L. W. Uccellini, 1985: *VAS demonstration: (VISSR Atmospheric Sounder) Description and Final Report.* NASA Ref. Publication 1151, [NTIS Ref: 86N13867], 170 pp.

Mulders, M. A., 1987: *Remote Sensing in Soil Science*. Elsevier Science Pub. Co., New York.

Myneni, R. B., G. Asrar, D. Tanre, and B. J. Choudhury, 1992: Remote sensing of solar radiation absorbed and reflected by vegetated surfaces. *IEEE Tran. Geosci. and Remote Sensing,* **30,** 302–314.

NASA, 1987:. High Resolution Multifrequency Microwave Radiometer (HMMR) Earth Observing System (EOS) instrument panel report. **IIe,** 59 pp.

NASA, 1991: *EOS Reference Handbook.* David Dokken, Ed., NASA Goddard Space Flight Center, NP-144, 147 pp.

NASA, 1992: *EOS Data and Information System (EOSDIS).* Earth Science and Applications Division (Code SE), NASA Headquarters, Washington DC, 31 pp.

NCSA, 1994: *Hierarchical Data Format (HDF) Reference Manual V3.3.* National Center for Supercomputing Applications, University of Illinois at Urbana-Champaign.

Neale, C. M. U., M. J. McFarland, and K. Chang, 1990: Land-surface-type classification using microwave brightness temperatures from the Special Sensor Microwave/Imager. *IEEE Tran. Geosci. and Remote Sensing,* **28,** 829–838.

Nemani, R. R., and S. W. Running, 1989: Estimation of regional surface resistance to evapotranspiration from NDVI and thermal-IR AVHRR data. *J. Appl. Meteor.*, **28,** 267–284.

Nemani, R., L. Pierce, S. Running, and S. Goward, 1993: Developing satellite-derived estimates of surface moisture status. *J. Appl. Meteor.*, **32,** 548–557.

Nemani, R. R., S. W. Running, R. A. Pielke, and T. N. Chase, 1996: Global vegetation cover changes from coarse resolution satellite data. *J. Geophys. Res.*, **101,** 7157–7162.

Newton, R. W., 1977: *Microwave remote sensing and its application to soil moisture detection.* Tech. Rep. RSC-81, Remote Sensing Center, Tex. A&M Univ., College Station, 500 pp.

Newton, R. W., and J. W. Rouse, 1988: Microwave radiometer measurements of moisture content. *IEEE Trans. Antennas Propag.*, **AP-28,** 680–686.

Newton, R. W., Q. R. Black, S. Makanvand, A. J. Blanchard, and B. R. Jean, 1982: Soil moisture information and thermal microwave emission. *IEEE Tran. Geosci. and Remote Sensing,* **GE-20,** 275–281.

Nichols, W. D., 1992: Energy budgets and resistances to energy transport in sparsely vegetated rangeland. *Agr. Forest Meteor.*, **60,** 221–247.

Njoku, E. G., 1980: Antenna pattern correction procedure for the Scanning Multichannel Microwave Radiometer (SMMR). *Boundary-Layer Meteor.*, **18,** 79–98.

Njoku, E. G., 1982: Microwave remote sensing of the earth from space — a review. *Proceedings of the IEEE,* **70,** 728–750.

Njoku, E. G., 1994: Passive microwave remote sensing of soil moisture. *Soil Moisture Workshop*, Tiburon, CA, NASA.

Njoku, E. G., and J.-A. Kong, 1977: Theory for passive microwave remote sensing of near-surface soil moisture. *J. Geophys. Res.*, **82,** 3108–3118.

Nordberg, W., J. Conaway, D. B. Ross, and T. Wilheit, 1971: Measurements of microwave emission from a foam-covered, wind-driven sea. *Boundary-Layer Meteor.*, **28,** 429–435.

NSSDC, 1994: *CDF User's Guide, Version 2.4.* National Space Science Data Center, NASA/Goddard Space Flight Center.

Olioso, A., O. Taconet, B. Mehrez, D. Nivoit, F. Promayon, L. Rahmoune, 1995: Estimation of evapotranspiration using SVAT models and surface IR temperature. *IGARSS'95,* Vol. 1, IEEE Publications, 516–518, Firenze, Italy, 10-14 July.

Olioso, A., J. P. Wigneron, A. Chanzy, B. Seguin, 1994: A coupled model to simulate spectral reflectances, thermal infrared emission and microwave emission of a vegetation canopy. In *The Proceedings of the Workshop on Thermal Remote Sensing of the Energy and Water Balance over Vegetation in Conjunction with Other Sensors.* 20-23 September 1993, La Londe Les Maures, France, Penn State University-CETP-CEMAGREF, Editions du CEMAGREF, 251–254.

Ookouchi, Y., M. Segal, R. C. Kessler, and R. A. Pielke, 1984: Evaluation of soil moisture effects on the generation and modification of mesoscale circulations. *Mon. Wea. Rev.*, **112,** 2281–2292.

Ormsby, J. P., B. J. Choudhury, and M. Owe, 1987: Vegetation spatial variability and its effect on vegetation indices. *Int. J. Remote Sens.*, **8,** 1301–1306.

Oye, R., and E. Mueller, 1986: A media efficient common logical format for radar and lidar data. Preprints, *23d Radar Meteorology Conf.,* Snowmass, CO, Amer. Meteor. Soc., JP361-JP362.

Pampaloni, P., editor, 1989: *Microwave Radiometry and Remote Sensing Applications: Proceedings of the Specialist Meeting Held in Florence, Italy, 9-11 March, 1988,* Utrecht, The Netherlands, 362 pp.

Pan, H.-L., and L. Mahrt, 1987: Interactions between soil hydrology and boundary-layer development. *Boundary-Layer Meteor.*, **37,** 185–202.

Pan, Z., M. Segal, R. Turner, and E. Takle, 1995: Model simulation of impacts of transient surface wetness on summer rainfall in the United States Midwest during drought and flood years. *Mon. Wea. Rev.,* **123,** 1575–1581.

Paris, J. F., and H. H. Kwong, 1988: Characterization of vegetation with combined Thematic Mapper (TM) and Shuttle Imaging Radar (SIR-B) image data. *Photogram. Eng. Remote Sens.*, **54,** 1187–1193.

Peake, W. H., 1959: Interaction of electromagnetic waves with some natural surfaces. *IRE Trans.*, **AP-7,** 5342.

Peck, E. L., and A. S. Hope, 1995: Spatial patterns of soil moisture for the FIFE study area derived from remotely sensed and ground data. *J. Geophys. Res.*, **100,** 25463–25468.

Perry, E. M., and M. S. Moran, 1994: An evaluation of atmospheric corrections of radiometric surface temperatures for a semiarid rangeland watershed. *Water Resources Res.*, **30,** 1261–1269.

Perry, E. M., and T. N. Carlson, 1988: Comparison of active microwave soil water content with infrared surface temperatures and surface moisture availability. *Water Resources Res.*, **24,** 1818–1824.

Perry, J., and A. Straiton, 1973: Revision of the "dielectric constant" of ice in the millimeter-wave spectrum. *J. Appl. Phys.*, **44,** 5180.

Petty, G. W., and K. B. Katsaros, 1994: The response of the SSM/I to the marine environment. Part II: A parameterization of the effect of the sea surface slope distribution on emission and reflection. *J. Atmos. and Oceanic Technol.*, **11,** 617–628.

Pielke, R. A., 1984: *Mesoscale Meteorological Modeling.* Academic Press Inc., Orlando, FL.

Pielke, R. A., W. R. Cotton, R. L. Walko, C. J. Tremback, W. A. Lyons, L. D. Grasso, M. E. Nicholls, M. D. Moran, D. A. Wesley, T. J. Lee, and J. H. Copeland, 1992: A comprehensive meteorological sysem — RAMS. *Meteor. Atmos. Phys.*, **49,** 69–91.

Poe, G. A., 1990: Optimum interpolation of imaging microwave radiometer data. *IEEE Tran. Geosci. and Remote Sensing,* **28,** 800–810.

Poe, G. A., and R. W. Conway, 1990: A study of the geolocation errors of the Special Sensor Microwave/Imager (SSM/I). *IEEE Tran. Geosci. and Remote Sensing,* **28,** 791–799.

Prevot, L., R. Bernard, O. Taconet, D. Vidal-Madjar, and J. L. Thony, 1984: Evaporation from a bare soil evaluated from a soil water transfer model using remotely sensed surface soil moisture data. *Water Resources Res.*, **20,** 311–316.

Price, J. C., 1982: On the use of satellite data to infer surface fluxes at meteorological scales. *J. Appl. Meteor.*, **21,** 1111–1122.

Price, J. C., 1990: Using spatial context in satellite data to infer regional scale evapotranspiration. *IEEE Trans. Geosci. Remote Sens.*, **28,** 940–948.

Price, J. C., 1991: Timing of NOAA afternoon passes. *Int. J. Remote Sens.*, **12,** 193–198.

Prisley, S. P., T. G. Gregoire, and J. L. Smith, 1989: The mean and variance of area estimates computed in an arc-node geographic information system. *Photogram. Eng. Remote Sens.*, **55,** 1601–1612.

Purdom, J. F. W., and P. N. Dills, 1994: Cloud motion and height measurements from multiple satellites including cloud heights and motions in polar regions. Preprints, *Seventh Conf. on Satellite Meteorology and Oceanography,* Monterey, CA, Amer. Meteor. Soc., 408–411.

Rabin, R. M., S. Stadler, P. J. Wetzel, D. J. Stensrud, and M. Gregory, 1990: Observed effects of landscape variability on convective clouds. *Bull. Amer. Meteor. Soc.*, **71,** 272–280.

Ray, P. S., 1972: Broadband complex refractive indices of ice and water. *Applied Optics*, **11,** 1836–1843.

Raymond, D. J., 1988: A C language-based modular system for analyzing and displaying gridded numerical data. *J. Atmos. Oceanic Technol.*, **5,** 501–511.

Reitz, J. R., F. J. Milford, and R. W. Christy, 1979: *Foundations of Electromagnetic Theory.* Addison-Wesley Publishing Co., 534 pp.

Rew, R. K., and G. Davis, 1990: NetCDF: An interface for scientific data access. *IEEE Comput. Graphics Appl.*, **10,** 76–82.

Roberti, L., J. Haferman, and C. Kummerow, 1994: Microwave radiative transfer through horizontally inhomogeneous precipitating clouds. *J. Geophys. Res.*, **99,** 16707–16718.

Rodgers, R. R., 1979: *A Short Course in Cloud Physics.* Pegamon Press, Great Britain, 235 pp.

Rosenkranz, P. W., 1975: Shape of the 5 mm oxygen band in the atmosphere. *IEEE Trans. Antennas Propag.*, **AP-23,** 498–506.

Sasaki, Y., I. Asanuma, K. Muneyama, G. Naito, and T. Suzuki, 1987: The dependence of sea-surface microwave emission on wind speed, frequency, incidence angle, and polarization over the frequency range from 1 to 40 GHz. *IEEE Tran. Geosci. and Remote Sensing,* **25,** 138–146.

Schaake, J., 1990: From climate to flow. Waggoner, P., editor, *Climate Change and U.S. Water Resources*, Chapter 8, pages 177–206. John Wiley and Sons, New York.

Schmalensee, R., 1993: Symposium on global climate change. *J. of Economic Perspectives*, 7(4), 3–10.

Schmugge, T. J., 1980: Effect of texture on microwave emission from soils. *IEEE Tran. Geosci. and Remote Sensing,* **GE-18,** 353–361.

Schmugge, T. J., 1983: Remote sensing of soil moisture: recent advances. *IEEE Tran. Geosci. and Remote Sensing,* **GE-21,** 336–344.

Schmugge, T. J., 1985: Remote sensing of soil moisture. Anderson, M. G., and Burt, T. P., editors, *Hydrological Forecasting.* Wiley, New York.

Schmugge, T. J., 1989: Microwave sensing of soil moisture. Toselli, F., editor, *Applications of Remote Sensing to Agrometeorology*, pages 257–284. ECSC, EEC, EAEC, Brussels and Luxembourg.

Schmugge, T. J., and André, J.-C., editors, 1991: *Land Surface Evaporation: Measurement and Parameterization.* Springer Verlag, New York, 424 pp.

Schmugge, T. J., and B. J. Choudhury, 1981: A comparison of radiative transfer models for predicting the microwave emission from soils. *Radio Sci.*, **16,** 927–938.

Schmugge, T. J., F. Becker, and Z.-L. Li, 1991: Spectral emissivity variations observed in airborne surface temperature measurements. *Remote Sens. Environ.*, **35,** 95–104.

Schmugge, T. J., S. Hook, and A. Kahle, 1995: TIMS observation of surface emissivity in HAPEX-Sahel. Preprints, *International Geoscience Remote Sensing Symposium '95,* Florence, Italy, 10-14 July, 2224–2226.

Schmugge, T. J., T. J. Jackson, W. P. Kustas, R. Roberts, R. Parry, D. C. Goodrich, S. A. Amer, and M. A. Weltz, 1994: Push Broom Microwave Radiometer observations of surface soil moisture in MONSOON'90. *Water Resources Res.*, **30,** 1321–1327.

Schmugge, T., T. J. Jackson, W. P. Kustas, and J. R. Wang, 1992: Passive microwave remote sensing of soil moisture: Results from HAPEX, FIFE and MONSOON 90. *ISPRS J. of Photogrammetry and Remote Sensing,* **47,** 127–143.

Schmugge, T. J., T. J. Jackson, and H. L. McKim, 1980: Survey of methods for soil moisture determination. *Water Resources Res.*, **16,** 961–979.

Schmugge, T. J., J. M. Meneely, A. Rango, and R. Neff, 1977: Satellite microwave observations of soil moisture conditions. *Water Resources Bull.*, **13,** 265–281.

Schmugge, T. J., J. R. Wang, and A. Asrar, 1988: Results from the Pushbroom Microwave Radiometer flights over the Konza Prairie in 1985. *IEEE Tran. Geosci. and Remote Sensing,* **GE-26,** 590–596.

Segal, M., R. Avissar, M. C. McCumber, and R. A. Pielke, 1988: Evaluation of vegetation effects on the generation and modification of mesoscale circulations. *J. Atmos. Sci.*, **45,** 2268–2292.

Segal, M., W. E. Schreiber, G. Kallos, J. R. Garratt, A. Rodi, J. Weaver, and R. A. Pielke, 1989: The impact of crop areas in northeast Colorado on midsummer mesoscale thermal circulations. *Mon. Wea. Rev.*, **117,** 809–825.

Sellers, P. J., 1990: A review of satellite data algorithms for studies of the land surface. *Bull. Amer. Meteor. Soc.*, **71,** 1429–1447.

Sellers, P. J., F. G. Hall, G. Asrar, D. E. Strebel, and R. E. Murphy, 1988: The First ISLSCP Field Experiment (FIFE). *Bull. Amer. Meteor. Soc.*, **69,** 22–27.

Serafini, Y. V., 1990: The time scale of land surface hydrology in response to initial soil moisture anomalies: A case study. *Tellus*, **42A,** 390–400.

Shaw, B. L., 1995: *The Effect of Soil Moisture and Vegetation Heterogeneity on a Great Plains Dryline: A Numerical Study.* M.S. thesis, Colorado State University, 93 pp. [Available as Atmospheric Science Paper No. 576]

Shuttleworth, W. J., and R. J. Gurney, 1990: The theoretical relationship between foliage temperature and canopy resistance in sparse canopies. *Quart. J. Royal Meteor. Soc.*, **116,** 497–519.

Simpson, J., R. F. Adler, and G. R. North, 1988: A proposed Tropical Rainfall Measuring Mission (TRMM) satellite. *Bull. Amer. Meteor. Soc.*, **69,** 278–295.

Skou, N., 1989: A sea salinity/soil moisture push-broom radiometer system for future high capacity space platforms. Pampaloni, P., editor, *Microwave Radiometry and Remote Sensing Applications*, pages 299–313, VSP, Utrecht, The Netherlands.

Slobin, S. D., 1982: Microwave noise temperature and attenuation of clouds: Statistics of these effects at various sites in the United States, Alaska, and Hawaii. *Radio Sci.*, **17,** 1443–1454.

Smagorinsky, J., 1963: General circulation experiements with the primitive equations. Part 1: The basic experiment. *Mon. Wea. Rev.*, **91,** 99–164.

Smith, R. C. G., and B. J. Choudhury, 1991: Analysis of normalized difference and surface temperature observations over southeastern Australia. *Int. J. Remote Sens.*, **12,** 2021–2044.

Soarès, J. V., R. Bernard, O. Taconet, D. Vidal-Madjar, and A. Weill, 1988: Estimation of bare soil evaporation from airborne measurements. *J. Hydrology*, **99,** 281–296.

Spencer, R. W., 1984: Satellite passive microwave rain rate measurement over croplands during spring, summer, and fall. *J. Climate and Appl. Meteor.*, **23,** 1553–1562.

Spencer, R. W., H. M. Goodman, and R. E. Hood, 1989: Precipitation retrieval over land and ocean with the SSM/I, Identification and characteristics of the scattering signal.*J. Atmos. and Oceanic Technol.*, **6,** 254–273.

Star, J. L., J. E. Estes, and F. Davis, 1991: Improved integration of remote sensing and geographic information systems: A background to NCGIA initiative 12. *Photogram. Eng. Remote Sens.*, **57,** 643–645.

Stauffer, D. R., N. L. Seaman, and F. S. Binkowski, 1991: Use of four-dimensional data assimilation in a limited-area mesoscale model, Part II: Effects of data assimilation within the planetary boundary layer. *Mon. Wea. Rev.*, **119,** 734–754.

Steffen, K., and A. J. Schweiger, 1990: Multisensor approach to sea ice classification for the validation of DMSP-SSM/I passive microwave derived sea ice products. *Photogram. Eng. Remote Sens.*, **56,** 75–82.

Stephens, G. L., 1980: Radiative properties of cirrus clouds in the infrared region. *J. Atmos. Sci.*, **37,** 435–446.

Stiles, W. H., and F. T. Ulaby, 1980: The active and passive microwave response to snow parameter, Part 1: Wetness. *J. Geophys. Res.*, **85,** 1037–1044.

Stogryn, A., 1967: The apparent temperature of the sea at microwave frequencies. *IEEE Trans. Antennas Propag.*, **15,** 278–286.

Stokes, G. M., and S. E. Schwartz, 1994: The Atmospheric Radiation Measurement (ARM) Program: Programmatic background and design of the Cloud and Radiation Test Bed. *Bull. Amer. Meteor. Soc.*, **75,** 1201–1221.

Stowe, L. L., R. M. Carey, and P. P. Pelegrino, 1992: Monitoring the Mt. Pinatubo aerosol layer with NOAA-11 AVHRR data. *Geophys. Res. Lett.*, **19,** 159–162.

Straka, J., J. Klokoenik, and H. Graβl, 1993: Navigation of satellite measurements without ground control points. *Int. J. Remote Sens.*, **14,** 1981–2004.

Sun, W.-Y., and L. Mahrt, 1995: Determination of surface fluxes from the surface radiative temperature. *J. Atmos. Sci.*, **52,** 1096–1106.

Sun, W.-Y., and Y. Ogura, 1979: Boundary layer forcing as a possible trigger to squall-line formation. *J. Atmos. Sci.*, **36,** 235–254.

Sun, W.-Y., and C.-C. Wu, 1992: Formation and diurnal variation of the dryline. *J. Atmos. Sci.*, **49,** 1606–1618.

Suomi, V. E., R. Fox, S. S. Limaye, and W. L. Smith, 1983: McIDAS III: A modern data access and analysis system. *J. Climate Appl. Meteor.*, **22,** 766–778.

Swift, C. T., 1974: Microwave radiometer measurements of the Cape Cod Canal. *Radio Sci.*, **9,** 641–653.

Swift, C. T., 1980: Passive microwave remote sensing of the ocean — A review. *Boundary-Layer Meteor.*, **18,** 25–54.

Swift, C. T., 1993: *ESTAR* — The Electronically Scanned Thinned Array Radiometer for remote sensing measurement of soil moisture and ocean salinity. NASA Technical Memorandum 4523, NASA/Goddard Space Flight Center, Greenbelt, MD.

Tarpley, D., 1994: Monthly evapotranspiration from satellite and conventional meteorological observations. *J. Climate,* **7,** 704–714.

Thelin, G. P., and F. J. Heimes, 1987: *Mapping Irrigated Cropland from Landsat Data for Determination of Water Use from the High Plains Aquifer in Parts of Colorado, Kansas, Nebraska, New Mexico, Oklahoma, South Dakota, Texas, and Wyoming.* Geological Survey Professional Paper 1400-C, 38 pp.

Thelin, G. P., F. J. Heimes, and J. R. Wray, 1987: *Irrigated Cropland, the High Plains, 1980,* Geological Survey Professional Paper 1400-C, Plate 1.

Townshend, J., C. Justice, and W. Li, 1991: Global land cover classification by remote sensing: Present capabilities and future possibilities. *Remote Sens. Environ.*, **35,** 243–256.

Treinish, L. A., 1989: An interactive, discipline-independent data visualization system. *Comput. Phys.*, **3,** 55–64.

Treinish, L. A., and M. L. Gough, 1987: A software package for the data independent management of multi-dimensional data. *EOS Trans.*, **68,** 633–635.

Tremback, C. J., and R. Kessler, 1985: A surface temperature and moisture parameterization for use in mesoscale models. *Proc. Seventh Conference on Numerical Weather Prediction,* Amer. Meteor. Soc., Boston, MA, 355–358.

Tsang, L., and R. W. Newton, 1982: Microwave emission from soils with rough surfaces. *J. Geophys. Res.*, **87,** 9017–9024.

Tsang, L. E., E. Njoku, and J. A. Kong, 1975: Microwave thermal emission from a stratified medium with nonuniform temperature distribution. *J. Appl. Phys.*, **46,** 5127–5133.

Tucker, C. J., 1979: Red and photographic infrared linear combinations for monitoring vegetation. *Remote Sens. Environ.*, **8,** 127–150.

Ulaby, F. T., A. Aslam, and M. C. Dobson, 1983: Effects of vegetation cover on the radar sensitivity to soil moisture. *IEEE Tran. Geosci. and Remote Sensing,* **GE-21,** 300–307.

Ulaby, F. T., R. K. Moore, and A. K. Fung, 1981: *Microwave Remote Sensing Active and Passive*, volume I Microwave Remote Sensing Fundamentals and Radiometry. Addison-Wesley Publishing Co., Reading, MA, 456 pp.

Ulaby, F. T., R. K. Moore, and A. K. Fung, 1986: *Microwave Remote Sensing Active and Passive,* Vol. 3, *From Theory to Applications.* Addison-Wesley Publishing Co., 1097 pp.

Unidata, 1993: *NetCDF User's Guide, Version 2.3.* Unidata Program Center, Boulder, CO, 118 pp.

USAF, 1977: *USAFETAC DATSAV Data Base Handbook, Appendix B: DATSAV Upper-Air File Construction and Format.* Technical Report USAFETAC-TN-77-2, 19–35.USAF, 1986: *USAFETAC Climatic Database Users Handbook No. 4: DATSAV2 Surface.* Technical Report USAFETAC-UH-86-004, 52 pp.

Valley, S. L., 1965: *Handbook of Geophysics and Space Environment.* Office of Aerospace Research, USAF, Cambridge Research Labs.

van de Griend, A. A., and R. J. Gurney, 1988: Satellite remote sensing and energy balance modeling for water balance assessment in (semi-) arid regions. Reidel, E., editor, *Estimation of Natural Groundwater Recharge*, pages 89–116, I. Simmers.

van de Griend, A. A., and M. Owe, 1993: On the relationship between thermal emissivity and the normalized difference vegetation index for natural surfaces. *Int. J. Remote Sens.*, **14,** 1119–1131.

van de Griend, A., P. J. Camillo, and R. J. Gurney, 1985: Discrimination of soil physical parameters, thermal inertia and soil moisture from diurnal surface temperature fluctuations. *Water Resources Res.*, **21,** 997–1009.

van de Hulst, H. C., 1957: *Light Scattering by Small Particles.* Wiley, 470 pp.

Van Vleck, J. H., 1947a: Absorption of microwaves by oxygen. *Phys. Rev.*, **71,** 413–424.

Van Vleck, J. H., 1947b: Absorption of microwaves by water vapor. *Phys. Rev.*, **71,** 425–433.

Vant, M. R., R. B. Gray, R. O. Ramseier, and V. Makios, 1974: Dielectric properties of fresh sea ice at 10 and 35 GHz. *J. Appl. Phys.*, **45,** 4712–4717.

Walko, R. L., L. E. Band, J. Baron, T. G. F. Kittel, R. Lammers, T. J. Lee, R. A. Pielke, C. Tague, C. J. Tremback, 1996: Coupled atmosphere-terrestrial ecosystem-hydrology models for environmental modeling. in preparation.

Wang, J. R., 1985: Effect of vegetation on soil moisture sensing observed from orbiting microwave radiometers. *Remote Sens. Environ.*, **17,** 141–151.

Wang, J. R., 1995: Some features observed by the L-band push broom microwave radiometer over the Konza Prairie during 1985-1989. *J. Geophys. Res.*, **100,** 25469–25479.

Wang, J. R., and B. J. Choudhury, 1981: Remote sensing of soil moisture content over bare field at 1.4 GHz frequency. *J. Geophys. Res.*, **86,** 5277–5282.

Wang, J. R., and T. J. Schmugge, 1980: An empirical model for the complex dielectric permittivity of soils as a function of water content. *IEEE Tran. Geosci. and Remote Sensing,* **GE-18,** 288–295.

Wang, J. R., P. E. O'Neill, T. J. Jackson, and E. T. Engman, 1983: Multifrequency measurements of the effects of soil moisture, soil texture, and surface roughness. *IEEE Tran. Geosci. and Remote Sensing,* **GE-21,** 44–51.

Warren, S. G., 1984: Optical constants of ice from the ultraviolet to the microwave. *Applied Optics*, **23,** 1206–1225.

Waters, J. R., 1976: Absorption and emission by atmospheric gases. Meeks, M. L., editor, *Methods of Experimental Physics,* **12B,** Academic Press Inc.,

Webster, W. J., T. T. Wilheit, D. B. Ross, and P. Gloersen, 1976: Spectral characteristics of the microwave emission from a wind-driven foam-covered sea. *J. Geophys. Res.*, **81,** 3095–3099.

Welch, R., and M. Ehlers, 1987: Merging multiresolution SPOT HRV and Landsat TM data. *Photogram. Eng. Remote Sens.,* **53,** 301–303.

Wentz, F. J., 1983: A model function for ocean microwave brightness temperatures. *J. Geophys. Res.*, **88,** 1892–1908.

Wentz, F. J., 1988: *User's Manual SSM/I Antenna Temperature Tapes.* Remote Sensing Systems Technical Report 032588, 1101 College Ave., Suite 220, Santa Rosa, CA, 24 pp.

Wentz, F. J., 1992: Measurement of oceanic wind vector using satellite microwave radiometers. *IEEE Tran. Geosci. and Remote Sensing,* **30,** 960–972.

Westwater, E. R., 1972: *Microwave Emission from Clouds.* NOAA Tech. Rep. 219-WPL 18, WPL, Boulder, CO, 43 pp.

Wetzel, P. J., 1978: *A Detailed Parameterization of the Atmospheric Boundary Layer.* PhD dissertation, Colorado State University, 195 pp.

Wetzel, P. J., and J.-T. Chang, 1987: Concerning the relationship between evapotranspiration and soil moisture. *J. Climate and Appl. Meteor.*, **26,** 18–27.

Wetzel, P. J., and J.-T. Chang, 1988: Evapotranspiration from nonuniform surfaces: a first approach for short-term numerical weather prediction. *Mon. Wea. Rev.*, **116,** 600–621.

Wetzel, P. J., and R. H. Woodward, 1987: Soil moisture estimation using GOES-VISSR infrared data: A case study with a simple statistical method. *J. Climate and Appl. Meteor.*, **26,** 107–117.

Wetzel, P. J., D. Atlas, and R. H. Woodward, 1984: Determining soil moisture from geosynchronous satellite infrared data: A feasibility study. *J. Climate and Appl. Meteor.*, **23,** 375–391.

Wilheit, T. T., 1978a: Radiative transfer in a plane stratified dielectric. *IEEE Tran. Geosci. Electron.*, **GE-16,** 138–143.

Wilheit, T. T., 1978b: A review of applications of microwave radiometry to oceanography. *Boundary-Layer Meteor.*, **13,** 277–293.

Wilheit, T. T., 1979a: The effect of wind on the microwave emission from the ocean's surface at 37 GHz. *J. Geophys. Res.*, **84,** 4921–4926.

Wilheit, T. T., 1979b: A model for the microwave emissivity of the ocean's surface as a function of wind speed. *IEEE Tran. Geosci. Electron.*, **GE-17,** 244–249.

Wilheit, T. T., A. T. C. Chang, M. S. V. Rao, E. B. Rodgers, and J. S. Theon, 1977: A satellite technique for quantitatively mapping rainfall rates over the oceans. *J. Appl. Meteor.*, **16,** 551–559.

Wilheit, T., A. T. C. Chang, and A. S. Milman, 1980: Atmospheric corrections to passive microwave observations of the ocean. *Boundary-Layer Meteor.*, **18,** 65–77.

Wilke, G. D., and M. J. McFarland, 1986: Correlations between Nimbus-7 Scanning Multichannel Microwave Radiometer data and an antecedent precipitation index. *J. Climate Appl. Meteor.*, **25,** 227–238.

Wolberg, G., 1990: *Digital Image Warping.* IEEE Computer Society Press, Los Alamitos, CA, 318 pp.

Wood, E. F., D.-S. Lin, M. Mancini, D. Thongs, P. A. Troch, T. J. Jackson, J. S. Famiglietti, and E. T. Engman, 1993: Intercomparisons between passive and active microwave remote sensing, and hydrological modeling for soil moisture. *Adv. Space Res.*, **13,** (5)167–(5)176.

Wu, R., and J. A. Weinman, 1984: Microwave radiances from precipitation clouds containing aspherical ice, combined phase, and liquid hydrometeors. *J. Geophys. Res.*, **89,** 7170–7178.

Wu, S. T., and A. K. Fung, 1972: A noncoherent model for microwave emissions and backscattering from the sea surface. *J. Geophys. Res.*, **77,** 5917–5929.

Xue, Y., P. J. Sellers, J. L. Kinter III, and J. Shukla, 1991: A simplified biosphere model for global climate studies. *J. Climate*, **4,** 345–364.

Zhang, D., and R. A. Anthes, 1982: A high-resolution model of the planetary boundary layer — sensitivity tests and comparisons with SESAME-79 data. *J. Appl. Meteor.*, **21,** 1594–1609.

Ziegler, C. L., W. J. Martin, R. A. Pielke, and R. L. Walko, 1995: A modeling study of the dryline. *J. Atmos. Sci.*, **52,** 263–285.

Ziltinkevich, S. S., 1970: *Dynamics of the Atmospheric Boundary Layer.* Hydrometeorol, Leningrad.